THE UNIVERSITY OF
SYDNEY

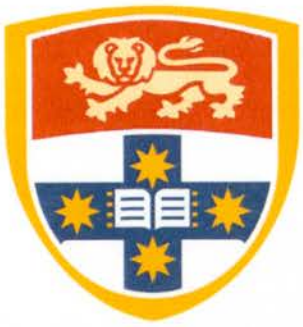

THE UNIVERSITY OF SYDNEY

HEAT TRANSFER IN MICROCHANNELS - TAYLOR FLOW

A thesis submitted for the degree of

Doctor of Philosophy

by

Sharon Shui Yee Leung

School of Chemical and Biomolecular Engineering

The University of Sydney

March 2012

Declaration

I declare the work presented in this thesis is to the best of my knowledge original, except as acknowledged in the text, and has not been submitted for a degree at any other university. Some parts of this research work have been published and a list of publications arising from this research is included in this thesis.

Sharon Shui Yee Leung

March, 2012

Acknowledgement

I wish to express my upmost gratitude to the many people for their continual support towards the successful completion of this thesis:

First and foremost, I am heartlily thankful to my supervisors Professors Brian S. Haynes and David F. Fletcher. Their invaluable guidance, support and encouragement througout my PhD enabled me to develop an understanding of the subject. They have introduced me to the world of academic research and help me develop the important research skills of attention-to-detail, objectivity, critical thinking and respect for scholarships.

The financial support from the Endeavour International Postgraduate Research Scholarship (EIPRS) granted by the Australian Department of Education, Science and Training (DEST), and the International Postgraduate Award (IPA) by the University of Sydney are gratefully acknowledge.

I would like to thank Professor Tim Langrish, Dr. Alejandro Montoya, Dr. Jeffrey Shi, Dr. Bogumil Eichstaedt, Dr. Don Chiou, Gary Towell, Alex Farago and staff members of the School of Chemical and Biomolecular Engineering for their support and assistance. My sincere thanks also go to Dr. Raghvendra Gupta, Dr. Yang Liu and Azadeh Najfi Asadolahi. Discussions on the subject with them were always enjoyable and inspiring. It is pleasure to thank all members of the combusiton group and my fellow postgraduate students in the Department for their friendship and help. Many thank to Joe Buda and his family who always treat me as a member of the family. I am also indebted to Dr. Alex Cheung and his family for taking good care of me when I first arrived in Australia.

Last but not least, I would like to express my deepest gratitude to my family for their constant encouragement and belief in me. This thesis would not have been possible without their unconditional love and support.

Abstract

With the rapid development of micro-reactors and compact heat exchangers, the unique thermal-hydraulic characteristics of gas-liquid, non-boiling Taylor flow in microchannels have attracted much attention recently. For proper design of micro-systems operating under Taylor flow conditions, it is important to understand the transport processes and hence the underlying heat transfer mechanisms. This work aims to obtain more insights into the hydrodynamics of gas-liquid Taylor flow in microchannels and their relation to heat transfer by performing systematic adiabatic visualization tests and heat transfer experiments for constant wall heat flux boundary conditions.

Investigations into the flow behaviour and heat transfer characteristics of Taylor flow in the vertical upward direction were carried out in a circular channel of 2.00 mm internal diameter. Nitrogen was used as the gas phase and three fluids, namely water, 50 wt% ethylene glycol/water mixture and pure ethylene glycol, were used as the liquid phase to cover a wide range of Capillary numbers ($0.001 < Ca < 0.180$). Three circular T-junction mixers with different diameters were used to generate gas bubbles and liquid slugs of different lengths (1–220d) with controlled mixture velocities ($0.10 < U_{TP} < 0.53$ m s^{-1}, $10 < Re_{TP} < 1100$) and homogeneous void fractions ($0.03 < \beta < 0.90$).

Taylor flow with regular bubble and slug lengths was characterized by performing visualization tests under isothermal condition (21 °C). The thickness of the liquid film surrounding the gas bubble is found to increase with increasing Ca and to agree well with the established literature (Irandoust and Andersson, 1989, Aussillous and Quéré, 2000). Accurate predictions of bubble and slug lengths, which are important parameters for pressure drop, heat and mass transfer for Taylor flow in microchannels, are essential for reactor and process designs. Generally, good agreement was found between the generated bubble lengths and the scaling law modified from Garstecki *et al.* (2006). For flows for which the curvature of the bubble caps and tails can be neglected, the corresponding slug length can be approximated as $L_S \approx L_B(1-\beta)/\beta$.

A multi-block heating section, which was calibrated and validated carefully with single-phase flow, was used to perform systematic heat transfer experiments for well-characterized Taylor flow for constant wall heat flux boundary conditions. From a parametric study, the mixture velocity, slug length, homogenous void fraction and liquid properties were identified as key

factors governing heat transfer enhancement of Taylor flow. The two-phase Nusselt number was found to increase with increasing mixture velocity, decreasing slug length and for systems with a thinner liquid film. Depending on the mixture velocity, unit cell length and the fluid used, an optimal homogeneous void fraction, varying between $0.1 < \beta < 0.3$, was noted. The maximum heat transfer enhancement achieved in the present study was 3.2 times that of single-phase fully-developed laminar flow.

Three physical mechanisms governing the heat transfer of gas-liquid Taylor flow were suggested for systems with constant wall heat flux boundary conditions imposed. The bubble film provides a significant energy storage region, with that energy being taken up by mixing with the overtaking slug and hence most of the heat is carried by the liquid slug. Since the flow and heat transfer behaviour in the slug region remains hydrodynamically and thermally developing laminar flow, the slug heat transfer coefficient ($Nu_L^* = Nu_{TP} \cdot L_{UC}/L_S$) is found to be well correlated by a dimensionless slug length equivalent to an inverse Graetz number based on the slug length ($L_S^* = L_S/(Re_{TP} \cdot Pr \cdot d)$). Interactions between the bubble film and the recirculating flow in the slug and heat transfer from the wall in the slug region are found to depend strongly on the thickness of the bubble film, the size of the recirculation zones in the slug region and the efficiency of the recirculation, which are strong functions of the Capillary number (Ca). An empirical model correlating all the identified dimensionless groups was proposed for heat transfer of Taylor flow, taking the form

$$Nu_L^* = Nu_{LO} + c(L_S^*)^p(Ca)^q$$

where $c = 0.13$, $p = -0.46$ and $q = -0.30$.

The effect of gravity on the bubble behaviour for horizontal gas-liquid Taylor flow in millimetre-sized channels was examined and quantified. From the high quality white light images, significant bubble asymmetry was observed for nitrogen-ethylene glycol Taylor flow in three circular channels of different internal diameters (d = 1.12, 1.69, 2.12 mm giving Bond numbers (Bo) of 0.287, 0.653 and 1.028). A parabolic drainage profile inside the liquid film surrounding the bubble was noted through performing Micro-Particle Image Velocimetry (μPIV) measurements in that region. A simplified model based on Nusselt's solution for laminar film condensation on a horizontal tube was derived to describe the drainage velocity profile in the liquid film at a cross-section away from the bubble ends and was able to explain the observed tilt of the bubble. A non-dimensional analysis of the model

showed that the ratio of the average drainage to bubble velocities is a function of the Bond and Capillary numbers. The gravitational effects on the bubble behaviour vanish for small value of Bo and/or Ca or as $Ca \rightarrow \infty$. Heat transfer experiments showed that gravitational effects had no significant effect on Taylor flow heat transfer for the conditions studied.

The suitability of extending the experimental techniques which were developed for Taylor flow to study the flow and heat transfer characteristics of non-boiling, gas-liquid annular flow in microchannels was also explored. To reduce the time required to reach steady state operation, a bare tube heating test section with a short thermal time constant (~5 ms) was constructed to replace the multi-block heating system. Preliminary visualization and heat transfer tests in a vertical upward flow in a 2.00 mm diameter tube for different flow conditions ($2 < Re_L < 217$, $530 < Re_G < 2890$) were performed to identify the potential experimental challenges. Tiny bubbles were observed in the liquid film when ethylene glycol was used as the liquid phase. The transient waviness at the gas-liquid interface for nitrogen-water annular flow was captured successfully and found to be asymmetric. However, difficulties in identifying the gas-liquid interface at the near wall region arose from the combination of the inner surface curvature and the mismatch of refractive indices between the silica tube and water. The cooling ability of gas-liquid annular flow was found to be much more effective than that of the single-phase flow. The heat transfer augmentation was attributed to the combination of evaporation of the liquid film and convective heat transfer. Using water as the liquid phase, the effect of evaporation cannot be decoupled from the convective heat transfer.

In conclusion, the key contribution contained in this work is a better understanding of the hydrodynamics and their relation to heat transfer of non-boiling, gas-liquid Taylor flow in circular microchannels. A new vision of the effect of gravity for horizontal gas-liquid Taylor flow in millimetre-size channels which has generally been neglected in the past is also provided. Additionally, potential experimental challenges for a comprehensive study of the hydrodynamics and heat transfer characteristics of non-boiling, gas-liquid annular flow in microchannels, which has not been studied systematically in the literature, are identified through extending the techniques developed for Taylor flow.

Aussillous, P. and Quéré, D. 2000. Quick deposition of a fluid on the wall of a tube. *Physics of Fluids,* 12, 2367-2371.

Garstecki, P., Fuerstman, M. J., Stone, H. A. and Whitesides, G. M. 2006. Formation of droplets and bubbles in a microfluidic T-junction - scaling and mechanism of break-up. *Lab on a Chip,* 6, 437-446.

Irandoust, S. and Andersson, B. 1989. Liquid-film in Taylor flow through a capillary. *Industrial & Engineering Chemistry Research,* 28, 1684-1688.

List of Publications

Journals

Leung, S. S. Y., Liu, Y., Fletcher, D. F. and Haynes, B. S. 2010. Heat transfer in well-characterised Taylor flow. *Chemical Engineering Science*, 65, 6379-6388.

Leung, S. S. Y., Gupta, R., Fletcher, D. F. and Haynes, B. S. 2012. Effect of flow characteristics on Taylor flow heat transfer. *Industrial & Engineering Chemistry Research*, 51, 2010-2020.

Leung, S. S. Y., Gupta, R., Fletcher, D. F. and Haynes, B. S. 2012. Gravitational effect on Taylor flow in horizontal microchannels. *Chemical Engineering Science*, 69, 553-564.

Conference Poster Presentation

Leung, S. S.Y., Gupta, R., Hägnefelt, H., Fletcher, D. F. and Haynes, B. S. Gravitational effect on Taylor flow in horizontal microchannels. *2nd Australian and New Zealand Micro and Nanofluidics Symposium 2011*, Sydney, 28-29 April 2011.

Table of Contents

List of Figures

List of Tables

Nomenclature

a, b	Constant
A_M	Cross-sectional area of a T-junction mixer (m^2)
$\Delta A_{\text{Projected}}$	Projected area of the bubble (m^2)
A_S	Surface area (m^2)
B_G	Pressure gradient in the gas phase (Pa m^{-1})
B_L	Pressure gradient in the liquid phase (Pa m^{-1})
Bo	Bond number ($\Delta\rho d^2 g/\sigma$)
c_1, c_2, c_3	Constant
C_{loss}	Overall heat loss constant (W K^{-1})
C_i^a	Thermal conductance between block i and the environment (W K^{-1})
$C_{i,i+1}^b$	Thermal conductance between block i and $i+1$ (W K^{-1})
Ca	Capillary number ($\mu_L U_{TP}/\sigma$)
$Ca_{L,M}$	Mixer Capillary number ($\mu_L Q_L/\sigma A_M$)
$\hat{C}_p$	Average specific heat capacity (J kg^{-1} K^{-1})
$C_{p,wall}$	Specific heat capacity of wall (J kg^{-1} K^{-1})
d	Channel diameter (m)
d_B	Bubble diameter (m)
d_{particle}	Diameter of fluorescent particles (m)
d_M	Internal diameter of a circular T-junction mixer (m)
e, f	Exponents
F_B	Bubble frequency (Hz)
$f_{n,i}, f_{t,i}$	Frame numbers when the i^{th} bubble nose and tail appear on the video image
g	Acceleration due to gravity (m s^{-2})
Gz	Graetz number ($L/(Re \cdot Pr \cdot d)$)
h	Heat transfer coefficient (W m^{-2} K^{-1})
Δh	Displacement of the bubble (m)
$\hat{H}$	Average specific enthalpies (J kg^{-1})
H_{lv}	Enthalpy of vaporization (J kg^{-1})
h_S	Slug heat transfer coefficient (W m^{-2} K^{-1})
h_{TP}	Two-phase eat transfer coefficient (W m^{-2} K^{-1})

k_L	Thermal conductivity (W m^{-1} K^{-1})
L	Length (m)
L_B	Bubble length (m)
l_e	Bubble length developed in the expansion stage (m)
$L_{heating}$	Total heating length (m)
L_S	Liquid slug length (m)
L_S^*	Dimensionless slug length ($L_S/(Re_{TP} \cdot Pr \cdot d)$)
L_{UC}	Unit cell length (m)
$\dot{m}$	Total mass flow rate (kg s^{-1})
$\dot{m}_G$	Gas mass flow rate (kg s^{-1})
M_G	Molecular weight of gas phase (kg mol^{-1})
M_L	Molecular weight of liquid phase (kg mol^{-1})
$\dot{m}_{vi}$	Total mass of liquid evaporated from the entrance to block i (kg s^{-1})
n	Exponent
Nu^*	Normalized Nusselt number (Nu_{TP}/Nu_{LO})
Nu_i	Experimental Nusselt number of block i ($h_i d/k_L$)
Nu_{LO}	Fully-developed liquid-only Nusselt number for constant heat flux conditions
Nu_L^*	Apparent slug Nusselt number ($Nu_L^* = Nu_{TP} L_{UC}/L_S$)
Nu_S	Slug Nusselt number ($h_S d/k_L$)
Nu_{TP}	Two-phase Nusselt number ($h_{TP} d/k_L$)
p, q	Exponents
P	Pressure (Pa)
P_{sat}	Saturated vapour pressure (Pa)
Pe	Péclet number ($Re_{TP} \cdot Pr$)
Pr	Prandtl number ($C_p \mu_L/k_L$)
Q_{ai}	Heat loss to the ambient for block i (W)
q_{av}	Average wall heat flux (W m^{-2})
Q_E	Heat needed for liquid phase evaporation (W)
Q_G	Gas volumetric flow rate (m^3 s^{-1})
Q_f, Q_{exch}	Heat transferred to the fluid (W)
Q_i	Heat input to block i (W)
$Q_{i,i-1}$, $Q_{i,i+1}$	Heat transferred from block i to blocks $i-1$ and $i+1$ (W)

q_i	Wall heat flux to block i (W m^{-2})
Q_i	Heat input to block i (W)
Q_{in}	Total heat input (W)
Q_L	Liquid volumetric flow rate (m^3 s^{-1})
Q_{loss}	Heat loss to the environment (W)
r	Radial position (m)
r_0, r_1	Radial positions of the recirculation centre and the dividing streamline (m)
r_F	Radial position of the gas-liquid interface of the fully-developed film (m)
R	Channel radius (m)
R_B	Bubble radius (m)
R_i	Resistance of band heater i (Ω)
Re_G	Gas Reynolds number ($U_G \rho_G d/\mu_G$)
Re_L	Liquid Reynolds number ($U_L \rho_L d/\mu_L$)
Re_{TP}	Two-phase Reynolds number ($U_{TP} \rho_L d/\mu_L$)
S	Height of a rectangular channel (m)
Δt	Time difference (s)
T_a	Ambient temperature (K)
T_{bi}	Mean fluid temperature at the centre of block i (K)
T_{in}	Inlet temperature (K)
ΔT_{lm}	Log mean temperature difference (K)
T_{out}	Outlet temperature (K)
T_{wi}	Mean wall temperature for block i (K)
u	Velocity component in the x-direction (m s^{-1})
U	Velocity (m s^{-1})
U_B	Bubble velocity (m s^{-1})
U_d	Drainage velocity (m s^{-1})
U_F	Film velocity (m s^{-1})
U_G	Superficial gas velocity (m s^{-1})
U_L	Superficial liquid velocity (m s^{-1})
U_{TP}	Two-phase mixture velocity, $U_{TP} = U_G + U_L$ (m s^{-1})
v	Velocity component in the y-direction (m s^{-1})
V	Input voltage (V)
ΔV	Volume displaced due the bubble rise (m^3)

$v(r)$	Relative velocity in the liquid slug at the radial position r (m s^{-1})
V_B	Volume of bubble at the core (m^3)
V_{body}	Body volume of wall (m^3)
v_x	Local axial velocity (m s^{-1})
V_S	Volume of slug at the core (m^3)
w	Width of a rectangular channel (m)
w_B	Bubble width (m)
We	Webber number ($\rho_L U_{TP}^2 d/\sigma$)
x_G	Mass fraction of the gas phase
x	Cartesian coordinate ($R\theta$) (m)
y	Cartesian coordinate ($R - r$) (m)
z	Axial location (m)
ΔZ	Distance moved by the bubble nose in a time of τ (m)

Greek Symbols

$\alpha_1, \alpha_2, \alpha_3$	Constants
β	Homogeneous void fraction (U_G/U_{TP})
δ_F	Film thickness (m)
δ_z	Displacement of the moving interface within one frame period (m)
ε_G	Void fraction
θ	Circumferential position
θ_C	Contact angle
ρ_L	Density of liquid phase (kg m^{-3})
ρ_G	Density of gas phase (kg m^{-3})
ρ_{wall}	Density of wall (kg m^{-3})
$\Delta\rho$	Density difference ($\rho_L - \rho_G$) (kg m^{-3})
μ_b	Liquid viscosity at the bulk fluid temperature (kg m^{-1} s^{-1})
μ_G	Viscosity of gas phase (kg m^{-1} s^{-1})
μ_L	Viscosity of liquid phase (kg m^{-1} s^{-1})
μ_w	Liquid viscosity at the heat transfer boundary surface temperature (kg m^{-1} s^{-1})
ξ	Normalized radial position (r/R)
ξ_B	Dimensionless interfacial radius (R_B/R)
σ	Surface tension (N m^{-1})

τ	Frame period (s)
τ_B	Bubble period (s)
τ_{wall}	Thermal time constant of the wall material (s)

Subscripts

b	Bulk
B	Bubble
cal	Calculated value
cr	Critical value
exp	Experimental value
G	Gas phase
i	Zone i
in	Inlet
L	Liquid phase
Lo	Liquid-only
out	Outlet
ref	Reference
S	Liquid slug
TP	Two-phase
w	Wall
z	Axial location

Chapter 1
Introduction

With the rapid development of micro-fabrication techniques, there is a significant drive towards the miniaturisation of process equipment in many industrial applications, such as chemical processing, electronics cooling, compact heat exchangers, lab-on-a-chip devices, biochemical analysis instruments and micro-electro-mechanical systems (MEMS). These applications generally involve the use of microchannels with the characteristic length of the order of a few hundred micrometers to a few millimetres. The reduced length scale results in larger surface-to-volume ratio, offering significant potential to enhance the heat and mass transfer rates over those for conventional-sized systems. Implementation of process intensification, which is a practice of miniaturising and integrating process equipment to provide significant production benefits, such as requiring less capital and operating expenditure, reducing the amount of material undergoing processing and making the processes safer, is therefore feasible. However, challenges in understanding the fluid dynamics and transport behaviour arise in systems with a reduced length-scale and have lead to significant research and publications on transport processes in micro-structured devices over the last few decades.

When the experimental conditions are consistent with the theoretical ones, flow and heat transfer behaviour of single-phase flow in microchannels can be well predicted by correlations extrapolated from macro-scale systems (Hetsroni *et al.*, 2005, Park and Punch, 2008). Due to the small length and velocity scales, single-phase flow in microchannels is often laminar, limiting the potential for further heat and mass transfer enhancement offered by micro-structure devices. Therefore, additional means are required to promote fluid mixing in order to increase the heat and mass transfer rates in microchannels.

In heat transfer applications, there is a strong demand for more effective cooling for advanced micro-technology, especially microchip processers for which the advancement is limited by the cooling ability. This has led to much recent microchannel research focusing on three main areas to enhance heat transfer performance: (1) using physical structures like micro-fins (Foong *et al.*, 2009, Hong and Cheng, 2009) and tortuous flow paths (Geyer *et al.*, 2006, Rosaguti *et al.*, 2007) to enhance local mixing, (2) use of flow boiling to provide high heat

removal capability (Kandlikar, 2004, Thome, 2004), and (3) employing gas-liquid two-phase flow without phase change to promote fluid mixing and enhance the heat transfer rate over that of the fully-developed single-phase laminar flow (Hetsroni *et al.*, 2009, Betz and Attinger, 2010). This study focuses on the last of these.

For gas-liquid flow in microchannels, the flow pattern can be bubbly, Taylor, slug-annular, annular and churn flow. Taylor flow is one of the most common two-phase flow patterns encountered in nature and industrial applications. This flow regime is characterised by regular capsular gas bubbles separated by co-current liquid slugs and surrounded by a thin liquid film at the tube wall. Due to the introduction of gas, the flow characteristics of Taylor flow differ markedly from those of single-phase flow (Taylor, 1961). Internal recirculation (in a reference frame moving with the bubble) within the liquid slug promotes radial mixing of the fluid, resulting in significant enhancements of heat and mass transfer rates. In addition, the separation of two consecutive liquid slugs by a gas bubble inhibits axial mixing and gives a larger interfacial area and a shorter diffusion path between the gas and liquid phases and/or between the liquid and the solid wall. These unique thermal-hydraulic characteristics of the non-boiling, gas-liquid Taylor flow make it especially attractive to industries focusing on process intensification and miniaturization.

While the hydrodynamics and mass transfer in Taylor flow have been studied extensively, the study of convective gas-liquid Taylor flow heat transfer without phase change in microchannels has received relatively little attention. Several experimental and numerical studies have been carried out to understand the heat transfer behaviour and various empirical two-phase heat transfer correlations have been proposed. However, no general form is noted among them and the underlying physical mechanisms governing the hydrodynamics and heat transfer, knowledge of which is essential for optimal process design and control of micro-systems, are not yet fully understood. Therefore, a fundamental understanding of the heat transfer augmentation brought about by non-boiling, gas-liquid Taylor flow is required.

The objective of the present study is to gain more insights into the hydrodynamics and heat transfer of Taylor flow in microchannels through performing systematic experiments across a wide range of conditions. The effects of the mixture velocity, homogeneous void fraction, fluid properties and geometry of the mixer, parameters which can be manipulated directly, on the hydrodynamics and hence the heat transfer rates are examined in detail. Physics-based

correlations that would be helpful for designs of micro-structured systems employing Taylor flow are deduced from new experimental data.

1.1 Thesis Structure

In Chapter 2, a review of the available literature on the flow characteristics and heat transfer rates of Taylor flow in microchannels is provided and knowledge gaps are identified.

In Chapter 3, detailed descriptions of the experimental setup and conditions are presented. Data acquisition and reduction procedures are provided together with the results of the single-phase validation experiments.

In Chapter 4, the flow characteristics of gas-liquid Taylor flow obtained for isothermal conditions (21 °C) across a wide range of conditions are presented. A modified scaling law based on the Garstecki approach is proposed to predict the length of bubbles generated in systems with differences in the tube diameter between the mixer and the test section.

In Chapter 5, a comprehensive study of the heat transfer behaviour of non-boiling gas-liquid Taylor flow is conducted. The mixture velocity, homogeneous void fraction and thickness of the liquid film surrounding the gas bubbles are recognized as important parameters governing Taylor flow heat transfer.

In Chapter 6, three pathways governing heat transfer in Taylor flow are suggested. A correlation is developed specifically for systems using water as the liquid phase. Based on the results obtained from all the fluid systems studied, an empirical heat transfer correlation is developed for general application.

In Chapter 7, the effect of gravity on the flow behaviour of horizontal gas-liquid Taylor flow in millimetre-sized channels is examined and quantified.

In Chapter 8, preliminary work on the flow and heat transfer characteristics of gas-liquid annular flow in microchannels is presented. The challenges to be overcome prior to a comprehensive annular flow study are identified.

Finally, Chapter 9 presents the conclusions and recommendations for future work.

Chapter 2
Literature Review

Gas-liquid, non-boiling flow in microchannels has shown great potential to enhance heat and mass transfer rates over single-phase flow. In the last few decades, significant efforts have gone into identifying the flow regime map (Triplett *et al.*, 1999a, Yang and Shieh, 2001, Zhao and Bi, 2001, Waelchli and von Rohr, 2006, Shao *et al.*, 2009) and determining the applicability of the correlations developed for macro-channels to predict the pressure drop and void fraction of two-phase flow in microchannels (Bao *et al.*, 1994, Triplett *et al.*, 1999b, Bao *et al.*, 2000, Saisorn and Wongwises, 2008, Cioncolini *et al.*, 2010).

For Taylor flow in particular, the hydrodynamic characteristics, including bubble velocity, liquid film thickness, void fraction, pressure loss (Fairbrother and Stubbs, 1935, Bretherton, 1961, Taylor, 1961, Suo and Griffith, 1964, Irandoust and Andersson, 1989a, Thulasidas *et al.*, 1995, Aussillous and Quéré, 2000, Kreutzer *et al.*, 2005a, 2005b, Liu *et al.*, 2005, Akbar and Ghiaasiaan, 2006, Walsh *et al.*, 2009, Warnier *et al.*, 2010), and the mass transfer enhancement (Irandoust and Andersson, 1989b, Bercić and Pintar, 1997, Kreutzer *et al.*, 2001) have been extensively reported. Comprehensive reviews have also been published (Ghiaasiaan and Abdel-Khalik, 2001, Kreutzer *et al.*, 2005c, Angeli and Gavriilidis, 2008, Gupta *et al.*, 2010a). There is also a growing interest in the study of convective gas-liquid Taylor flow heat transfer without phase change in microchannels (Oliver and Wright, 1964, Oliver and Young Hoon, 1968, Horvath *et al.*, 1973, Fukagata *et al.*, 2007, Lakehal *et al.*, 2008, Betz and Attinger, 2010, Gupta *et al.*, 2010b, He *et al.*, 2010, Walsh *et al.*, 2010, Muzychka *et al.*, 2011). In this chapter, a review of the hydrodynamic characteristics of non-boiling, gas-liquid two-phase flow in microchannels and the associated heat transfer mechanisms is presented.

2.1 Definition of microchannels

As the channel size is reduced, certain physical phenomena negligible in conventional channels become more significant. The relative importance of different forces, including the gravitational, interfacial, inertial and viscous forces, were examined in Gupta *et al.* (2010a)

through introduction of the relevant non-dimensional numbers governing multiphase flow in microchannels. Table 2.1 gives a list of the relevant non-dimensional numbers. The importance of choosing the right characteristic velocity and length-scale to define the non-dimensional terms for a particular problem was also highlighted (Gupta *et al.*, 2010a). For example, to characterise the film flow for the thin liquid film surrounding the gas bubble in Taylor flow and the gas core in annular flow at the wall, the liquid film thickness and the average film velocity should be used as the characteristic length-scale and velocity, respectively. In Taylor flow, the mixture velocity can be used as a characteristic velocity as the bubble velocity is not known a priori.

Table 2.1: A list of the non-dimensional numbers characterising the multiphase flow in microchannels. Taken from Gupta *et al.* (2010a).

Non-dimensional parameters	Physical Interpretation	Formula
Bond/ Eötvös number	$\frac{\text{Gravitational force}}{\text{Surface tension force}}$	$\frac{\Delta\rho d^2 g}{\sigma}$
Froude number	$\frac{\text{Inertial force}}{\text{Gravitational force}}$	$\frac{\rho_L U^2}{\Delta\rho g d}$
Capillary number	$\frac{\text{Viscous force}}{\text{Surface tension force}}$	$\frac{\mu_L U}{\sigma}$
Reynolds number	$\frac{\text{Inertial force}}{\text{Viscous force}}$	$\frac{\rho_L U d}{\mu_L}$
Weber number	$\frac{\text{Inertial force}}{\text{Surface tension force}}$	$\frac{\rho_L U^2 d}{\sigma}$

A critical Bond number (Bo_{cr}), below which the surface tension forces dominate the gravitational forces, was generally accepted to distinguish small channels from conventional channels. Bretherton (1961) proposed a value of 4.37 for Bo_{cr}. For value below which ($Bo <$ 4.37) he demonstrated that the bubble rise velocity vanished in a vertical channel filled with the liquid phase, indicating a negligible gravitational effect on the bubble movement. Due to

the diminished importance of gravity, stratified flow is not observed in gas-liquid flow in microchannels. Barnea *et al.* (1983) applied a force balance between the surface tension and gravitational force at which stratified flow changes to slug flow to determined the critical Bond number as

$$Bo_{cr} = \frac{1}{\frac{\rho_L}{\rho_L - \rho_G} - \frac{\pi}{4}} \tag{2.1}$$

For gas-liquid flow with $\rho_G << \rho_L$, the critical Bond number is 4.7 which is very close to the value reported by Bretherton (1961). For a nitrogen-water system under atmospheric pressure, these criteria signify channel sizes $d < 5.7$ mm as microchannels.

In fact, there is much taxonomical discussion in the literature about what physical duct size earns the title ''microchannel'' (Bretherton, 1961, Brauner and Maron, 1992, Triplett *et al.*, 1999b, Ghiaasiaan and Abdel-Khalik, 2001, Chen *et al.*, 2006). Fouilland *et al.* (2010) highlighted that dimensional quantities inevitably give rise to arbitrary classifications. Therefore, they suggested that the nomenclature ''microchannel'' should be used as a qualitative descriptor implying channels much smaller than conventional and with a different balance of forces, especially the surface tension force, which is usually neglected in conventional channels. The same perception is adopted in this thesis.

2.2 Flow regime map

The distribution of the gas and liquid, and their interaction determines the behaviour of two-phase flow in a channel. The phase distribution is commonly called the flow pattern or flow regime. Since the flow characteristics of different flow regimes have strong influences on the critical thermo-hydraulic properties, such as the pressure drop, heat and mass transfer rates, correct prediction of two-phase flow patterns and flow pattern transition in microchannels is essential for successful application design and better control of micro-systems where two-phase flow is involved.

Though two-phase flow regimes in microchannels have been investigated extensively (Triplett *et al.*, 1999a, Yang and Shieh, 2001, Chen *et al.*, 2002a, Akbar *et al.*, 2003, Chung and Kawaji, 2004, Chen *et al.*, 2006, Pehlivan *et al.*, 2006, Waelchli and von Rohr, 2006, Ide

et al., 2007), a universal flow regime map does not seem to exist (Shao *et al.*, 2009). Nonetheless, six major gas-liquid flow configurations, namely bubbly, Taylor, Taylor-annular, churn, annular and dispersed flows, are identified in microchannels, depending on the relative gas and liquid properties, flow rates, inlet conditions, channel geometries and dimensions (Triplett *et al.*, 1999a, Shao *et al.*, 2009). Summarizing different flow regime maps available in the literature, Shao *et al.* (2009) suggested that using the superficial gas and liquid velocities as coordinates (U_G, U_L) provides the best representation of the transition between patterns.

Figure 2.1 shows (a) the general classification of different flow patterns using the superficial gas velocity (U_G) and the superficial liquid velocity (U_L) as coordinates and (b) the morphology of the representative flow regimes of air-water flow in a 1 mm and a 3 mm horizontal tube. At high liquid and low gas flow rates, gas bubbles with diameters significantly smaller than the channel diameter are distributed in the continuous liquid phase. At low gas and liquid flow rates, regular periodic Taylor bubbles which are longer than the channel diameter and with consecutive bubbles separated by a liquid slug are obtained. As the gas flow rate increases at low liquid flow rates, bubbles become longer and bubble coalescence may occur to give a continuous gas core with large-amplitude waves on the gas-liquid interface. This flow pattern is called Taylor-annular or slug-annular flow. A further increase in the gas velocity gives rise to annular flow with only small amplitude waves present on the gas-liquid interface. Churn flow appears at medium gas velocities and high liquid velocity due to either the instabilities that arise at the rear of the bubble to give dispersed bubbles or the occurrence of churning waves to give frothy slugs and droplets in the gas core (Triplett *et al.*, 1999a). Dispersed flow, in which the liquid is dispersed in the continuous gas as droplets with a small liquid film present at the wall, occurs at very high gas and liquid velocities. This flow pattern is rarely reported because it requires very high gas and liquid velocities to generate or it might have been included in the churn or annular flow regimes by some researchers (Shao *et al.*, 2009).

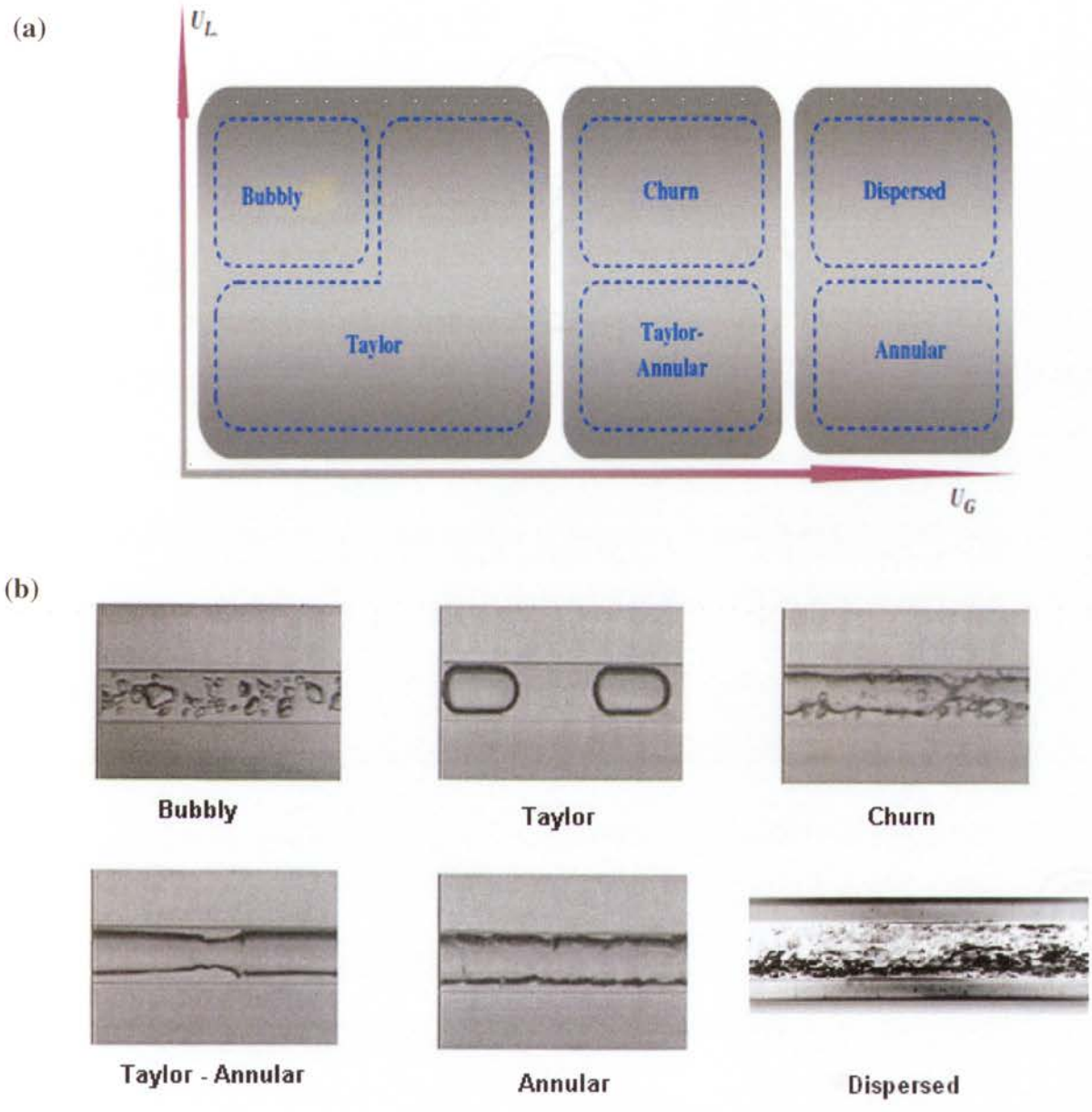

Figure 2.1: (a) General classification of flow patterns suggested by Shao *et al.* (2009) and (b) morphology of the bubbly, Taylor, churn, Taylor-annular and annular air-water flows obtained by Triplett *et al.* (1999a) from a horizontal circular tube of 1 mm diameter and dispersed air-water flow obtained by Yang and Shieh (2001) from a 3 mm tube.

2.2.1 Effect of wall wettability

The three-phase contact angle (θ_C), which is the angle between the solid wall and the gas-liquid interface in contact with it, is used to measure wettability of a liquid on solid wall. For $0° < \theta_C < 90°$, the liquid is considered as a partially wetting liquid, for which the wall is

always in contact with the liquid. For $90° < \theta_C < 180°$, the liquid is considered as a partially non-wetting liquid, for which dry flow (absence of a liquid film) may occur. The effect of wall wettability on the two-phase flow structures in microchannels was demonstrated (Barajas and Panton, 1993, Serizawa et al., 2002, Cubaud and Ho, 2004, Cubaud et al., 2006, Lee, C.Y. and Lee, S.Y. 2008). Figure 2.2 shows flow pattern morphologies for air-water flows in a d_h = 525 μm square channel of both hydrophilic and hydrophobic surfaces. It is clear that the liquid does not lubricate the wall well and the flows become asymmetric in the hydrophobic (non-wetted) channel. In this thesis, only two-phase flows in which a liquid film always exists on the wall are considered.

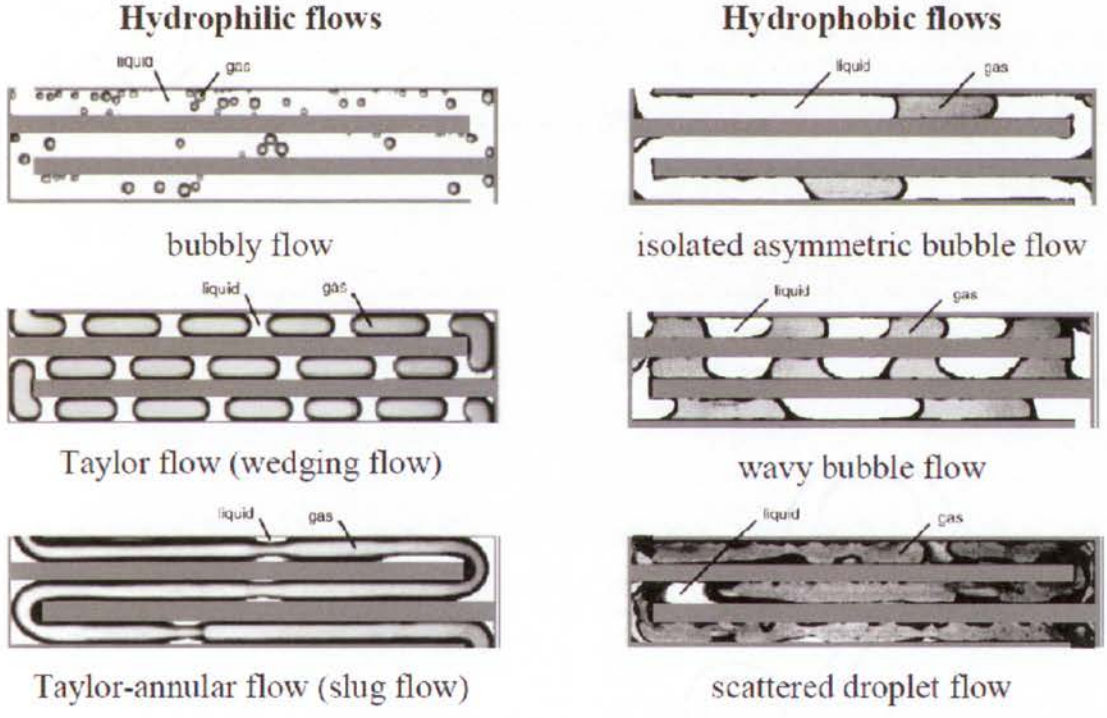

Figure 2.2: Effect of wall wettability on flow pattern morphologies for air-water flows in a square channel with d_h = 525 μm. The hydrophilic flows were carried out in a silicon channel with glass top ($\boldsymbol{\theta_C}$ ~ 9° for silicon and $\boldsymbol{\theta_C}$ ~ 25° for glass) and the hydrophobic flows were carried out in the same channel with Teflon coating ($\boldsymbol{\theta_C}$ ~ 120°). Taken from Cubaud et al., 2006.

2.2.2 Industrial applications

Typical operating conditions for different micro-chemical applications employing two-phase flow are shown in Figure 2.3. Since Taylor flow in microchannels occurs over a wide range of conditions (Figure 2.1) and is used in various industrial applications (Figure 2.3), a brief review of the main applications is presented in Table 2.2.

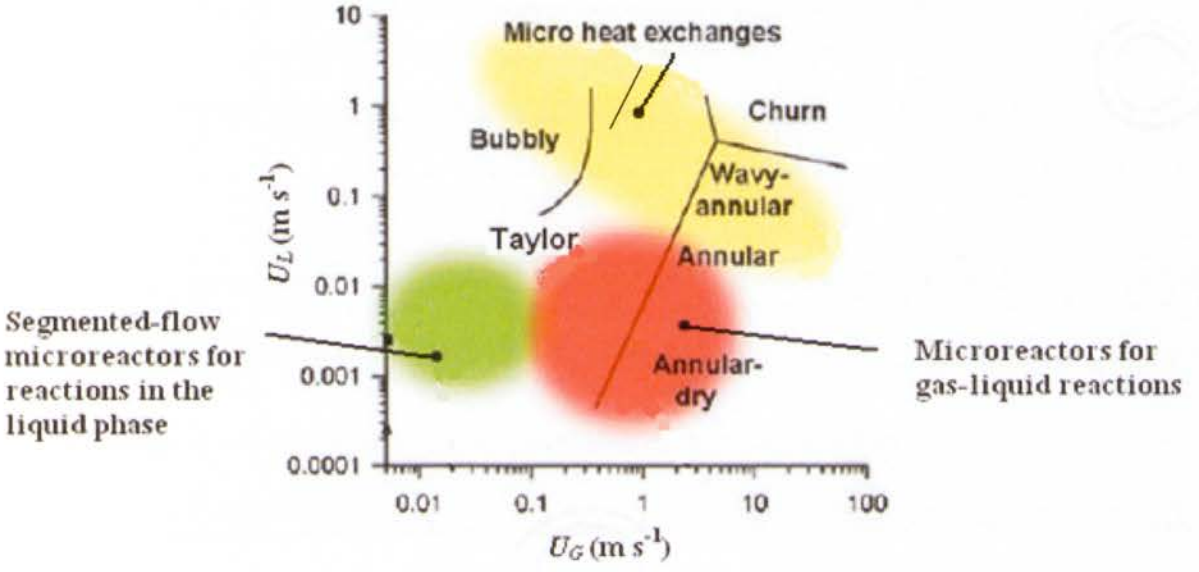

Figure 2.3: Typical operating conditions for different micro-chemical applications, modified from Günther and Jensen (2006).

Despite Taylor flow having been used in a few industrial applications, details of the flow characteristics and the resulting transport rates of heat, mass and momentum which are important information for rector designs and operations are not yet clear. Therefore, this thesis focuses on the study of the details of the hydrodynamics of non-boiling, gas-liquid Taylor flow in microchannels and hence provides better understanding of the underlying heat transfer mechanisms.

Table 2.2: Industrial applications of Taylor flow in microchannels.

Industrial Applications	Examples
Chemical processing	• Monolith catalytic reactor for gas-liquid-solid reactions (Kapteijn *et al.*, 2001, Nijhuis *et al.*, 2001, Kreutzer *et al.*, 2005c) • Catalyst hydrogenation (Kobayashi *et al.*, 2004) • Direct fluorinations (Chambers and Spink, 1999);
Biomedical	• Blood analysis (Thiers *et al.*, 1971) • DNA analysis (Burns *et al.*, 1998) • Cell stimulus and lysis (El-Ali *et al.*, 2005) • Lung airway opening (Suresh and Grotberg, 2005, Zheng *et al.*, 2007)
Electronics cooling	• Cooling of high performance electronics, supercomputers, high-powered X-ray, high-powered lasers (Zhao and Bi, 2001, Saisorn and Wongwises, 2008)
Heat exchangers	• Compact heat exchanger (Bao *et al.*, 2000) • High-flux heat exchanger in aerospace system, cryogenic cooling system in satellites (Zhao and Bi, 2001)
Chemical and material synthesis	• Studies of chemical kinetics and reaction pathways (Song *et al.*, 2003) • Synthesis of nano- and micro-particles (Khan *et al.*, 2004)

2.3 Taylor flow

Taylor flow is characterized by regular capsular gas bubbles separated by co-current liquid slugs and surrounded by a thin liquid film at the tube wall, as seen in Figure 2.1(b). This flow pattern is also known as slug flow, plug flow, bolus flow, segmented flow, intermittent flow and bubble-train flow. Due to the introduction of gas, the flow characteristics of two-phase Taylor flow differ markedly from those of single-phase flow. Internal recirculations within the gas bubble and the liquid slug promote radial mixing of the fluids, resulting in significant enhancement of heat and mass transfer rates. Also, the separation of liquid slugs by gas bubbles reduces axial liquid mixing, and gives a large interfacial area and a short diffusion path between the gas and liquid phases and/or between the liquid and the solid wall.

As mentioned at the beginning of this chapter, the hydrodynamics including bubble velocity, void fraction, liquid film thickness, pressure drop, and mass transfer of Taylor flow have been studied and reviewed extensively. Therefore, this section reviews only the available literature covering the bubble formation mechanisms, the detailed flow structures in the slug and film regions, and the heat transfer mechanisms of Taylor flow, in order to identify the knowledge gaps.

2.3.1 Bubble formation and bubble length

Due to the increasing popularity of microfluidic devices, significant effort has been devoted to exploring the techniques to generate uniform bubbles and droplets. Geometries that are generally used to create gas-liquid Taylor flow in microchannels include T-junctions (Garstecki *et al.*, 2006, van Steijn *et al.*, 2007, 2010, Christopher *et al.*, 2008, Fu *et al.*, 2010a, Leclerc *et al.*, 2010), Y-junctions (Yue *et al.*, 2008), co-flowing configurations (Hong and Wang, 2007, Xiong *et al.*, 2007) and flow-focusing inlet structures (Anna *et al.*, 2003, Fu *et al.*, 2010b). Highly uniform bubbles and droplets generated with these devices were reported.

The importance of the bubble and liquid slug lengths on the pressure drop (Kreutzer *et al.*, 2005b), mass transfer (Bercić and Pintar, 1997) and heat transfer (Walsh *et al.*, 2010) of gas-liquid Taylor flow in microchannels has been reported. However, the measurement and prediction of the absolute bubble and slug lengths are generally ignored due to the strong dependence of the length information on the inlet configurations, as well as the degree of pre-mixing. Nonetheless, the absolute bubble and slug lengths generated by different mixing

systems have been studied by various investigators (Laborie *et al.*, 1999, Kreutzer *et al.*, 2005a, Liu *et al.*, 2005, Akbar and Ghiaasiaan, 2006, Qian and Lawal, 2006). Several empirical correlations have been proposed, with most of them expressing the lengths as a function of the Reynolds numbers and/or the phase holdup. However, there is a lack of agreement between them, reflecting the fact they are only applicable to specific working fluids and inlet structures.

Since Taylor bubble coalescence and/or breakage after their formation is rarely observed in microchannels, the lengths of the bubbles and slugs are strongly dependent upon the dynamics of the contact between two phases at the inlet. Therefore, a good understanding of the mechanisms of Taylor bubble formation in microchannels becomes important for accurate bubble and slug length predictions. Considerable studies, both experimental (Garstecki *et al.*, 2006, van Steijn *et al.*, 2007) and computational (de Menech *et al.*, 2008, Shao *et al.*, 2008, Dai *et al.*, 2009) on the bubble formation mechanisms have been reported.

The bubble formation mechanisms can be distinguished by the Capillary number based on the liquid flow rate at the mixing section ($Ca_{L,M}$). Garstecki *et al.* (2006) postulated that there is a critical Capillary number ($Ca_{cr} = 0.02$) distinguishing two commonly observed bubble formation mechanisms. Below Ca_{cr} ($Ca_{L,M} < 0.02$), the bubble formation is categorized to be in the squeezing regime, where the interfacial forces dominate the shearing forces and the dynamics of the break-up process are controlled by the pressure drop across the bubble as it forms. Above Ca_{cr} ($Ca_{L,M} > 0.02$), the bubble formation is in the shearing regime, where the shearing force starts playing a role and the dynamics of the break-up process are controlled by the force balance between the shear and interfacial forces.

de Menech *et al.* (2008) investigated numerically the transition from squeezing to shearing regimes in a T-junction connected to a rectangular microchannel. In addition to the above two mechanisms, a jetting regime was identified at larger values of mixer Capillary number and very high flow rates. Figure 2.4 shows a sequence of images illustrating the bubble formation at different regimes.

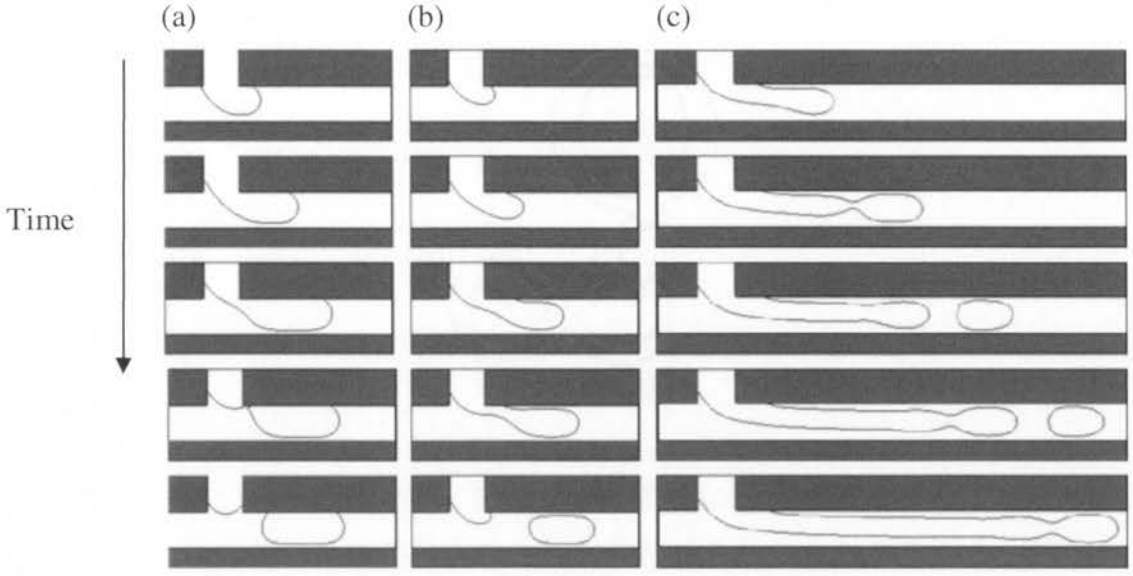

Figure 2.4: Bubble formation mechanisms as a function of the mixer Capillary number: (a) squeezing regime, $Ca_{L,M}$ = 0.004, (b) transition to shearing regime, $Ca_{L,M}$ = 0.035, and (c) jetting regime, $Ca_{L,M}$ = 0.05. Taken from de Menech *et al.* (2008).

2.3.1.1 Squeezing regime

Garstecki *et al.* (2006) investigated experimentally the bubble/droplet formation process in T-junctions connected to rectangular microchannels (S = 0.033 mm, w = 0.05–0.2 mm). In the squeezing regime, they suggested that there are two stages in the bubble break-up process, named the filling and squeezing stages. The gas phase enters and blocks the main channel and the pressure in the liquid phase builds up during the filling stage. Then in the squeezing stage, the increased liquid pressure starts to squeeze the gas thread until the neck is pinched off to form a bubble, as seen in Figure 2.4 (a). Based on their experimental results, they developed a scaling model (Eq. 2.2) to predict the lengths of bubbles (L_B) generated in the squeezing regime ($Ca_{L,M} < 0.02$)

$$\frac{L_B}{w} = \alpha_1 + \alpha_2 \frac{Q_G}{Q_L} \tag{2.2}$$

where w is the width of a rectangular channel; α_1 and α_2 are constants of the order of one, with particular values depending on the geometry of the T-junction, Q_G and Q_L are the gas and liquid flow rates, respectively. The first and second terms in Eq. (2.2) correspond to the length developed in the filling and squeezing stages of the bubble formation process,

respectively. During the filling stage, the bubble expands to a length proportional to the diameter of the main channel. In the squeezing stage, the increased pressure in the liquid phase starts to squeeze the neck of the gas thread. Garstecki *et al.* (2006) measured the bubble/droplet size over a wide range of flow rates using different fluids and channel sizes. They found that the length of the bubble/droplet was determined by the ratio of the volumetric flow rates of the two phases solely, regardless of the fluid properties. Good agreement was achieved between their experimental data obtained for liquid-liquid Taylor flow and gas-liquid Taylor flow with small bubbles and the proposed scaling law. They attributed the discrepancy observed for long bubble systems to the overestimation of the resistance to flow in the outlet channel at high volume fraction of the gaseous phase.

The three-dimensional flow field of the liquid phase during bubble formation in a 800 μm square T-junction in the squeezing regime was studied experimentally by van Steijn *et al.* (2007) using Micro-Particle Image Velocimetry (μPIV) techniques. They highlighted that there was no instance at which the growing bubble fully blocked the square channel as part of the liquid leaks through the corners. Guo and Chen (2009) studied the bubble formation process in a rectangular T-junction channel computationally. Their simulation results demonstrated that the liquid phase formed a toroidal vortex below the gas-liquid interface due to the blockage of the gas phase. The circulating liquid phase pushes the gas-liquid interface toward the corner of the wall where the break-off takes place. Dai *et al.* (2009) studied numerically the bubble formation of gas-liquid flow in a T-junction microchannel of 100 μm diameter in the squeezing regime and confirmed the scaling argument proposed by Garstecki *et al.* (2006).

Apart from the T-junction mixers (van Steijn *et al.*, 2007, Leclerc *et al.*, 2010), the Garstecki *et al.* (2006) scaling law has been applied successfully to the prediction of bubble lengths in Y-junction rectangular microchannels (Yue *et al.*, 2008), rectangular co-flowing microchannels (Xiong *et al.*, 2007), and circular flow-focusing devices (Shao *et al.*, 2008) operating in the squeezing regime. Different from the observations reported by Garstecki *et al.* (2006), other studies (Laborie *et al.*, 1999, Xiong *et al.*, 2007, Shao *et al.*, 2008) found a dependence of bubble diameter and hence the resulting length on liquid properties, including viscosity and surface tension. In order to allow for films with non-negligible thickness, Xiong *et al.* (2007) modified the above scaling law by replacing the channel width (w) by the bubble width (w_B).

2.3.1.2 *Shearing regime*

In the shearing regime ($Ca_{L,M} > 0.02$), de Menech *et al.* (2008) showed that the gas stream occupies only part of the main channel and the liquid phase flows below the gas-liquid interface, as seen in Figure 2.4 (b). For fixed liquid flow rate, the liquid phase flows faster through the gap between the interface and the wall of the channel and exerts a large shear stress on the gas stream which is the main driving force for the pinching off process. The gas thread breaks off at the upper wall, when the interfacial force is nearly balanced by the shearing force. Guo and Chen (2009) showed similar numerical observations and highlighted that the circulation flow below the gas-liquid interface they observed in the squeezing regime disappeared, with the liquid flowing along the interface. However, they found the transition Capillary number from the squeezing to shearing regime was around 0.0058 which is much lower than that reported by Garstecki *et al.* (2006).

The bubble size generated in the shearing regime was found to depend strongly on the mixer Capillary number rather than the flow rate ratio (de Menech *et al.*, 2008). While some authors suggested an inversely proportional relationship between the bubble/droplets size and the mixer Capillary number ($Ca_{L,M}$) (Thorsen *et al.*, 2001, Husny and Cooper-White, 2006) or a modified local Capillary number based on the velocity of the liquid phase between the interface and wall (Xu *et al.*, 2008), others suggested the dependence of the bubble/droplet size on both the mixer Capillary number and shear rate (de Menech *et al.*, 2008) as the bubble break-off process are controlled by the local shear stress, as well as the surface tension force.

2.3.1.3 *Transition regime*

Instead of a sharp transition of the bubble formation regimes, it is suggested that there is a transition regime between the squeezing and shearing regimes where the bubble/droplet break-up process is controlled by a combination of the shear stress and the squeezing pressure (Christopher *et al.*, 2008, de Menech *et al.*, 2008, Xu *et al.*, 2008, Fu *et al.*, 2010a).

Xu *et al.* (2008) examined their previous experimental data in which droplets were generated in rectangular T-junctions (Xu *et al.*, 2006a, 2006b, 2006c) and identified a transition regime for $0.002 < Ca_{L,M} < 0.01$. They proposed Eq. (2.3) to predict the lengths of bubbles/droplets generated in the transition regime by considering the influences of both the shear stress and the squeezing pressure. The bubble length is given by

$$\frac{L_B}{w_B} = \alpha_3 Ca_{L,M}^{e} \left(\frac{Q_G}{Q_L}\right)^{f} \tag{2.3}$$

where w_B is the bubble width; α_3 is a constant, and e and f are the exponents with values depending on the geometry of the mixer. The ratio of e and f represents the contribution of the two different bubble formation mechanisms. Using a best fitting technique for their experimental data, they found $\alpha_3 = 0.75$, $e = -1/5$ and $f = 1/3$ for their T-junction geometries.

Christopher *et al.* (2008) studied the bubble break-off mechanisms by performing systematic experiments in rectangular microfluidic T-junctions of varied inlet width ratios over a wide range of Capillary numbers ($0.0005 < Ca_{L,M} < 0.3$) and flow rate ratios ($0.05 < Q_G/Q_L < 0.5$). Over the range of flow conditions considered, they observed that the bubble size decreased as the Capillary number increased and the flow rate ratio decreased. They found that squeezing was not the only mechanism causing breakup and the detachment actually began before the gas phase had completely filled the channel (in a similar sense of Figure 2.4 (b)). Assuming the Capillary number controls the thread length in the expansion stage and the flow rate ratio determining the length in the collapse stage, they proposed a two-stage model to predict the droplet size in the transition regime, given as

$$\frac{L_B}{w} \approx \frac{l_e}{w} + \frac{w}{l_e}\frac{Q_G}{Q_L} \tag{2.4}$$

where l_e is the final tip length in the expansion stage and is calculated as

$$\left(1 - \frac{l_e}{w}\right)^3 = \frac{l_e}{w} Ca_{L,M} \tag{2.5}$$

Fu *et al.* (2010b) investigated the squeezing-to-shearing transition during the bubble formation experimentally using a rectangular microfluidic T-junction (w = 120 μm and S = 40 μm). They compared their experimental results obtained in the range $0.0058 < Ca_{L,M} < 0.013$ with the correlations proposed by Christopher *et al.* (2008) and reported a maximum relative standard deviation of 28%.

2.3.1.4 *Jetting regime*

In the jetting regime, the gas thread protrudes into the main channel as a finger-like fluid structure oriented towards the channel outlet, as shown in Figure 2.4 (c). The gas thread pinches off at its end as it propagates downstream to give a gas bubble (de Menech *et al.*, 2008). The jetting regime was also observed experimentally by Santos and Kawaji (2010) who studied two-phase flow in a square microchannel of 113 μm hydraulic diameter with gas-liquid mixture generated through a T-junction. They highlighted that this break-up process was similar to the instability propagation typically found in the formation of bubbles/droplets from jets.

2.3.2 Bubble shape

With most of visualization experiments focusing on the identification of different flow regimes in microchannels, detailed configurations of the Taylor bubble are generally ignored. Nonetheless, the effects of dimensionless parameters, such as Capillary number and Reynolds number, on the shape of Taylor bubbles were well reported analytically (Bretherton, 1961, de Ryck, 2002) and computationally (Edvinsson and Irandoust, 1996, Taha and Cui, 2004, Feng, 2009).

Edvinsson and Irandoust (1996) studied computationally the variations of bubble shapes with different flow parameters, as shown in Figure 2.5. For flows with low Capillary number and negligible gravitational effects, the bubble shape can be described as a symmetrical cylinder with two hemispherical caps at the ends, similar to the Taylor bubbles observed in Figure 2.1 (b). Ripples in the gas-liquid interface near the tail region for flow with $500 < Re_{TP} < 2000$ and $Ca = 0.01$ were observed (Figure 2.5 (a) – (c)). The amplitudes of the undulations were found to increase with the Reynolds number. As Ca increases, the gas bubble attains a bullet-shape, where the bubble head becomes sharper and the bubble tail becomes flatter (Figure 2.5 (d) – (f)) and no wavy pattern was observed at the bubble tail. Other computational (Taha and Cui, 2004, Gupta *et al.*, 2010b) and analytical (de Ryck, 2002) studies have also shown the length of the transition region between the bubble cap and the constant film surrounding the bubble increases with increasing Ca, resulting in a sharper nose. When Ca increases further at high velocity, a concave deformation at the bubble tail results, as seen in Figure 2.5 (g). Similar observations were reported by Goldsmith and Mason (1963), Taha and Cui (2004) and Feng (2009).

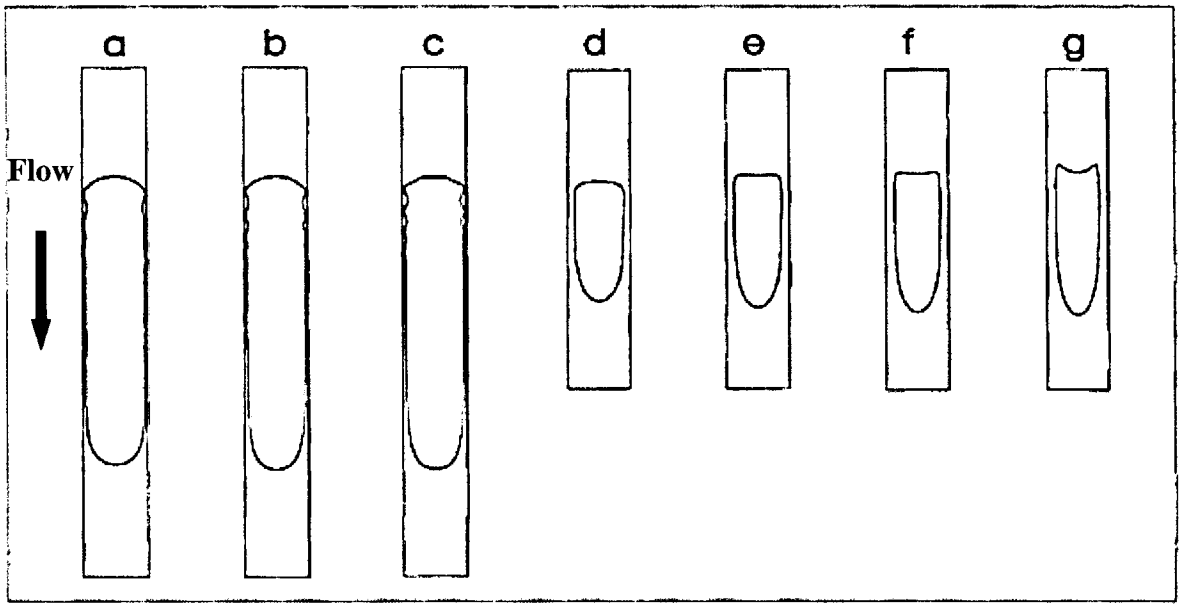

Figure 2.5: Variation of bubble shapes with different flow parameters: (a) β = 0.5, Re_{TP} = 500, Ca = 0.01, (b) β = 0.5, Re_{TP} = 1000, Ca = 0.01, (c) β = 0.5, Re_{TP} = 2000, Ca = 0.01, (d) β = 0.2, Re_{TP} = 20, Ca = 0.20, (e) β = 0.2, Re_{TP} = 20, Ca = 0.38, (f) β = 0.2, Re_{TP} = 20, Ca = 0.50, and (g) β = 0.2, Re_{TP} = 20, Ca = 1.0. Modified from Edvinsson and Irandoust (1996).

When the gravitational effect on Taylor flow in a microchannel is non-negligible, distortion of the bubble symmetry in horizontal fine passages was reported by Bretherton (1961). However, he could not obtain the analytical solution for the relevant partial differential equation and no quantitative analysis was provided. Jensen *et al.* (1987) showed analytically and experimentally that the transition region between the bubble nose and constant film at the bottom was longer than that at the top. They also pointed out that the film at the bottom was much thicker than that at the top for large Bond numbers (Bo > 1) and small Capillary numbers (Ca < 0.1). As the mixture velocity increased (increased Ca and Re_{TP}), the gas bubble regained its symmetry and moved along the channel centre because the gravitational force became less significant when compared with the viscous and inertial forces.

The effects of gravity and channel orientation on the propagation of liquid slugs in a two-dimensional liquid-lined microchannel were studied analytically by Suresh and Grotberg (2005). When gravity is non-negligible for non-vertical channel orientations, they demonstrated a bubble shape distortion and an asymmetric liquid distribution: the ratio of liquid volume above and below the centreline of the channel was smaller than unity. Based

on a force balance analysis, they suggested the thickness of the bottom film and top film should scale as $Ca^{2/3}$ and $Ca^{1/2}$, respectively, for Taylor flow under the effect of gravity. They then applied matched asymptotic expansions and lubrication theory using the above scalings and obtained analytical solutions for flows with non-negligible gravitational force at small Capillary numbers to give assymetric bubble shapes.

Han and Shikazono (2009) measured the film thickness at the channel top, bottom and side in five horizontal channels of different diameters (d = 0.3–1.3 mm). For flow with Re_{TP} ~1200, they found that the liquid film thickness at the top decreased while that at the bottom increased linearly along the bubble in a 1.3 mm horizontal channel. They attributed this linear change of the film thickness to the effect of gravity. While the gravitational effect on the film thickness variation became more apparent with increasing Bo, the difference in thickness between the bottom and side films was also found to increase with increasing Ca, which is different from the observation reported by Jensen *et al.* (1987) who reported the gravitational effect diminished with increasing Ca.

Recently, Gupta *et al.* (2010c) studied the effects of gravity on nitrogen-ethylene glycol Taylor flow experimentally in a 1.97 mm horizontal channel. Distortion of the bubble symmetry was observed (Figure 2.6) – the bottom film was thicker than the top film and the gas bubble became longer at the top and shorter at the bottom. They also performed three-dimensional CFD simulations to explore the effect of gravity in both rectangular and circular microchannels of different hydraulic diameters. For flow with Re_{TP} ~12 and Ca ~ 0.036 in a circular channel of 2 mm diameter, a pressure gradient was observed between the bubble top and bottom in the film region, causing a drainage flow from the top to bottom along the film. Their computational results also showed that drainage flow takes place along the entire bubble length. Due to the drainage of liquid, the thickness of the top film decreased and that of the bottom film increased gradually from the nose to the tail region, where more pronounce distortion was observed at the bubble tail.

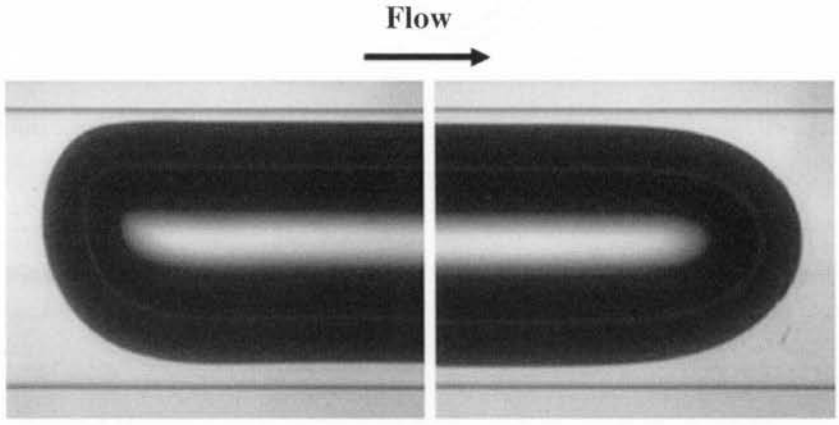

Figure 2.6: The bubble shape obtained in a 1.97 mm horizontal channel for flow with Re_{TP} ~12 and Ca ~ 0.036 (Gupta *et al.*, 2010c).

2.3.3 Velocity field

The flow field in the liquid slug and the liquid film surrounding the gas bubbles provide important information about the mixing of fluids and hence the rates of heat and mass transfer.

2.3.3.1 Velocity profile in the liquid slug

In a reference frame moving with the bubble, three possible streamline patterns inside the liquid slug, depending upon the ratio of the bubble velocity to mixture velocity (U_B/U_{TP}), were first postulated by Taylor (1961). For $U_B/U_{TP} > 2$, a complete bypass flow pattern was found (Figure 2.7 (a)). For $U_B/U_{TP} < 2$, the liquid phase can be divided into closed streamlines within the slug core forming a recirculation zone and open-ended streamlines passing through the liquid film along the wall layer. Two possible reversal flow patterns: (1) a stagnation ring on the bubble surface (Figure 2.7 (b)) and (2) a stagnation point on the bubble tip and a second stagnation point inside the liquid slug (Figure 2.7 (c)) were suggested.

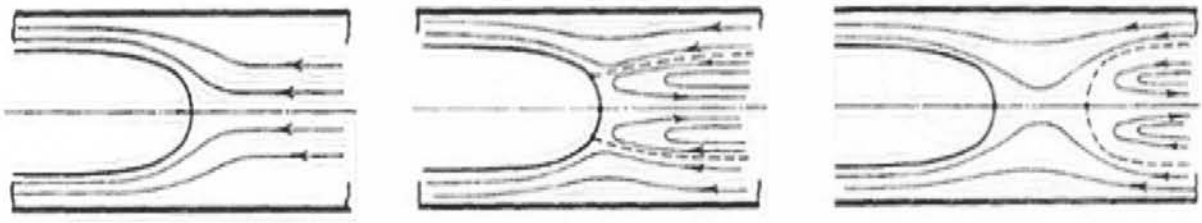

(a) $U_B/U_{TP} > 2$ (b) $U_B/U_{TP} < 2$ (c) $U_B/U_{TP} < 2$

Figure 2.7: Possible streamline patterns in a reference frame moving with the bubble for different ratios of bubble to mixture velocities suggested by Taylor (1961).

The suggested streamline patterns were verified experimentally by Cox (1964). The complete bypass flow for $U_B/U_{TP} > 2$ and reversal flow with a stagnation ring on the bubble surface for $U_B/U_{TP} < 2$ were identified but not the other reversal flow pattern. The same experimental observations were reported by Thulasidas *et al.* (1997) who visualized streamline patterns using PIV techniques. Thulasidas *et al.* (1997) also calculated the radial locations of the recirculation centre and the dividing streamline separating the recirculation zone from the wall film layer. As *Ca* increases, they highlighted that the recirculation zone inside the liquid slug became smaller and the radial position of the vortex centre shifted towards the tube centre. The effect of *Ca* on the recirculation size was reported from computational studies by Edvinsson and Irandoust (1996), Taha and Cui (2004) and Feng (2009), as shown in Figure 2.8. Feng (2009) further pointed out that with an increasing *Ca*, the stagnation ring on the bubble surface (Figure 2.7 (b)) collapsed into a stagnation point at the bubble tip. When *Ca* was increased further, the recirculating flow detached from the bubble surface and formed a second stagnation point inside the slug centre (Figure 2.7 (c)). They highlighted that this reversal flow pattern only appeared for a very small range of *Ca*. Bypass flow was observed with a further increase in *Ca*. Their numerical observations were in good agreement with the analytical findings reported by Giavedoni and Saita (1997).

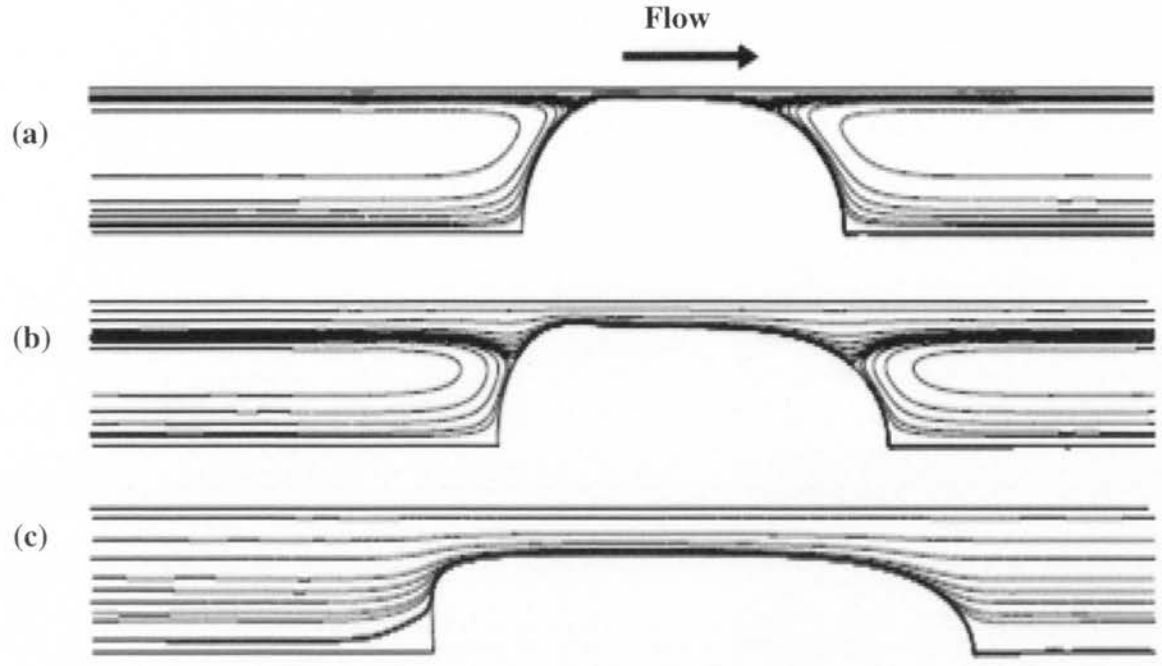

Figure 2.8: Effects of Capillary number on the streamline pattern for Re_{TP} = 10 at (a) Ca = 0.01, (b) Ca = 0.1 and (c) Ca = 1. Taken from Feng (2009).

Waelchli and von Rohr (2006) used the μPIV technique to visualize the recirculation motion (in a frame of reference moving with the bubble) inside the liquid slug for horizontal flow in a rectangular microchannel with the hydraulic diameter of 187.5 μm, as shown in Figure 2.9. They showed that the counter-rotating vortex pair is symmetric about the centreline of the channel without any interactions between the upper and lower regions taking place. The influence of the liquid properties was examined. A stagnation ring along the bubble surface was observed for the nitrogen-ethanol systems (Figure 2.9 (a)). Two stagnation points at the centreline were observed for the nitrogen-10 wt% glycerol aqueous solution system (Figure 2.9 (b)). This recirculation pattern was different from the computational and analytical results described by Feng (2009) and Giavedoni and Saita (1997), where recirculation zone shrunk dramatically before its detachment from the bubble surface.

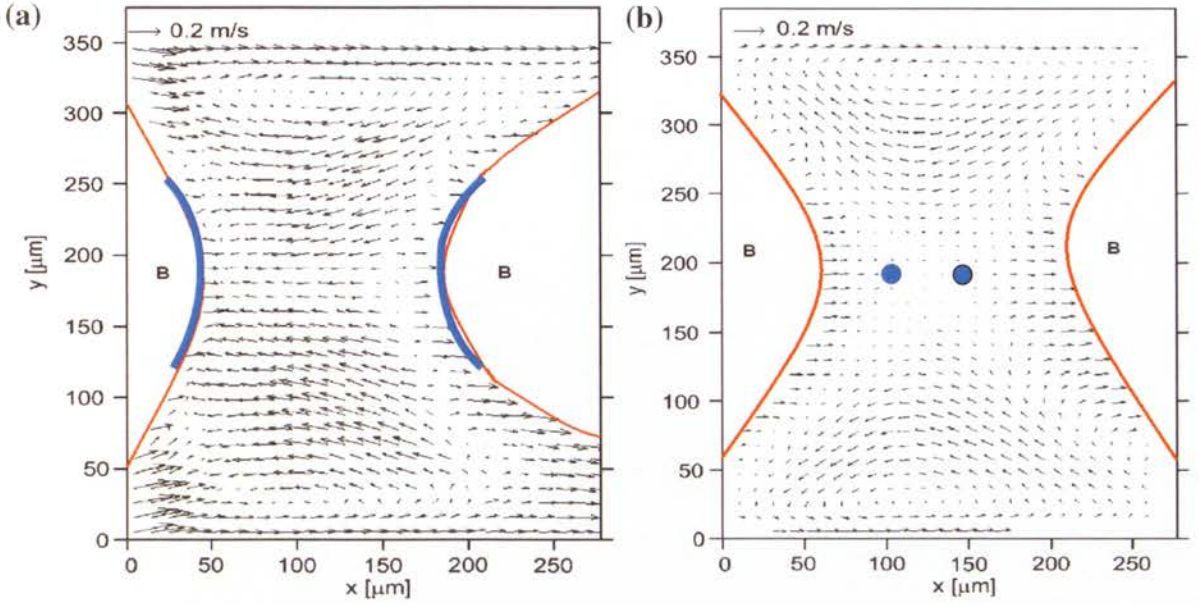

Figure 2.9: Velocities relative to the bubble inside the liquid slug for a horizontal rectangular microchannel (d_h = 187.5 μm) using (a) ethanol and (b) 10 wt% glycerol/water mixture as the liquid phase. The red curves indicate the interface, and blue curves and dots indicate the stagnation rings and points, respectively. Modified from Waelchli and von Rohr (2006).

Waelchli and von Rohr (2006) also showed the asymmetry of the rotating vortices about the plane perpendicular to the flow direction at the slug centre as a result of the different bubble end configurations, as shown in Figure 2.10.

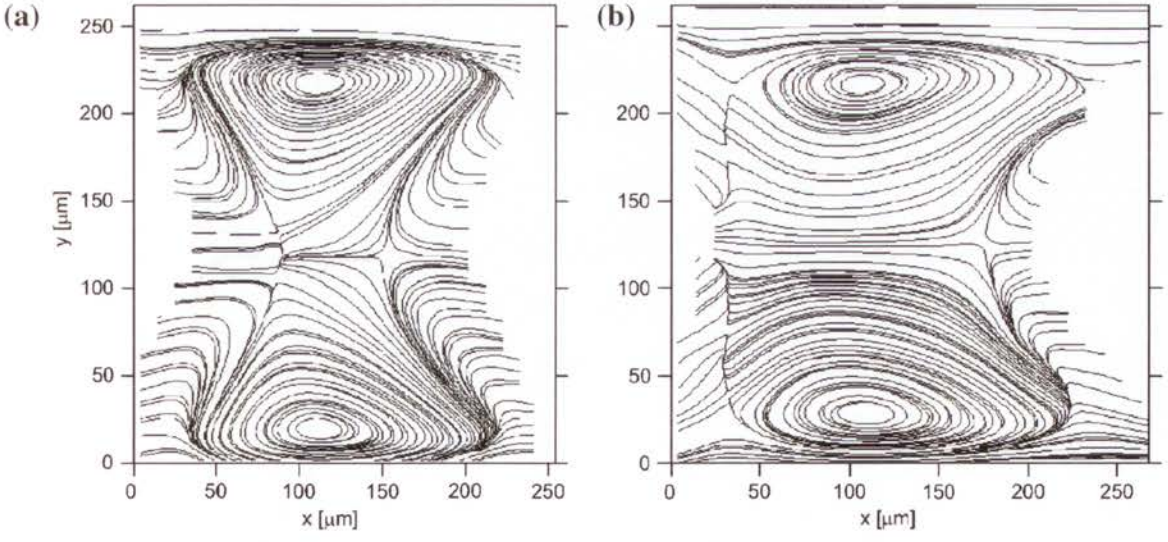

Figure 2.10: Asymmetric flow patterns due to the different configurations of the bubble ends in a d_h = 187.5 μm horizontal rectangular microchannel using (a) water and (b) ethanol as the liquid phase. Taken from Waelchli and von Rohr (2006).

The combined effects of gravity, mixture velocity and liquid slug length on the flow field inside the liquid slug in a two-dimensional liquid-lined microchannel were examined numerically by Zheng *et al.* (2007). They showed that flow interactions between the upper and lower regions give an asymmetric flow pattern about the channel axis when gravity started gaining importance in a horizontal flow. As seen in Figure 2.11, part of the liquid flows from the upper film through the core region of the liquid slug to the bottom film with the upper and lower recirculation zones being pushed towards the preceding and trailing bubble interface, respectively. These flow interactions also caused the bottom film to be thicker than the upper one. As the Bond number increases, the size and strength of flow recirculation decreases and the number of vortices present in the liquid slug can be zero, one or two depending on the flow parameters. The difference between the upper and lower films was reported to increase with increasing *Bo* but to decrease with either an increasing liquid slug length or mixture velocity (increasing *Ca* and Re_{TP}). The flow interactions between the upper and lower regions in horizontal flow in microchannels described above have not yet been confirmed by experimental studies.

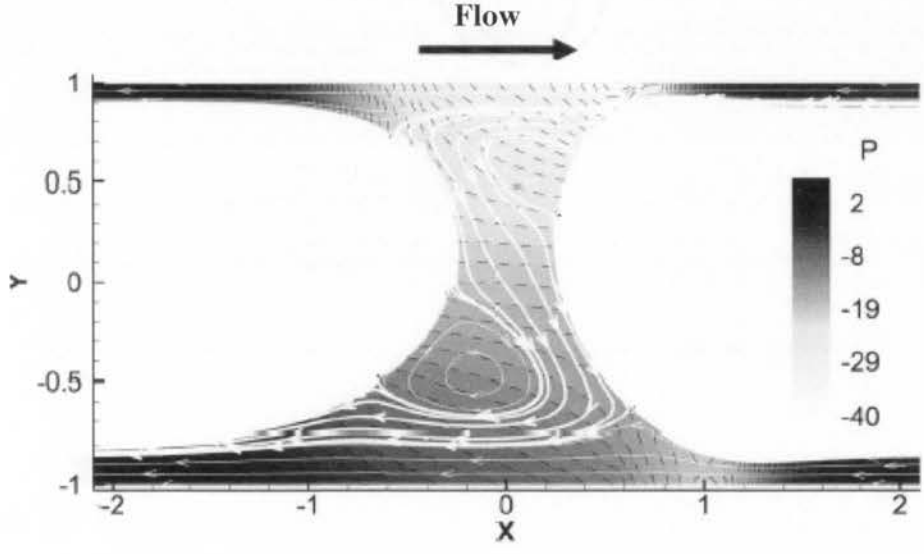

Figure 2.11: Effect of gravity in horizontal microchannels for Re_{TP} = 0, *Ca* = 0.05 and *Bo* = 0.6. The greyscale contour plot shows pressure, the dashed lines are constant pressure lines and the white solid lines with arrows are streamlines (Zheng *et al.*, 2007).

In a laboratory reference frame, a nearly full-developed laminar flow velocity profile in the middle part of the liquid slug was shown in most computational reports (Fukagata *et al.*, 2007, Lakehal *et al.*, 2008, Gupta *et al.*, 2010b, He *et al.*, 2010). Gupta *et al.* (2010b) mentioned that the flow in the liquid slug did not reach the laminar, liquid-only, fully-developed flow for

any of the mixture velocities they simulated because the liquid slug lengths (0.9–1.1*d*) they studied were too short to allow significant flow development. Thulasidas *et al.* (1997) showed experimentally that the flow in the liquid slug only became fully-developed and gave a parabolic profile when the slug length was longer than 1.5*d*. For slugs shorter than 1.5*d*, a non-parabolic velocity profile was observed everywhere in the liquid slug, indicating the flow was not completely developed.

2.3.3.2 Flow field in the liquid film

The velocity field of the liquid film surrounding the bubble in microchannels are scarcely reported. For most two-phase Taylor flow studies, either a stagnant film (Bretherton, 1961, Suo and Griffith, 1964, Warnier *et al.*, 2008) or a fully-developed flow velocity profile in the liquid film (Thulasidas *et al.*, 1995) with a no shear boundary condition at the interface was assumed. This assumption was confirmed to be reasonable for slow-moving bubble systems by Chen *et al.* (2009) and Kreutzer *et al.* (2005b) who showed computationally that there was no pressure gradient in a typical Taylor bubble (Figure 2.12). Gupta *et al.* (2010b) performed detailed Taylor flow CFD studies and reported similar observations for flow at low mixture velocities. However, for fast-moving bubble systems, they found that the interfacial shear stress became significant and the pressure gradient in the film region began to contribute significantly to the overall pressure drop.

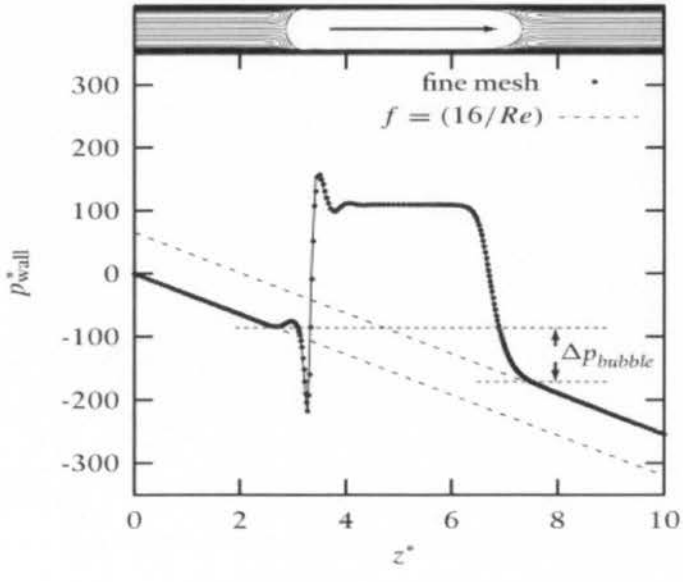

Figure 2.12: A profile of the wall pressure distribution in the axial direction for flow with Ca = 0.01, Re_{TP} = 100, β = 0.65 calculated for a circular tube of 2.3 mm. Taken from Kreutzer et al. (2005b).

Fouilland *et al.* (2010) studied the flow characteristics of a nitrogen-water system in a 1.73 mm horizontal channel for flow regimes spanning Taylor to annular flow. They obtained time-resolved velocity profiles in the liquid film surrounding the bubble using μPIV techniques. They found the film velocity was low when compared with the bubble velocity (< 4%) and demonstrated a smooth velocity distribution during the passage of a gas bubble and a velocity spike when a liquid slug passed through. They highlighted that the velocity distribution relaxed back to the characteristic steady value after the passage of each liquid slug when the length of the gas bubble was sufficiently long. To interpret their PIV data, they derived an expression (Eq. 2.6) analytically for the mean film velocity normalised by the mixture velocity as a function of the pressure gradient ratio between the liquid film and the gas core for a given dimensionless interfacial radius ($\xi_B = R_B/R$)

$$\frac{U_F}{U_{TP}} = \frac{(1-\xi_B^2)^2 - 2\xi_B^2(1-\xi_B^2+2\xi_B^2\ln\xi_B)\left(1-(B_G/B_L)\right)}{(1-\xi_B^2)[1-\xi_B^4+(\mu_L/\mu_G)(B_G/B_L)\xi_B^4 - 2\xi_B^2(1-\xi_B^2)(B_G/B_L)]} \tag{2.6}$$

where U_F is the average velocity in the liquid film; B_G and B_L are the pressure gradients in the gas and liquid phases, respectively; μ_G and μ_L are the gas and liquid viscosities, respectively. One extreme, where the shear at the gas-liquid interface is zero ($B_G = 0$, i.e. inviscid flow of the gas) corresponds to Taylor flow at low bubble velocities as mentioned previously. At the other extreme, where the film is driven by interfacial shear alone in negligible gravity ($B_G = B_L$) corresponds to annular flow behaviour.

Gupta (2010) also performed a similar continuity analysis, assuming a zero shear stress boundary condition at the interface, to obtain a fully-developed velocity profile in the liquid film surrounding the slow-moving gas bubbles, which except at the bubble ends gives

$$\frac{v_x}{U_F} = \frac{2(1-\xi^2+2\xi_B^2\ln\xi)(1-\xi_B^2)}{(1+3\xi_B^4-4\xi_B^2-4\xi_B^4\ln\xi_B)} \tag{2.7}$$

where v_x is the local velocity in the liquid film; ξ is the normalized radial position (r/R). Good agreement was achieved between the velocity profile obtained from his CFD simulation in a 0.5 mm horizontal channel and the analytical solution.

The effect of gravity on the flow field in the liquid film was studied both experimentally and computationally by Gupta *et al.* (2010c). They performed μPIV measurements in the liquid film to visualize the flow fields for horizontal and vertical upward flows in a 1.97 mm

microchannel. A negative vertical velocity component at different distances from the wall inside the film was reported for the horizontal case, indicating a drainage flow from the channel top to bottom across the bubble region. A difference in thickness between the top and bottom films was observed in white light images as presented earlier in Figure 2.6. For the vertical upward case, backflow in the liquid film appeared. For their computational results obtained from a 2 mm circular channel with a mixture velocity of 0.1 $m\,s^{-1}$ and a homogeneous void fraction of 0.66, liquid at the bubble surface was found to drain from the top to the bottom as shown by the streak-lines originating from the bubble surface (Figure 2.13). Although significant non-physical spurious currents were observed in their simulations due to the inaccurate discretization of surface tension forces in the circular channel, their preliminary results showed that the gravitational force played a role for the conditions they studied.

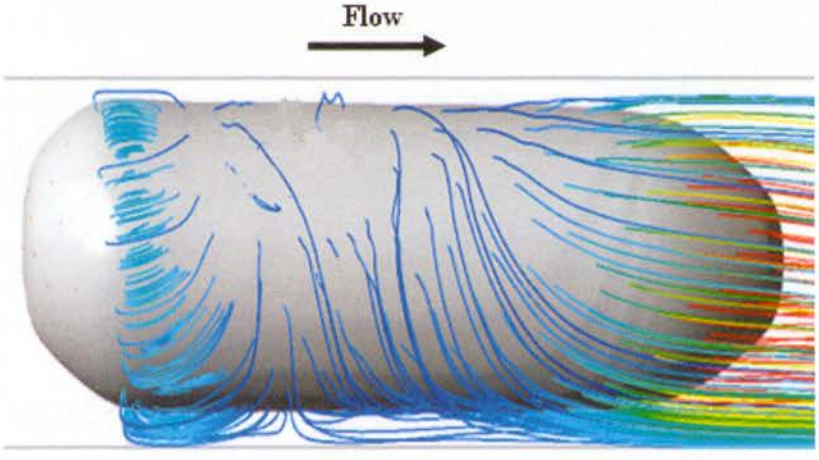

Figure 2.13: Streamlines originating from the bubble surface in a 2 mm circular channel for a mixture velocity of 0.1 $m\,s^{-1}$ and a homogeneous void fraction of 0.66 in a stationary reference frame (Gupta *et al.*, 2010c).

Since both the film thickness and flow patterns are key parameters for Taylor flow heat and mass transfer, bubble asymmetry and flow interactions between the upper and lower halves of the liquid slug caused by gravity may have a considerable effect on the resulting heat transfer rates. A good understanding of the conditions where gravity ceases to be important, therefore, becomes essential for better application design.

2.3.4 Heat transfer

Generally, the heat transfer rates for gas-liquid Taylor flow in microchannels without phase change are up to 2–3 times higher than that of the single-phase fully-developed laminar flow, depending on the flow characteristics. Several studies have been carried out to understand the enhancement mechanisms brought about by such flows and a few heat transfer models were proposed. A brief review of the current understanding of the dependence of Taylor flow heat transfer on the flow characteristics is provided here.

The periodic passage of bubbles and slugs that occurs in Taylor flow has led many authors to invoke the Graetz number to characterise heat transfer in the slug region. The Graetz number is the dimensionless group that characterises thermal-development in laminar flows, $Gz = Re \cdot Pr \cdot (d/L)$. However, there is confusion as to whether the characteristic length in the Taylor flow case should be the total length from the entrance or the slug length.

The effect of void fraction and film thickness on two-phase heat transfer was investigated experimentally by Oliver and Wright (1964) in a 6.4 mm circular channel for Newtonian and non-Newtonian liquids for a constant wall temperature boundary condition. They reported the heat transfer enhancement was up to 2.5 times greater than that for single-phase flow, with shorter slugs and thin film systems giving a greater enhancement. Based on their experimental data, they modified the Graetz-Leveque solution for thermally-developing laminar flow to obtain

$$Nu_{TP} = 1.615 \left(Re_{TP} \cdot Pr \cdot \frac{d}{L}\right)^{1/3} \left(\frac{1.2}{(1-\beta)^{0.36}} - \frac{0.2}{1-\beta}\right) \left(\frac{\mu_b}{\mu_w}\right)^{0.14} \tag{2.8}$$

where μ_b and μ_w are the liquid viscosity at the bulk fluid temperature and the heat-transfer boundary surface temperature, respectively. Although they used a modified Graetz-Leveque solution, they highlighted the fact that the heat transfer mechanisms occurring in Taylor flow could be very different from those of single-phase laminar developing flow, as a result of the recirculation effect within the liquid slugs. Due to limitations of the experimental apparatus, they failed to control the slug length and no quantitative analysis of its effect was provided. In their follow-up work, Oliver and Young Hoon (1968) developed an experimental facility which allowed variation of the slug length at fixed void fraction. Experiments with slug lengths spanning from 1–80 tube diameters in a 6.4 mm circular tube were conducted for a

constant wall temperature boundary condition. They concluded that the two-phase Nusselt number varied approximately as $L_S^{-1/3}$ for a small range of homogeneous void fractions (0.24–0.39).

Hughmark (1965) proposed an alternative modification of the thermally-developing laminar flow theory. The two-phase Nusselt number was rescaled to account for the fraction of the tube cross-section occupied by the liquid. The two-phase Nusselt number is given by

$$Nu_{TP}\sqrt{1-\beta} = 1.75\left(Re_{TP}\cdot Pr\cdot\frac{d}{L}\right)^{1/3}\left(\frac{\mu_b}{\mu_w}\right)^{0.14} \tag{2.9}$$

Good agreement was reported when the model was compared with the experimental data of Oliver and Wright (1964).

Through measuring the mass transport data, Horvath *et al.* (1973) assessed the effect of the slug length ($1.6 < L_S/d < 16$) as well as the Reynolds number ($28 < Re_{TP} < 220$) for a constant homogeneous void fraction of 0.5 on the apparent Nusselt number of the liquid slug ($Nu_S = Nu_{TP}/(1-\beta)$) for gas-liquid Taylor flow in a tube of 2.32 mm diameter. They found that the value of Nu_S increased with decreasing slug length and increasing Reynolds number. The maximum slug Nusselt number was found to be ~100 for $L_S/d =$ 1.6 and $Re_{TP} = 220$.

The dependence of the heat transfer rate on slug length was also recognized by Kreutzer *et al.* (2001) who performed two-dimensional, axisymmetric CFD simulations in a cylinder of 1 mm diameter with a moving wall. They examined a wide range of conditions ($1 < L_S/d < 16$, $7 < Pr < 700$, $10 < Re_{TP} < 400$) and suggested a Nusselt number correlation for the slug region (Nu_S) as a function of a modified Graetz number based on the slug length

$$Nu_S = 20\left[1 + 0.003\left(\frac{L_s}{Re_{TP}\cdot Pr\cdot d}\right)^{-0.7}\right] \tag{2.10}$$

Fukagata *et al.* (2007) carried out two-dimensional, axisymmetric numerical simulations in a periodic domain for a channel of 20 μm inner diameter to understand the flow and heat transfer characteristics of air-water Taylor flow without phase change. A wide range of conditions ($16 < Re_L < 490$, $0.3 < Re_G < 13$, $0.26 < \beta < 0.72$) were studied and a two-phase Nusselt number up to about twice that for the single-phase was reported.

Lakehal *et al.* (2008) investigated computationally the convective heat transfer for gas-liquid flow in a microchannel in the slug flow regime for a constant wall temperature boundary condition. In the presence of gas bubbles, the heat transfer rates were reported to be 3–4 times higher than those of the liquid-only flow. They drew an analogy with the internal recirculations in Taylor flow with the eddies in turbulent flow and correlated their computational two-phase heat transfer data with a modified Dittus–Boelter expression for single-phase turbulent flow (Eq. 2.11) using a best fitting technique.

$$Nu_{TP} \approx Nu_{LO} + 0.022(\beta Re_{TP})^{4/5} Pr^{2/5} \tag{2.11}$$

Good agreement was found between their simulated Nusselt number and the proposed model.

Walsh *et al.* (2010) studied the effect of slug length on the heat transfer rate experimentally using a 1.5 mm stainless steel tube for a constant wall heat flux condition. They varied the slug length-to-diameter ratio from 1.6 to 14.3 for a fixed Reynolds number of 112.7 and homogeneous void fraction of 0.66. They identified an entrance region of about one slug length in which initially high values of the Nusselt number relaxed towards a constant asymptotic value. In correlating their results for this asymptotic "fully-developed" region, they argued that the effective heat transfer surface area is the fraction of the wall area covered by the liquid slugs and they reported very good agreement with the following correlation

$$Nu_{TP} = Nu_{LO}(1-\beta)\left[1 + 5.7\left(\frac{L_S}{d}\right)^{-0.5}\right] \tag{2.12}$$

He *et al.* (2010) performed a numerical study of heat transfer in Taylor flow with constant wall heat flux. They highlighted the fact that the overall heat transfer rate should depend on the thermal resistances in the slug and film regions. They derived an analytical model in which the overall heat transfer rate was modelled using one-dimensional, unsteady heat conduction inside the liquid film with a time-dependent heat transfer rate between the film and the train of gas bubbles and liquid slugs. In their model, the heat transfer process in which the overall heat transfer coefficient is, as in Walsh *et al.* (2010), largely controlled by the value for the slug region and the fraction of the wall occupied by the slug. They verified their model using numerical heat transfer data obtained from a wide range of conditions ($100 < Re_{TP} \cdot Pr < 6000$, $1 < L_S/d < 7$) and reported that all data fell within $\pm 25\%$ of the

proposed model. They suggested that the validity of the model can be improved by better prediction of the liquid film thickness and the heat transfer rate in the liquid slug.

Gupta *et al.* (2010b) studied numerically the flow and heat transfer for Taylor flow in a 0.5 mm horizontal channel for both constant wall heat flux and constant wall temperature conditions. They found that the Nusselt number was ~2.5 times higher than that obtained from single-phase flow for both boundary conditions. They also noted that the Nusselt number was independent of the mixture velocity but increased with decreasing homogeneous void fraction for the conditions they studied ($168 < Re_{TP} < 560$, $0.3 < \beta < 0.7$).

Muzychka *et al.* (2011) reanalysed the existing Taylor flow heat transfer data in the literature for both the constant wall temperature (Oliver and Young Hoon, 1968, Horvath *et al.*, 1973, Vrentas *et al.*, 1978, Narayanan and Lakehal, 2008) and the constant wall heat flux boundary conditions (Walsh *et al.*, 2010) and demonstrated an excellent correlation between the apparent mean slug Nusselt number ($\overline{Nu_L^*} = \overline{Nu_{TP}}/(1-\beta)$) and a dimensionless slug length ($L_S^* = L_S/(Re_{TP} \cdot Pr \cdot d)$). They showed that the constant wall temperature heat transfer data followed the theoretical Graetz solution for the mean Nusselt number for thermally developing single-phase laminar flow with a small root mean square (rms) error of 10–15%. A larger rms error (24%) was noted when data obtained from a constant wall heat flux study (Walsh *et al.*, 2010) were included in their analysis.

Though the internal recirculation within the liquid slug (in a reference frame moving with the bubble) has been reported to be the primary mechanism responsible for this heat transfer enhancement, no quantitative analysis of the effects of recirculation on the heat transfer rate have been reported in the literature. A reduction of recirculation size and an increase in recirculation time with increasing Capillary number (*Ca*) were reported by Thulasidas *et al.* (1997) and it might be expected that this would lead to a dependence of heat transfer rates on *Ca* (i.e. on fluid properties, especially the liquid viscosity).

In conclusion, various parameters, including slug length, void fraction and film thickness, have been recognized as key factors governing the heat transfer enhancement brought about by Taylor flow in microchannels. However, although various two-phase heat transfer models have been proposed, the underlying mechanisms controlling heat transfer, knowledge of which is essential for optimal process design and control of micro-systems, are not yet fully understood.

2.4 Annular flow

Annular flow is another frequently encountered two-phase flow regime in microchannels characterised by a central gas core surrounded by a thin liquid film at the wall, as seen in Figure 2.1(b). Whilst the hydrodynamics and heat and mass transfer characteristics of gas-liquid Taylor flow in microchannels have received significant attention, studies of the intermittent slug-annular/annular flow regimes have been generally neglected. It can be attributed mainly to the greater complexity associated with these flow regimes. The work that has been done on gas-liquid annular flow in microchannels is reviewed here.

Fouilland *et al.* (2010) showed extensive bubble merging of nitrogen-water flow in a 1.73 mm horizontal tube for a flow condition at U_L = 0.071 m s^{-1} and U_G = 1.77 m s^{-1}. The flow comprised quasi-annular flow periods disturbed by apparently random flow features where the transient large-amplitude wave structures can be clearly seen in Figure 2.14. With a further increase in gas velocity, the waviness at the gas-liquid interface became smaller to give a relatively smoother annular flow. They also reconstructed the film velocity profile using μPIV techniques and proposed a model (Eq. (2.6)) to determine the ratio of the average film and the mixture velocities for annular flow where the pressure gradients in the gas and liquid are equal ($B_G = B_L$).

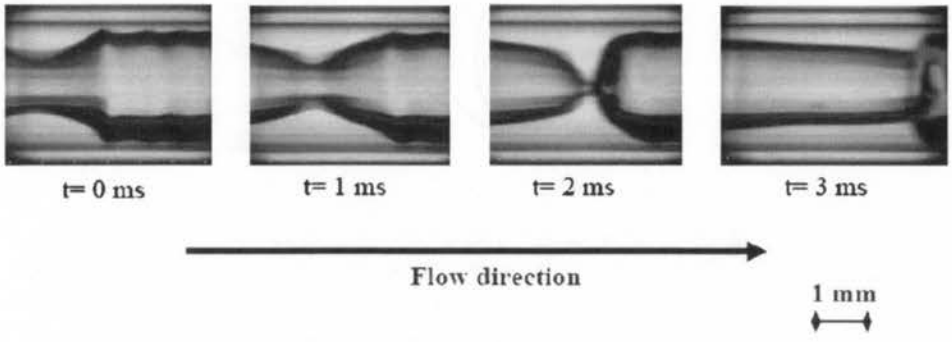

Figure 2.14: Transient large-amplitude wave formation of nitrogen-water slug-annular flow in a 1.73 mm tube for a flow condition at U_L = 0.071 m s^{-1} and U_G = 1.77 m s^{-1}. Taken from Fouilland et al. (2010).

Gupta (2010) performed CFD simulations to study the transient annular flow in a circular microchannel of 0.5 mm diameter. The waves at the gas-liquid interface were successfully captured and the amplitudes of waves were found to increase with increasing gas flow at a

constant liquid flow rate. However, he highlighted that his results were grid size dependent and the outflow boundary condition was not ideal, where interfacial waves were trapped in the computational domain at the exit.

Several studies extended the available annular flow models for large channels to predict the hydrodynamic parameters, including the pressure drop and void fraction, of annular flow in microchannels (Bao *et al.*, 2000, Chen *et al.*, 2002b, Cioncolini *et al.*, 2010). Only fair agreement was reported between the experimental data for small channels ($0.5 < d < 10$ mm) with the correlations. The discrepancy can be possibly due to some fundamental differences between gas-liquid annular flow in microchannels and conventional channels. For example, the assumption of a turbulent film velocity profile associated with the models for large diameter channels is not appropriate for annular flow in microchannels, where the flow in the liquid film is generally laminar. Moreover, most of the available separated flow models, like the Lockhart-Martinelli correlation (1949) and the Chisholm correlation (1967), for large channels do not include surface tension effects which may be important in small channels.

Bao (1995) and Bao *et al.* (2000) investigated convective heat transfer experimentally for air-water flow in a circular channel of 1.95 mm diameter for a constant wall heat flux over a large range of gas and liquid flow rates encompassing Taylor flow, slug-annular flow and annular flow regimes. They found that the heat transfer rate was enhanced considerably by the presence of the gas, especially at higher gas and liquid velocities. A sharp jump in the heat transfer rate was observed above a critical gas velocity, which they believed to correspond to a flow regime transition from Taylor to annular flow.

Bar Cohen *et al.* (1995) reported a high cooling ability when nitorgen-FC72 annular flow was employed to cool a 0.5 mm asymmetrically-heated parallel plate channel. The heat transfer coefficients were found to be 3 to 4 times higher than the liquid only flow. They attributed the heat transfer enhancement to the coupled evaporative cooling and convective heat transfer. The effect of evaporation for non-boiling, gas-liquid annular flow was also reported experimentally by Liu *et al.* (2006). They found that the wall temperature in the heated section can be divided into two zones: a sharp increase of the wall temperature for a region near the inlet, followed by a zone of almost constant wall temperature where evaporative heat transfer of the liquid film was dominant.

Though the potential of gas-liquid annular flow in microchannel to enhance the heat transfer rate over that of the liquid-only flow significantly is recognized, no systematic study of such flow in microchannel is available in the literature.

2.5 Summary

Based on the above review, several knowledge gaps in non-boiling, gas-liquid two-phase flow in microchannels are identified:

1. Taylor flow heat transfer experiments were conducted without either careful control or measurement of the slug length in the past. New experimental data with good control of the slug length are required to elucidate its effect on the Taylor flow heat transfer rate.

2. The heat transfer enhancement brought about by Taylor flow is reported and several correlations are proposed. However, the mechanisms of this enhancement and the effect of various flow parameters, including liquid slug length, mixture velocity, homogeneous void fraction, film thickness and size of the recirculation zone on heat transfer are not fully understood. A heat transfer correlation for non-boiling, gas-liquid Taylor flow combining these knowledge for general application is required for better reactor designs and operations.

3. The effects of gravity on the Taylor bubble shape, velocity field in both the liquid film and slug regions have been observed in a few preliminarily experimental and computational studies. Systematic data to show the importance of gravitational effects on bubble behaviour are required.

4. The ability of gas-liquid annular flow in microchannels to enhance the heat transfer rate has been demonstrated. However, the hydrodynamics and heat transfer characteristics of this flow regime in microchannels remain largely an un-explored area in the literature.

In this thesis, flow and heat transfer in Taylor flow are studied experimentally to address the gaps in the knowledgebase of gas-liquid flow in microchannels and potential experimental challenges for a comprehensive study of the annular flow regime are identified. In the next chapter the experimental apparatus and conditions used in this study are described in detail.

Chapter 3

Experimental Apparatus and Method Validation

Flow characteristics and heat transfer rates of laminar gas-liquid Taylor flow in microchannels are investigated by performing systematic experiments which cover a wide range of conditions ($10 < Re_{TP} < 1100$, $0.001 < Ca < 0.180$, $0.03 < \beta < 0.9$, $1 < L_S/d < 220$). As discussed in the previous chapter, most of the Taylor flow heat transfer experiments were conducted without either careful control or measurement of the slug length in the past. To elucidate the effect of slug length on the Taylor flow heat transfer, a reliable and repeatable technique is first established to produce Taylor bubbles with good control of the slug length. Careful characterizations of the flow structures under different flow conditions are performed using well-developed visualization techniques germinated in our group (Fouilland, 2008, Hägnefelt, 2009, Liu, 2011). High quality pictures for Taylor flow obtained from a circular tube of 2.00 mm diameter are achieved by the combination of the fast frame rate recording (up to 1000 frame per second) and wall curvature correction schemes (using a refractive index matching system to correct refraction at the outer surface and using a liquid phase, ethylene glycol (RI = 1.432), with similar refractive index as the tube material, silica (RI = 1.459), to correct the refraction at the inner surface). New heat transfer data for well-characterized Taylor flow are then collected using an apparatus with small experimental uncertainties (< 15%), in order to provide new insights for better understanding of the enhancement mechanisms brought about by Taylor flow.

The experimental conditions and facilities employed in the present study are described in detail here. Justifications for the choice of working fluids and conditions are provided in Section 3.1. In Section 3.2, the detailed designs for the flow characterisation and heat transfer experiments for vertical upward Taylor flow, together with the data reduction procedures and system validation using single-phase flow are presented. An uncertainty analysis of the individual measurements and calculated Nusselt number is presented in Section 3.3. Section 3.4 introduces the visualization techniques employed for investigation of the gravity effect on Taylor flow in horizontal microchannels.

3.1 Choice of working fluids and conditions

Generally, the fully-developed Nusselt number for Taylor flow is up to 2–3 times higher than that of the single-phase fully-developed laminar flow, depending on the flow characteristics (Oliver and Wright , 1964, Oliver and Young Hoon, 1968, Walsh *et al.*, 2010, He *et al.*, 2010, Gupta *et al.*, 2010b). The internal recirculation within the liquid slug (in a reference frame moving with the bubble) has been reported to be the primary mechanism responsible for this heat transfer enhancement. However, no quantitative analysis of the effects of recirculation on the heat transfer rate has yet been reported. Reductions in recirculation size with increasing Capillary number (*Ca*) were widely reported (Taylor, 1961, Edvinsson and Irandoust, 1996, Giavedoni and Saita, 1997, Thulasidas *et al.*, 1997, Feng, 2009) and it might be expected that these would lead to a dependence of heat transfer rates on *Ca* (i.e. on fluid properties, especially the liquid viscosity). Also, the film thickness which is an important parameter for Taylor flow heat transfer was reported to depend on *Ca*, so one might expect this dimensionless group to capture heat transfer effects arising from that source as well. Therefore, experiments on fluids covering a wider range of Capillary numbers become an important step to develop a better understanding of the underlying mechanisms controlling heat transfer in non-boiling, gas-liquid Taylor flow.

Nitrogen was used as the gas phase in the present study. To cover a wide range of Capillary numbers ($0.001 < Ca < 0.180$), three fluids, water (W), 50 wt% ethylene glycol/water mixture (EG/W) and pure ethylene glycol (EG) were employed as the liquid phases. In addition to yielding a large range of Capillary number, the use of pure ethylene glycol as the liquid phase also allows direct visualization of the gas-liquid interface, as demonstrated in Hägnefelt (2009) and Gupta *et al.* (2010c). For all liquids, the contact angles between the liquid and the copper and silica surface are < 90°, indicating that the walls are always wet with a liquid film existing on the wall.

Table 3.1 shows the properties of all working fluids at 25 °C and atmospheric pressure. The ranges of flow parameters studied and the related dimensionless numbers are given in Table 3.2. As seen in Table 3.1, the viscosities of the three liquid phase fluids are significantly different. Using these three fluids, a wide range of Capillary numbers was easily achieved for a similar range of mixture velocities ($0.10 < U_{TP} < 0.53$ m s^{-1}). The Reynolds number ($10 < Re_{TP} < 1100$) spanned over two orders of magnitude and was kept in the laminar flow regime.

The homogeneous void fraction ranged from 0.03 to 0.9 to allow a comprehensive assessment of its effect on flow and heat transfer characteristics.

All visualization experiments were conducted under isothermal condition (21 °C) and the working temperature for all two-phase heat transfer experiments was controlled so that the temperature rise was never more than 20 °C (and, typically, <10 °C). It is noted that temperature and pressure varied along the test section; however, for the purposes of reporting characteristic conditions (such as velocity and homogeneous void fraction) for each heat transfer condition, the temperature and pressure at the mid-point of the test section were used.

Table 3.1: Physical properties of the working fluids at 25 °C and atmospheric pressure.

Fluid	**Nitrogen**	**Water (W)**	**50 wt% Ethylene glycol / water mixture (EG/W)**	**Ethylene glycol (EG)**
Density (kg m^{-3})	-	997	1063	1113
Viscosity (kg m^{-1} s^{-1})	2.10×10^{-5}	9.78×10^{-4}	3.17×10^{-3}	1.71×10^{-2}
Surface tension (N m^{-1})	-	0.073	0.056	0.048
Specific heat capacity (J kg^{-1} K^{-1})	1040	4182	3648	2405
Thermal conductivity (W m^{-1} K^{-1})	-	0.607	0.402	0.258
Prandtl number, *Pr*	-	6.7	28.8	163.3
Contact angle (copper)	-	~74°	62°-74°	~62°
Contact angle (silica)	-	~35°	35°-83°	~83°
Refractive index	-	1.333	1.382	1.432

Table 3.2: Operating conditions and related dimensionless numbers.

Parameters	Water (W)	50 wt% Ethylene glycol / water mixture (EG/W)	Ethylene glycol (EG)
Mixture velocity, U_{TP} (m s^{-1})	0.11- 0.53	0.10- 0.51	0.10- 0.49
Homogeneous void fraction, β	0.03-0.90	0.09-0.80	0.07- 0.80
Reynolds number, Re_{TP}	210-1100	70-350	10-65
Péclet number, Pe	1460-7280	2020-10080	1630-10610
Capillary number, Ca	0.001-0.007	0.007-0.033	0.037-0.177
Mixer Capillary number, $Ca_{L,M}$	0.0001-0.005	0.001-0.013	0.011-0.088

3.2 Apparatus for vertical Taylor flow experiments

3.2.1 Flow loop design

Two flow loop designs were used for the vertical Taylor flow experiments, depending on the fluids used. An open-loop system was employed when water was used as the liquid phase, whilst a closed-loop system was employed for experiments involved the use of ethylene glycol due to its hygroscopic nature.

3.2.1.1 Nitrogen-water experiments

The experimental facility used to determine the hydrodynamic characteristics and the heat transfer rates of vertical upward Taylor flow using water as the liquid phase and nitrogen as the gas phase in a circular channel of internal diameter, d = 2.00 mm is shown in Figure 3.1. The tube diameter was confirmed by comparing the measured pressure drops of single-phase flows in the laminar flow regime with the prediction for standard laminar friction factor. The liquid was introduced using a HPLC pump (Gilson, Model 305) and the gas flow was regulated by a calibrated mass flow controller (Sierra Smart-Trak, C100L) with a maximum flow rate of 100 sccm. The gas and liquid were mixed in a T-junction prior to entering the

circular microchannel test section. Beyond the test section, the fluids were discharged to the atmosphere.

The liquid inlet, mixture outlet and block temperatures were measured with tip-sensitive K-type thermocouples calibrated to $\pm$ 0.08 K, and data were acquired when steady-state operation was reached. All outputs of the thermocouples were acquired by a data logger (Agilent 34970A). The pressure oscillations and absolute pressure at the liquid inlet were recorded using another data-logger (USB-1608FS) which allows a measurement frequency up to 1000 Hz. The liquid flow rate was monitored by weighing the liquid discharged to a container with an electronic balance (A&D HP320) over a preset period of time.

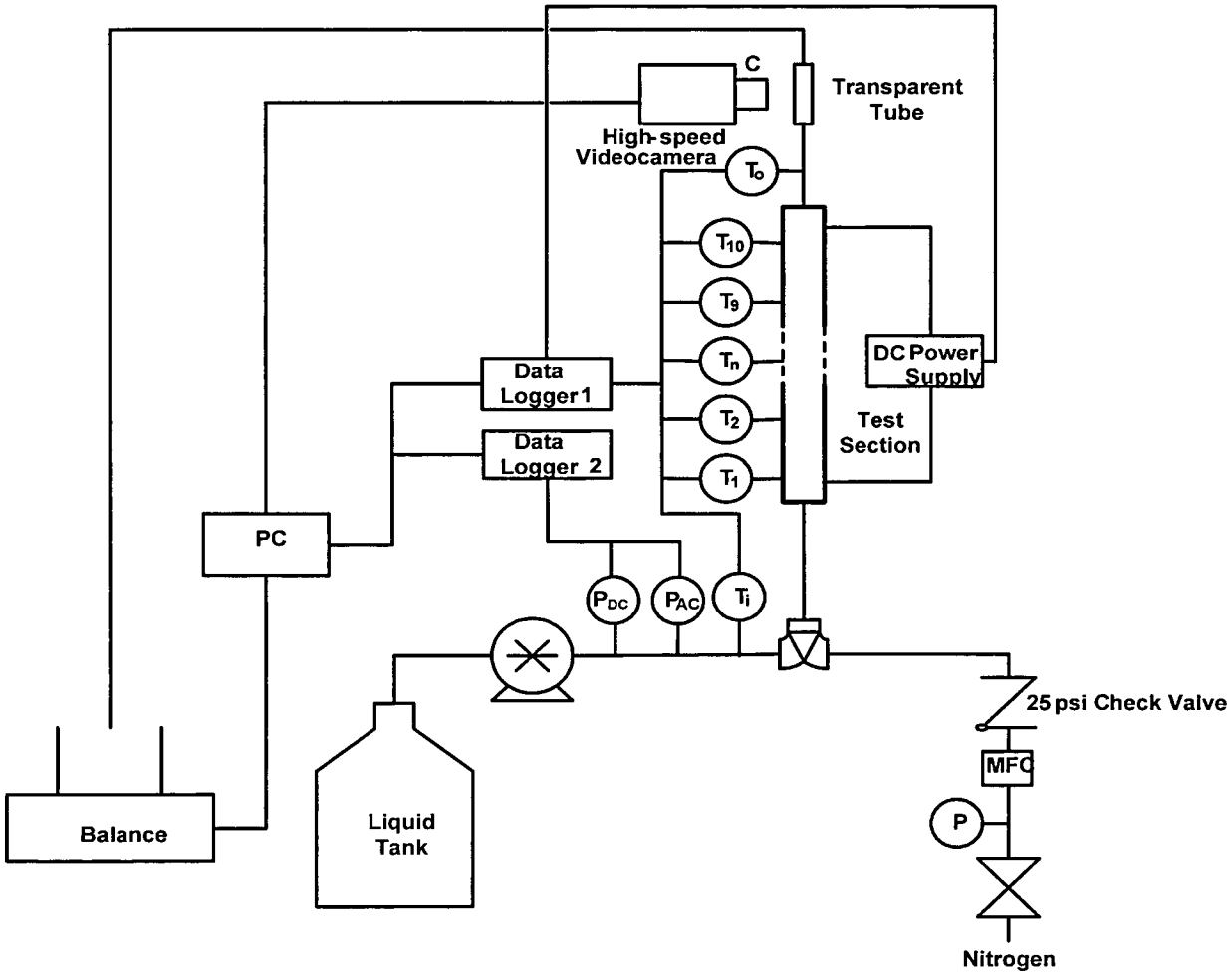

Figure 3.1: Schematic of the experimental apparatus for nitrogen-water Taylor flow. (P_{AC} = piezoelectric pressure transducer, P_{DC} = absolute pressure transducer, T_i = inlet temperature thermocouple, T_o = outlet temperature thermocouple, T_n (n = 1, 2...10) = thermocouples for block temperature measurement.

3.2.1.2 *Experiments involving ethylene glycol*

The experimental facility used to study the flow characteristics and the heat transfer rates of vertical upward gas-liquid Taylor flow in a circular channel (d = 2.00 mm) involving the use of ethylene glycol is modified from the setup used for the nitrogen-water experiments to include a closed-loop for liquid recycling, as shown in Figure 3.2. After the test section, the fluids returned back to the liquid reservoir and the gas was discharged to the atmosphere, after bubbling through a flask partially filled with oil. Since ethylene glycol is highly hygroscopic and its properties change significantly with water content, the closed-loop was designed to prevent contact of the working fluids with any moisture in air.

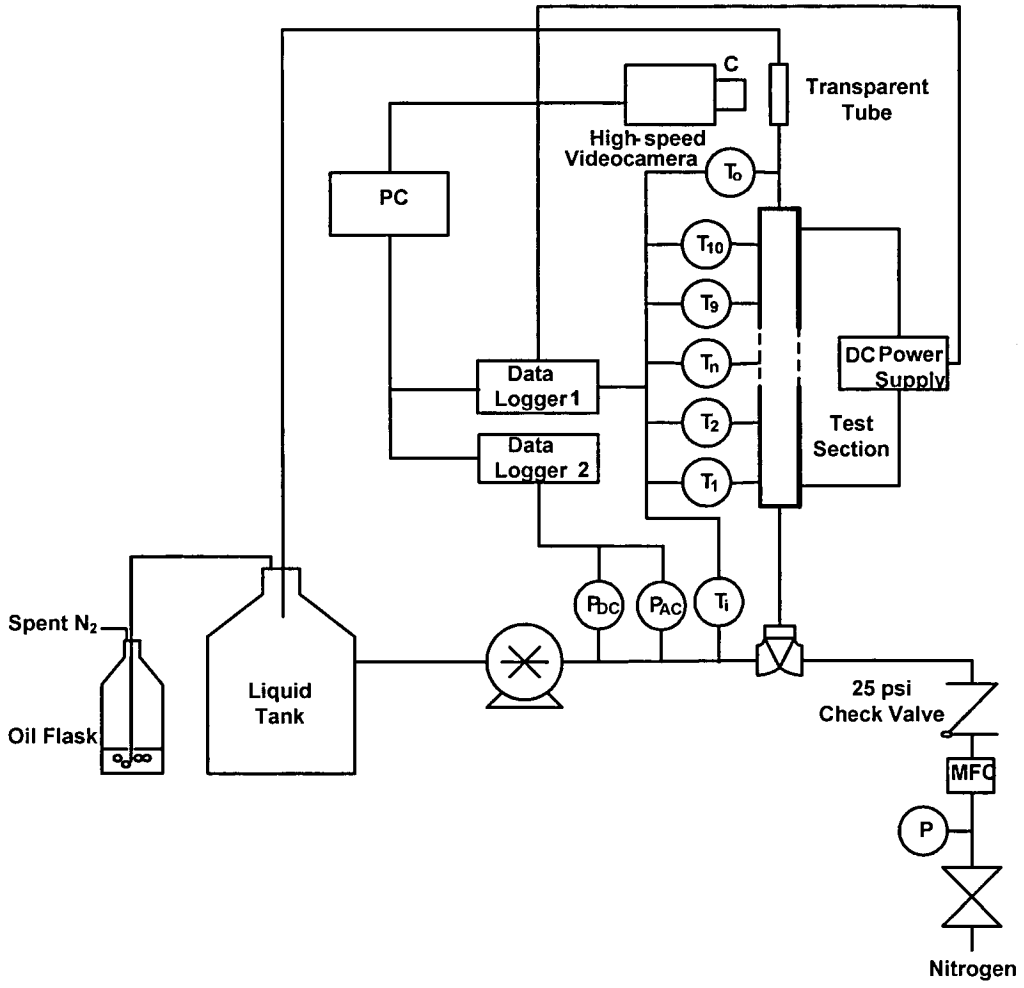

Figure 3.2: Schematic of the modified system for Taylor flow heat transfer and visualization experiments involving the use of ethylene glycol.

3.2.2 Mixer design

Figure 3.3 shows (a) a schematic diagram of the mixer design and (b) the centre plane of the T-mixer and microchannel. Three Swagelok T-junctions with different internal bore diameters were used in this study to generate different bubble and slug lengths for the same mixture velocity and homogeneous void fraction. The dimensions of the three T-mixers are given in Table 3.3. The internal bore diameters of the T-mixers were determined by measuring the mass of liquids (water and ethanol) with known density that were required to fill the mixers. The standard deviation for three repeats was less than 5%. Since the diameters of all T-mixers are larger than that of the test section (d = 2.00 mm), flow contraction occurred at the inlet of the test section. The T-mixer was operated with head-on flows of gas and liquid with the two-phase mixture exiting vertically upward to the test section. A check valve was mounted next to the gas injection port to reduce the effect of pressure pulsation on the compressible gas stream during bubble generation. A piezoelectric pressure sensor (Kistler Instruments, model 211B5) and an absolute pressure sensor (Druck, PMP 1400) were connected close to the liquid inlet to allow the system pressure and flow stability to be monitored, while also providing a means of measuring the frequency of bubble generation.

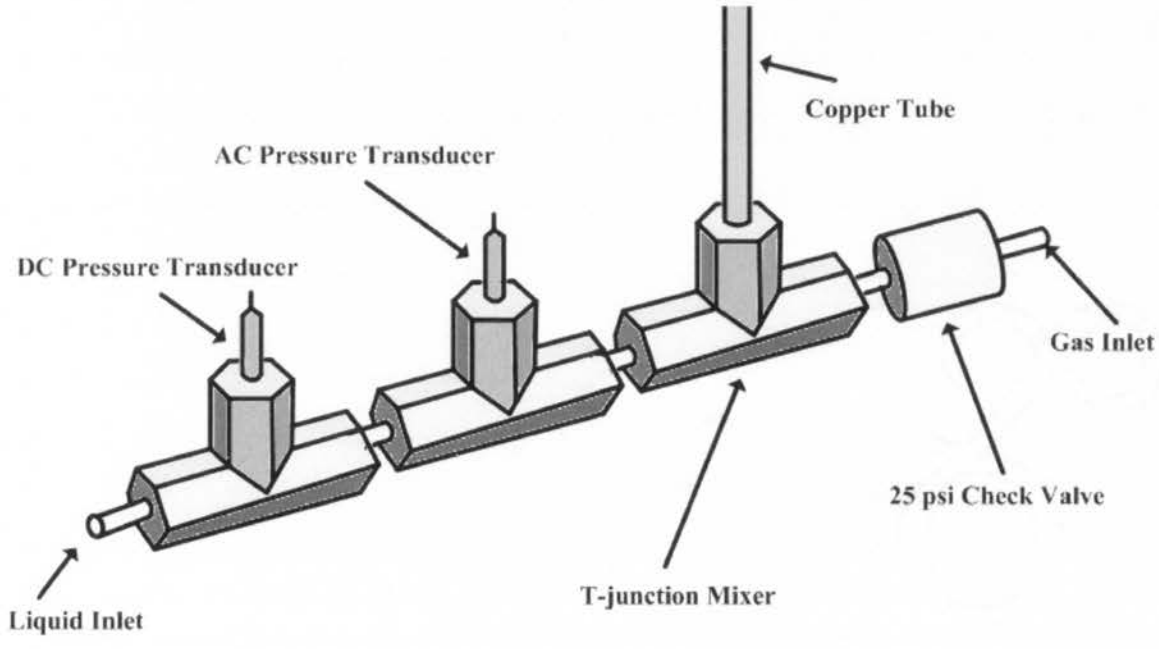

Figure 3.3 (a): Schematic of the mixer design.

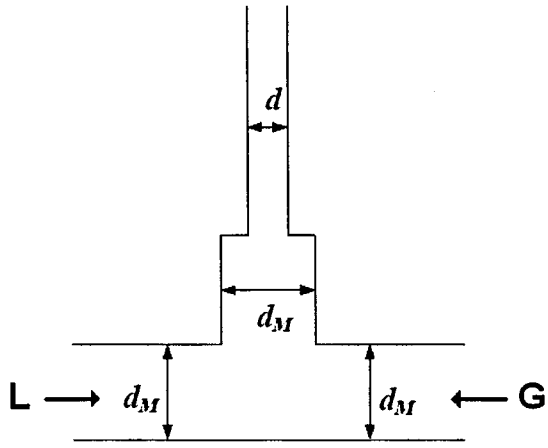

Figure 3.3 (b): View of the centre plane of the circular T-junction mixer and the test section microchannel.

Table 3.3: Geometrical parameters of the T-mixers.

Mixer	Tube Outer Diameter (inch)	Internal Bore Diameter, d_M (mm)	Standard deviation of d_M (mm) (%)
TM1	1/8	2.27	0.08 (3.5)
TM2	3/16	3.10	0.05 (1.6)
TM3	1/4	4.81	0.07 (1.5)

3.2.3 Brightfield flow visualization

The transparent test section comprises a 300 mm long silica tube of internal diameter d = 2.00 mm to allow flow observation with the use of a Photron high-speed PIV camera (Fastcam1024PCI). A back-lit illumination system and epifluorescent microscope (Olympus, IX71) were employed for lighting and magnification, respectively, for the visualization experiments. Due to the mismatch of refractive indices between air (RI = 1.000) and the silica tube (RI = 1.459), optical distortion arises from both the outer and inner curved surfaces of the tube. The effect of refraction at the outer surface was corrected using a square refractive index matching (RIM) system filled with ethylene glycol (RI = 1.432) for all fluid systems. A schematic of the RIM system is shown in Figure 3.4.

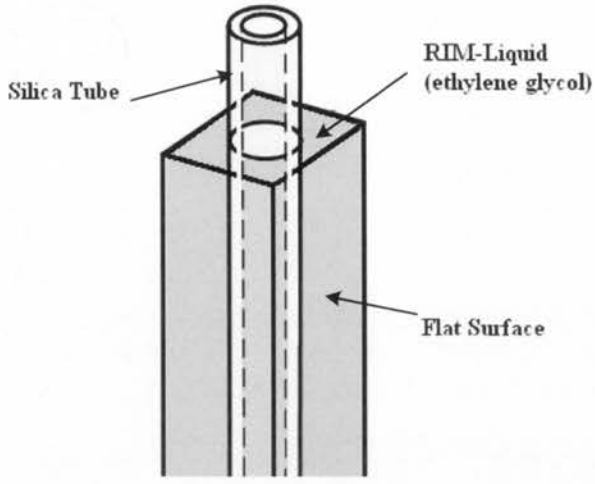

Figure 3.4: Schematic diagram of the RIM-system.

All visualization experiments were conducted under isothermal condition (21 °C) with the heating test section in Figures 3.1 and 3.2 removed. Depending upon the bubble and slug lengths, backlit images of the two-phase flow were recorded by the high-speed camera at rates of 250-1000 frames per second (fps) with a resolution of 1024×1024 pixels and a shutter speed of ~1/500,000 s. Images were recorded with an objective of 4× magnification, which gave a 4.35 × 4.35 mm^2 area of view. The image recordings were always made under conditions where regular pressure oscillations were observed, indicating the achievement of a stable flow. The measurement period varied between 3.2 and 12.8 s, depending on the frame rate, to give 3200 frames per recording. The bubble velocity, U_B, bubble length, L_B, slug length, L_S, and bubble frequency, F_B were then determined by performing a frame-by-frame analysis of the recorded images using the following equations

$$U_B = \Delta Z/\tau \tag{3.1a}$$

$$L_B = U_B(f_{t,i} - f_{n,i})\tau \tag{3.1b}$$

$$L_S = U_B(f_{n,i+1} - f_{t,i})\tau \tag{3.1c}$$

$$F_B = (f_{n,i+1} - f_{n,i})/\tau \tag{3.1d}$$

where τ is the frame period; ΔZ is distance moved by the bubble nose in a time of τ; $f_{n,i}$ and $f_{t,i}$ are the frame numbers when the i^{th} bubble nose and tail appear on the video image

respectively, $f_{n,i+1}$ is that when the bubble nose of the next bubble appears on the video image. The bubble generation frequency can also be determined from a Discrete Fourier Transform of the oscillating pressure signals. As seen in Figure 3.5, good agreement is achieved between the two methods in determining bubble frequency, with less than 1% difference for most cases.

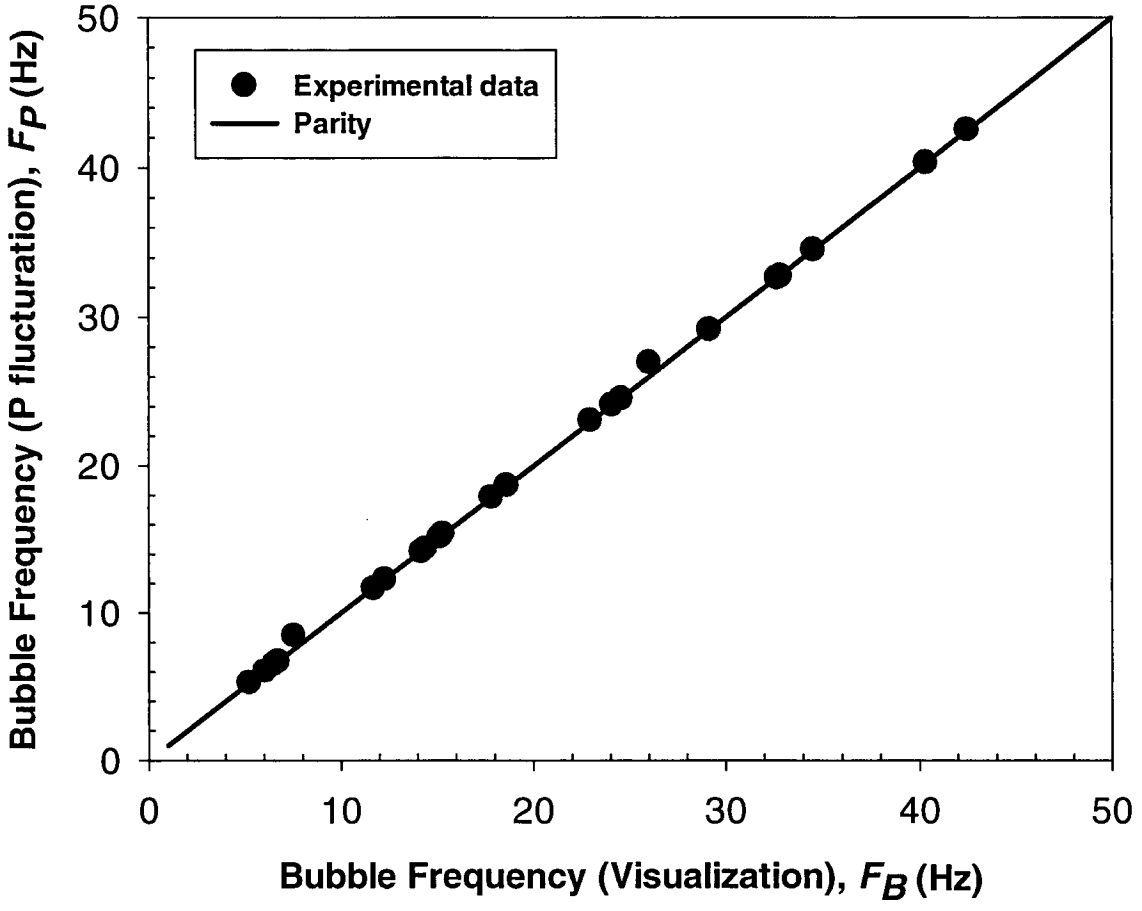

Figure 3.5: Optical bubble frequency against pressure fluctuation frequency.

3.2.4 Multi-block heat transfer measurements

The experimental rig, which allows pseudo-local heat transfer rate determination in single-phase flow, was made of a continuous hard drawn copper tube of 2.00 mm inner diameter which has a surface roughness < 1.5 μm, using the same design as that used in Bao *et al.* (2000). A 400 mm unheated region served to enable the flow to become hydrodynamically fully-developed before entering the heating section. The heating section consisted of ten

25 mm long cylindrical copper blocks of 25 mm in diameter, via soldering, with each block being surrounded by a separate resistance band heater. A K-type thermocouple was embedded at the mid-point of each block which was isolated from the next by a 2 mm-thick fibre sheet to minimize inter-block heat conduction. Bao *et al.* (2000) found that only one thermocouple was required to measure the temperature of each block as a nearly isothermal condition was achieved within individual heating blocks. A 200 mm unheated section following the heating zones minimized the exit effect. A schematic of the ohmically heated test section and a picture of the actual test section are shown in Figure 3.6.

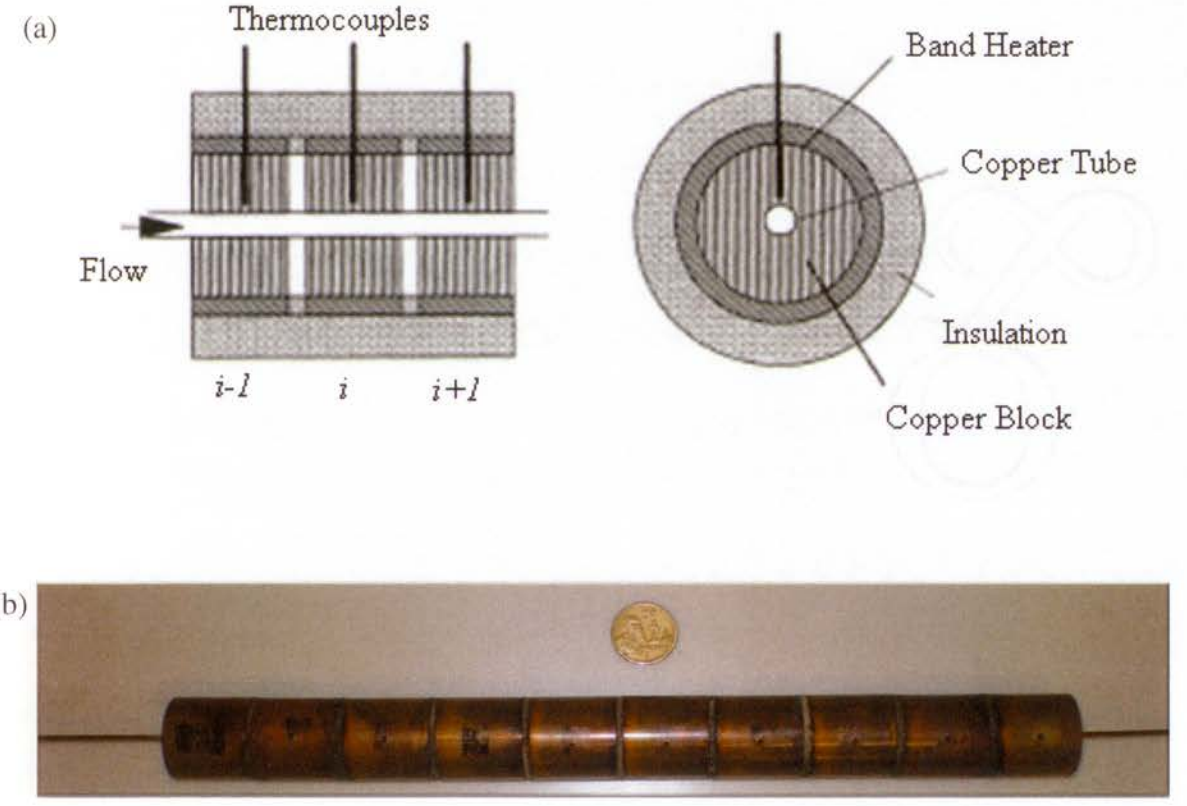

Figure 3.6: (a) Schematic of the ohmically heated test section and (b) a picture of actual test section (lagging removed).

The whole system was insulated by foam to minimise ambient heat loss and the effect of environmental changes. Power was supplied to the band heaters by a DC power source (Densei-Lambda, GEN40-38) at constant voltage. The heat input to each block, Q_i, is calculated from the input voltage, V, and the resistance of each band heater, R_i, which were

found to be independent of temperature over the temperature range 20 °C to 100 °C, given in Table 3.4.

$$Q_i = \frac{V^2}{R_i} \tag{3.2}$$

Table 3.4: Electrical resistance of the band heaters in the temperature range of 20–100 °C.

Heater	Resistance (Ω)
1	730
2	739
3	759
4	725
5	715
6	736
7	746
8	752
9	725
10	731

3.2.4.1 Heating zone calibration

Heat losses to the environment and to adjacent blocks are inevitable, despite the use of insulation. Therefore, a series of calibration experiments were first performed under conditions of zero fluid flow to determine the conductance loss coefficients for both the ambient loss and the inter-block loss. The detailed procedures for the determination of heat losses and the heat transferred to the fluid for each block, Q_{fi}, were documented in Bao (1995), Bao *et al.* (2000), Baird (2001) and Liu (2011). Figure 3.7 gives a schematic arrangement of the heat flows in the heating zone.

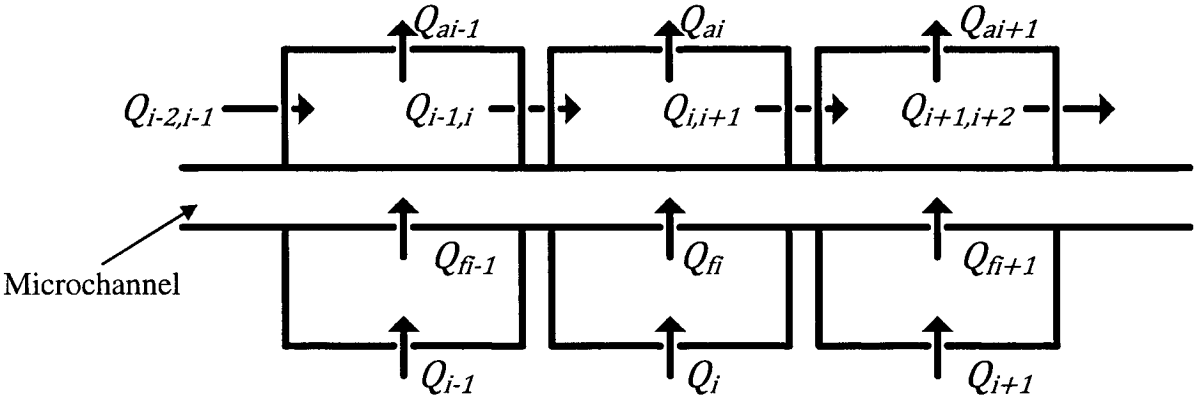

Figure 3.7: Schematic of the heat flows in the heating zone.

Under steady-state condition, the heat balance for each block is expressed as

For block 1: $Q_1 = Q_{f1} + Q_{a1} + Q_{1,2}$ (3.3)

For blocks 2 to 9 ($i = 2,3 \ldots$): $Q_i = Q_{fi} + Q_{ai} + Q_{i,i-1} + Q_{i,i+1}$ (3.4)

For block 10: $Q_{10} = Q_{f10} + Q_{a10} + Q_{10,9}$ (3.5)

where Q_{ai} is the heat lost to the ambient; $Q_{i,i-1}$ and $Q_{i,i+1}$ are the heat transferred from block i to blocks $i-1$ and $i+1$, respectively.

In the absence of fluid flow, $Q_{fi} = 0$, the heat input to individual blocks, Q_i, is balanced by the sum of the heat lost to the environment and adjacent blocks. Since conduction is the major heat transfer mechanisms in these zero fluid flow experiments, the heat losses to the environment and adjacent blocks are determined as

Heat loss to the ambient environment for block 1 to 10 ($i = 1,2 \ldots 10$)

$$Q_{ai} = C_i^a (T_{wi} - T_a) \quad (3.6)$$

Heat loss from block i to $i+1$ for $i = 1,2 \ldots 9$

$$Q_{i,i+1} = -Q_{i+1,i} = C_{i,i+1}^b (T_{wi} - T_{wi+1}) \quad (3.7)$$

where C_i^a is the thermal conductance between block i and the environment; T_{wi} is the wall temperature of block i; T_a is the ambient temperature; $C_{i,i+1}^b$ is the thermal conductance between block i and $i+1$.

Therefore, the heat input into each block is determined as

For block 1: $Q_1 = C_1^a(T_{w1} - T_a) + C_{1,2}^b(T_{w1} - T_{w2})$ (3.8)

For blocks 2 to 9 ($i = 2,3 \ldots 9$):

$$Q_i = C_i^a(T_{wi} - T_a) + C_{i,i-1}^b(T_{wi} - T_{wi-1}) + C_{i,i+1}^b(T_{wi} - T_{wi+1}) \quad (3.9)$$

For block 10: $Q_{10} = C_{10}^a(T_{w10} - T_a) + C_{10,9}^b(T_{w10} - T_{w9})$ (3.10)

A series of 36 calibration experiments were conducted, with heating blocks operating individually at three different power levels and all heating blocks operating together at six other power levels. The Singular Value Decomposition (SVD) method was employed to determine the conductance losses to the environment and adjacent blocks for the present multi-block heating system and the results are shown in Table 3.5.

Table 3.5: Conductance loss to the surroundings and adjacent blocks.

Block No.	Mean C_i^a (W K^{-1})	Standard Deviation of C_i^a (%)	Mean $C_{i,i+1}^b$ (W K^{-1})	Standard Deviation of $C_{i,i+1}^b$ (%)
1	0.03915	3.66	0.320	3.92
2	0.01796	5.16	0.312	7.10
3	0.01765	4.61	0.304	8.43
4	0.01726	1.23	0.321	2.43
5	0.01695	6.69	0.317	6.30
6	0.01670	2.64	0.328	3.91
7	0.01698	7.25	0.315	1.32
8	0.01717	8.90	0.309	1.08
9	0.01803	9.25	0.311	1.94
10	0.03865	6.04	-	-

Figure 3.8 shows the typical block temperature distributions obtained from the zero fluid flow experiments. The accuracy of the values of the conductances presented in Table 3.5 was verified by comparing the wall temperatures calculated from Eqs. (3.8)–(3.10) with the measured wall temperature. As seen in Figure 3.8, good agreement was found between the predicted and measured values, with the largest deviation (3%) observed at the end blocks.

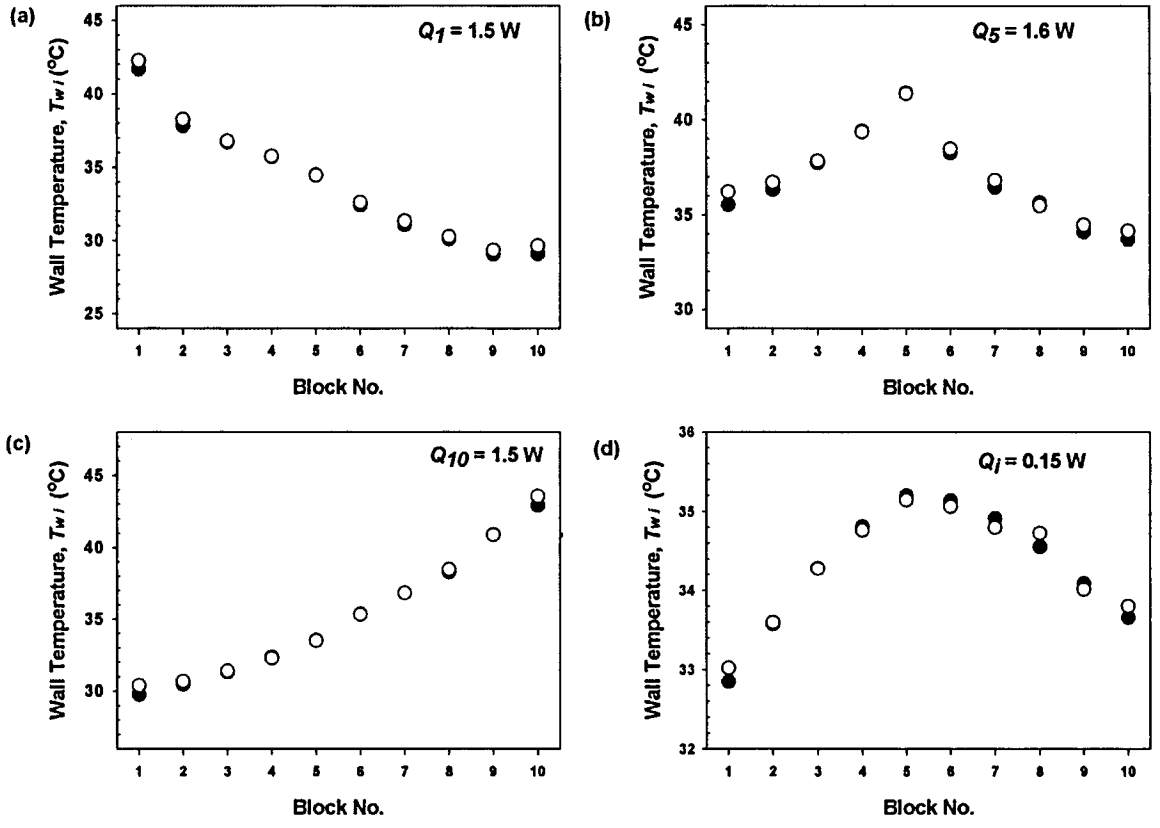

Figure 3.8: Typical wall temperature distributions of zero fluid flow experiments with both experimental (●) and calculated (○) wall temperatures of different blocks shown.

3.2.4.2 Thermal time constant of the heating system

The thermal time constant (τ_{wall}), which is the response time required for a body to change its bulk temperature by ~60% of a specified temperature jump, is an important characteristic of the heating system and is estimated using a lumped capacity analysis method as

$$\tau_{wall} = \frac{\rho_{wall} C_{p,wall} V_{body}}{h A_S} \tag{3.11}$$

where ρ_{wall} and $C_{p,wall}$ are the density and specific heat capacity of the wall material, respectively; h is heat transfer coefficient; V_{body} is the body volume and A_S is the surface area. The thermal time constant for each heating block is approximately 200 s.

3.2.4.3 System validation using single-phase laminar flow

After zero flow calibration tests, a series of single phase laminar flow heat transfer experiments were performed using water (W), 50 wt% ethylene glycol/water mixture (EG/W) and pure ethylene glycol (EG) for Reynolds numbers varied from 5 to 1200 to validate the system. All thermodynamic and thermo-physical properties of water were determined from the IAPWS-IF97 database, while the properties of 50 wt% ethylene glycol/water mixture and pure ethylene glycol were determined using the correlations suggested by Sun and Teja (2003).

At steady-state, the overall heat balance for the heating system can be expressed as

$$Q_f = \dot{m}\hat{C}_p(T_{in} - T_{out}) = Q_i - Q_{loss} = \sum_{i=1}^{10}\left(\frac{V^2}{R_i} - C_i^a(T_{wi} - T_a)\right) = Q_{exch} \tag{3.12}$$

where $\dot{m}$ is the total mass flow rate; $\hat{C}_p$ is the average specific heat capacity across the heating test section; T_{in} and T_{out} are the inlet and outlet temperature, respectively; Q_{loss} is the heat loss to the environment; Q_f and Q_{exch} are the heat transferred to the fluid.

In general, the heat loss to the environment, Q_{loss}, was less than 15% of the total power input, indicating that most of the heat input was transferred predominately into the fluid streams passing through the block. Also, a satisfactory overall heat balance for the heating section was obtained over the range of power input (4–38 W) used in this study, as confirmed in Figure 3.9 (< 5% for most cases, with a few falling in the 5–15% range).

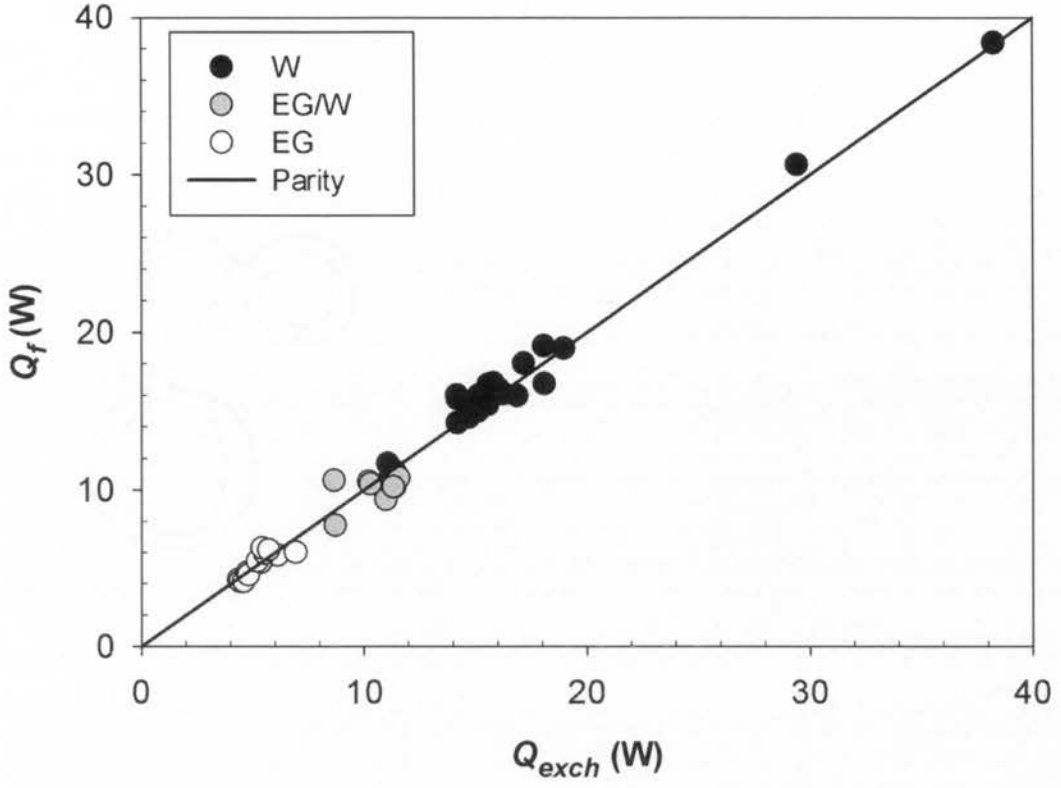

Figure 3.9: Overall heat balance for the heating system.

The bulk mean fluid temperature at the outlet of each block ($T_{bi,out}$) was calculated as

$$\dot{m}\hat{C}_{pi}\left(T_{bi,out} - T_{bi,in}\right) = \dot{m}(\widehat{H}_{i,out} - \widehat{H}_{i,in}) = Q_{fi} \tag{3.13}$$

where $\hat{C}_{pi}$ is the average specific heat capacity of block i; $T_{bi,in}$ is the bulk mean temperature at the inlet of block i, taking a value of the outlet temperature of the previous block ($T_{bi-1,out}$); $\widehat{H}_{i,in}$ and $\widehat{H}_{i,out}$ are the specific enthalpies at the inlet and outlet of block i, respectively.

The pseudo-local Nusselt number, Nu_i, was defined as

$$Nu_i = \frac{h_i d}{k_L} = \frac{q_i}{\Delta T_{lm}} \cdot \frac{d}{k_L} = \frac{q_i}{\dfrac{T_{bi,out} - T_{bi,in}}{\ln\left(\dfrac{T_{wi} - T_{bi,in}}{T_{wi} - T_{bi,out}}\right)}} \cdot \frac{d}{k_L} \tag{3.14}$$

where h_i is the pseudo-local heat transfer coefficient; q_i is the wall heat flux; ΔT_{lm} is the log-mean temperature difference in each heating block.

With this experimental rig, a step change in wall temperature is achieved from one block to the next and an approximately constant wall temperature is imposed in each block, with the blocks all having nearly the same average heat flux. While the experimental arrangement does not correspond strictly to any standard thermal boundary condition for laminar flow, it has been shown with single-phase flows to produce pseudo-local heat transfer coefficients that agree closely with theoretical results for constant heat flux thermal boundary conditions. As seen in Figure 3.10, most of the experimental Nusselt numbers fall within 10% (some are in the range 10–20%) of the standard Graetz solution (Shah and London, 1978). One point to note here is that data for the first and last blocks were not included in the comparison due to the uncertainties arising from the end-block effects.

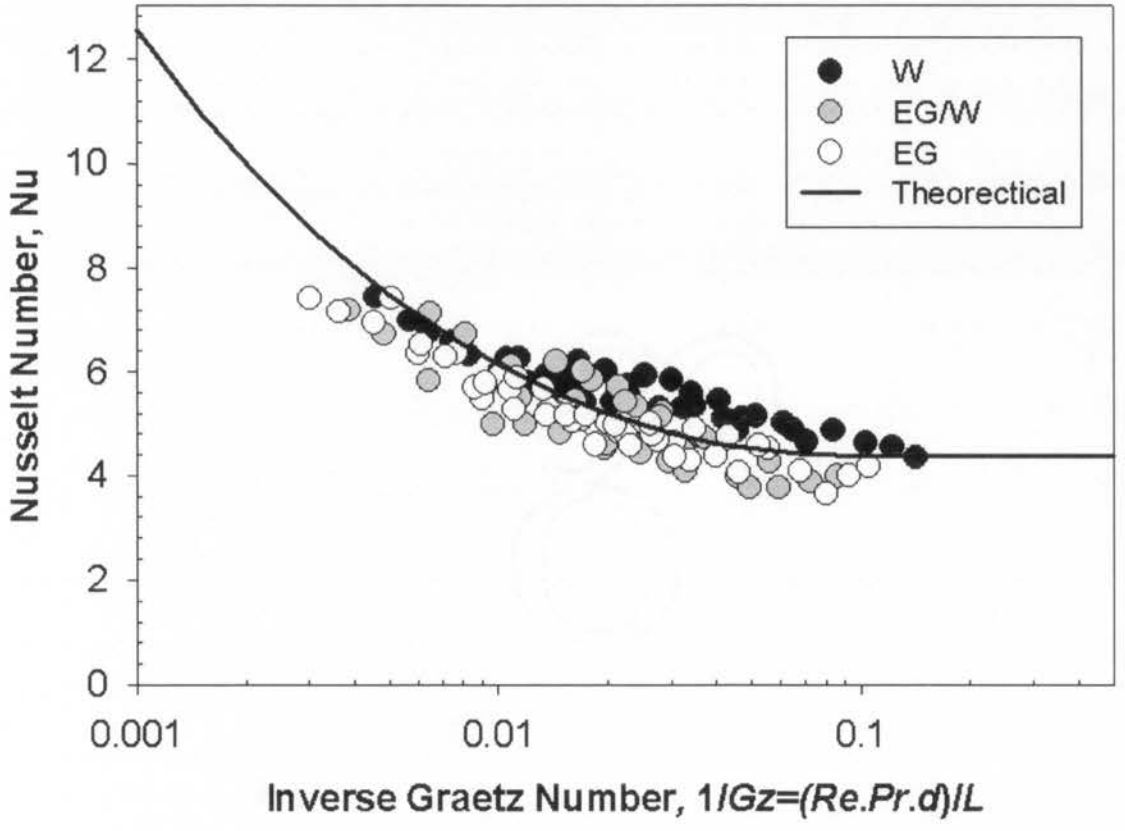

Figure 3.10: Comparison of the experimental single-phase local Nusselt numbers with the theoretical results for thermally-developing and hydrodynamically fully-developed laminar flow for constant wall boundary conditions suggested by Shah and London (1978).

3.2.4.4 *Two-phase heat transfer*

In determining the two-phase heat transfer rate, a homogeneous mixture of the two fluids was assumed. The bulk mean temperature was determined in a similar way to that used in the single-phase experiments, except a two-phase specific heat capacity, $C_{p,TP}$ and specific enthalpy, H_{TP}, were used and the evaporation of the liquid phase was taken into account.

$$C_{p,TP} = x_G C_{p,G} + (1 - x_G) C_{p,L} \tag{3.15}$$

$$H_{TP} = x_G H_G + (1 - x_G) H_L \tag{3.16}$$

where $C_{p,G}$ and $C_{p,L}$ are the specific heat capacity and H_G and H_L are the specific enthalpies of the gas and liquid phases, respectively; x_G is the mass fraction of the gas phase. With the introduction of gas into the system, evaporation occurs. The mass of fluid evaporated, $\dot{m}_{vi}$, from the entrance to heating block i is estimated based on the saturated vapour pressure, $P_{sat,i}$, at the measured wall temperature (T_{wi}), assuming that gas-liquid equilibrium is reached immediately

$$\dot{m}_{vi} = \dot{m}_G \frac{M_L P_{sat,i}}{M_G (P_i - P_{sat,i})} \tag{3.17}$$

where $\dot{m}_G$ is the gas mass flow rate; M_L and M_G are the molecular weight for the gas and liquid phases, respectively; P_i is the pressure at the mid-point of block i.

The heat needed for liquid phase evaporation ($Q_{E,i}$) is then calculated as

$$Q_{E,i} = (\dot{m}_{vi} - \dot{m}_{vi-1}) H_{lv,i} \tag{3.18}$$

where $H_{lv,i}$ is the enthalpy of vaporization in zone i.

The working temperature for all two-phase heat transfer experiments was controlled so that the temperature rise was never more than 20 °C (and, typically, <10 °C). Figure 3.11 shows the variation of the saturation vapour pressure, P_{sat}, with temperature. It can be seen that the saturation vapour pressures for all liquid phase fluids are well below the system pressure, which is always higher than atmospheric pressure, for the temperature range used in the present study (20-50 °C). Using Eqs. (3.17) and (3.18), the fraction of the wall heat flux that

results in evaporation (Q_E/Q_f) was found to be negligible (< 2%) for the range of gas flow rate (0.02–0.56 kg m^{-2} s^{-1}) and heat flux (0.5–12 kW m^{-2}) used in the present study.

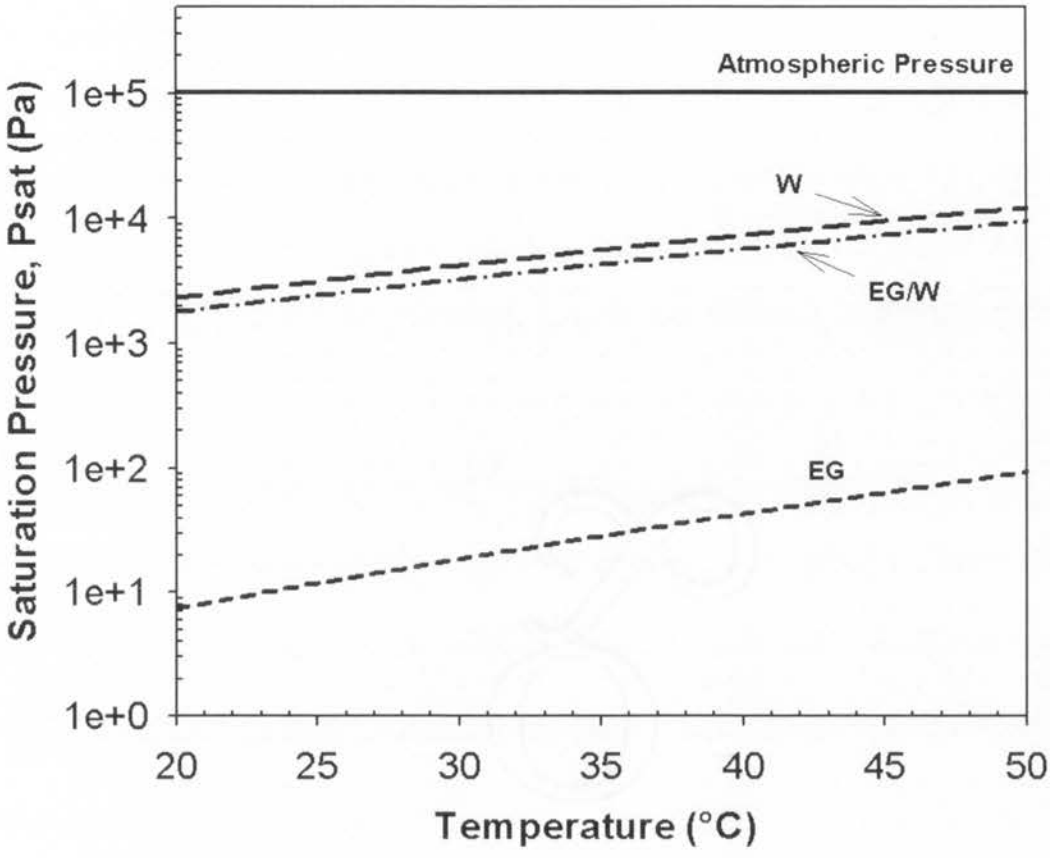

Figure 3.11: Variation of the saturation vapour pressure, P_{sat}, with temperature for water (W), 50 wt% ethylene glycol/water mixture (EG/W) and ethylene glycol (EG).

Taking the energy used for evaporation into account, the bulk mean fluid temperature at the outlet of each block ($T_{bi,out}$) for two-phase flow was calculated as:

$$\dot{m}\hat{C}_{p,TPi}\left(T_{bi,out} - T_{bi,in}\right) = \dot{m}(\widehat{H}_{TPi,out} - \widehat{H}_{TPi,in}) = Q_{fi} - Q_{E,i} \tag{3.19}$$

The two-phase Nusselt number for each block (Nu_i) were then determined in the same manner as that used for the single-phase system (Eq. 3.14), using the liquid thermal conductivity.

As discussed in the single-phase validation section, the present experimental arrangement does not correspond strictly to any standard thermal boundary condition for laminar flow

even though the heat flux in each heating zone is approximately the same. Although the apparatus returns accurate pseudo-local heat transfer coefficients for steady, developing single-phase flows with a constant heat flux thermal boundary condition, the long thermal time constant associated with the heating blocks (~200 s) means that its response to a pulsatile pattern like Taylor flow with a frequency of a few Hz represents a time-average for the flow. Therefore, this apparatus were used to determine the mean heat transfer rate for hydrodynamically and thermally fully-developed Taylor flow.

3.3 Uncertainties in the two-phase heat transfer analysis

With the inclusion of viscous fluids in the study, the inlet pressures increased somewhat, from ~105 kPa with water to as high as 170 kPa with ethylene glycol at the maximum velocity, thus giving rise to significant gas volume and mixture velocity changes from inlet to outlet. The magnitude of this effect was estimated from the estimated fraction of the overall system pressure drop that occurred between the inlet pressure measurement (in the liquid, upstream of the mixer, Figure 3.1 and 3.2) and the observation point near the end of the transparent tube, being typically about 35% of the total pressure drop. For the worst case (ethylene glycol, $U_{TP} = 0.42$ m s^{-1}, $\beta = 0.42$, $L_S/d \sim 2.3$), the bubble volume was calculated to increase 13% for isothermal condition. This calculation was confirmed experimentally by comparing the bubble lengths at the entrance and exit of the visualization test section at room temperature. The variability in the mixture velocity and bubble length due to pressure drop effects are therefore <13% in the worst case, and considerably less than this in general.

In the heat transfer experiments, the wall heat flux was controlled to ensure that the temperature rise was never more than 20 °C (and, typically, <10 °C). Therefore, the volume change due to thermal expansion of the gas was never more than a few percent. This effect was easy to determine accurately via the block-to-block heat balances employed for the data analysis. In correlating the results from individual blocks, the local estimates of temperature and pressure were used. However, for the purposes of reporting characteristic conditions (such as velocity and homogeneous void fraction) for each heat transfer condition, the temperature and pressure at the mid-point of the multi-block test section were used.

Estimates of the uncertainties in the individual measurements needed to evaluate the two-phase Nusselt number (Nu_{TP}) are presented in Table 3.6. Measurements of local single-

phase heat-transfer coefficients in thermally-developing laminar flow agree with theoretical predictions to within 10%. An additional source of error in the two-phase flow heat transfer experiments is the estimation of the energy going to evaporation, but as shown above this is a minor effect (< 2%) because of the low working temperature (20-50 °C) so any error in its calculation will have a negligible effect on the results. The resulting uncertainty in Nu_{TP} is therefore no more than 15% of the measured value.

Table 3.6: Uncertainties of individual measurements and calculated Nusselt number.

Parameter	Range	Uncertainty
Tube internal diameter, d (mm)	2.00	±1%
Inlet pressure (kPa)	105-170	±0.25%
Heat flux (kW m^{-2})	0.5-12	±5%
Gas mass flux (kg m^{-2} s^{-1})	0.02-0.56	±1%
Liquid mass flux (kg m^{-2} s^{-1})	24-296	±1%
Wall to bulk mean temperature difference (°C)	1-8	±7%
Two-phase Nusselt number, Nu_{TP}	0.8-14.0	±15%

3.4 Apparatus for horizontal Taylor flow experiments

Both brightfield microscopy and Micro-particle Image Velocimetry (μPIV) experiments were performed to obtain the bubble shape and detailed flow field in the liquid phase to investigate the effect of gravity on Taylor flow in a horizontal direction.

3.4.1 Flow loop design

Figure 3.12 shows a schematic of the experimental facility used for Taylor flow visualization experiments performed in 300 mm long silica tubes of three different inside diameters (d = 1.12, 1.69 and 2.12 mm) in the horizontal direction. Nitrogen and ethylene glycol were used as the gas and liquid phases, respectively. The flow loop design is the same as that used for the nitrogen-ethylene glycol vertical visualization experiments with the heating section disconnected. For all horizontal flow experiments, the smallest T-mixer (TM1) was used.

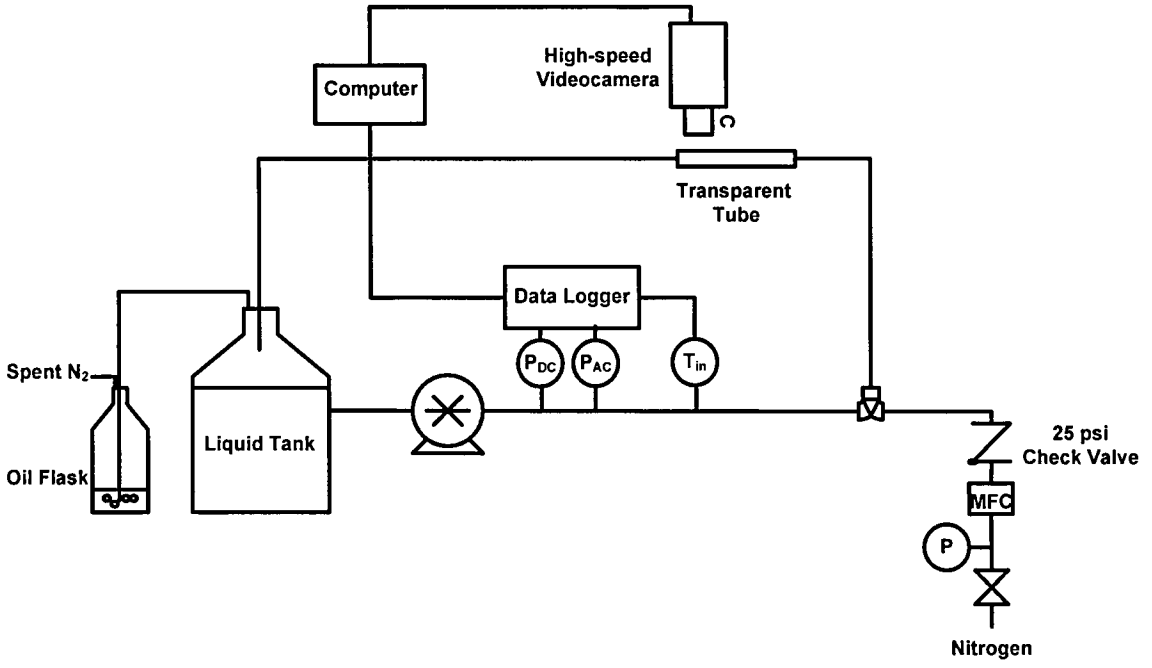

Figure 3.12: Schematic of visualization experimental apparatus for the investigation of the gravity effect on Taylor flow (P_{AC} = piezoelectric pressure transducer, P_{DC} = absolute pressure transducer, T_{in} = inlet temperature thermocouple).

3.4.2 Brightfield microscopy

Brightfield microscopy was first performed with pure ethylene glycol using the Photron high-speed PIV camera (Fastcam1024PCI) as that used for the vertical Taylor flow visualization to collect backlit images of the two-phase flow. Variations of film thickness in the circumferential direction were established by placing the camera at four different positions to yield eight visualization angles, as shown in Figure 3.13. The bubble shapes obtained at the vertical plane passing through the channel axis were digitized using digitization software (DigitizeIt) to allow quantitative comparisons of the upper and lower bubble interfaces for different flow conditions. The thickness of the film, δ_F, surrounding the gas bubble was determined by direct measurement of the distance from the wall to the gas-liquid interface. The bubble velocity, U_B, bubble length, L_B, slug length, L_S, and bubble frequency, F_B, were determined by performing a frame-by-frame analysis of the recorded images, as described in Section 3.1.3.

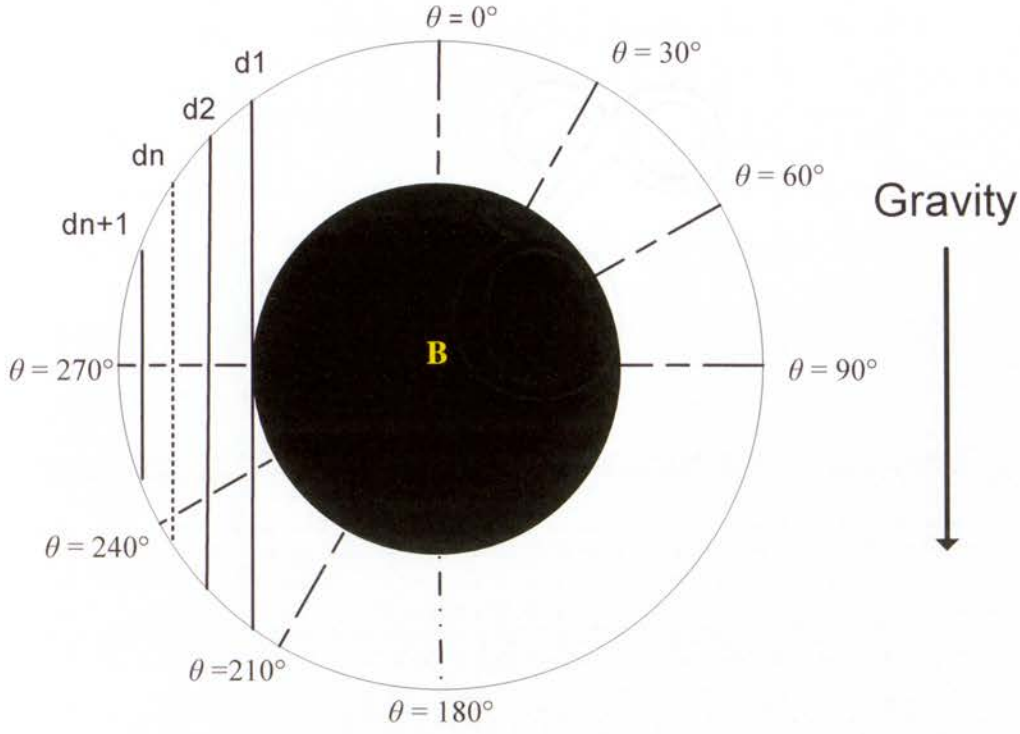

Figure 3.13: An arbitrary cross-section in the bubble region showing the visualization angles for brightfield microscopy and the focal planes for μPIV measurements.

3.4.3 Micro-particle Image Velocimetry (μPIV) visualization

A Micro-particle Image Velocimetry (μPIV) system was established successfully in our laboratory and its ability to produce high quality flow field measurement of two-phase flow have been demonstrated (Fouilland, 2008, Hägnefelt, 2009, Liu, 2011).

The μPIV measurements in this study were undertaken using ethylene glycol seeded with 0.024% by volume fluorescent particles ($d_{particle}$ = 3 μm) to obtain the time-resolved velocity data. Figure 3.14 shows a schematic of a μPIV system showing its working principles. A high-speed double pulsed laser (New Wave Pegasus-PIV dual-cavity Nd-YLF laser, capable of up to 10 mJ per pulse per laser head at 1 kHz, with a pulse duration < 180 ns) was used to excite the fluorescent seed particles at the 527 nm wavelength through a 10× objective with a numerical aperture (N.A.) equal to 0.3. The reflected particle signals, which have a longer wavelength (λ > 550 nm), were separated from the illuminating light by a filter cube and captured by the same high-speed PIV camera as that used in the brightfield visualization

experiments. The camera was synchronized with the laser pulses using an ILA synchroniser (Jülich, Germany) to obtain image pairs with known time interval from 10–1000 μs. Images recorded with the 10× objective had an area of view of 1.74 × 1.74 mm^2 at full 1024 × 1024 pixels resolution. The recorded images were pre-processed using the ImageJ software to improve the image contrast by removing low-intensity images of out-of-focus particles. Then, the Vidpiv software from ILA was used to process the PIV images to yield the velocity field. Details of the μPIV system and velocity data capturing techniques can be found in Fouilland *et al.* (2010) and the Appendix.

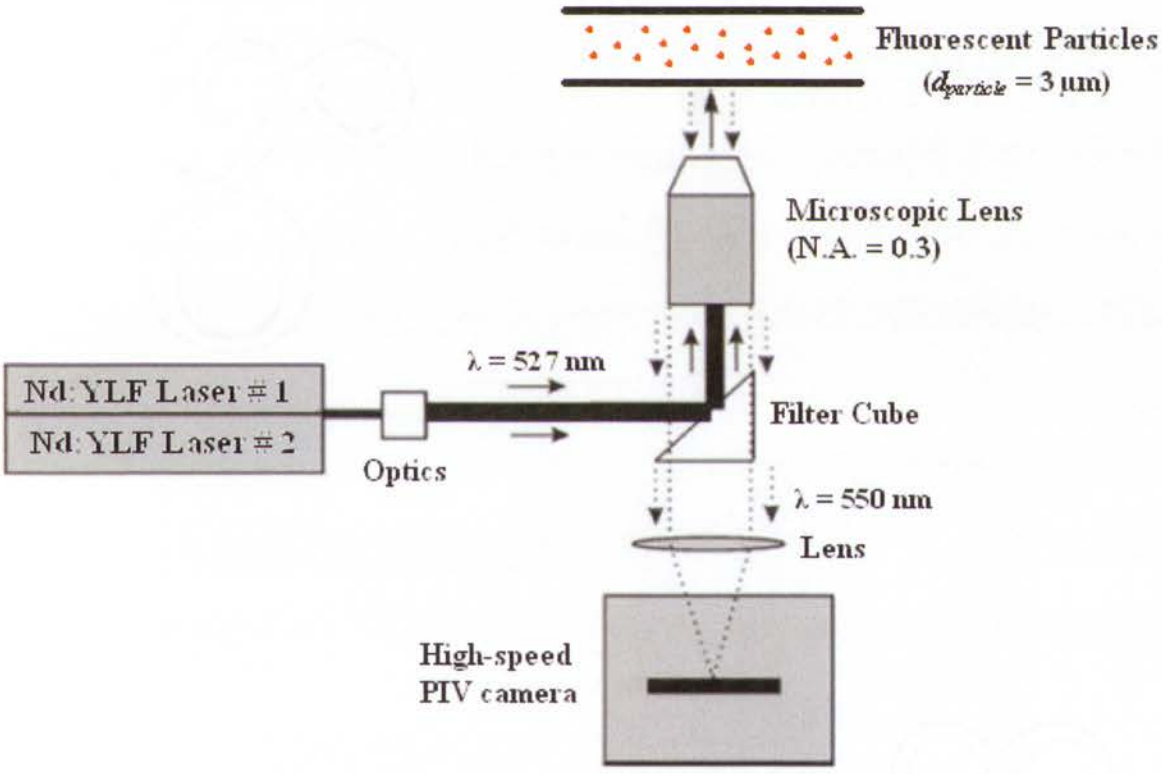

Figure 3.14: A schematic of a μPIV system showing the pathways for illuminating and reflected lights. Modified from Fouilland (2008).

3.4.3.1 Single-phase flow validation

μPIV measurements for single-phase laminar flow with a Reynolds number of 6 were first performed to validate the system. Since the measurements were done at a location ~300 mm

downstream from the inlet of the test section, a fully-developed laminar flow was established and a parabolic velocity profile was expected. 150 image pairs were recorded and analysed to obtain the time-averaged velocity vectors at each measurement depth which were then used to reconstruct the velocity profile at the horizontal centreline of the cross-section. Figure 3.15 compares the normalized experimental velocity profile with the parabolic profile for single-phase fully-developed laminar flow. Good agreement was achieved between the measurement and the theoretical value (within 4%).

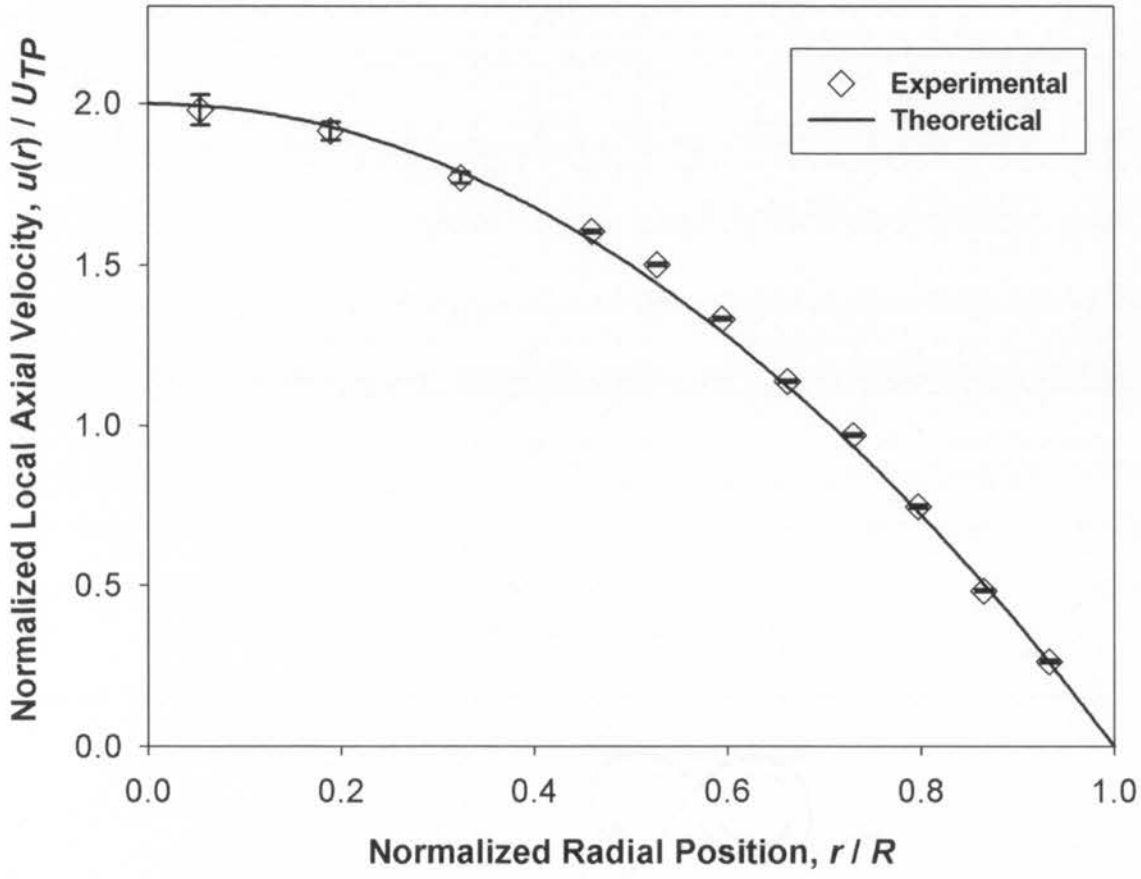

Figure 3.15: Comparisons of the experimentally determined velocity profile at the horizontal centreline for a single-phase laminar flow (Re_L = 6) with the parabolic velocity profile for single-phase fully-developed laminar flow. The tube diameter is 2.12 mm.

3.4.3.2 Taylor flow measurements

The alternate passage of gas bubbles and liquid slugs through the system provides some challenges for the PIV measurement. When measuring velocities near the wall, the

background noise was much lower during the passage of a gas bubble than during the passage of a liquid slug as more out-of-focus particles were present in the slug region. Also, the velocities of the near wall liquid in the slug region are much greater than in the liquid film surrounding a gas bubble. Therefore, it is not possible to measure velocities of the near wall liquid in the bubble and slug regions at the same time. The PIV conditions (pulse separation) and analysis procedure (image pre-processing) had to be adjusted depending on the region to be examined.

By optimizing the measurement parameters for a specific region, the velocity profile of the liquid film surrounding the bubble and that of the liquid slug for the horizontal centre plane passing through channel axis ($\theta = 90°$) were constructed by performing measurements at different focal depths (Figure 3.13).

3.4.4 Heat transfer measurements

The effect of gravity on the heat transfer rate of nitrogen-ethylene glycol Taylor flow was investigated by performing heat transfer experiments using the flow loop design as shown in Figure 3.2 with the heating section put in a horizontal direction. The mean fluid temperature at the centre of each block (T_{bi}) and the Nusselt number (Nu_i) were calculated in the same manner as those used for the vertical system.

3.5 Summary

This chapter provided a detailed description of the experimental apparatus and the data reduction procedures for the investigation of the flow characteristics and heat transfer rate for Taylor flow in fine passages. Calibration of the multi-block heating system used in this study were performed carefully and verified with the single-phase laminar flows. Good agreement was found between the experimental data and the theoretical results. An uncertainty analysis was conducted and the calculated heat transfer rates are within 15% uncertainty. In the next chapters, results for Taylor flow visualization and heat transfer experiments are presented.

Chapter 4
Hydrodynamics of Vertical Taylor Flow

From the literature various parameters, including slug length, void fraction and film thickness, have been recognized as key factors governing heat transfer enhancement for Taylor flow. Therefore, careful characterisation of the flow pattern becomes essential for accurate Taylor flow heat transfer prediction. Furthermore, it is very important to understand how to control the Taylor flow hydrodynamics by parameters that can be manipulated directly, for example the superficial gas and liquid velocities, geometry of the mixing zone, etc., if this flow regime is used for engineering applications.

In this chapter, the dependence of the hydrodynamic characteristics on fluid properties and flow parameters, including mixture velocity, homogeneous void fraction, and the dimension of the T-mixer, is investigated by performing systematic visualization experiments under isothermal condition (21 °C) using a 300 mm long silica tube of internal diameter $d = 2.00$ mm in a vertical upward direction. Details of the experimental setup and image analysis procedures are provided in Chapter 3. The results for pressure drop of Taylor flow for the present study conditions are presented in Section 4.1. The flow visualization results are shown in Section 4.2. A modified scaling law for bubble length prediction is presented in Section 4.3.

4.1 Pressure drop

For gas-liquid Taylor flow in a microchannel, pressure drop is mainly due to the frictional loss of the liquid slug and the additional pressure drop over the gas bubbles due to effects near the caps of the bubbles. The pressure drop due to the frictional loss in the gas bubble, as well as that in the liquid film surrounding the bubble are often neglected when compared with the pressure drop in the liquid slug (Kreutzer *et al.*, 2005a, Kreutzer *et al.*, 2005b, Walsh *et al.*, 2009, Warnier *et al.*, 2010).

Based on their experimental and computational results, Kreutzer *et al.*(2005b) suggested that the total pressure drop can be calculated by summing the pressure drop for fully-developed

laminar tube flow acting over the slug length and the pressure drop over the front and rear bubble caps using Bretherton's correlation (1961) for flow with negligible inertia

$$\frac{\Delta P}{\Delta L} = \left(\frac{L_S}{L_{UC}}\right)\frac{4}{d}\left(\frac{1}{2}\rho_L U_{TP}^2\right)\frac{16}{Re_{TP}}\left[1 + \frac{7.16(3Ca)^{2/3}}{32Ca}\frac{d}{L_S}\right] \tag{4.1}$$

The performance of Eq. (4.1) in estimating the pressure drop along the test section was examined by comparing the measured inlet pressures and the calculated values, as shown in Figure 4.1.

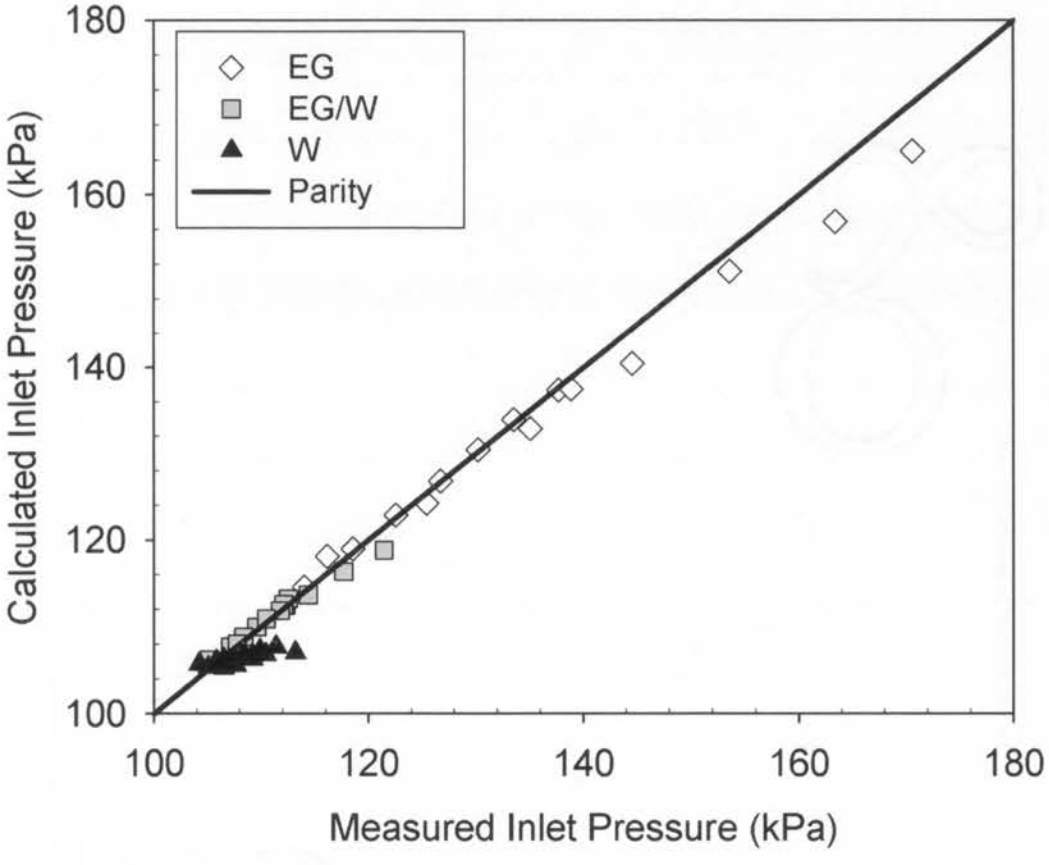

Figure 4.1: Comparison of the measured inlet pressure with the calculated values using Eq. (4.1).

Good agreement between the experimental data and Eq. (4.1) is achieved for the EG and the EG/W mixture systems for flows with low Reynolds and Capillary numbers. However, the predicted values start deviating from measured data as the mixture velocity increases (for

flow with higher inlet pressure). Kreutzer *et al.* (2005b) highlighted that Bretherton's theory only works well for flow with negligible inertia at which bubble caps are hemispherical in shape. As the mixture velocity increases (increasing Re_{TP} and Ca), bubble ends change from having hemispherical caps to a sharp nose and a flattened tail, leading to breakdown of the lubrication approximation used by Bretherton and hence discrepancies between the experimental data and predicted values.

In general, Eq. (4.1) under-predicts the pressure drop for the water experiments. As seen in Figure 4.2, most calculated pressure drops are considerably smaller than the measured value for $Re_{TP} > 100$. When the inertial effects become more important ($100 < Re_{TP} < 1000$), Kreutzer *et al.* (2005b) also reported a significant increase in pressure drop. Due to the large Reynolds number for water ($210 < Re_{TP} < 1100$), Eq. (4.1) fails to give an accurate pressure drop prediction for experiments using water as the liquid phase.

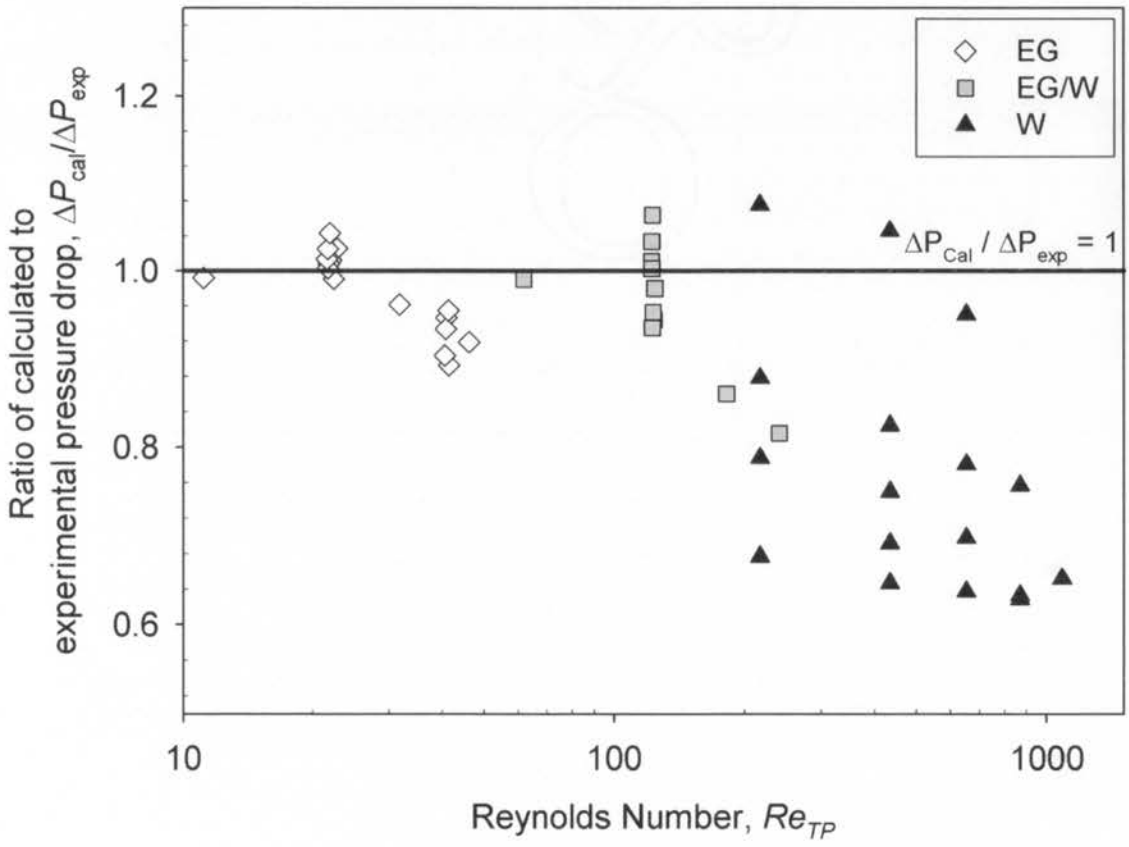

Figure 4.2: Variation of the ratio of calculated to experimental pressure drop, $\Delta P_{cal}/\Delta P_{exp}$, with the Reynolds number, $Re_{TP} = \rho_L U_{TP} d/\mu_L$.

For Taylor flow with significant inertial effects ($100 < Re_{TP} < 1000$), Kreutzer *et al.* (2005b) suggested Eq. (4.2) to predict the pressure drop

$$\frac{\Delta P}{\Delta L} = \left(\frac{L_S}{L_{UC}}\right)\frac{4}{d}\left(\frac{1}{2}\rho_L U_{TP}^2\right)\frac{16}{Re_{TP}}\left[1 + a\frac{d}{L_S}\left(\frac{Re}{Ca}\right)^{0.33}\right] \tag{4.2}$$

where the value of constant a was found to be 0.07 and 0.17 from their computational and experimental results, respectively. They attributed the difference to the presence of impurities in the liquid for the experiments. Walsh *et al.* (2009) confirmed experimentally the form of Eq. (4.2) in predicting pressure drop of Taylor flow in microchannels and found that the value of constant a was an average of the values reported by Kreutzer *et al.* (2005b). Figure 4.3 compares the experimental inlet pressure and the values calculated using Eq. (4.2) with $a = 0.17$ for experiments using water as the liquid phase. The experimental data agree reasonablly well with the precdiction values.

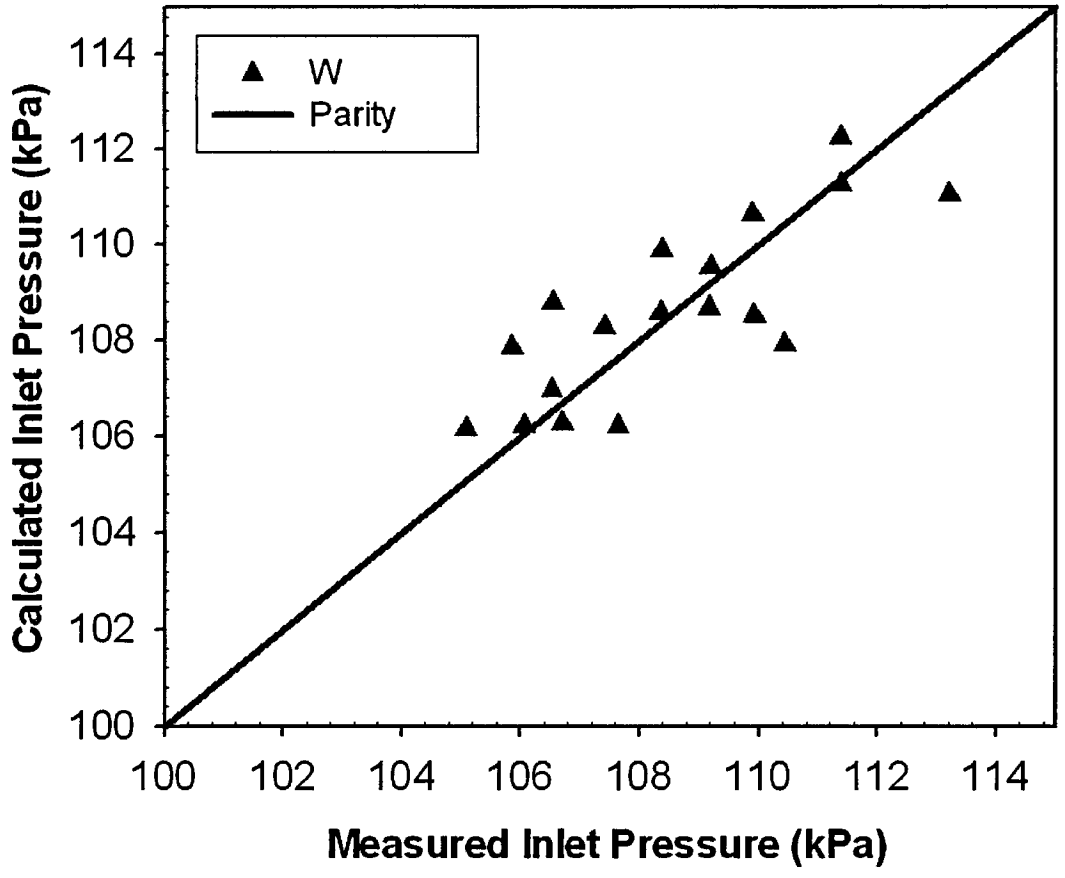

Figure 4.3: Comparison of the measured inlet pressure with the calculated values using Eq. (4.2) for experiments using water as the liquid phase.

4.2 Flow Visualization

All flow structures were confirmed to be in the Taylor bubble regime for the conditions studied. Recall, the flow pattern is characterized by periodic gas bubbles and liquid slugs of almost constant lengths, with the gas bubble separated from the wall by a liquid film. Figure 4.4 shows typical images of the bubble head and tail obtained at different mixture velocities. At low U_{TP}, the gas bubble has a symmetrical ellipsoidal head and tail. As U_{TP} is increased, the bubble head becomes sharper and the bubble tail becomes flatter, and finally the bubble attains a bullet-shape. Ripples are observed at the bubble tail region at high U_{TP} (0.42 and 0.53 m s^{-1} for W, 0.40 and 0.51 m s^{-1} for EG/W) when water and ethylene glycol/water mixture are used as the liquid phase. However, such wavy patterns were not found in the EG system. This difference can be explained by the different viscosities of the three fluids, resulting in different ranges of Re_{TP} and Ca for the similar range of mixture velocities. Edvinsson and Irandoust (1996) showed computationally that ripples were found at the tail region for flows with $500 < Re_{TP} < 2000$ and $Ca = 0.01$, whereas no undulation was observed for flows with $Re_{TP} = 20$ and $0.2 < Ca < 1.0$.

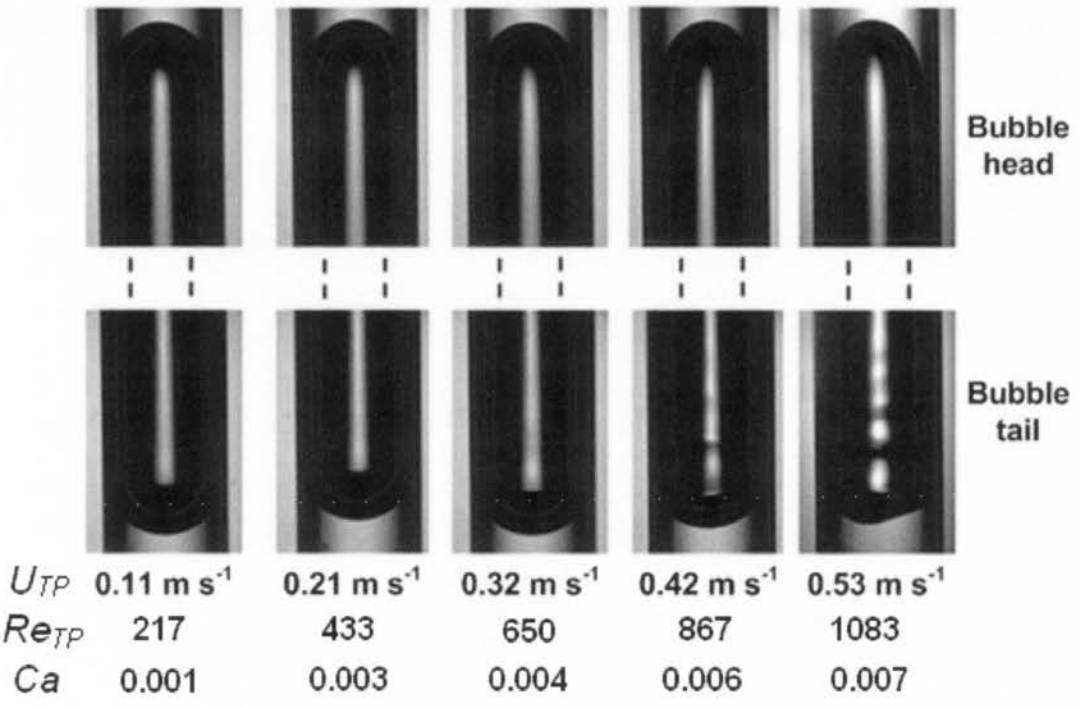

Figure 4.4 (a): Typical images of bubble heads and tails for $\beta \sim 0.5$ at different mixture velocities for fluids of water system.

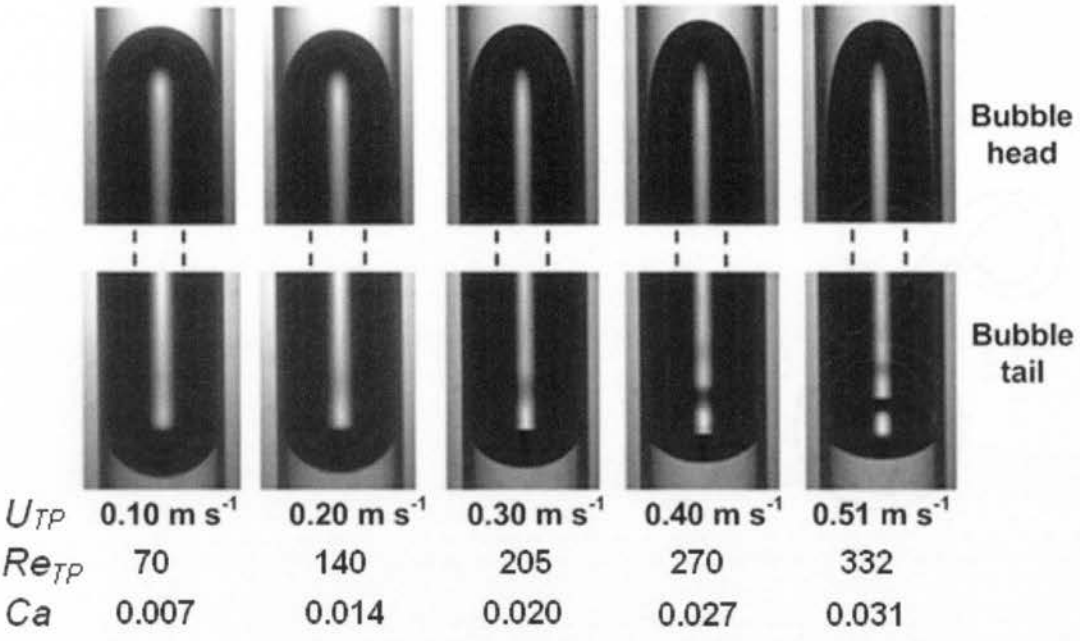

Figure 4.4 (b): Typical images of bubble heads and tails for $\beta \sim 0.5$ at different mixture velocities for ethylene glycol/water mixture system.

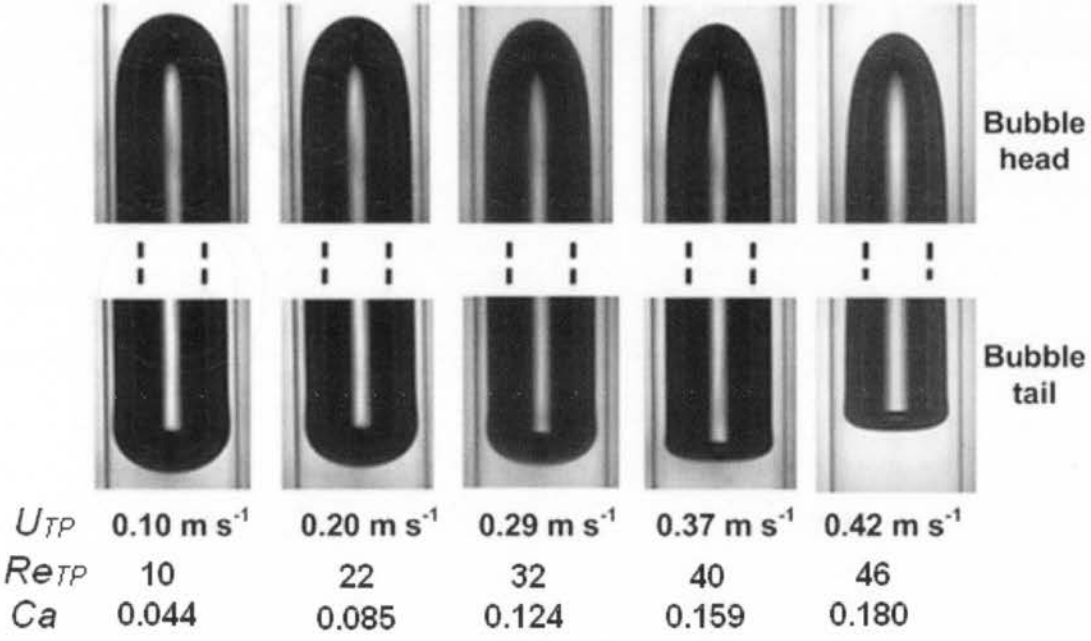

Figure 4.4 (c): Typical images of bubble heads and tails for $\beta \sim 0.5$ at different mixture velocities for ethylene glycol system.

The use of a Refractive Index Matching (RIM) system eliminated the refraction due to the outer curvature of the silica tube effectively to enhance the visualization quality. However, difficulties in identifying the gas-liquid interface still existed due to the combination of the

inner surface curvature effect and the mismatch of refractive indices between water (RI = 1.33) or 50 wt% ethylene glycol/water mixture (RI = 1.38) and the tube material (RI = 1.46) as observed in Figure 4.4 (a) and (b). Nonetheless, the existence of the liquid film between the tube wall and the bubble is indirectly indicated by the bubble velocity (U_B) being greater than the mixture velocity (U_{TP}). By careful matching of the refractive indices between the tube material and the liquid phase, as for ethylene glycol (RI = 1.43) in Figure 4.4 (c), a well-defined gas-liquid interface is visible, allowing direct measurement of the film thickness as well as digitization of the bubble shape.

Figure 4.5 shows a schematic diagram of the flow structure of Taylor flow. There is a continuous thin liquid film of uniform thickness (δ_F) surrounding both the gas bubbles and the liquid slugs (defining there to be a liquid film around the slugs is conventional as it simplifies modelling) at any channel cross-section and alternate gas bubbles and liquid slugs occupying the centre of the tube. In Taylor flow, the flow structures are highly periodic and the lengths of the bubbles and slugs are almost constant. Therefore, a unit cell composed of a gas bubble of length (L_B) surrounded by a thin layer of liquid and a liquid slug of length (L_S) is usually employed for analytical studies (Suo and Griffith, 1964, Warnier *et al.*, 2008). The length of a unit cell (L_{UC}) is the sum of the gas bubble and liquid slug lengths.

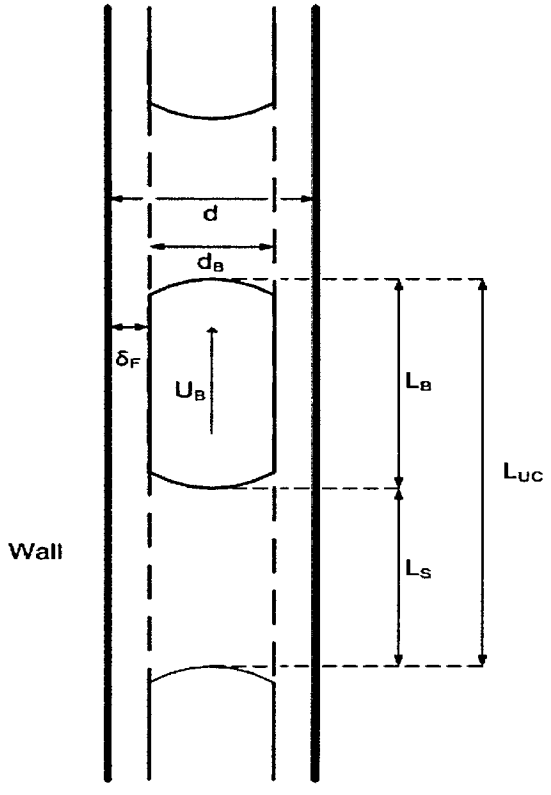

Figure 4.5: Schematic representation of the flow structure for Taylor flow.

4.2.1 Void fraction

The void fraction or gas hold up (ε_G) is a measure of the percentage of the volume occupied by the gas phase during gas-liquid two-phase flow in a channel. In Taylor flow, the ratio of the void fraction and the homogeneous void fraction (ε_G/β) is commonly used for flow characterization. The Armand correlation ($\varepsilon_G/\beta = 0.83$) (Armand and Treschev, 1964) and homogeneous flow model ($\varepsilon_G/\beta = 1$) for large channels have been extrapolated to predict the void fraction in the Taylor flow regime in microchannels. While some researchers have found good agreement between their experimental data and the Armand correlation (Serizawa *et al.*, 2002, Warnier *et al.*, 2008, Yue *et al.*, 2008), others obtained better agreement with the homogeneous model (Triplett *et al.*, 1999b, Saisorn and Wongwises, 2008). Most of the available data are distributed between the two limits ($0.84 < \varepsilon_G/\beta < 1$). However, Kawahara *et al.* (2002) found their experimental data obtained from a d = 100 μm tube deviated significantly from both the Armand correlation and the homogeneous flow model. They attributed the difference to the much larger slip ratio when compared with flows in channels of 1 mm hydraulic diameter. In their later study (Kawahara *et al.*, 2009) in which a d = 250 μm microchannel was used, they found better agreement with the Armand correlation and highlighted that the void fraction decreased with increasing liquid viscosity and/or decreasing surface tension.

Applying a simple volume balance for the gas phase, ε_G/β can be related to the velocity ratio as

$$\frac{\varepsilon_G}{\beta} = \frac{U_{TP}}{U_B} \tag{4.3}$$

For the EG system, a well-defined gas-liquid interface can be clearly visualized (as seen in Figure 4.4 (c)) which allows direct estimation of the void fraction through digitization of the bubble images (10 bubbles for each condition) to obtain the area ratio of the bubble and unit cell areas. Figure 4.6 compares the void fraction obtained from experiments with that obtained from Eq. (4.3) and good agreement was achieved between the two methods.

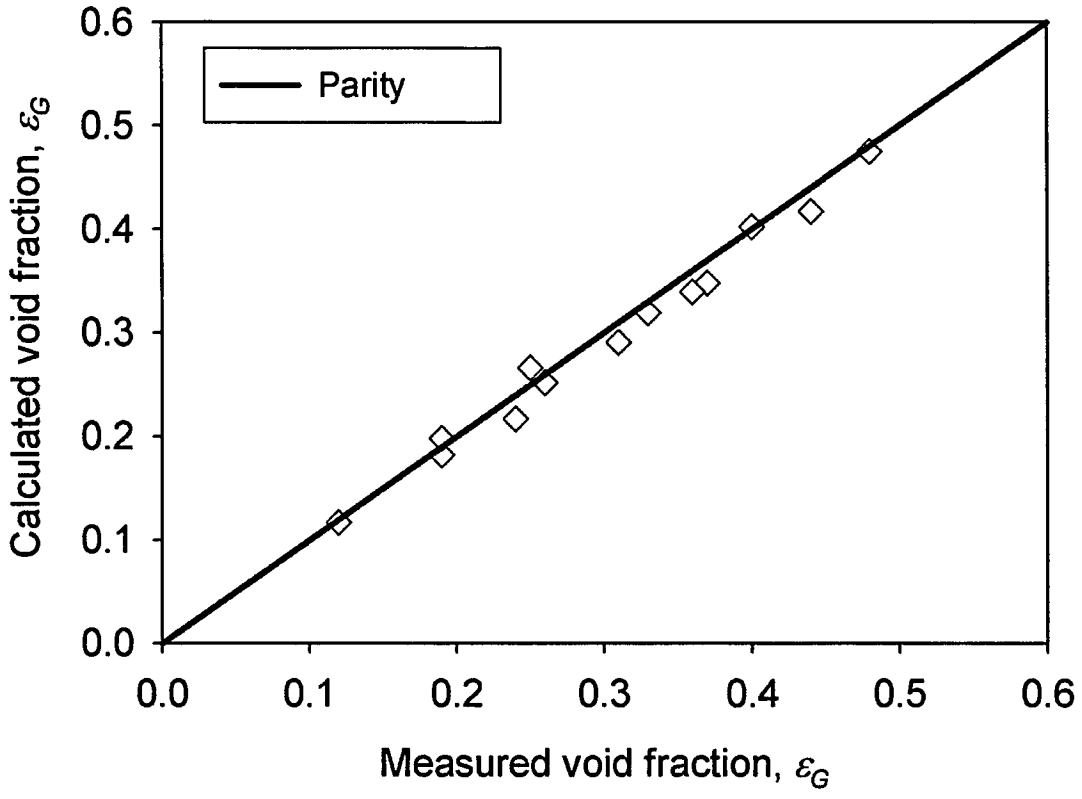

Figure 4.6: Comparison between the experimental void fraction calculated from measured film thicknesses with values obtained using the experimental bubble velocity in Eq. (4.3) for the EG system.

Fairbrother and Stubbs (1935) measured the bubble velocity in a d = 2.25 mm horizontal capillary. Based on their experimental results, they suggested a correlation (Eq. 4.4) to predict the velocity ratio for horizontal flows with $7.5 \times 10^{-5} < Ca < 0.014$.

$$\frac{U_{TP}}{U_B} = 1 - bCa^n \tag{4.4}$$

where the value of the constant b and exponent n are 1.0 and 0.5, respectively. Taylor (1961) extended the validity of the above correlation for Ca values up to 0.09 by performing experiments over a large range of Ca. Correlating all the vertical upward Taylor flow experimental data over a wide range of Capillary number ($2 \times 10^{-4} < Ca < 0.39$), Liu *et al.* (2005) obtained a correlation which was expressed in the same form of Eq. (4.4) for vertical flow with the values of the constant b and exponent n were 0.61 and 0.33, respectively.

Apart from the Capillary number, Suo and Griffith (1964) demonstrated the effect of the ratio Re_{TP}/Ca on the velocity ratio prediction using a circular channel of 1 mm diameter. They showed that U_{TP}/U_B is a decreasing function of Ca until a minimum value is reached. Then it increases with increasing Ca and levels off at a value of 0.84 in the range 59,000 < Re_{TP}/Ca < 133,000. Their observations differed from Fairbrother and Stubbs (1935) and Taylor (1961), who reported that the velocity ratio decreases monotonically with Ca until it reached an asymptotic limit of 0.44 at large Ca using very viscous fluids ($Re_{TP}/Ca \sim 0$).

The variation of the ratios of the void fraction and homogeneous void fraction (ε_G/β), which are obtained from direct measurement for EG system and estimated using Eq. (4.3) for W and EG/W systems, with the Capillary number (Ca) is compared with the correlations in the literature in Figure 4.7. Since there is a liquid film surrounding the gas bubble, the bubble velocity (U_B) is always larger than the mean slug velocity (U_{TP}) and hence, ε_G/β is always smaller than unity. Both the experimental data and the correlations show that ε_G/β is a decreasing function of the Capillary number. It is also noted that the ratio of the void fraction and homogeneous void fraction (ε_G/β) scatter at a given Ca due to the use of different homogeneous void fractions (β). The dependence of ε_G/β on β was reported by Gupta *et al.* (2010b). In their simulation work, they showed that the velocity ratio decreases with increasing β. However, no significant trend between ε_G/β and β can be drawn from this study.

In general, the Fairbrother and Stubbs (1935) correlation over-predicts the experimental data. A possible reason is that their model was derived from data for horizontal flow with negligible inertia, while all data collected here are in a vertical upward flow direction and cover a wide range of Reynolds numbers for which inertia may not be negligible. A reasonable good agreement is obtained between the Liu *et al.* (2005) correlation and the experimental data for the W and EG/W systems. However, it over-estimates ε_G/β for all the data obtained from the EG system. A better representation of the present experimental data was obtained by changing the constant b from 0.61 to 0.75 in the correlation of Liu *et al.* (2005), indicating by a broken line in Figure 4.7. Even so, it is apparent that the simple Ca correlations cannot describe the variation of the ratio of the void fraction and homogeneous void fraction precisely and need to be modified, perhaps to take into account inertial effects and/or the effect of homogenous void fraction.

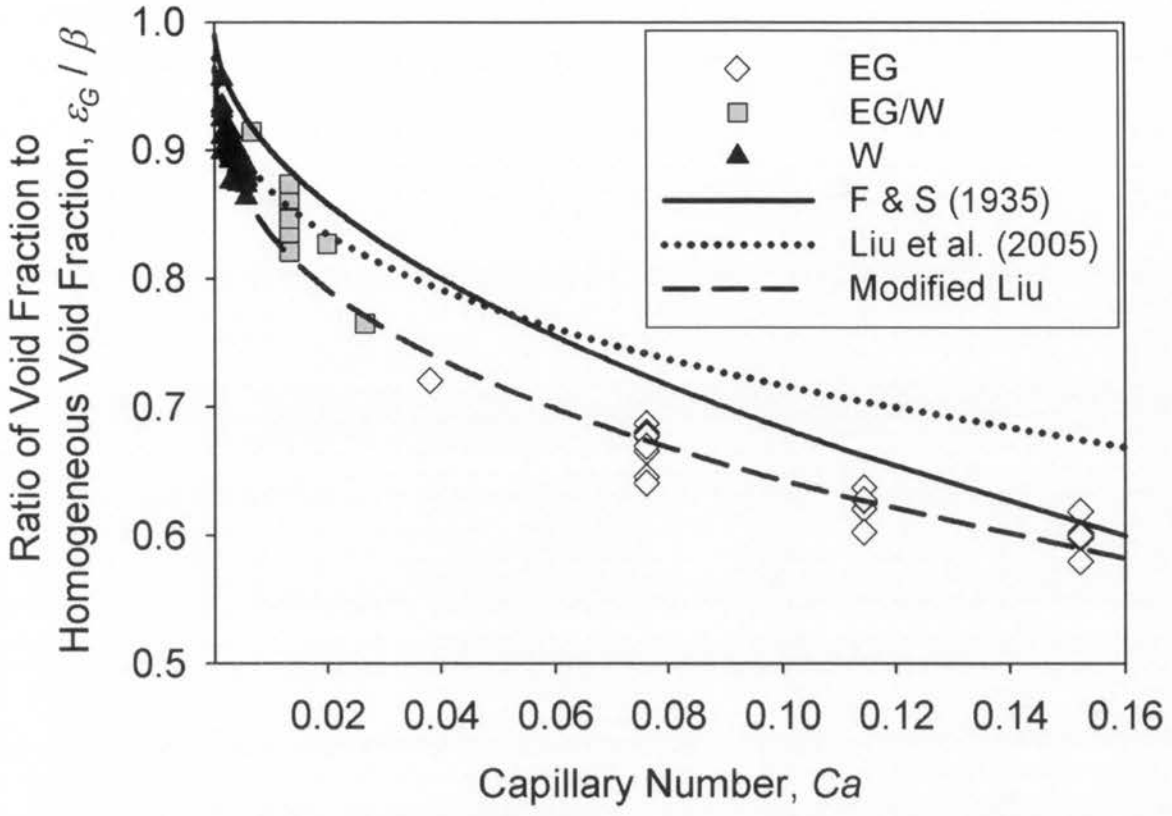

Figure 4.7: Comparison of the experimental velocity ratio with the correlations suggested by Fairbrother and Stubbs (1935) and Liu *et al.* (2005) and a modified Liu's correlation.

4.2.2 Film thickness

The film thickness has been reported to be an important parameter in mass and heat transfer in microchannels (Kreutzer *et al.*, 2005c, He *et al.*, 2010). For the W and EG/W systems for which the gas-liquid interface could not be visualized, the normalized film thickness was determined from the bubble velocity using volume conservation as described by Suo and Griffith (1964). Assuming the film is stagnant around the gas bubble and the thickness is constant along the wall, the normalized film thickness is estimated as

$$\frac{\delta_F}{d} = \frac{1}{2}\left(1 - \sqrt{\frac{U_{TP}}{U_B}}\right) \tag{4.5}$$

Using the high quality pictures (Figure 4.4 (c)), the normalized film thickness for the EG system was obtained directly by measuring the distance between the wall and the gas-liquid

interface. The differences between the measured and calculated normalized film thickness for the EG system are within 8% for most cases.

For sufficiently long bubbles, the film attains a constant thickness sufficiently far behind the bubble head but short bubbles, especially at higher velocities, do not show this behaviour, with the film thickness diminishing smoothly from nose to tail, as shown for U_{TP} = 0.42 m s^{-1} in Figure 4.4 (c), where the film thickness changes from 361 μm at the bubble nose to 234 μm at the tail. Computational (Taha and Cui, 2004, Gupta *et al.*, 2010b) and analytical (de Ryck, 2002) studies have shown the length of the transition region between the bubble cap and the constant film surrounding the bubble increases with increasing *Ca*. Therefore, the disappearance of the constant film region can be expected to arise first with shorter bubbles at higher *Ca*, as observed here.

Figure 4.8 shows the fully-developed film thickness as a function of the Capillary number. For bubbles without a fully-developed film, the reported film thickness is that obtained near the bubble tail. The film thickness is found to increase with increasing *Ca* and agrees well with the literature (Bretherton, 1961, Taylor, 1961, Irandoust and Andersson, 1989a, Aussillous and Quéré, 2000). Based on scaling arguments and the experimental data obtained by Taylor (1961), Aussillous and Quéré (2000) suggested Eq. (4.6) to estimate the film thickness over a wide range of Ca for flow with negligible inertia.

$$\frac{\delta_F}{d} = \frac{1}{2}\left(\frac{1.34\,Ca^{2/3}}{1 + 3.35\,Ca^{2/3}}\right) \tag{4.6}$$

As seen in Figure 4.8, Eq. (4.6) gives a good representation of the experimental film thickness obtained from the EG system. However, it generally underpredicts the data obtained from the W and EG/W systems. The thickening effect of inertia on film thickness at high Reynolds numbers or large Reynolds number to Capillary number ratio (Re_{TP}/Ca) has been reported previously (Giavedoni and Saita, 1997, Heil, 2001, de Ryck, 2002). Therefore, the discrepancy can be attributed to the inertial effect on the film thickness in the W and EG/W systems, as the Re_{TP}/Ca values for the W (150,000) and EG/W (8,000) systems are significantly higher than that for the EG system (260).

Irandoust and Andersson (1989a) measured the film thickness over a wide range of conditions ($9.5 \times 10^{-4} < Ca < 1.90$, $0.42 < Re_{TP} < 860$ and $1 < Re_{TP}/Ca < 140{,}000$) and proposed an empirical correlation (Eq. 4.7) to predict their experimental film thickness.

$$\frac{\delta_F}{d} = 0.18[1 - \exp(-3.08Ca^{0.54})] \tag{4.7}$$

As the ranges of Re_{TP} and Re_{TP}/Ca of the present study are almost overlapping with that used in Irandoust and Andersson (1989a), the experimental film thicknesses obtained here are also compared with Eq. (4.7) in Figure 4.8. Eq. (4.7) appears to represent something of a lower limit to the experimental data for the W system and to give a better representation of the experimental film thickness for the EG/W system, but always over-predicts the data for EG system.

Significant scattering at a given Ca is observed for the W and EG/W system. As mentioned in the previous section, U_{TP}/U_B or ε_G/β scatter about the same Ca due to the different homogeneous void fractions used in the experiments.

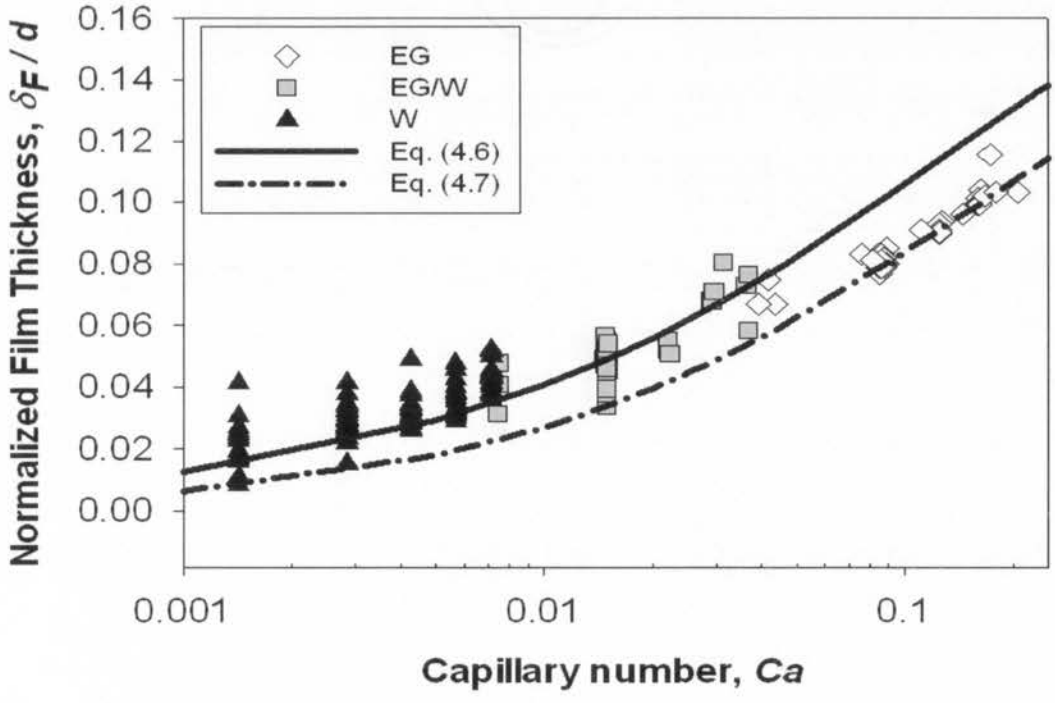

Figure 4.8: Comparison of the normalized experimental film thickness versus Capillary number with the correlations derived by Aussillous and Quéré (Eq. 4.6) and Irandoust and Andersson (Eq. 4.7).

4.2.3 Bubble length, liquid slug length and bubble frequency

The lengths of the individual bubbles and slugs were measured as described in the experimental section, while the values reported here were obtained by averaging the values over the entire recording period (5-100 bubbles per recording). Depending on the fluids, operating conditions and T-mixers used, the bubble and slug lengths varied from 1 to 220*d*. Figure 4.9 shows typical plots of the normalized bubble length (L_B/d), slug length (L_S/d), unit cell length (L_{UC}/d), and bubble frequency (F_B) as a function of β obtained for experiments using water as the liquid phase for all three T-mixers at U_{TP} = 0.21 m s^{-1}. The trends of the various lengths and the frequency are similar for all mixers used. Longer bubbles and shorter slugs were observed as β increases, which can be explained simply by the increasing gas-to-liquid ratio used to form the gas-liquid mixture. The normalized unit cell length (L_{UC}/d) first decreases with increasing β, then remains relatively constant until β = 0.5 and increases again with larger β. The bubble frequency is related to the bubble velocity and unit cell length as

$$F_B = \frac{U_B}{L_{UC}} \tag{4.8}$$

Thus, the variation of F_B with β has an opposite trend to that of L_{UC}/d as the bubble velocity remained relatively constant at the same mixture velocity. Similar trends were observed for other mixture velocities. The standard deviations of the measured lengths for most flow conditions are less than 5%, with a few falling in the 5-15% range.

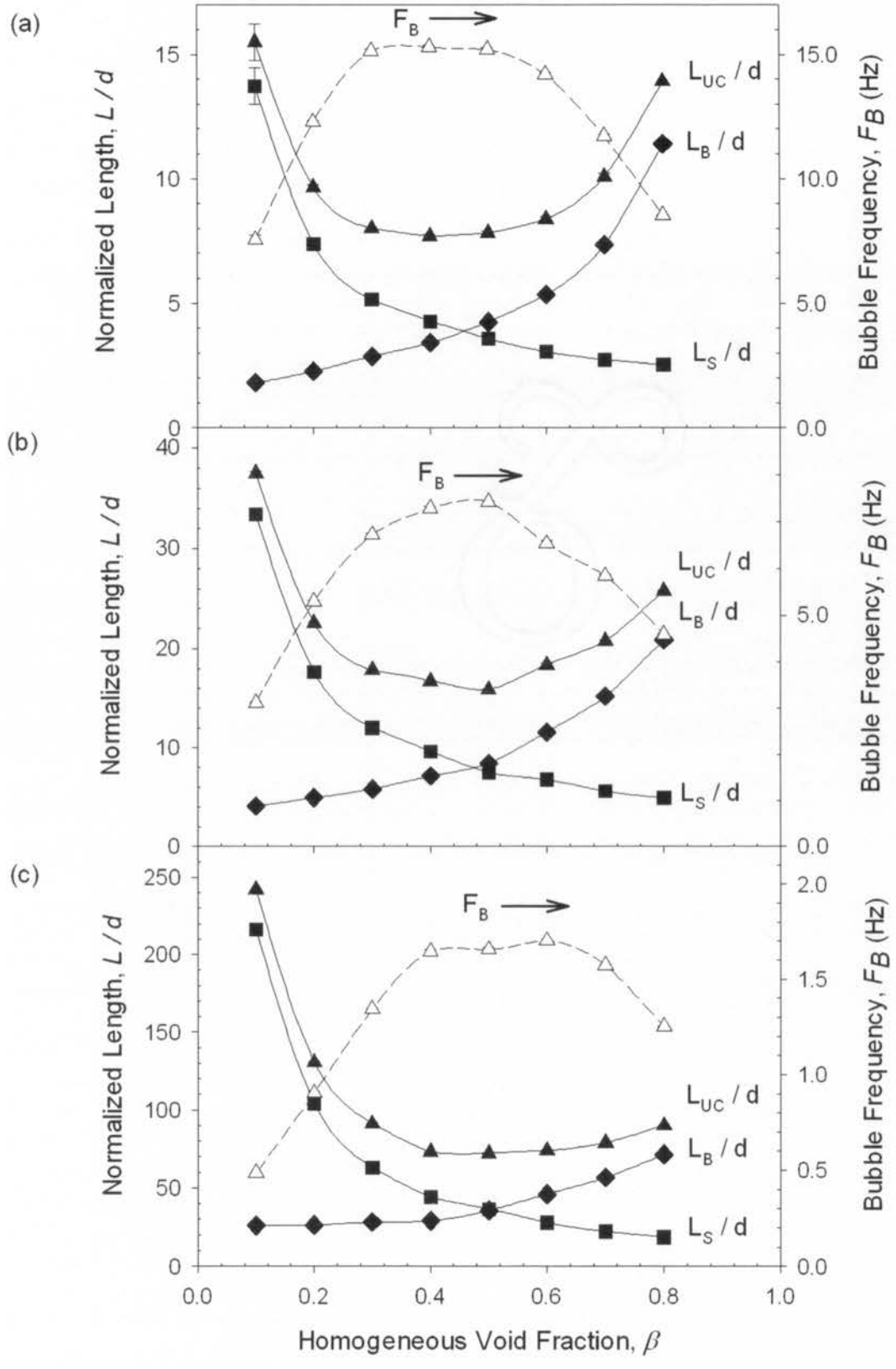

Figure 4.9: The effect of β on normalized bubble length, liquid length and unit cell length and bubble frequency at U_{TP} = 0.21 m s^{-1} obtained using the (a) TM1, (b) TM2 and (c) TM3 T-mixers and water as the liquid phase.

As seen in Figure 4.10, similar variations of the lengths and the frequency with the homogeneous void fraction are observed in experiments using EG/W and EG as the liquid phase and the smallest mixer at $U_{TP} \sim 0.21$ m s^{-1}. Again small standard deviations (less than 10%) of the measured lengths are noted for both fluid systems, confirming the suitability of the experimental setup to generate flows which can be characterised precisely.

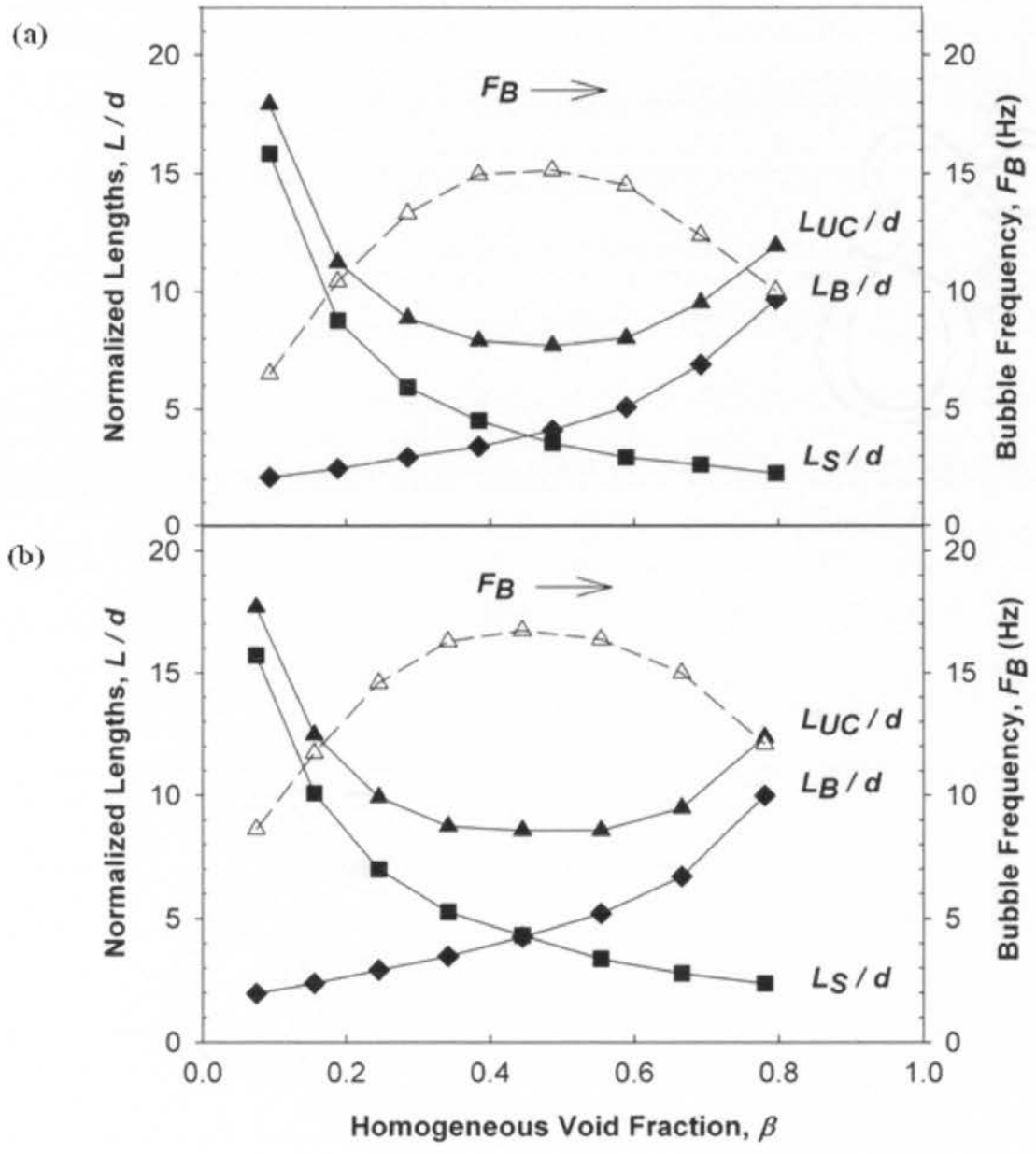

Figure 4.10: Plots of the relationship between the normalized bubble length, liquid slug length, unit cell length and bubble frequency with the homogeneous void fraction for (a) EG/W system and (b) EG system using TM1 mixer at $U_{TP} \sim 0.21$ m s^{-1}.

4.3 Bubble and slug lengths prediction

Several empirical correlations have been proposed for prediction of the absolute bubble length, with most of them expressed as a function of the Reynolds numbers and/or the phase holdup (Laborie *et al.*, 1999, Kreutzer *et al.*, 2005a, Liu *et al.*, 2005, Akbar and Ghiaasiaan, 2006, Qian and Lawal, 2006). However, there is a lack of agreement between them, reflecting the fact they are only applicable to specific working fluids and inlet structures. Some authors suggested that the sizes of the bubbles and slugs are strongly dependent upon the dynamics of the contact between the two phases at the inlet, in other words, the bubble formation mechanisms which are independent of the inlet configurations (Garstecki *et al.*, 2006, de Menech *et al.*, 2008, Xu *et al.*, 2008).

The bubble formation mechanisms can be distinguished by the mixer Capillary number based on the liquid flow rate at the mixing section ($Ca_{L,M} = \mu_L Q_L / \sigma A_M$). Garstecki *et al.* (2006) postulated that there is a critical Capillary number (Ca_{cr} ~ 0.02) separating two commonly observed bubble formation mechanisms. Below Ca_{cr} ($Ca_{L,M} < 0.02$), the bubble formation process is determined by the pressure drop across the bubble as it forms. This bubble generation mechanism is categorized as "squeezing" with the bubble length controlled by the ratio of the gas to liquid flow rates (Q_G/Q_L). Above Ca_{cr} ($Ca_{L,M} > 0.02$), the bubble formation process is dominated by the balance between the shear and interfacial forces and is described as "shearing", with the bubble length controlled by the mixer Capillary number ($Ca_{L,M}$).

For bubbles generated in the squeezing regime, Garstecki *et al.* (2006) developed a scaling law (Eq. 4.9) to determine the bubble size formed via a T-junction connected to a rectangular microchannel (S = 0.033 mm, w = 0.05–0.2 mm).

$$\frac{L_B}{w} = \alpha_1 + \alpha_2 \frac{Q_G}{Q_L} \tag{4.9}$$

where w is the width of a rectangular channel; α_1 and α_2 are constants of the order of unity, with the particular values depending on the geometry of the T-junction. The first and second terms in Eq. (4.9) correspond to the length developed in the filling and squeezing stages of the bubble formation process, respectively.

van Steijn *et al.* (2007) measured the three-dimensional flow field of the liquid phase during bubble formation in a 800 μm squared T-junction operated in the squeezing regime using μPIV. They confirmed the scaling argument of Garstecki *et al.* (2006). The dependence of bubble diameter and hence the resulting length on liquid properties, including viscosity and surface tension, was reported (Laborie *et al.*, 1999, Xiong *et al.*, 2007, Shao *et al.*, 2008). In order to allow films with non-negligible thickness, Xiong *et al.* (2007) modified the above scaling law by replacing the channel width (w) by the bubble width (w_B).

The Garstecki *et al.* (2006) scaling law has been applied successfully to the prediction of bubble length in rectangular and square T-junction mixers (van Steijn *et al.*, 2007, Leclerc *et al.*, 2010), Y-junction rectangular microchannels (Yue *et al.*, 2008), rectangular co-flowing microchannels (Xiong *et al.*, 2007), and circular flow-focusing devices (Shao *et al.*, 2008) operating in the squeezing regime. For a T-junction mixer with circular cross-section and systems with thin films, replacement of w in Eq. (4.9) with the channel diameter d is an obvious substitution. Since the bubble length was measured in the test section which has a smaller diameter than the mixer in which the bubbles are produced (d = 2.00 mm versus d_M = 2.27, 3.10 and 4.81 mm), a volume balance ($L_B d^2 = L_B|_{Mixer}\, d_M{}^2$) is applied, assuming negligible pressure drop from the mixer to the exit of the test section, to obtain

$$\frac{L_B}{d} = \left(\frac{d_M}{d}\right)^3 \left(\alpha_1 + \alpha_2 \frac{Q_G}{Q_L}\right) \tag{4.10}$$

According to Figure 4.1 and 4.3, the assumption of negligible pressure drop across the test section works reasonably well for the water system. In addition, all water experiments fall in the squeezing bubble generation regime, as the mixer Capillary numbers ($0.0001 < Ca_{L,M} < 0.005$) fall well below the critical Capillary number ($Ca_{cr} \sim 0.02$). Therefore, values of the constants α_1 and $\alpha_2$were determined based on the data obtained from the water experiments. Using a linear regression technique, $\alpha_1 = 1.10$ and $\alpha_2 = 1.25$ were found. As seen from Figure 4.11, good agreement is achieved between the experimental data and calculated values, with the experimental data scattering within ±30% of the predictions.

To examine the validity of Eq. (4.10) for the other two fluid systems, the normalized experimental bubble length obtained from the EG/W and EG experiments are also compared with Eq. (4.10) in Figure 4.11. Apparently, the experimental data agree reasonably well with the prediction as most bubble lengths fall within the ±30% bounds. Larger scatter is observed

for the EG system as some bubbles are generated in the shearing regime according to the range of mixer Capillary numbers ($0.011 < Ca_{L,M} < 0.088$) when using this liquid.

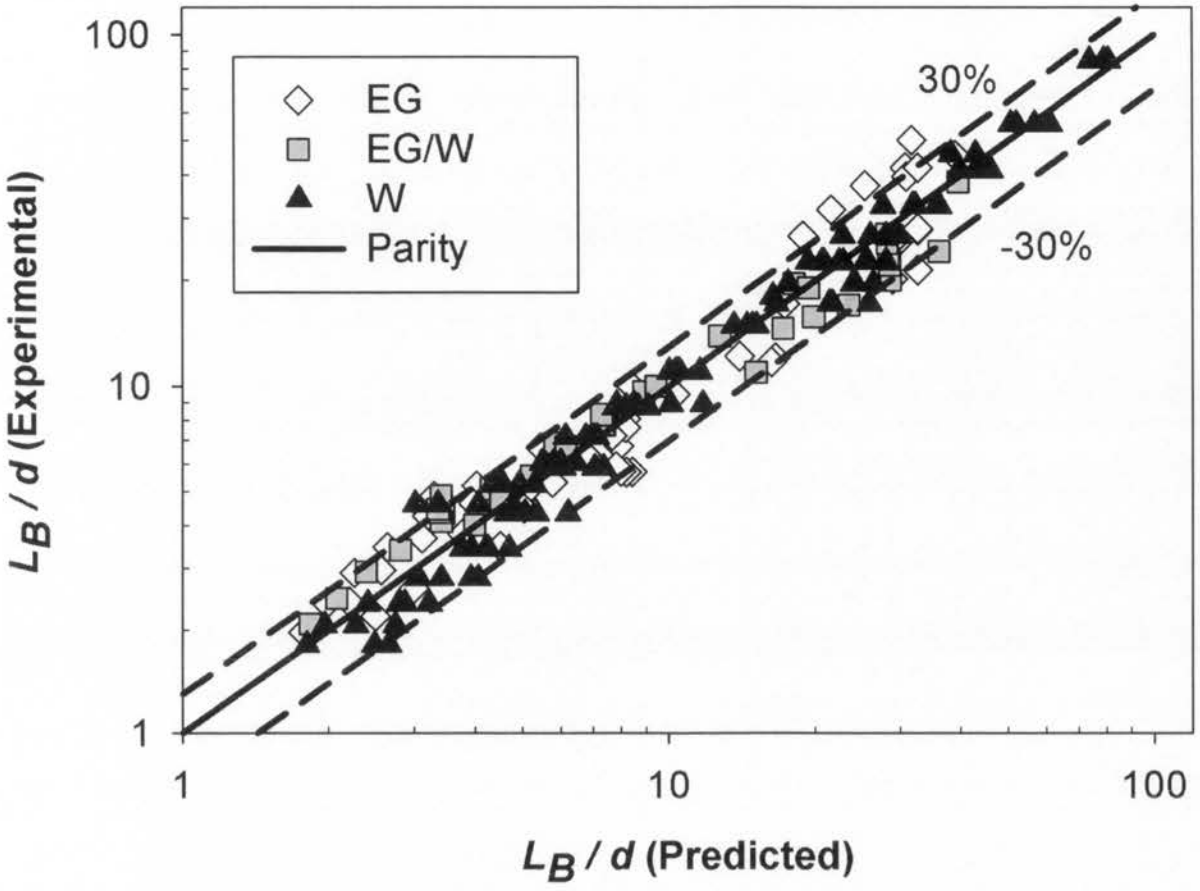

Figure 4.11: Comparison of the normalized bubble length between the experimental data and the predicted values obtained from Eq. (4.10). The broken lines represent the $\pm$30% bounds of the prediction value.

The film velocity is low when compared with the bubble velocity (Fouilland *et al.*, 2010) and is often taken as zero, with a continuous liquid film of constant thickness surrounding both the gas bubbles and liquid slugs being assumed (Suo and Griffith, 1964, Warnier *et al.*, 2008). For a negligible film velocity, the slug length can be estimated from (Eq. 4.11), when the bubble length is known.

$$\frac{L_B}{L_S} \approx \frac{V_B}{V_S} \approx \frac{\beta}{(1-\beta)} \tag{4.11}$$

As seen in Figure 4.12, the data from all the visualization studies do not exactly follow Eq. (4.11), with L_B/L_S systematically exceeding the homogeneous gas-liquid volume ratio, $\beta/(1-\beta)$, on average by 13%. This error arises because L_B is defined simply as the length of the bubble from nose-top to tail and L_B/L_S does not precisely represent the volume ratio V_B/V_S. When the volume ratio of the gas bubble and the liquid slug (V_B/V_S) at the core (assuming a continuous film of constant thickness surrounding both the bubble and slug) was determined directly from the visualization images such as Figure 4.4 (c), we find less than 1% difference between the volume ratio and the ratio of homogeneous volume fractions.

Though deviation (~15% for short bubbles generated in the smallest T-mixer and <10% for long bubbles generated in the larger T-mixers) arises in the approximation, $L_B/L_S \approx \beta/(1-\beta)$, the combination of Eqs. (4.10) and (4.11) is able to provide a reasonable estimation of the slug length for a specific homogeneous void fraction, especially for systems with long bubbles and slugs.

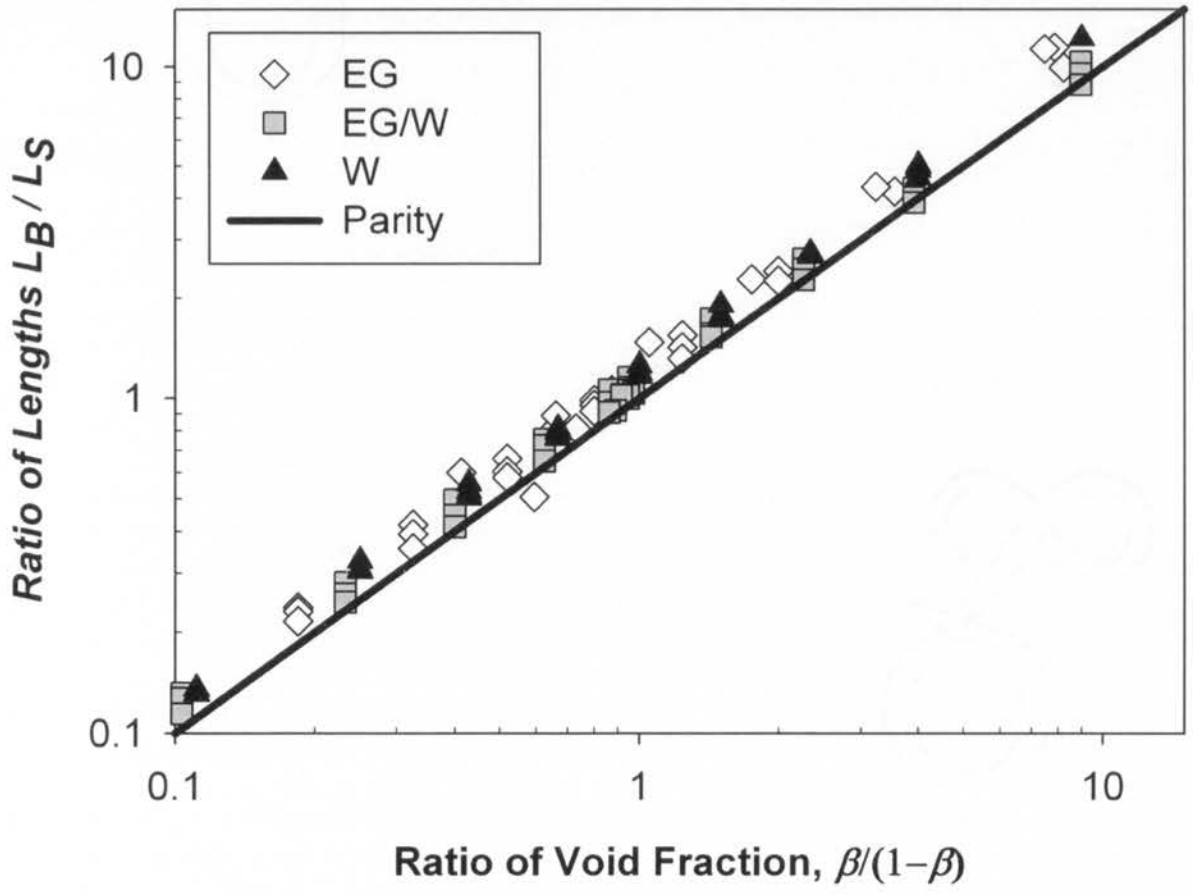

Figure 4.12: Comparison of the ratio of bubble to slug lengths with $\beta / (1-\beta)$.

4.4 Summary

The effects of fluid properties and flow parameters on the flow characteristics of Taylor flow were investigated experimentally using a 2.00 mm diameter tube in a vertical upward flow direction. Visualization experiments were conducted for 0.10 m s^{-1} < U_{TP} < 0.53 m s^{-1} and 0.03 < β < 0.90. The Capillary number, an important parameter characterizing the two-phase flow pattern, was varied over a wide range of values (0.001 < Ca < 0.180) by using three liquid phases, water (W), 50 wt% ethylene glycol/water mixture (EG/W) and pure ethylene glycol (EG). Bubble and slug lengths ranging from 1 to 220 tube diameters were studied.

Well-defined Taylor flow with regular bubble and slug lengths was achieved with the present experimental set-up, as confirmed by the visualization tests. The bubbles and slugs were created using opposing gas and liquid flow in a T-junction mixer. Mixers of three different diameters were used to cover the desired range of flow conditions. By careful matching of the refractive indices of the tube material and the liquid phase, the film between the wall and the gas bubble was clearly seen in the high quality pictures taken for the ethylene glycol system. The ratio of the void fraction to the homogenous void fraction (ε_G/β) was found to be a decreasing function of the Capillary number and scatter at a given Ca due to the use of different homogeneous void fractions. The fully-developed film thickness obtained from the present study agrees well with the literature, with the normalized film thickness increasing with increasing Ca.

A scaling law, based on the Garstecki approach was modified to allow for differences in diameter between the mixer and the test section to predict the bubble length. Generally, good agreement was found between the lengths of the bubbles and modified scaling law, with most experimental data falling within 30% of the calculated values. For flow for which the curvature of the bubble caps and tails can be neglected, the corresponding slug length can be approximated as $L_S \approx L_B(1-\beta)/\beta$, as the film velocity is negligible in both the thin and thick film systems.

Through careful design of the mixing section, stable and reproducible Taylor flow patterns were achieved. In the next chapter, the heat transfer characteristics for well-characterized Taylor flow are studied.

Chapter 5
Heat Transfer of Vertical Taylor Flow

The suitability of the experimental set-up to generate regular Taylor flow which can be characterised precisely was confirmed in the visualization experiments. Heat transfer experiments are performed for the same operating conditions as those used in the visualization tests, with all flow structures studied confirmed to be in the Taylor bubble regime. With the use of three T-junctions of different internal diameters (TM1 = 2.27 mm, TM2 = 3.10 mm and TM3 = 4.81 mm), bubbles and slugs of different lengths for the same mixture velocity (U_{TP}) and homogeneous void fraction (β) are achieved, and a wide range of slug lengths (1–220d) is achieved in the conditions studied ($0.10 < U_{TP} < 0.53$ m s^{-1} and $0.03 < \beta < 0.90$). These allow a direct examination of the effect of the slug length on Taylor flow heat transfer without the interference of effects arise from other flow parameters due to the use of different U_{TP} and β.

The film thickness, recirculation size and recirculation time (more details are given in the next Chapter) which are important parameter governing heat transfer in the non-boiling gas-liquid Taylor flow are reported to be strongly dependent on the Capillary number (Taylor, 1961, Thulasidas *et al.*, 1997). Therefore, one might expect this group to capture heat transfer effects arising from these sources. Using the three selected liquid phase fluids, water (W), 50 wt% ethylene glycol/water mixture (EG/W) and pure ethylene glycol (EG), which are of significant difference in viscosity, a wide range of Capillary number ($0.001 < Ca < 0.180$) were achieved to reveal its effect on Taylor flow heat transfer.

The experimental apparatus used to determine the heat transfer rates of vertical upward Taylor flow in a circular channel (d = 2.00 mm) is a multi-block heating section. The system design and calibration, data acquisition and data reduction procedures were detailed in Chapter 3. Recall that, the present experimental arrangement does not correspond strictly to any standard thermal boundary condition for laminar flow even though the heat flux in each heating zone is approximately the same. The apparatus does provide accurate pseudo-local heat transfer coefficients for steady single-phase flow consistent with a constant wall heat flux thermal boundary condition (Bao, 1995, Bao *et al.*, 2000, Baird, 2001, Liu, 2011). It is in fact clear that the present apparatus actually provides mean values in pulsatile flow because

of the temporal integration that its block-wise structure imposes. Nonetheless, the experimentally determined two-phase heat transfer rates are rather precise and accurate, with the uncertainty being <15%.

Together with the flow characterization results, a comprehensive study of the dependence of the heat transfer on slug length, mixture velocity, homogeneous void fraction and fluid properties is performed. Results obtained for water are presented in Sections 5.1 and comparison of the heat transfer results for all fluids are made in Section 5.2.

5.1 Multi-block heat transfer results for the nitrogen-water system

Typical results for the wall heat flux (q_i), the wall temperature (T_{wi}) and the calculated mean fluid temperature (T_{bi}) and the time-averaged Nusselt numbers (Nu_i) of each heating zone using water as the liquid phase are shown in Figure 5.1. It can be seen that the block-wise Nusselt number remains almost constant throughout all heating zones except the first one, indicating thermally fully-developed flow is achieved after the first heating block. In order to minimize the entrance effects and the uncertainties arising from the end-block effects, the data for the first and last blocks are not used in subsequent analysis. Thus, the average two-phase Nusselt number (Nu_{TP}) for the water experiments is determined by averaging the Nusselt numbers from blocks 2 to 9.

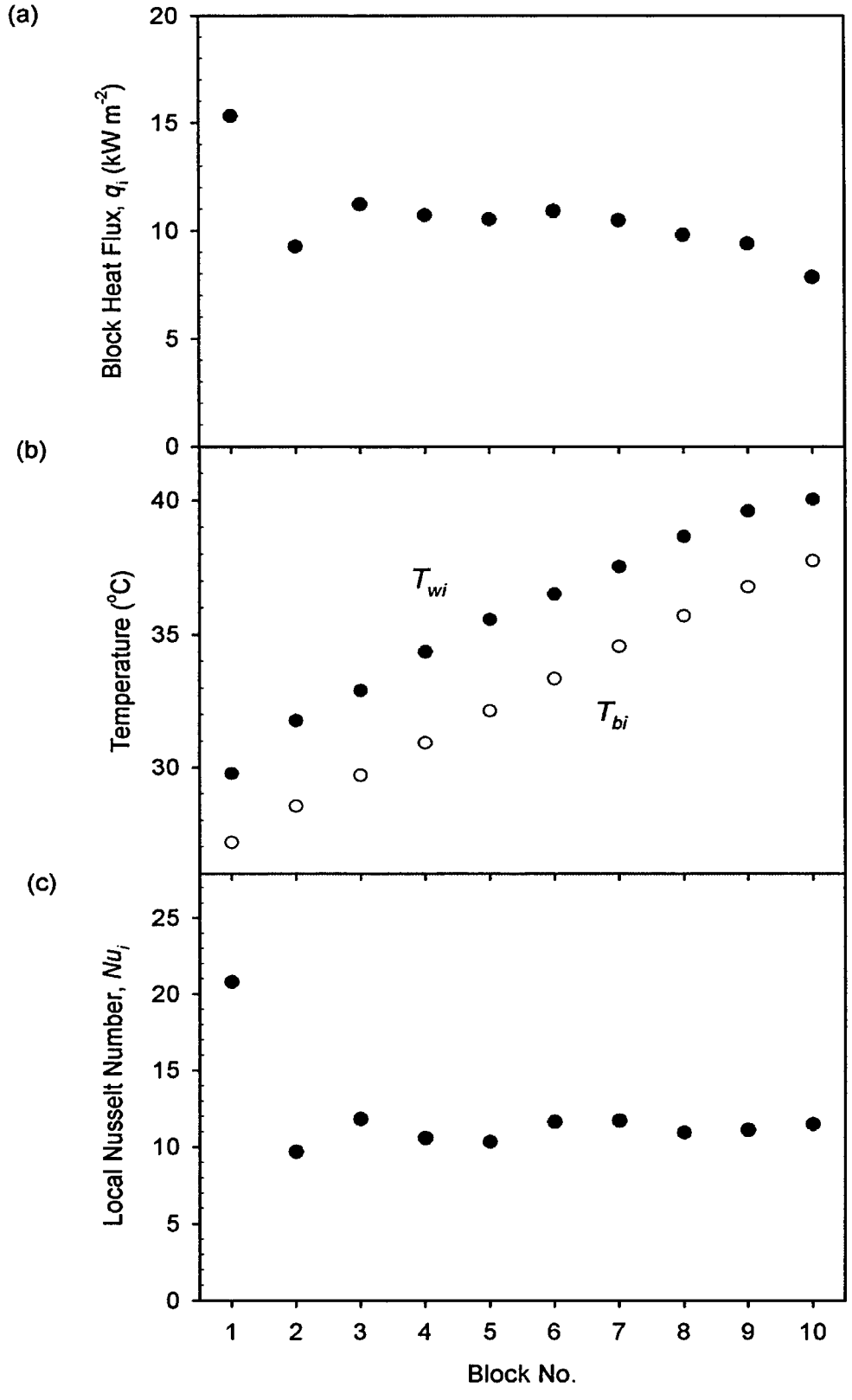

Figure 5.1: Typical results for (a) the wall heat flux, (b) the mean wall and fluid temperatures and (c) the Nusselt number of each heating zone at $U_{TP} = 0.21$ m s^{-1}, $\beta = 0.5$, $L_S/d = 7.46$ using the TM2 mixer.

5.1.1 Effect of mixture velocity

Figure 5.2 (a) shows the variation of the normalized Nusselt number (Nu^*) with the mixture velocity at $\beta \sim 0.5$, where the gas-liquid mixtures were generated using the three T-mixers with different internal bore diameters. The normalized Nusselt number is defined as

$$Nu^* = \frac{Nu_{TP}}{Nu_{LO}} \tag{5.1}$$

where Nu_{TP} is the overall two-phase Nusselt number and Nu_{LO} is the Nusselt number for the liquid-only, fully-developed flow for constant heat flux boundary conditions, having a value of 4.364.

According to Figure 5.2 (a), the value of Nu^* increases with the mixture velocity. This is not an effect of slug length, since, for a given T-mixer, the slug lengths are essentially independent of U_{TP} (Figure 5.2 (b)). The influence of mixture velocity itself, however, is greatest for the shortest slugs, ($L_S/d \sim 3$). While a 61% heat transfer enhancement was noted for the TM1 mixer as the mixture velocity increased from 0.11 to 0.53 m s^{-1}, only ~45% increment was found for the other two mixer systems for this set of experiments.

In earlier computational work, Gupta *et al.* (2010b) found $Nu^* \sim 2.5$ for short slugs ($L_S/d \sim 1$, $\beta = 0.51$), independent of U_{TP} in the range 0.3 to 1.0 m s^{-1} using water as the liquid phase. They showed that the difference between the wall and the bulk temperature remained almost the same with an increase in the mixture velocity, leading to an insensitive response of the Nusselt number to the increasing mixture velocity. The effect of mixture velocity (or Reynolds number) on nitrogen-water Taylor flow heat transfer was also investigated computationally by He *et al.* (2010). They found that the two-phase Nusselt number increased from 4.7 to 8.0 when the Reynolds number increased from 32 to 390 for flow with $L_S/d \sim 1.6$ and $\beta \sim 0.45$. Horvath *et al.* (1973) also showed experimentally that the mean Nusselt number for the slug is an increasing function of the Reynolds number for $1.6 < L_S/d < 16$ and $30 < Re_{TP} < 220$. The precise conditions studied by Gupta *et al.* (2010b) were not accessible with the current experimental setup and no further comments on the different trends between flows with very short slugs ($L_S/d \sim 1$) can be provided. Therefore, this thesis focuses on longer bubbles obtainable with the T-mixers used in the present study.

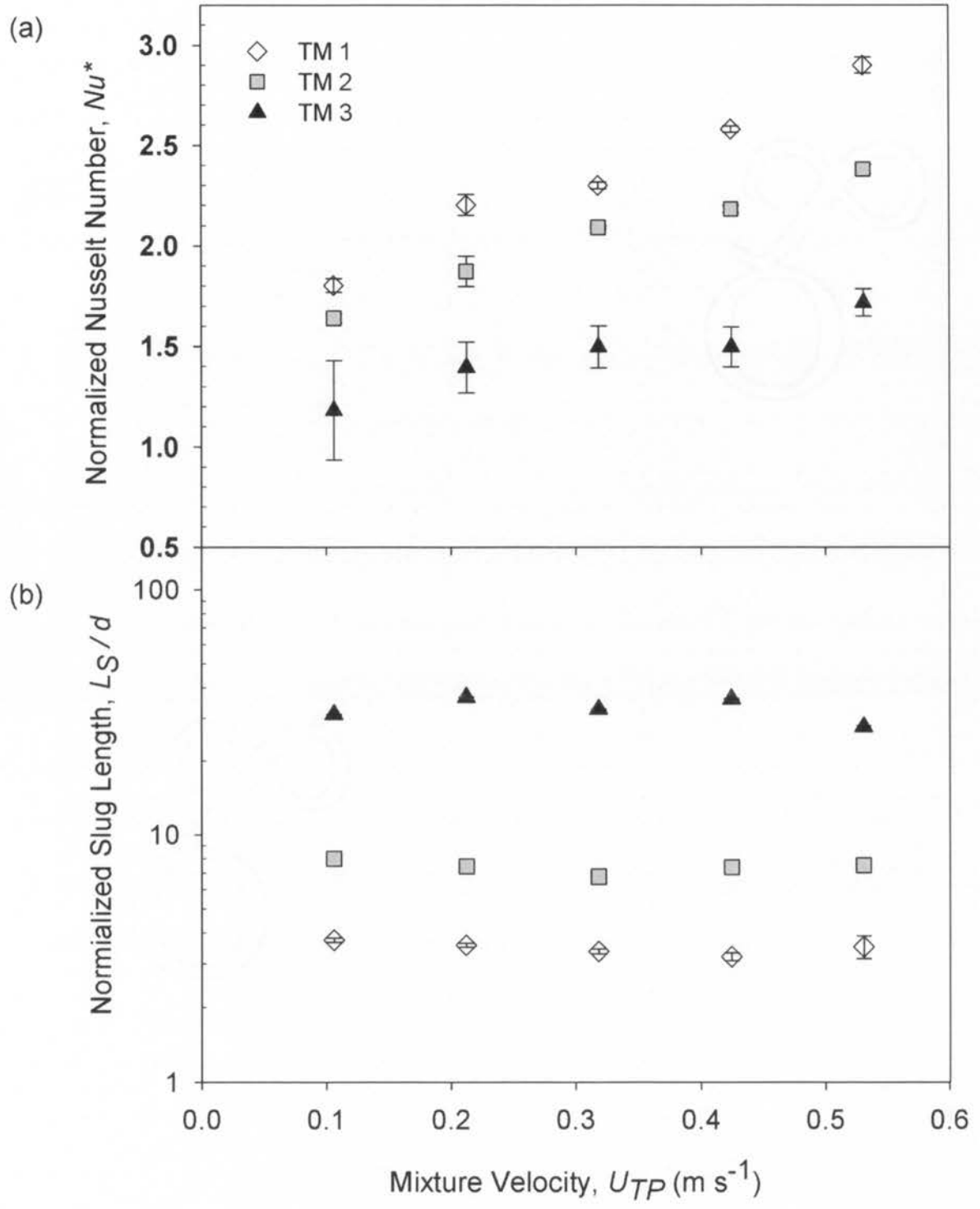

Figure 5.2: The effect of mixture velocity on (a) the normalized Nusselt number (Nu^*) and (b) the normalized slug length (L_S/d) at $\beta = 0.5$. The error bars represent one standard deviation for three replicates.

5.1.2 Effect of slug length

In Figure 5.2 (a) it is clear that the Nu^* values for the different mixers are not the same at the same values of U_{TP} and β. The heat transfer rate is highest when the smallest mixer was used. These differences are attributed to the different slug lengths produced by the different mixers. The normalized slug length (L_S/d) obtained for adiabatic conditions is shown in Figure 5.2 (b). The liquid slugs are significantly longer when bigger mixers are used. For a given mixer, the slug length is relatively constant for a fixed value of β.

The effect of normalized slug length on the value of Nu^* is shown explicitly in Figure 5.3. The heat transfer enhancement becomes greater for shorter slugs and can be up to 2.90 times higher than the liquid-only flow at $\beta = 0.5$. The present finding is in agreement with the experimental work reported by Oliver and Wright (1964), Oliver and Yong Hoon (1968), Horvath *et al.* (1973) and more recently by Walsh *et al.* (2010). They all demonstrated augmentation of the heat transfer rate of up to 2.5-fold for non-boiling Taylor flow, with the enhancement increasing with decreasing liquid slug lengths.

For $10^{-4} < Ca < 10^{-2}$, Thulasidas *et al.* (1997) showed both theoretically and experimentally that the fluid in each individual liquid slug recirculates half of a cycle in the time required for it to travel a distance of twice its length. Therefore, at the same liquid and gas flow rates, the fluid in a shorter slug will undergo more complete cycles in the heating section when compared with a longer slug. An increase in radial heat transfer results, as the liquid near the tube wall is replaced by the cooler liquid from the tube centre at a higher frequency. Since the slug length is a key parameter in determining the heat transfer performance of Taylor flow, an understanding of bubble generation mechanisms and having good control of the slug length become important if this flow regime is used in engineering applications.

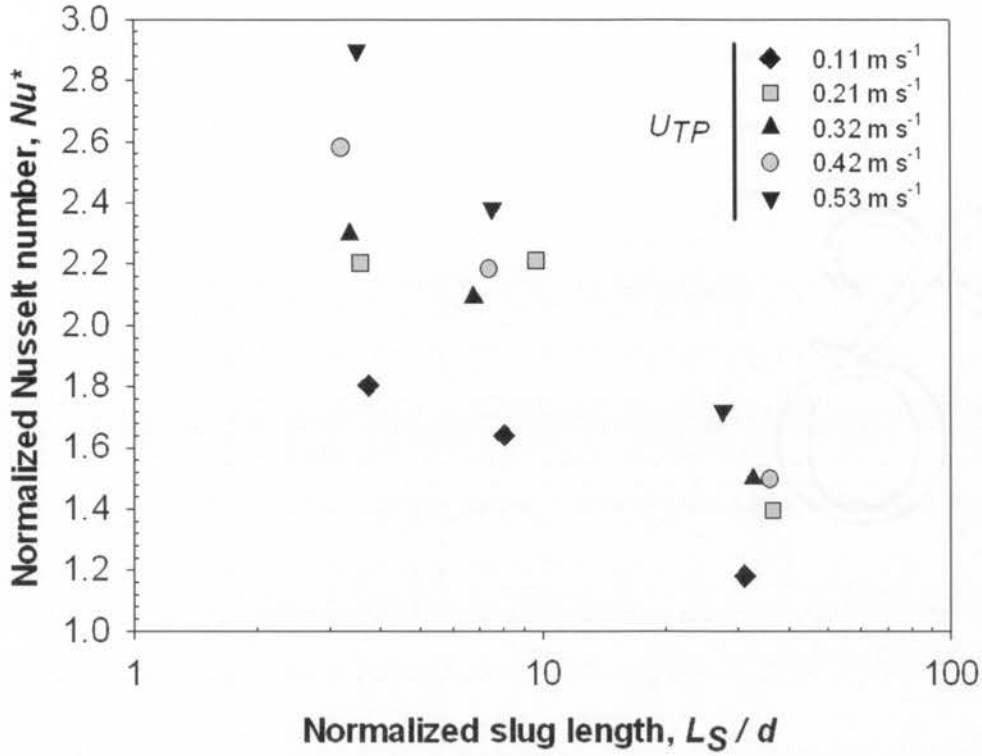

Figure 5.3: The effect of normalized slug length (L_S/d) on the normalized Nusselt number (Nu^*) at $\beta \sim 0.5$.

5.1.3 Effect of homogeneous void fraction

The variation of normalized Nusselt number (Nu^*) and slug length (L_S/d) with homogeneous void fraction (β) at different mixture velocities with gas-liquid mixtures generated using three different T-mixers is shown in Figure 5.4. The general trends of the heat transfer and slug length data are similar, regardless of the mixture velocities and/or the mixers used. With increasing β, Nu^* first increases above the limiting value of $Nu^* = 1$ at $\beta = 0$ until a maximum is reached, beyond which Nu^* declines steadily towards a gas-only value ($Nu^* \ll 1$) as $\beta \rightarrow 1$ values. The maximum value of Nu^* shifts to a smaller β value when the mixture velocity increases.

At high β values, Nu^* falls below one, as expected due to its approach to gas-only conditions. However, the effect is more obvious for flows generated with larger mixers which produce longer liquid slugs and gas bubbles. As seen from the open symbols in Figure 5.4, L_S/d

decreases monotonically with increasing β for all mixture velocities - the slug length depends inversely on U_{TP} at low β values but becomes independent of U_{TP} as β increases.

In Taylor flow, the internal recirculation within the liquid slug promotes radial mixing of the fluid and hence augments the heat transfer rate, with shorter slugs giving greater enhancement. Consequently, when the slug length decreases with increasing β, better heat transfer performance is expected. However, the volume fraction of liquid in a unit cell decreases with increasing β and gives poorer heat transfer as the contribution of the gas phase to heat transfer is negligible (Gupta *et al.*, 2010b). Therefore, the overall heat transfer rate for gas-liquid Taylor flow is determined by the two different effects: depending on the unit cell length and the mixture velocity, the heat transfer enhancement attains its maximum value when $0.1 < \beta < 0.3$. However, as β increases further, the increased heat transfer enhancement resulting from shorter slugs is offset by the greater liquid flow rate reduction. As a result, Nu^* decreases with increasing β. When the enhancement effect brought about by internal circulation in the liquid slug is exceeded by the reduction of liquid flux at high β value, the heat transfer rate falls below the liquid-only laminar flow. Longer liquid slugs behave like single-phase flows and the heat transfer enhancement brought by internal recirculation is limited. Therefore, Nu^* for the longest slug (TM3) drops below unity at a lower β value relative to the corresponding value of β for shorter slug systems (TM1 and TM2).

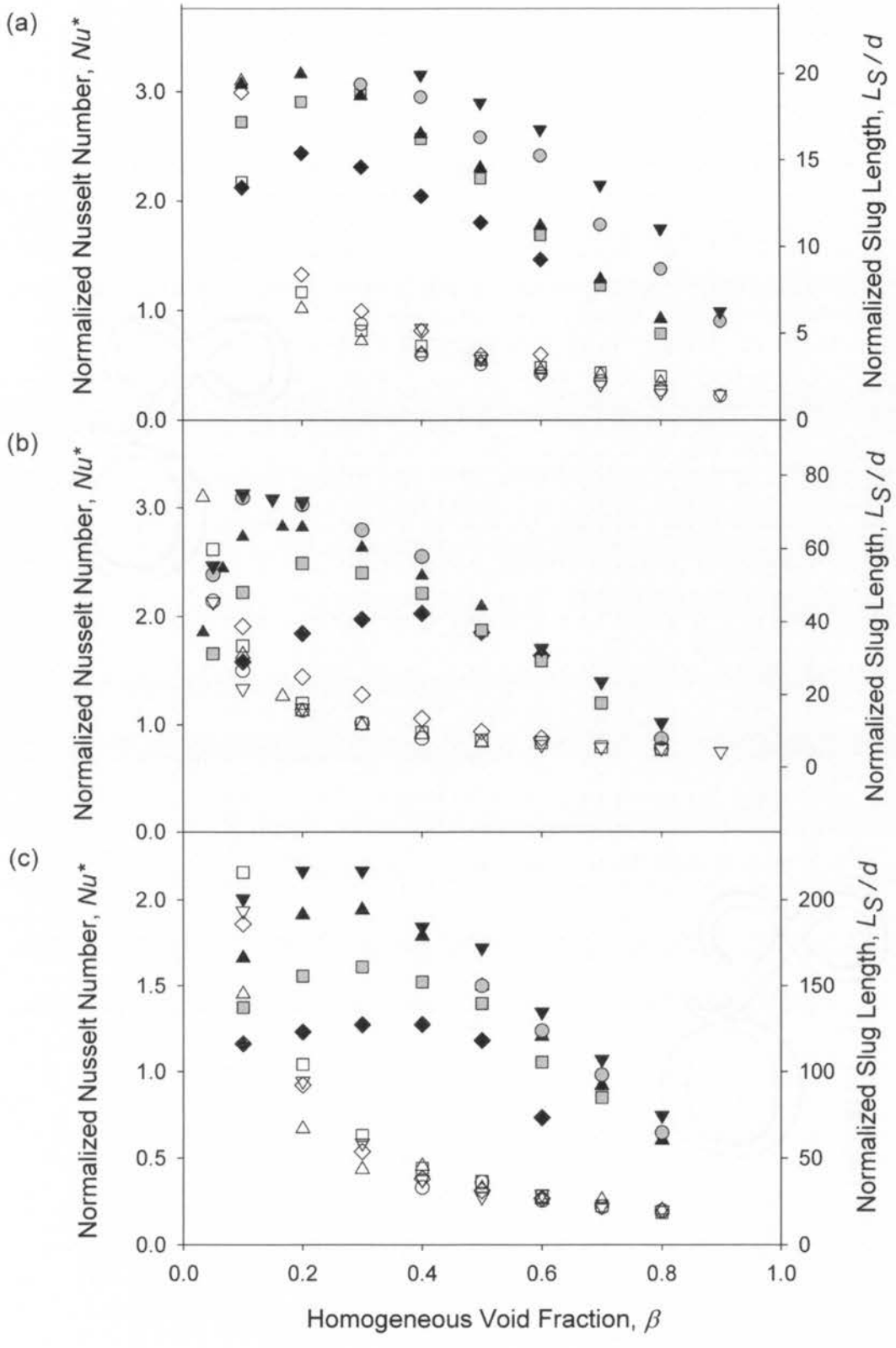

Figure 5.4: The effect of homogeneous void fraction (β) on the normalized Nusselt number (Nu^*) in solid symbols and slug length (L_S/d) in open symbols ($U_{TP} = 0.11$ m s^{-1} (◆), $U_{TP} = 0.21$ m s^{-1} (■), $U_{TP} = 0.32$ m s^{-1} (▲), $U_{TP} = 0.42$ m s^{-1} (●), $U_{TP} = 0.53$ m s^{-1} (▼)) with the gas-liquid mixture being generated using the (a) TM1, (b) TM2 and (c) TM3 mixers.

5.2 Multi-block heat transfer results for different liquid phase fluids

Typical results for the wall heat flux (q_i), the calculated wall temperature (T_{wi}) and mean fluid temperature (T_{bi}) and the time-averaged Nusselt numbers (Nu_i) of each heating zone for the EG/W and EG systems are shown in Figure 5.5 and 5.6, respectively. It can be seen that the Nusselt numbers are almost constant throughout blocks 4 to 9, indicating thermally fully-developed flow is achieved. The high values of the Nusselt number for the first few blocks are attributed to the entrance effect, while the fall of the Nusselt number at block 10 is due to the uncertainties arising from the end-block effect. It is worth mentioning that the long development length was not found in the heat transfer experiments using water as the liquid phase, where thermally fully-developed flow was generally achieved after the first heating block, as seen in Figure 5.1. Walsh *et al.* (2010) studied air-water Taylor flow heat transfer rates for various slug length-to-diameter ratios ($1.6 < L_S/d < 14$) and identified a thermal entrance region of about one slug length. However, our results suggest that the length of development can be longer in some cases (e.g. the cases presented in Figure 5.5 and 5.6, for which the slug length was $7.8d$ and $6.0d$, respectively, but 3-block lengths (~ $40d$) were required for the flow to become thermally fully-developed). In this thesis we focus on fully-developed heat transfer. To obtain the fully-developed heat transfer rate for the EG/W and EG systems, the average two-phase Nusselt numbers (Nu_{TP}) are determined by averaging the Nusselt numbers for blocks 4 to 9.

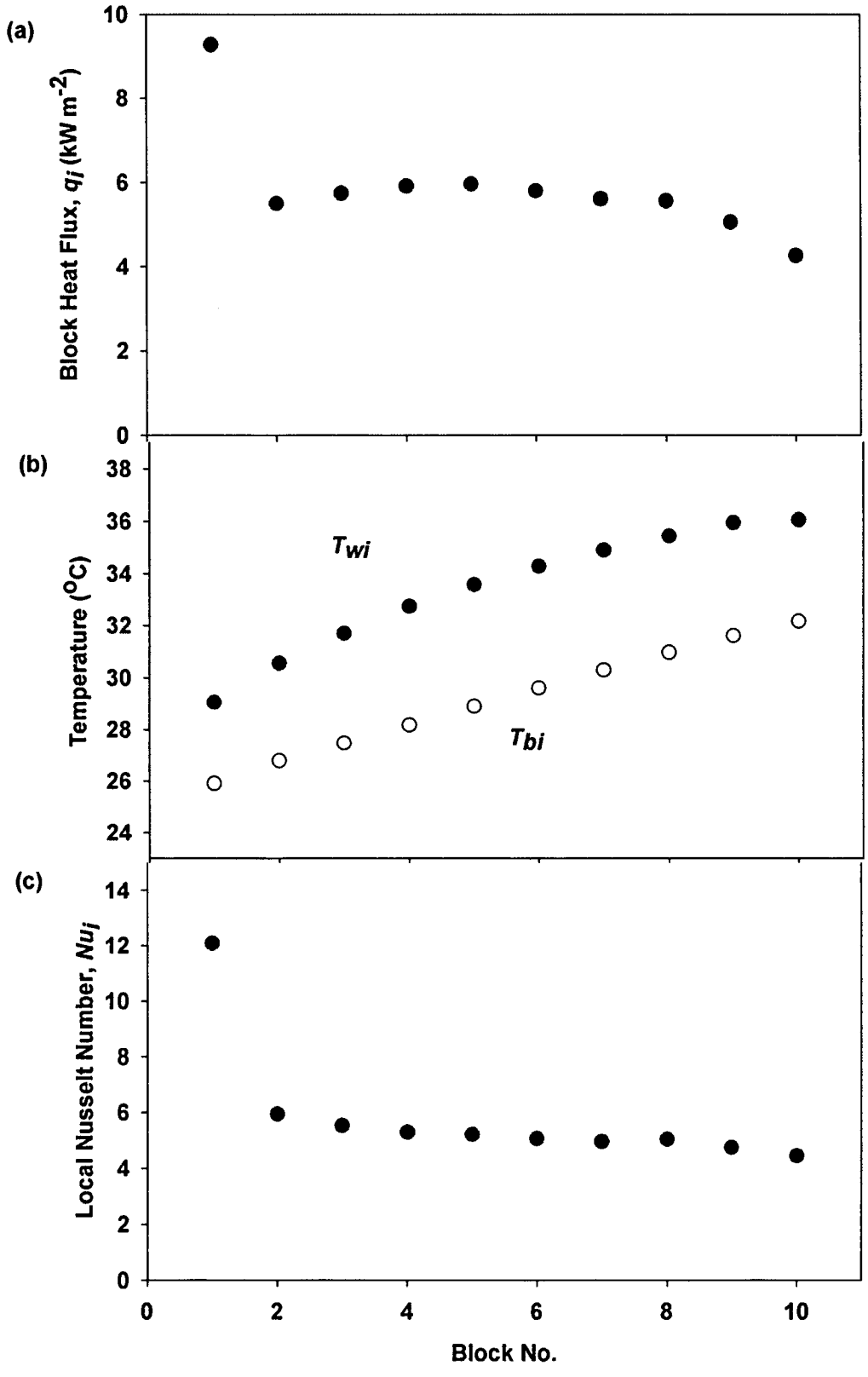

Figure 5.5: Typical results for (a) the wall heat flux, (b) the mean wall and fluid temperatures and (c) Nusselt number of each heating section at U_{TP} = 0.21 m s^{-1}, β = 0.49, L_S/d = 7.81 using EG/W as the liquid phase and the TM2 mixer.

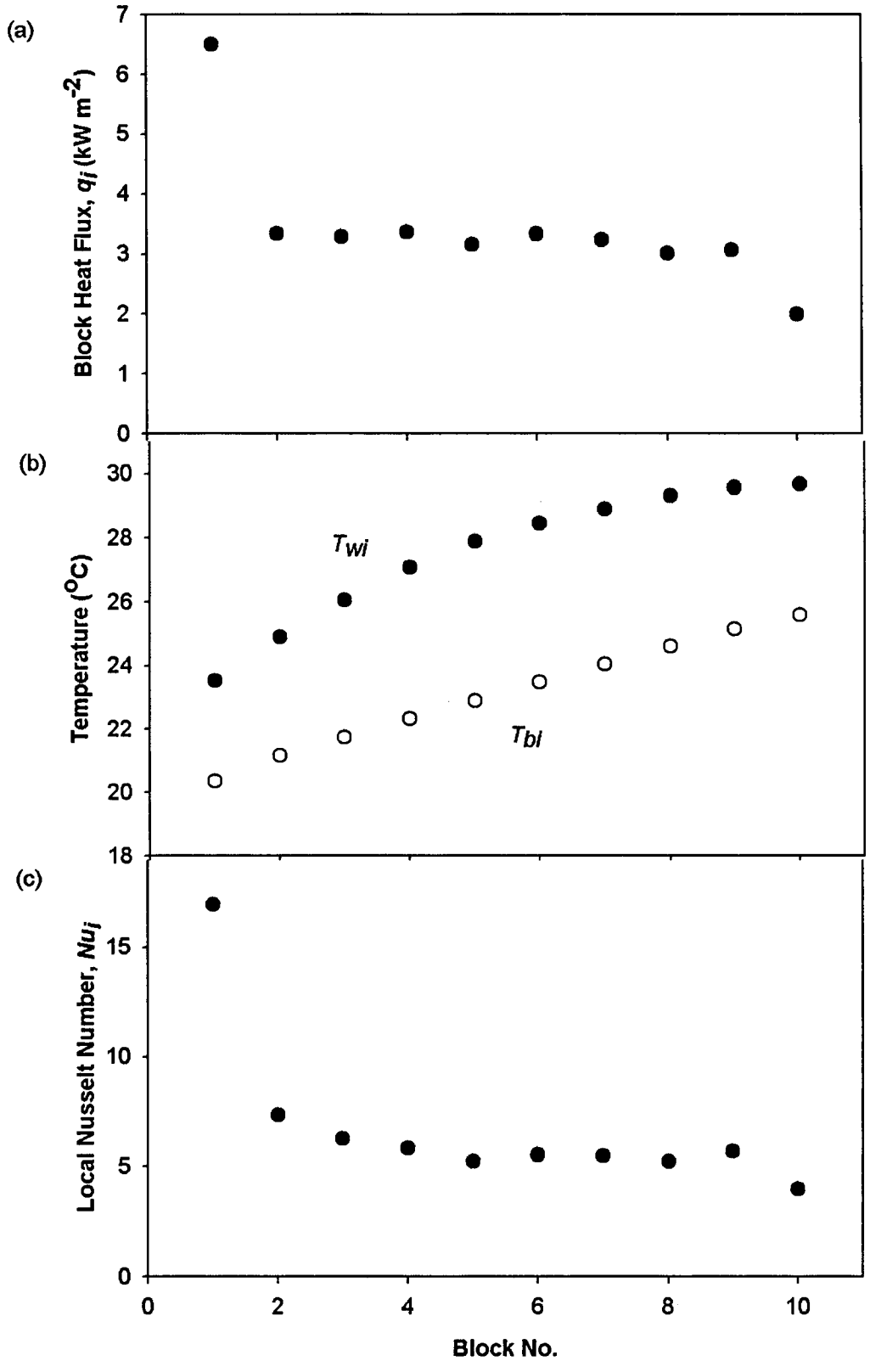

Figure 5.6: Typical results for (a) the wall heat flux, (b) the mean wall and fluid temperatures and (c) Nusselt number of each heating section at U_{TP} = 0.21 m s^{-1}, β = 0.48, L_S/d = 5.96 using EG as the liquid phase and the TM2 mixer.

5.2.1 Parametric study

Comparisons of the dependence of Nu^* on various parameters including the mixture velocity (U_{TP}), normalized slug length (L_S/d) and homogeneous void fraction (β), for the W, EG/W and EG systems are made in Figures 5.7, 5.8, and 5.9, where it is seen that similar trends are observed for each of the fluids.

Figure 5.7 (a) shows the variations of the normalized Nusselt number with the mixture velocity for all fluids. Though the value of Nu^* is found to increase with the mixture velocity for all systems, the increasing trend for the EG/W system is not as pronounced as that for the other two systems. The heat transfer enhancement for the W, EG/W and EG are 45%, 20% and 55%, respectively, as the mixture velocity increased from ~0.10 to ~0.42 m s^{-1}.

As seen in Figure 5.7 (b), the variations of normalized slug lengths with mixture velocity are slightly different in trends. While the slug lengths for W system remain relatively constant for the mixture velocities studied, the value of L_S/d for EG decreases and that of EG/W slightly increases with increasing mixture velocity. The value of Nu^* was found to increase with increasing mixture velocity and decreasing slug length in the water experiments, as discussed in Section 5.1. Therefore, the slight increase in slug length for the EG/W system may somehow offset the enhancement brought by the increasing mixture velocity and results a less significant effect of U_{TP}. Opposite to the EG/W system, the slug lengths obtained from the EG system decrease with increasing U_{TP} which may reinforce the heat transfer enhancement at higher mixture velocity.

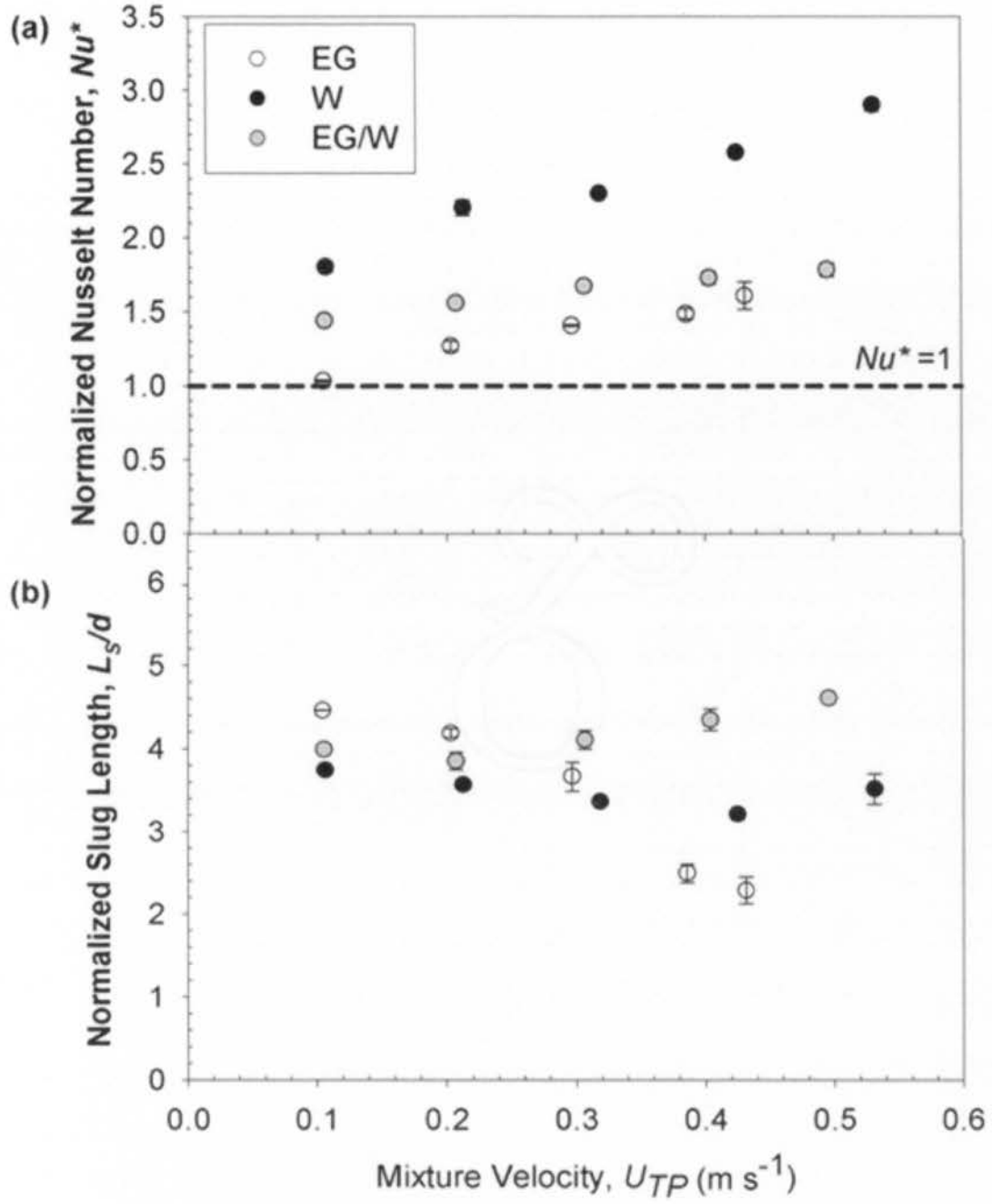

Figure 5.7: Comparisons of the dependence of (a) the normalized Nusselt number and (b) normalized slug length on mixture velocity ($\beta \sim 0.5$). The error bars represent one standard deviation of three replicates.

The effect of slug length on Taylor flow heat transfer of different fluid systems are compared in Figure 5.8. It is apparent that the heat transfer enhancement increases with decreasing liquid slug length for all fluids for both conditions studied, which is consistent with the resulted reported in the literature (Oliver and Young Hoon, 1968, Horvath *et al.*, 1973, Walsh

et al., 2010). However, the degree of enhancement for EG/W and EG systems is noticeably lower than that observed in the W experiments. For the longest slug flow using EG as the liquid phase at U_{TP} ~ 0.21, the heat transfer rate falls below that of the single-phase fully-developed laminar flow, indicating the heat transfer enhancement brought by the recirculation offset by the reduction of liquid flux.

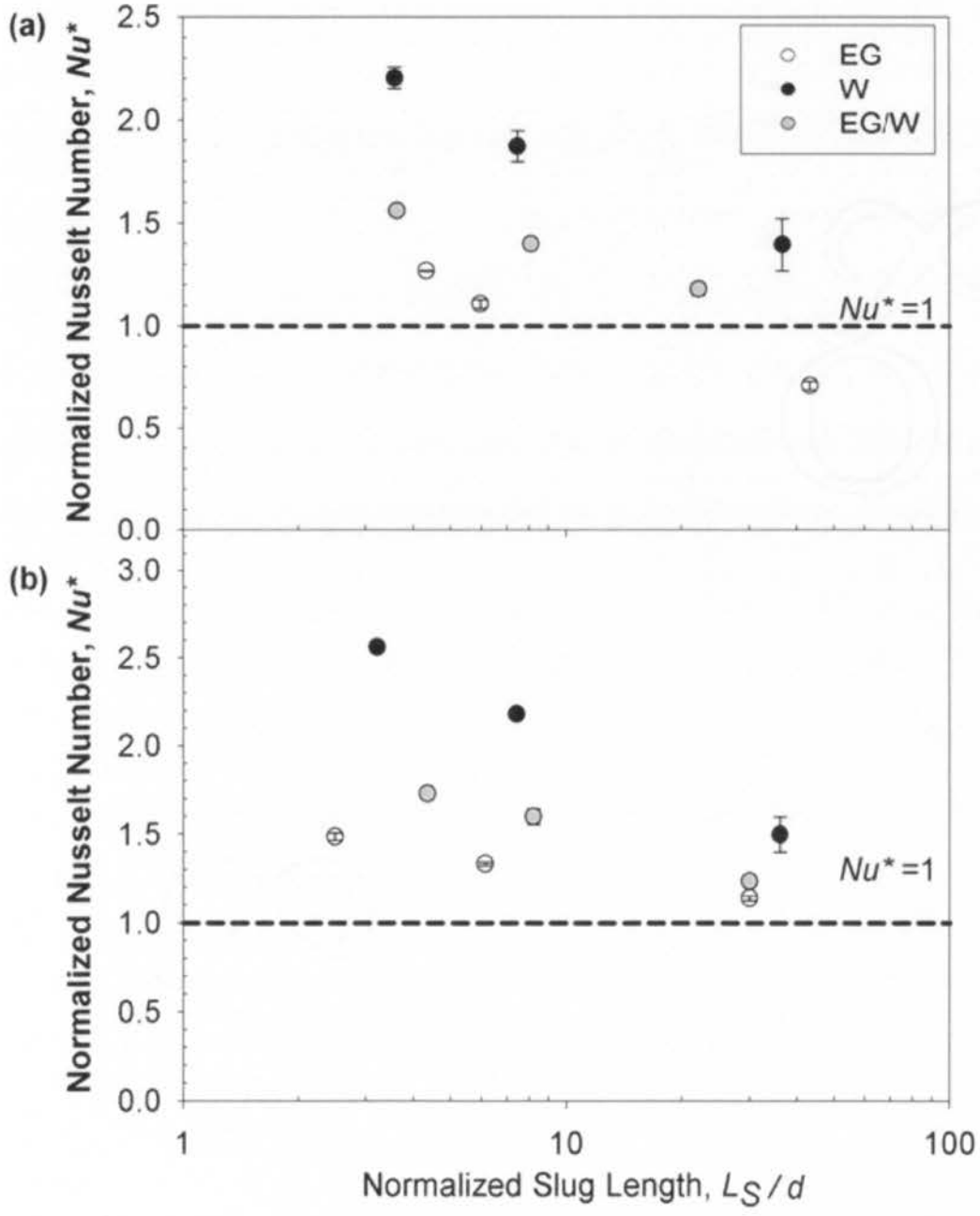

Figure 5.8: Comparisons of the dependence of the normalized Nusselt number on normalized slug length for (a) U_{TP} ~ 0.21 m s^{-1}, β ~ 0.5 and (b) U_{TP} ~ 0.42 m s^{-1}, β ~ 0.5. The error bars represent the standard deviation of three replicates.

Figure 5.9 shows the variation of normalized Nusselt number (Nu^*) and slug length (L_S/d) with homogeneous void fraction (β) at $U_{TP} \sim 0.21$ m s^{-1} with gas-liquid mixtures generated using three different T-mixers. The general trends of the heat transfer and slug length data are similar, regardless of the mixers and/or the fluids used. It is noted that Nu^* first increases with β to values above the limiting value of $Nu^* = 1$ at $\beta = 0$ until a maximum point is reached, beyond which it declines steadily towards a gas-only value as $\beta \rightarrow 1$. In addition to the unit cell length and mixture velocity identified in the heat transfer experiments using water as the liquid phase, the value of β for the maximum heat transfer rate is also found to vary between $0.1 < \beta < 0.3$, depending on the fluid used.

At high β values, Nu^* falls below one, as expected due to its approach to gas-only conditions. The effect is more obvious for flows generated with larger mixers which produce longer liquid slugs and gas bubbles and using EG as the liquid phase.

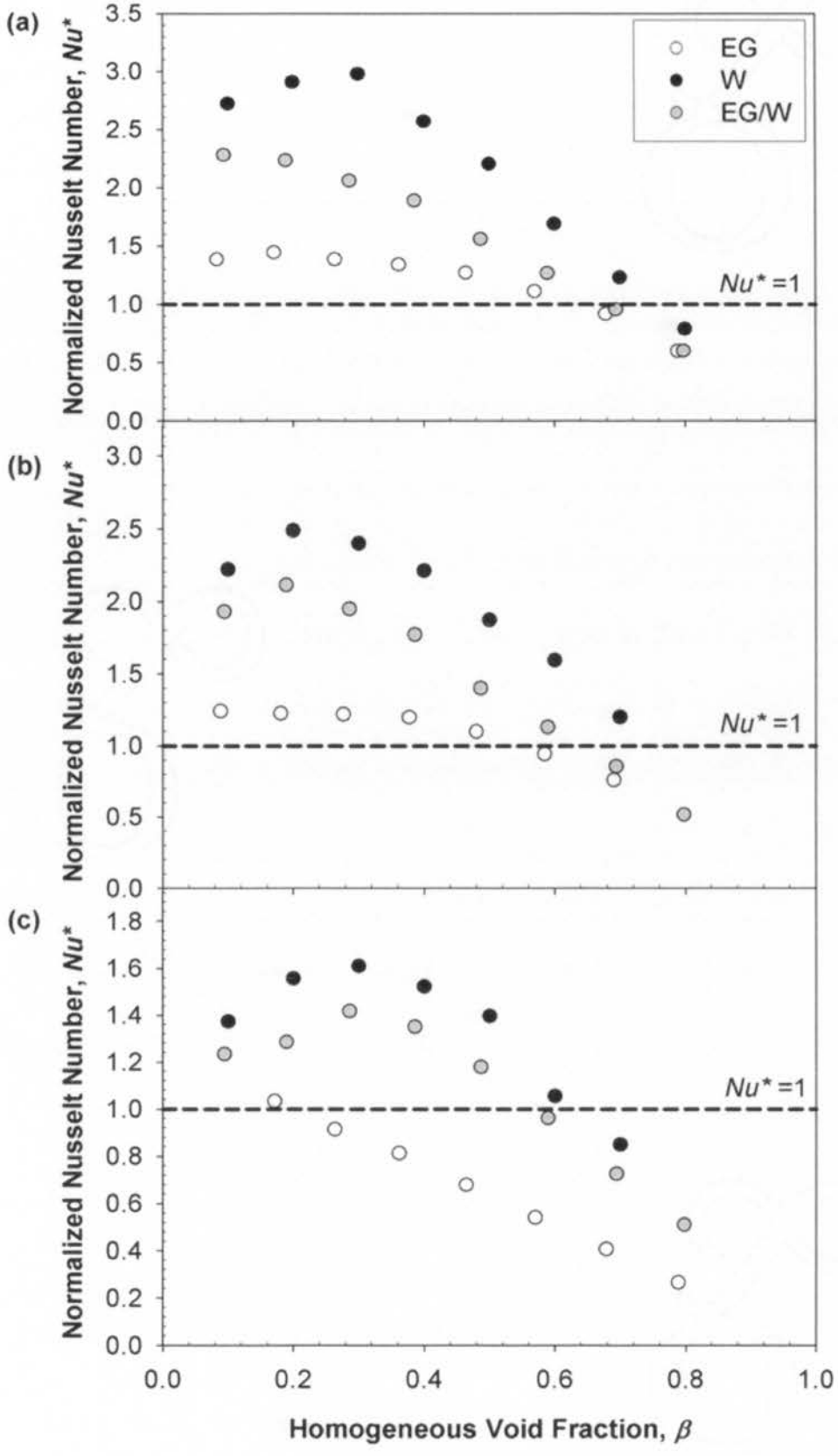

Figure 5.9: Comparisons of the dependence of the normalized Nusselt number on homogeneous void fraction (U_{TP} ~ 0.21 m s^{-1}) with the gas-liquid mixture being generated using the (a) TM1, (b) TM2 and (c) TM3.

For most of the studied conditions, the normalized Nusselt number is higher than 1, with the specific value of Nu^* dependent on the operating parameters as well as the fluid used. It is noted that the order of heat transfer augmentation is always W > EG/W > EG for flow with similar mixture velocity and homogeneous void fraction and slug length. A larger difference in Nu^* among the three systems is observed at low values of β and the greatest heat transfer enhancement factors are 3.2, 2.3, 1.6, respectively, for the conditions studied here.

According to Thulasidas *et al.* (1997), the time for a half recirculation cycle of fluid in the slug is that for the slug to travel a distance of twice its length for flow with $10^{-4} < Ca < 10^{-2}$, while for flow with a larger Capillary number, this time increases sharply and becomes infinity for Capillary numbers beyond a certain value, for which bypass flow occurs. For instance at $U_{TP} \sim 0.21$ m s^{-1}, the value of Ca for W, EG/W and EG are 0.003, 0.014 and 0.073, respectively. Therefore, for slugs of the same length moving at the same velocity, the recirculation time will follow the order W < EG/W < EG. Alternatively, the fluid in the water slug will undergo the highest number of complete recirculation cycles in the heating section, followed by the EG/W and then the EG slugs. An increase in radial heat transfer for the water system, therefore, results to give more effective heat transfer.

In addition to the difference in recirculation frequency, the order of heat transfer enhancement is in fact in the opposite trend of the thickness of the film surrounding the bubble. Oliver and Wright (1964) also reported that the heat transfer enhancement brought by Taylor flow decreased with increasing film thickness. Also, the recirculation size was reported to decrease with increasing Ca (Thulasidas *et al.* 1997). Due to the reduction of recirculating fluid, the efficiency for the slug to carry heat away from the wall may reduce and hence a lower overall heat transfer rate.

5.3 Summary

Systematic heat transfer experiments for constant wall heat flux boundary conditions were performed using a 2.00 mm diameter tube with fluids flowing in a vertical upward direction. Three liquid phase fluids, water, ethylene glycol/water mixture and ethylene glycol were employed to achieve a wide range of Capillary numbers ($0.001 < Ca < 0.180$) and Reynolds numbers ($10 < Re_{TP} < 1100$). With the three T-junction mixers of different internal diameters used here, the slug lengths were able to be varied from 1 to 220 tube diameters.

A multi-block heating section was employed to investigate the dependencies of the heat transfer rate on the slug length, mixture velocity, homogenous void fraction and fluid properties for flows which were well-characterized. The results are summarized as follows:

1. For flows of similar slug length and homogeneous void fraction, the two-phase Nusselt number increases with the mixture velocity for all fluid systems. The influence of mixture velocity is found to be the greatest for the shortest slugs.

2. Heat transfer enhancement brought about by Taylor flow is more pronounced for flow with shorter slugs, as the number of complete cycles of liquid recirculation in the same heating length increases with decreasing slug length.

3. The overall heat transfer rate for gas-liquid Taylor flow is determined by two different effects: (1) heat transfer enhancement due to the internal recirculation within the liquid slug and (2) thermal mass reduction due to the presence of the gas phase in a unit cell. Therefore, the heat transfer enhancement was found to attain a maximum value when $0.1 < \beta < 0.3$, depending on the unit cell length, the mixture velocity and the liquid phase fluid.

4. The overall heat transfer rate is found to be a strong function of fluid properties. For similar mixture velocity and homogeneous void fraction and slug length, the order of heat transfer augmentation is always found to be W > EG/W > EG.

The dependence of the thermal characteristics of Taylor flow on flow parameters, including the mixture velocity, slug length, homogeneous void fraction and fluid properties, is recognized. In the next chapter, the effects of these parameters are characterized and correlations to predict the heat transfer rates of gas-liquid Taylor flow are deduced from these experimental data.

Chapter 6
Modelling of Taylor Flow Heat Transfer

Due to the introduction of gas, the flow characteristics of Taylor flow differ significantly from their single-phase counterparts. The periodic passage of bubbles and slugs that occurs in Taylor flow has led many authors to invoke the Graetz number, $Gz = Re \cdot Pr \cdot (d/L)$, which is used for single-phase laminar flow thermal-development, to characterise heat transfer in the slug region. However, there is confusion as to whether the characteristic length in the Taylor flow case should be the total length from the entrance or the slug length. A brief review of the current understanding of the dependence of Taylor flow heat transfer enhancement on the flow characteristics was provided in Chapter 2. Although various two-phase heat transfer models have been proposed, the underlying heat transfer mechanisms, knowledge of which is essential for optimal process design and control of micro-systems, are not yet fully understood.

In Chapters 4 and 5, the hydrodynamics and heat transfer characteristics of vertical upward gas-liquid Taylor flow in a d = 2.00 mm channel were discussed. The effects of inlet geometries, operating conditions (mixture velocity and homogeneous void fraction) and the fluid properties on the flow structures were noted. Heat transfer of Taylor flow was found to be strongly dependent upon the flow pattern, including the slug length, volume fraction occupied by the liquid slug and thickness of the film surrounding the bubble which depend on the operating conditions, as well as the properties of the liquid phase fluids. The maximum Nusselt number for Taylor flow obtained in the present study is 3.2 times higher than that of the single-phase fully-developed laminar flow.

In this chapter, a detailed analysis based on the comprehensive set of data collected in this study using the multi-block heating system is performed to understand the underlying physical mechanisms governing the heat transfer behaviour for Taylor flow in microchannels. Possible heat transfer pathways are discussed in Section 6.1. In Section 6.2, a semi-empirical correlation is first derived based on the results obtained from the nitrogen-water experiments. The validity of the model for describing data in the literature and experimental results for other fluid systems obtained in this study is justified in Section 6.3 and the development of a model for general application is presented in Section 6.4.

6.1 Heat transfer mechanisms

The flow structure of the gas-liquid Taylor flow regime in microchannels is characterized by its high uniformity – gas bubbles and liquid slugs of almost constant length enter the system at a constant frequency. Heat transferred from the wall in Taylor flow, as a result, goes alternately to the bubble and slug regions as a succession of bubble and slug passes through the system. Due to the high periodicity of such flow structure, heat transfer analysis of Taylor flow is usually done based on a unit cell consisting of a gas bubble surrounded by a thin liquid film and a liquid slug, highlighted in the blue box in Figure 6.1.

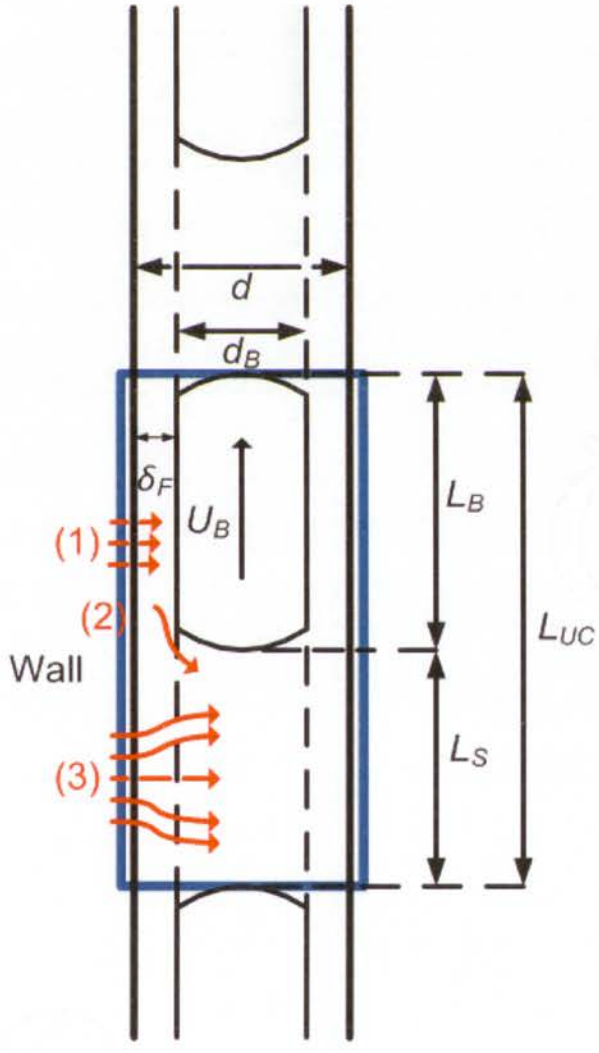

Figure 6.1: Schematic of Taylor flow with the blue box highlighting a unit cell which consists of a gas bubble and a liquid slug. The red arrows indicating possible heat transfer pathways: (1) heat transfer from the wall to the film around the bubble, (2) transfer of heat accumulated in the liquid film to the liquid slug and (3) heat transfer from the wall to the film and slug in the slug region.

At low pressures, the mass flow of gas is generally very much less than the mass flow of liquid, and when the liquid film is thin, the liquid mass flow contribution in the bubble region is only a small fraction of the total liquid flow. Even for systems with considerable film thickness, the bubble film is effectively stagnant as discussed in Chapter 4. Therefore, most of the heat transferred to the two-phase system is carried in the slugs. However, when the film in the bubble region comprises a significant fraction of the wall area in a unit cell and the subsequent fate of the energy deposited there must be considered – Gupta *et al.* (2010) showed computationally that only a tiny amount of heat is transferred from the liquid film surrounding the gas bubble to the gas bubble itself and this can be neglected in a heat balance – in essence, thermal energy transfer to the wall film in the bubble region is accumulated there until the slow-moving film is overtaken by the next slug. He *et al.* (2010) also showed in their computational results that most heat from the wall was transferred to the slug region due to the negligible contribution of the gas phase to heat transfer.

The role played by the bubble film in the overall heat transfer phenomenon in Taylor flow is depicted schematically in Figure 6.1, which shows the various heat flows: (1) heat transfer from the wall to the bubble film, where it accumulates until the passage of the next slug; (2) heat transfer from the bubble film to the liquid slug, and (3) heat transfer from the wall to the recirculating slug. If there is a constant wall temperature imposed on the system, the energy accumulated in the bubble film is usually negligible overall and processes (1) and (2) are unlikely to be important. However, this will not generally be the case when a constant wall heat flux is imposed because the energy deposited even in a thin film is a significant fraction of the total. Mechanism (3) is then always important, regardless of the boundary conditions imposed.

Since most of the heat is carried by the liquid slug for gas-liquid Taylor flow, a reduction of the liquid flux/liquid contact area resulted from the introduction of gas may lead to poorer heat transfer. However, it has been shown that the heat transfer rate for Taylor flow can be up to 2-3 times higher than that of the single-phase fully-developed laminar flow, depending on the flow characteristics (Oliver and Wright, 1964, Oliver and Young Hoon, 1968, Betz and Attinger, 2010, Gupta *et al.*, 2010, He *et al.*, 2010, Walsh *et al.*, 2010). Therefore, there must be some mechanisms to overcome the effect of liquid flux/liquid contact area reduction and to augment the heat transfer rate for Taylor flow.

Two possible mechanisms were identified in the past to be responsible for the heat transfer enhancement:

(1) Internal recirculation within the liquid slug (in a reference frame moving with the bubble). The liquid circulation promotes radial fluid mixing effectively – hot liquid near the wall is transported to the core at the bubble nose while cooler fluid at the tube centre moves to the wall near the bubble tail of previous bubble.

(2) Modification of the velocity profile inside the liquid slug due to the presence of gas bubbles. The velocity profile for each slug is developing from a relatively flat profile in front of the bubble nose to a parabolic profile in the middle of the slug for sufficiently long slugs.

The above heat transfer mechanisms for Taylor flow in microchannels can be examined through the development of some simple models using the experimental data collected in this study, as well as existing data in the literature. Before doing so, the available correlations for the prediction of Taylor flow heat transfer presented in Chapter 2 are summarized in Table 6.1. No general form is noted among these correlations and most of them are rather empirical and therefore provide little insight in the enhancement mechanisms of Taylor flow heat transfer. Therefore, a model derived based on the underlying heat transfer mechanisms over a wide range of operating conditions is required for general applications.

Table 6.1: Existing correlations for the Nusselt number of Taylor flow.

Reference	Boundary condition	Working conditions	Heat transfer coefficient correlation	
Oliver and Wright (1964)	Constant wall temperature	$d = 6.4$ mm $25 < \frac{Re_{TP} \cdot Pr \cdot d}{L} < 1900$	$Nu_{TP} = 1.615 \left(Re_{TP} \cdot Pr \cdot \frac{d}{L}\right)^{1/3} \left(\frac{1.2}{(1-\beta)^{0.36}} - \frac{0.2}{1-\beta}\right) \left(\frac{\mu_B}{\mu_W}\right)^{0.14}$	Eq. (2.8)
Hughmark (1965)	-	Using data of Oliver and Wright (1964)	$Nu_{TP}\sqrt{1-\beta} = 1.75 \left(Re_{TP} \cdot Pr \cdot \frac{d}{L}\right)^{1/3} \left(\frac{\mu_B}{\mu_W}\right)^{0.14}$	Eq. (2.9)
Kreutzer *et al.* (2001)	Constant wall temperature	$d = 1$ mm $1 < L_S/d < 16$, $7 < Pr < 700$, $10 < Re_{TP} < 400$	$Nu_S = 20 \left[1 + 0.003 \left(\frac{L_S}{Re_{TP} \cdot Pr \cdot d}\right)^{-0.7}\right]$	Eq. (2.10)
Lakehal *et al.* (2008)	Constant wall temperature	$d = 1$ mm $0.8 < L_S/d < 5.14$, $Pr = 5.5$, $10 < Re_{TP} < 400$	$Nu_{TP} \approx Nu_{LO} + 0.022(\beta Re_{TP})^{4/5} Pr^{2/5}$	Eq. (2.11)
Walsh *et al.* (2010)	Constant wall heat flux	$d = 1.5$ mm $0.67 < L_S/d < 28.9$, $Pr = 5.5$, $10 < Re_{TP} < 400$	$Nu_{TP} = Nu_{LO}(1-\beta)\left[1 + 7.2\left(\frac{L_S}{d}\right)^{-0.5}\right]$	Eq. (2.12)

6.2 Heat transfer correlation for nitrogen-water system

For most Taylor flow heat transfer studies (Fukagata *et al.*, 2007, Lakehal *et al.*, 2008, Narayanan and Lakehal, 2008, Betz and Attinger, 2010, Gupta *et al.*, 2010, He *et al.*, 2010, Walsh *et al.*, 2010), water was used as the liquid phase, as it offers high cooling capabilities due to its high specific heat capacity, and it has low vapour pressure where evaporation of liquid can be generally neglected for the conditions studied. Also, two-phase flow with water has been considered as an important option for system cooling for systems operating at temperatures lower than the saturation temperature of water (Bar Cohen *et al.*, 1995). Therefore, nitrogen-water Taylor flow was first studied due to its industrial importance and a heat transfer model was developed based on the water experimental data.

Recall that heat is continuously transferred from the wall to the fluid adjacent to a bubble and a slug alternately as a unit cell passes through the system. In the bubble region, where heat transfer occurs primarily via the thin liquid film, the local Nusselt number is very high (Lakehal *et al.*, 2008, Narayanan and Lakehal, 2008, Gupta *et al.*, 2010) as the temperatures of the wall film and the gas bubble approach quickly that of the wall. Since the heat transfer coefficient of the thin wall film is very high, there is negligible resistance to heat transfer here and the overall heat transfer coefficient (h_{TP}) is just that arising in the slug where the contact surface with the wall/liquid film has an area proportional to L_S/L_{UC}

$$h_{TP} \sim \frac{L_S}{L_{UC}} \cdot h_S \tag{6.1}$$

where h_S is the heat transfer coefficient in the liquid slug region. Normalization of the two-phase Nusselt number by the percentage of the area covered by the liquid slugs $(1-\beta)$, which approximately equals L_S/L_{UC} for systems with a thin film, was also suggested by Horvath *et al.* (1973), Walsh *et al.* (2010) and Muzychka *et al.* (2011).

As confirmed by both computational (Fukagata *et al.*, 2007, Lakehal *et al.*, 2008, Gupta *et al.*, 2010) and experimental results (Thulasidas *et al.*, 1997), the velocity profile within a slug develops from a relatively flat profile from the bubble front to a parabolic profile in the middle of a sufficiently-long slug. It has been suggested that this flow development can be likened quantitatively to developing laminar pipe flows, and that the heat transfer rates can

likewise be compared with thermally-developing flows (Kreutzer *et al.*, 2001). Despite the apparent similarity, however, there are profound differences between the development of the slug velocity and temperature profiles and the corresponding processes in single-phase tube flow. These differences include the existence of the characteristic recirculation zone (in the frame of reference moving with the bubble) and the mixing of the thermal energy contained in the bubble film when the film is overtaken by the slug. Such differences are most significant with shorter slugs but, even with long slugs in which a parabolic velocity profile is reached in the body of the slug, the analogy with pipe flow breaks down again closer to the trailing bubble.

While quantitative comparison with developing laminar pipe flow is not appropriate, there is no doubt that the flow and heat transfer behaviour in the slug remains a hydrodynamically and thermally developing laminar flow. It is therefore appropriate that heat transfer in Taylor flow should be characterised by a Graetz number as has been proposed in the past. However, it is also clear that the characteristic length should be the slug length, rather than the total heating length from the entrance. Therefore, results obtained from experiments using water as the liquid phase have been examined for slug heat transfer (calculated from the experimental results as $Nu_{L^*} = Nu_{TP} \cdot L_{UC}/L_S$, see Eq. (6.1)) in terms of the dimensionless slug length, or inversed Graetz number

$$L_S^* = \frac{L_S}{Re_{TP} \cdot Pr \cdot d} \tag{6.2}$$

As shown in Figure 6.2, a very good correlation is observed between Nu_{L^*} and L_S^* in this set of data. The theoretical mean Nusselt numbers for thermally developing single-phase laminar flows for the constant wall heat flux boundary condition ($Nu_{m,H}$) is also compared with the experimental data in Figure 6.2, as our multi-block heating system provides mean values in Taylor flow rather than local heat transfer coefficients as it does for steady single-phase flow. For flows away from the limiting cases $L_S^* \rightarrow 0$ and $L_S^* \rightarrow \infty$, the data follow the characteristic line of the theoretical length-mean heat transfer coefficient closely and hence a trend $Nu_{L^*} \propto 1/L_S^{*1/3}$ is observed. Therefore, a Hausen-type expression taking the limit for $L_S^* \rightarrow \infty$ as the value for fully-developed single-phase laminar flow with constant wall heat flux ($Nu_{LO} = 4.364$) is used to correlate the data

$$Nu_{L^*} = Nu_{LO} + \frac{c_1}{L_S^* + c_2 L_S^{*1/3}} \tag{6.3}$$

where the values of the constants are found by least-squares fitting to be c_1 = 0.29 and c_2 = 0.15. Good agreement is achieved between the experimental results and the prediction as is apparent in Figure 6.2, with most of the experimental data falling within $\pm 20\%$ of this correlation.

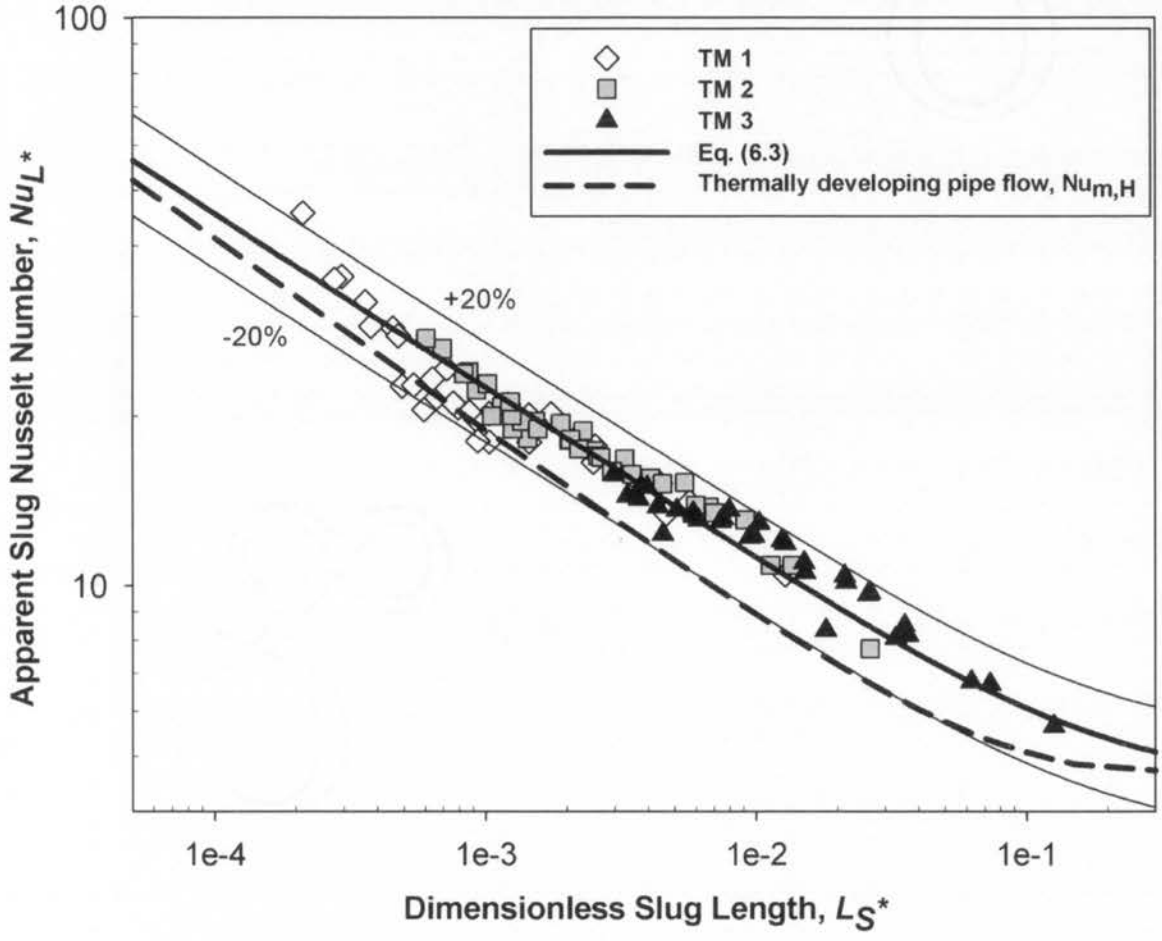

Figure 6.2: Comparison of experimental data obtained from the water experiments with the correlation proposed in Eq. (6.3) for Taylor flow heat transfer and the theoretical length-mean heat transfer coefficient for thermally developing single-phase laminar flow for constant wall heat flux boundary condition ($Nu_{m,H}$).

6.3 Validity of the nitrogen-water model for general applications

The suitability of applying the correlation derived based on water experiments for general applications can be justified through comparison of data in the literature, as well as results obtained from other working fluids used in this study, with Eq. (6.3).

6.3.1 Comparisons with data and correlations in the literature

Experimental and computational Taylor flow heat transfer results from the literature are compared with Eq. (6.3) in Figure 6.3. The correlation generally over-predicts the experimental data of Oliver and Young Hoon (1968) and Horvath *et al.* (1973), and the numerical results of Lakehal *et al.* (2008), which were obtained with constant wall temperature boundary conditions rather than with constant heat flux as in the current experiments and in the development of Eq. (6.3). The average absolute difference between the literature data and Eq. (6.3) is ~ 16%.

For experiments (Walsh *et al.*, 2010) and simulations (Gupta *et al.*, 2010, He *et al.*, 2010) performed with constant wall heat flux conditions, most of the heat transfer data scatter $\pm 20\%$ of the proposed correlation, Eq. (6.3). However, more significant differences are observed between the predicted values and the computational data of Gupta *et al.* (2010) for short slugs ($L_S/d \sim 1, \beta = 0.51$) and higher mixture velocities (0.7–1.0 m s^{-1}) – the value of L_S^* decreases with increasing mixture velocity but the heat transfer enhancement was found to be independent of mixture velocity in the simulation results. These precise conditions were not accessible with the current experimental setup so caution should be used in applying Eq. (6.3) to short bubbles, especially at high velocities.

The correlation of Kreutzer *et al.* (2001) (Eq. 2.10) is also presented in Figure 6.3. It can be seen that Eq. (2.10) over-predicts almost all the existing data and it levels off at a much smaller L_S^* value, compared with Eq. (6.3) and laminar developing flows. Moreover, the plateau value (~20) for Eq. (2.10) is significantly higher than that for fully-developed single-phase laminar flow with constant wall heat flux ($Nu_{LO} = 4.364$) which is expected for flows with very long slugs.

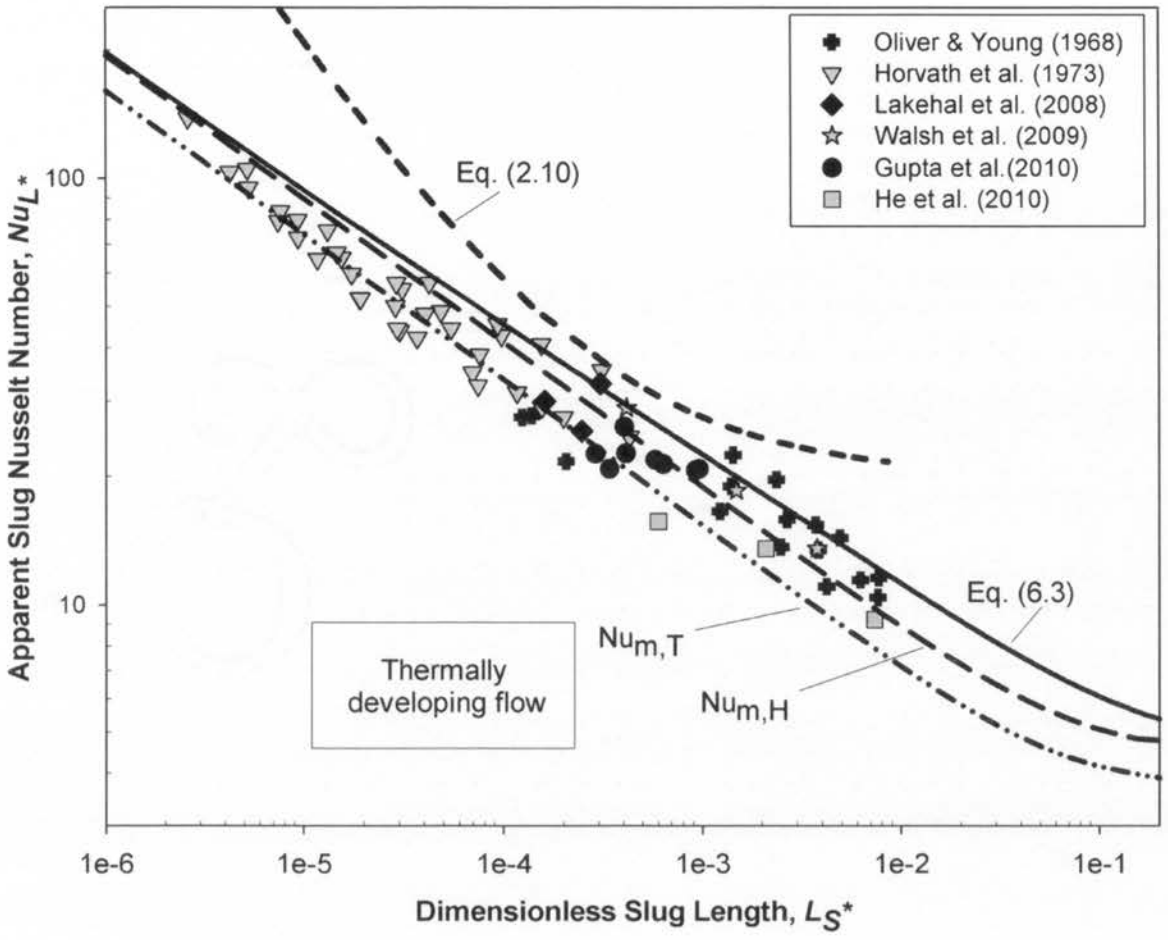

Figure 6.3: Comparison of data in the literature for the apparent slug Nusselt number ($\boldsymbol{Nu_L^*}$) with the correlation given in Eq. (6.3) for Taylor flow heat transfer derived based on data obtained from water-nitrogen experiments.

Muzychka *et al.* (2011) reanalysed the existing Taylor flow heat transfer data in the literature for both constant wall temperature (Oliver and Young Hoon, 1968, Horvath *et al.*, 1973, Vrentas *et al.*, 1978, Narayanan and Lakehal, 2008) and constant wall heat flux (Walsh *et al.*, 2010) boundary conditions and demonstrated an excellent correlation between the mean slug Nusselt number ($\overline{Nu_{L^*}} = \overline{Nu_{TP}}/(1-\beta)$) and L_S^*. They showed that the constant wall temperature heat transfer data followed the theoretical Graetz solution for the mean Nusselt number for thermally developing single-phase laminar flow with a small root mean square (rms) error of 10–15% and a larger rms error (24%) was noted when data obtained from a constant wall heat flux study (Walsh *et al.*, 2010) were included in their analysis. Figure 6.3 also shows the theoretical mean Nusselt numbers for thermally developing single-phase laminar flows for the constant wall heat flux ($Nu_{m,H}$) and the constant wall temperature

boundary conditions ($Nu_{m,T}$). It is noted that the experimental and computational results in the literature, as well as Eq. (6.3) derived based on results obtained from water experiments in the present study correspond closely to the length-mean heat transfer coefficient for their respective thermal boundary conditions. Gupta *et al.* (2010) found computationally that for Taylor flow a constant wall temperature boundary condition is accompanied by a decrease of approximately 15% in the slug heat transfer coefficient relative to the constant wall heat flux condition, which is consistent with the trends for single-phase developing flow, and with the differences between our results and the analysis of Muzychka *et al.* (2011).

6.3.2 Comparisons with results from the other two working fluids

As seen in Figure 6.2, there is little doubt that Eq. (6.3) is able to give a reasonable prediction of the heat transfer rate for Taylor flow when water is used as the liquid phase for constant wall heat flux conditions. However, Eq. (6.3) generally over-predicts the experimental data reported by Oliver and Young Hoon (1968) and Horvath *et al.* (1973), according to Figure 6.3. Apart from the difference in the boundary conditions imposed, the use of liquid phase fluids other than water may also attribute to the deviation of their results from ours. The dependence of flow characteristics and heat transfer rates on the liquid phase fluids has been demonstrated clearly in Chapter 4 and 5. For flow with a similar mixture velocity, homogeneous void fraction and slug length, the order of heat transfer augmentation is found to be W > EG/W > EG. Therefore, the applicability of Eq. (6.3) to predict the heat transfer in Taylor flow for fluid systems apart from water system is of concern.

Figure 6.4 shows the variation of the apparent slug Nusselt number (Nu_L^*) with the dimensionless slug length (L_S^*) for all the fluid systems (W, EG/W and EG) used in this study. For comparison, Figure 6.4 also shows the theoretical mean Nusselt numbers for thermally developing single-phase laminar flows for the constant wall heat flux boundary condition ($Nu_{m,H}$), as well as the correlation derived based on the water experiments (Eq. 6.3). It is apparent that the theoretical result, which Eq. (6.3) corresponds closely to, does not provide an accurate description for all fluids. Instead of falling on the characteristic line for the mean Nusselt numbers, experimental data for individual fluids follow the general form for heat transfer in developing laminar flow, but with $Nu_{L^*} = f(L_S^*)$ specific to each fluid and always appearing to converge to the same asymptotic limit for sufficiently large values of L_S^*.

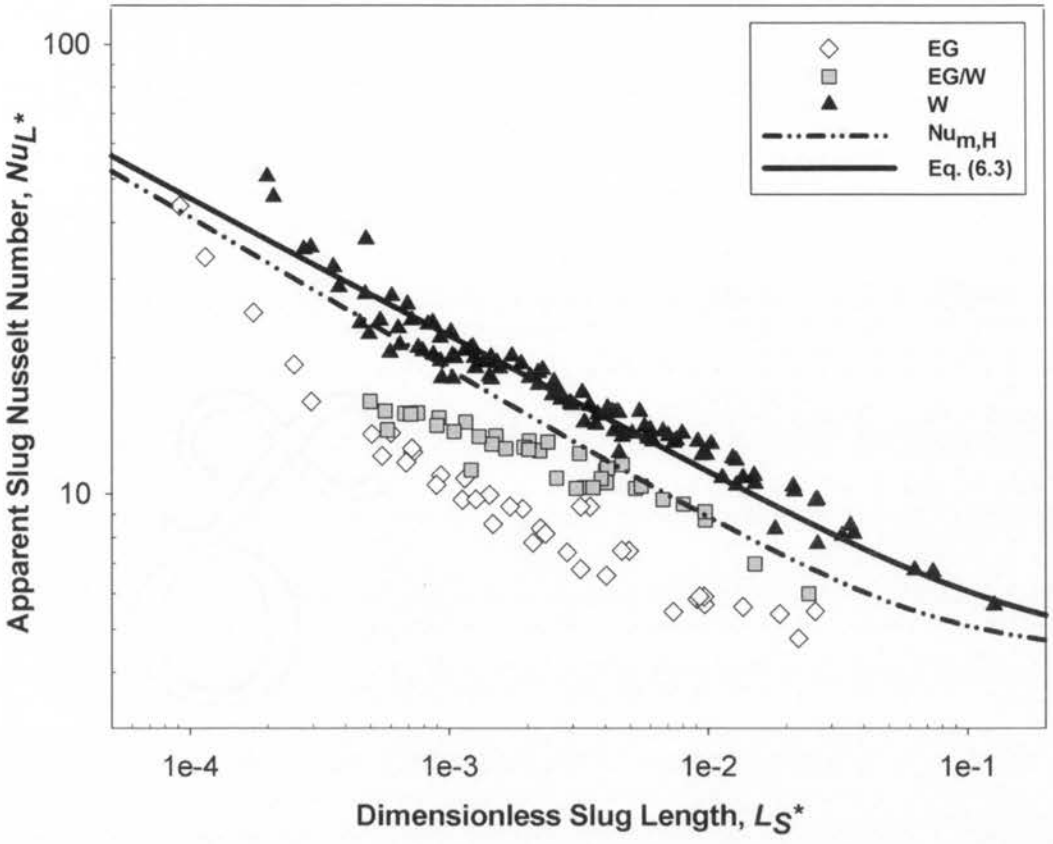

Figure 6.4: Comparison of experimental data obtained for the EG system with the theoretical length-mean heat transfer coefficient for thermally developing single-phase laminar flow for constant wall heat flux boundary condition ($Nu_{m,H}$) and Eq. (6.3).

The analogy between slug heat transfer and thermal entrance effects in single-phase flow appears very strong. However, there remain some underlying points requiring further consideration. In the first instance, it is noted that while the analogy implies that the heat transfer profile is developing throughout the length of the slug from the front (behind the leading bubble) to the rear (ahead of the nose of the following bubble), the flow at the rear of a slug also has a strong radial component that will break up the thermal boundary layer that has developed. Therefore, equating the developing flow length to the slug length cannot be exact. Based on the observations in Figure 6.4, it can be concluded that the analogy between Taylor flow slug heat transfer and developing laminar flow is incomplete. The roles played by the film surrounding the bubble, as well as the effect of internal recirculation inside the liquid slug could also be important on Taylor flow heat transfer. Therefore, re-examination of the heat transfer mechanisms is required to develop a Taylor flow heat transfer correlation for general applications.

6.4 Development of a model for general applications

The possible heat transfer pathways were indicated in Figure 6.1. As discussed in Section 6.1, energy is deposited in both the liquid film and the slug when a constant wall heat flux is imposed. Since the bubble film is effectively stagnant, the subsequent fate of the energy accumulated there must be considered. To understand the underlying mechanisms governing Taylor flow heat transfer, the interaction of the bubble film with the overtaking slug and heat transfer directly from the wall to the recirculating slug are investigated in detail below.

The flow pattern in the slug region, which can be expected to influence the apparent heat transfer coefficient for that region, is well known to depend on the fluid properties as expressed in terms of the Capillary number, *Ca*. Primarily, the dimensionless thickness of the bubble film increases with increasing *Ca*, as expressed in Eqs (4.6) and (4.7). This effect is accompanied by a decrease in the size and intensity of the recirculation zone that arises in the slug when viewed in a frame of reference moving with the bubble. Oliver and Wright (1964) observed that the heat transfer enhancement brought by Taylor flow decreased with increasing film thickness. Thulasidas *et al.* (1997) found that a smaller, slower recirculation zone accompanied thicker films, leading to less intensive transport of hot fluid from region near the wall to the tube centre. This picture is also clear in recent CFD simulations (Fukagata *et al.*, 2007, Lakehal *et al.*, 2008, Gupta *et al.*, 2010).

6.4.1 Size and efficiency of recirculation inside the liquid slug

The velocity profile within a slug develops from a relatively flat profile at the bubble nose to a parabolic profile in the middle for a sufficiently-long slug (Thulasidas *et al.*, 1997, Kreutzer *et al.*, 2001, Fukagata *et al.*, 2007, Lakehal *et al.*, 2008, Gupta *et al.*, 2010). Following Thulasidas *et al.* (1997), the velocity profile for a sufficiently long liquid slug is simply that for fully-developed pipe flow in a frame of reference moving with the bubble

$$v(r) = 2U_{TP}\left(1 - \left(\frac{r}{R}\right)^2\right) - U_B \tag{6.4}$$

where $v(r)$ is the relative velocity inside the liquid slug; r and R are the radial position and radius of the channel, respectively. It is important to note here that the average velocity at any cross-section of the channel is the sum of the gas and liquid superficial velocities (U_{TP}) (Suo and Griffith, 1964). For $U_B < 2U_{TP}$, there must be a radial position, r_0, where $v(r)$ is zero

$$r_0 = \frac{R}{\sqrt{2}}\sqrt{2 - \frac{U_B}{U_{TP}}} \tag{6.5}$$

Furthermore, there is a radial position, r_1, dividing the closed-streamlines in the recirculation zone from the open-streamlines in the film layer. Since the liquid is recirculating inside the dividing streamline ($r < r_1$), the net axial volumetric flow inside the dividing streamline must be zero

$$\int_0^{r_1} 2\pi r \left[2U_{TP}\left(1 - \left(\frac{r}{R}\right)^2\right) - U_B\right] \mathrm{d}r = 0 \tag{6.6}$$

from which:

$$r_1 = R\sqrt{2 - \frac{U_B}{U_{TP}}} \tag{6.7}$$

The radial positions of the recirculation centre, r_0, and the dividing streamline, r_1, separating the recirculation zone from the wall film layer are shown in Figure 6.5. From Eqs. (6.5) and (6.7), both r_0 and r_1 are functions of the velocity ratio only, and therefore, in the absence of inertial and gravitational effects, of *Ca* only.

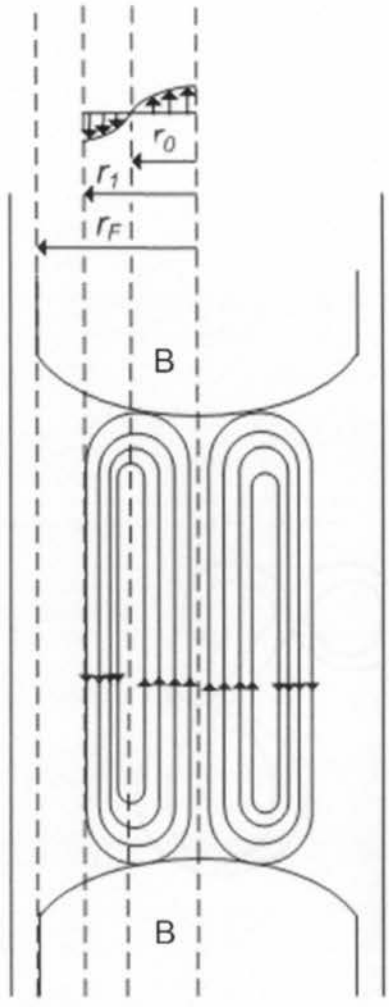

Figure 6.5: Schematic of the recirculation zone inside the slug and the radial locations of the recirculation centre, r_0, dividing streamline r_1 and gas/liquid interface r_F.

The slug recirculation zone impacts on the heat transfer process in the slug through interaction with the wall film. In the frame of reference moving with the bubble, the bubble film flows into the head of the slug with velocity $U_F - U_B \sim -U_B$ through the annular bubble film of thickness δ_F, expanding to thickness $R - r_1$ before contracting again to leave at the back of the slug. The recirculation flow rate relative to the wall film flow rate provides an indication of how well the energy in the wall film can be distributed to the bulk. A Recirculation number, ϕ, which compares the recirculation flow rate and the bypass flow rate in the liquid film is defined as

$$\phi = \left|\frac{\text{flowrate}_{\text{recirc}}}{\text{flowrate}_{\text{bypass}}}\right| = \left|\frac{\int_0^{r_0} 2\pi r\left[2U_{TP}\left(1-\left(\frac{r}{R}\right)^2\right)-U_B\right]\mathrm{d}r}{\int_{r_1}^{R} 2\pi r\left[2U_{TP}\left(1-\left(\frac{r}{R}\right)^2\right)-U_B\right]\mathrm{d}r}\right| = \frac{\left(2-\frac{U_B}{U_{TP}}\right)^2}{4\left(\frac{U_B}{U_{TP}}-1\right)} \quad (6.8)$$

Figure 6.6 shows the variation of the radial positions of the recirculation centre, r_0, the dividing streamline, r_1, and the gas-liquid interface in the fully-developed film region, $r_F = R - \delta_F$, and the Recirculation number, ϕ, with the Capillary number (Ca). The velocity ratio (U_B/U_{TP}) in Eq. (6.8) is estimated using Eqs. (4.5) and (4.6), with the calculated value at the corresponding Capillary number also shown in Figure 6.6. It can be clearly seen that the size of the recirculation zone decreases (decreasing values of r_0, r_1) with increasing U_B/U_{TP} and disappears when the value of U_B/U_{TP} reaches two. The shrinkage of the recirculation zone with increasing Ca was also reported experimentally (Thulasidas *et al.*, 1997), analytically (Taylor, 1961, Giavedoni and Saita, 1997), and computationally (Edvinsson and Irandoust, 1996, Feng, 2009). As Ca increases, the Recirculation number decreases exponentially from infinity at Ca = 0, where there is no film separating the bubble from the wall and the recirculation zone covers the whole liquid slug ($r_1 = r_F = R$), to a value of zero when the recirculation zone disappears ($r_1 = 0$). For the present study, the Recirculation number follows the order, W > EG/W > EG, which is in accordance with the increasing Capillary number of the working fluids.

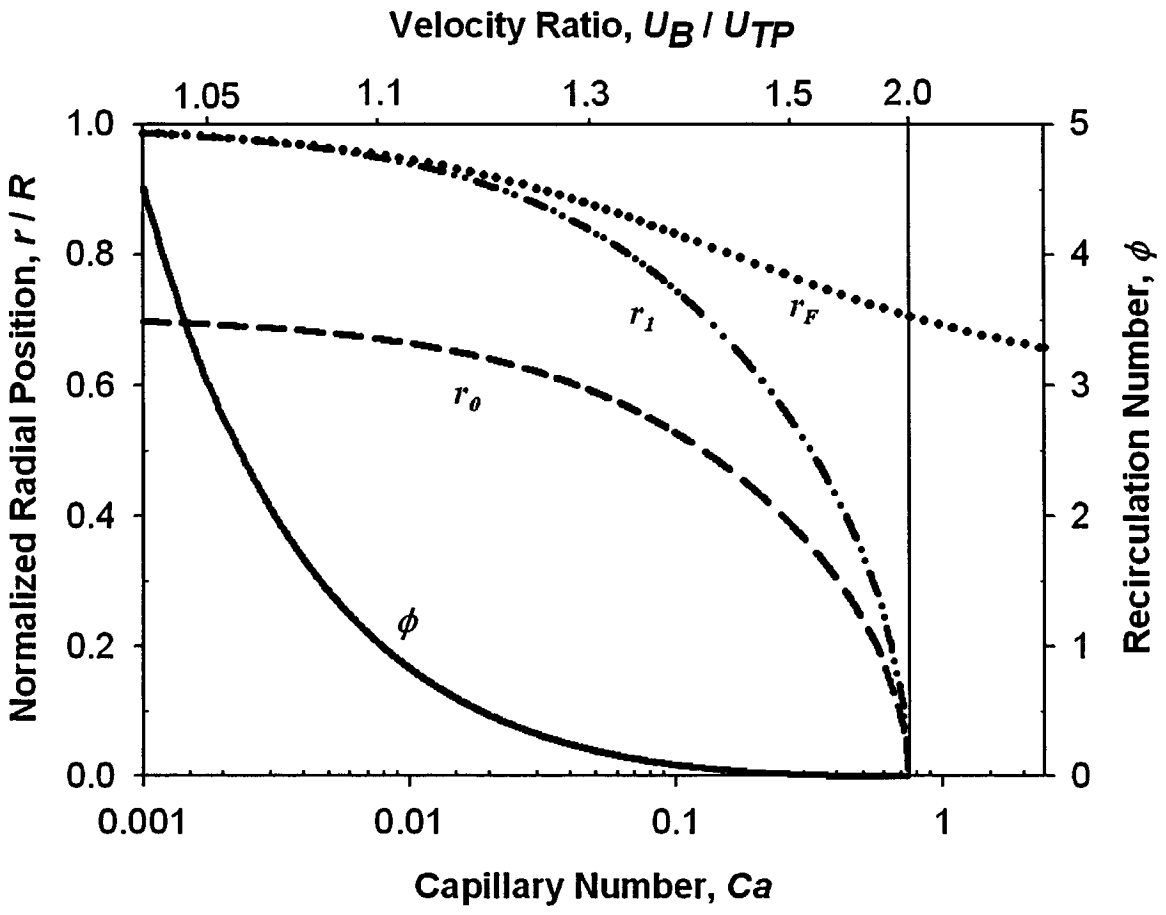

Figure 6.6: Locations of the recirculation centre, r_0, and dividing streamline, r_1, and the gas-liquid interface in the fully-developed film region, r_F, and the Recirculation number, $\emptyset$, as a function of the Capillary number and velocity ratio (U_B/U_{TP}) estimated using Eqs. (4.5) and (4.6).

6.4.2 General model for Taylor flow heat transfer

From Figure 6.4 it can be noted that the apparent slug Nusselt number (Nu_L^*) tends to a limit with increasing dimensionless slug length, which is apparently close to the value for fully-developed, single-phase laminar flow (Nu_{LO}) when $L_S^* \rightarrow \infty$. A combination of the influences of the dimensionless slug length (L_S^*) and the flow pattern in the slug region, which can be expressed in terms of the Capillary number (Ca), an empirical correlation for the heat transfer to the liquid slug is suggested as

$$Nu_L^* = Nu_{LO} + c_3(L_S^*)^p(Ca)^q \tag{6.9}$$

where the values of the constant c_3, and exponents p and q are determined by least-squares fitting to be $c_3 = 0.13$, $p = -0.46$ and $q = -0.30$. The exponent on L_S^* is consistent with expectations for developing laminar flow while that on Ca indicates the enhancing effect of having stronger recirculation at lower values of Ca. Figure 6.7 compares the experimental data with the correlation and a good agreement is achieved, with the broken lines indicating a 95% confidence interval for a relative standard deviation of 14%. Extrapolation of Eq. (6.9) to large Ca and/or L_S^* values is probably safe, but applying it to flows with very short slugs ($L_S^* < 10^{-4}$) or very low Capillary numbers ($Ca < 10^{-3}$) should be treated with care.

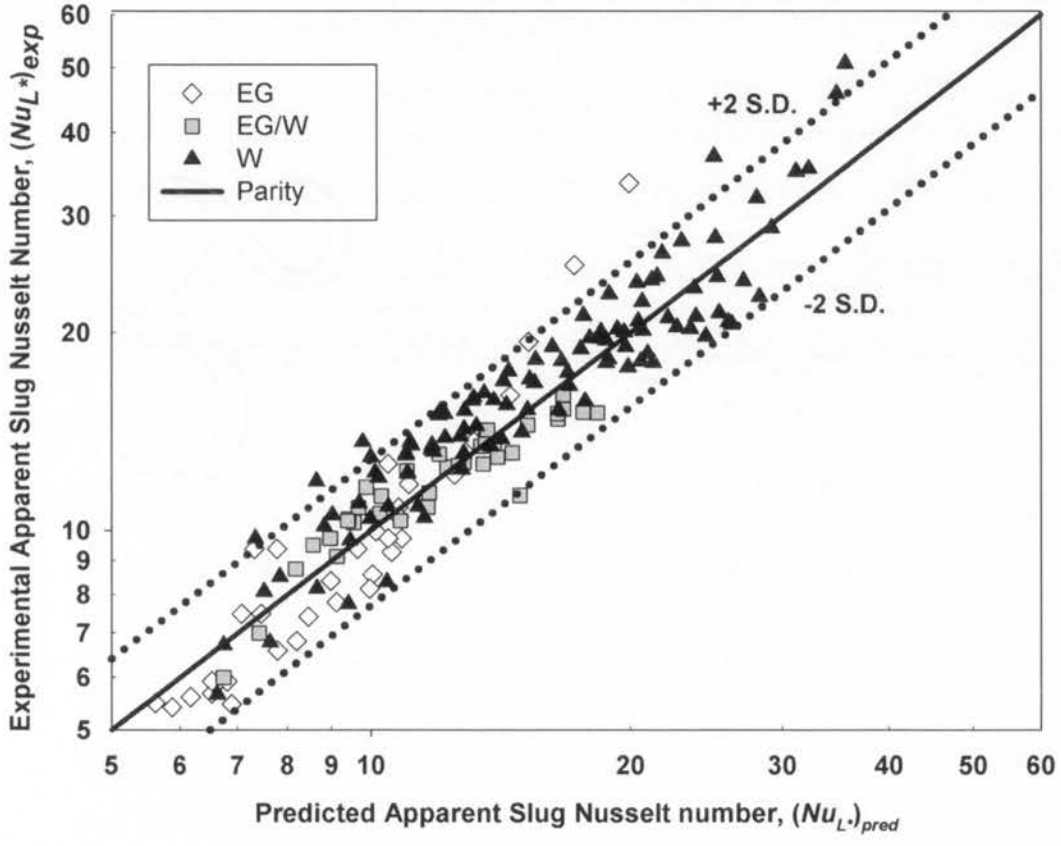

Figure 6.7: Comparisons of the apparent slug Nusselt number between the experimental data and the predicted values obtained from Eq. (6.9).

6.5 Summary

Three physical mechanisms governing the heat transfer of Taylor flow were suggested. Depending upon the wall boundary conditions imposed on the system, under thermally fully-developed conditions the bubble film plays different thermal roles: largely irrelevant for a constant wall temperature boundary but a significant energy storage region for a constant wall heat flux boundary, with that energy being taken up by mixing with the overtaking slug. Regardless of the boundary condition, heat transfer is controlled mainly by the slug region, with the overall heat transfer coefficient being that for the slug multiplied by the fraction of the tube occupied by the slug.

Due to the high popularity and potential for industrial use of water as the liquid phase for Taylor flow heat transfer, a correlation was first developed based on experimental data obtained for the water system. The flow in the slug region is a developing laminar flow and the slug heat transfer coefficient ($Nu_L^* = Nu_{TP}L_{UC}/L_S$) is found to be well correlated by a dimensionless slug length equivalent to an inverse Graetz number based on the slug length ($L_S^* = L_S/(Re_{TP} \cdot Pr \cdot d)$). As the slug heat transfer coefficient is found to follow closely with the theoretical mean Nusselt numbers for thermally developing laminar pipe flow, a Hausen-type correlation successfully describes the data, with most experimental data from the literature and from this work falling within 20% of the proposed model.

The validity of the correlation for general application was examined through comparisons with existing data in the literature for both constant wall heat flux and constant wall temperature boundary conditions, as well as with heat transfer data collected in this study using other liquid phase fluids. It is suggested that a constant wall temperature boundary condition is accompanied by a decrease of approximately 15% in the slug heat transfer coefficient relative to the constant wall heat flux condition. The correlation developed based only on results using water as the liquid phase was apparently not providing an accurate description for other fluids. Nonetheless, it is found that the result for individual fluid follows the general form for heat transfer in developing laminar flow, with $Nu_{L^*} = f(L_S^*)$ specific to each fluid.

When a constant wall heat flux is imposed on the system, interactions between the bubble film and the recirculating flow in the slug and heat transfer from the wall in the slug region depend strongly on the flow pattern in that region. The size of the recirculation zone and the

recirculation efficiency, which are important parameters for Taylor flow heat transfer, are found to be strong functions of the Capillary number.

Taking account of all of the identified important dimensionless groups, including the apparent slug Nusselt number, the dimensionless slug length and the Capillary number, an empirical correlation (Eq. 6.9) was proposed for the heat transfer of Taylor flow. Good agreement between the experimental data and the correlation was achieved, as indicated by the small relative standard deviation (14%).

Chapter 7

Taylor Flow in Horizontal Microchannels

As the channel size is reduced to the millimetre scale, the surface tension force becomes more important than the gravitational force and limited gravitational effects have been observed in previous experimental studies (Triplett *et al.*, 1999a, Waelchli and von Rohr, 2006). Therefore, a significant number of CFD simulation studies of the hydrodynamics, mass and heat transfer characteristics of Taylor flow in microchannels are based on the assumption of two-dimensional, axisymmetric flow (Kreutzer *et al.*, 2001, Taha and Cui, 2004, Akbar and Ghiaasiaan, 2006, Gupta *et al.*, 2010b). As discussed in the literature review presented in Chapter 2, however, a few recent analytical, numerical and experimental results have shown that the gravitational force can play a role in Taylor flow in millimetre-size horizontal channels for certain flow conditions.

Han and Shikazono (2009) reported experimentally that the liquid film thickness at the bottom immediately after the transition region was greater than that at the side by 5% or more in a 1.3 mm channel ($Bo \sim 1.9$, $Ca < 0.4$), but no significant difference was observed in a 0.3 mm channel ($Bo \sim 0.1$, $Ca < 0.4$). Gupta *et al.* (2010c) also showed experimentally and computationally that the bubble shapes were asymmetric for flow in a ~2 mm horizontal channel under the conditions they studied ($Bo \sim 0.915$, $0.024 < Ca < 0.262$ and $8 < Re_{TP} < 80$). They further reported a drianage flow from the channel top to the bottom, causing gradual changes in the thicknesses of the top and bottom films which gave rise to bubble asymmetry. Recently, Grotberg and co-workers (Suresh and Grotberg, 2005, Zheng *et al.*, 2007) demonstrated bubble shape distortions and flow interactions between the upper and lower regions about the channel axis for horizontal flow with non-negligible gravitational effect.

Since both the film thickness of the liquid film around the gas bubble and the flow field in the liquid slug are key parameters for Taylor flow heat and mass transfer, bubble asymmetry and flow interactions between the upper and lower halves of the liquid slug caused by gravity may have considerable effects on the resulting transport rates. A good understanding of the conditions where gravity ceases to be important, therefore, becomes important for better application designs. In this chapter, the effects of gravity in millimetre-size horizontal

channels are examined experimentally by performing visualization experiments over wide ranges of Bond ($0.287 < Ca < 1.028$) and Capillary ($0.038 < Ca < 0.193$) numbers. Heat transfer experiments for horizontal Taylor flow were also conducted using the multi-block heating system as that used for the vertical Taylor flow heat transfer experiments ($d = 2.00$ mm and $Bo = 0.915$). The detailed experimental setup and techniques are discussed in Chapter 3. Section 7.1 provides details of the working conditions. Results obtained from the brightfield microscopy and μPIV experiments are presented in Section 7.2 and 7.3, respectively. In Section 7.4, a simple fluid dynamics model is proposed to describe the drainage flow observed in the experiments and comparisons between the analytical solution and the experimental data are made. The heat transfer rates for horizontal and vertical Taylor flow are compared in Section 7.5.

7.1 Working conditions

For systematic examination of the flow parameters governing the bubble behaviour under the effect of gravity, visualization experiments were performed using three millimetre-sized channels of different internal diameters (d = 1.12, 1.69 and 2.12 mm corresponding to $Bo = 0.287$, 0.653 and 1.028) at various mixture velocities ($0.09 < U_{TP} < 0.45$ m s^{-1}) and homogeneous void fractions ($0.09 < \beta < 0.9$). Nitrogen and ethylene glycol were used as the gas and liquid phases, respectively. All visualization experiments were conducted under isothermal condition (21 °C) using the setup described in Chapter 3 and recordings were made near the end of the test section (~300 mm from the entrance). As discussed in Chapter 3, the pressure drop along the test section leads to bubble expansion and change of the mixture velocity between the entrance and the exit of the test section. The mixture velocity at the visualization point was estimated based on the pressure drop from the entrance with a maximum uncertainty of 15%. Table 7.1 gives the properties of the test fluids at 21 °C and atmospheric pressure and Table 7.2 shows the ranges of flow parameters studied and the related dimensionless numbers based on the liquid properties.

The bubble velocity, U_B, bubble length, L_B, slug length, L_S, and bubble frequency, F_B were determined by performing a frame-by-frame analysis of the image data, as described in Chapter 3. Regular and repeatable Taylor flow patterns were confirmed by small standard deviations (less than 10%) of the bubble and slug lengths which were obtained over a hundred bubbles and slugs.

Table 7.1: Properties of ethylene glycol and nitrogen at 21 °C and atmospheric pressure.

Fluid	Density ($kg\ m^{-3}$)	Viscosity ($kg\ m^{-1}\ s^{-1}$)	Surface tension ($N\ m^{-1}$)
Ethylene glycol	1114	2.04×10^{-2}	0.0477
Nitrogen	1.160	2.08×10^{-5}	

Table 7.2: The operating conditions and related dimensionless numbers.

Parameters	Range		
Tube diameter, d (mm)	1.12	1.69	2.12
Mixture velocity, U_{TP} ($m\ s^{-1}$)	0.17	0.11, 0.18	0.09-0.45
Homogeneous void Fraction, β	0.47	0.48	0.09-0.90
Bond number, Bo	0.287	0.653	1.028
Reynolds number, Re_{TP}	10	10, 17	10-52
Capillary number, Ca	0.071	0.046, 0.076	0.038-0.193

7.2 Brightfield Microscopy

Using ethylene glycol as the RIM liquid and the liquid phase, the curvature effects arising from both the outer and inner tube walls were minimized as the refractive index of ethylene glycol (1.432) is almost the same as that of the silica tube (1.459). As seen in Figure 7.1 (a), a well-defined gas-liquid interface is visible to allow direct measurement of the liquid film thickness and digitization of the bubble shape. Figure 7.1 (b) compares the digitized interfaces for the top and bottom halves of the bubble on the vertical plane passing through the channel axis. For better comparison, the digitized bubble interface obtained at $\theta = 90°$ is also shown in Figure 7.1 (b), where the film thickness remains relatively constant for regions far away from the bubble ends. As seen in Figure 7.1, the bubble obtained in the 2.12 mm horizontal channel (Bo = 1.028) at Re_{TP} = 10, Ca = 0.038, β = 0.47 is clearly asymmetric,

indicating a non-negligible gravitational effect on the bubble shape. While the bottom film thickness increases gradually, the top film thickness decreases from the bubble nose to tail. In addition, the bubble tail is deformed noticeably, making the bubble longer at the top and shorter at the bottom. The asymmetric bubble head and tail observed here are consistent with the analytical results reported by Suresh and Grotberg (2005) who studied the effect of gravity on the shapes of the bubble head and tail in a two-dimensional liquid-lined microchannel for non-vertical channel orientations. They showed the balance of forces for the upper interface was different from that for the lower interface when the gravitational effect is non-negligible and obtained asymmetric bubble heads and a tilted bubble tails for $Bo > 0$ and non-vertical orientations.

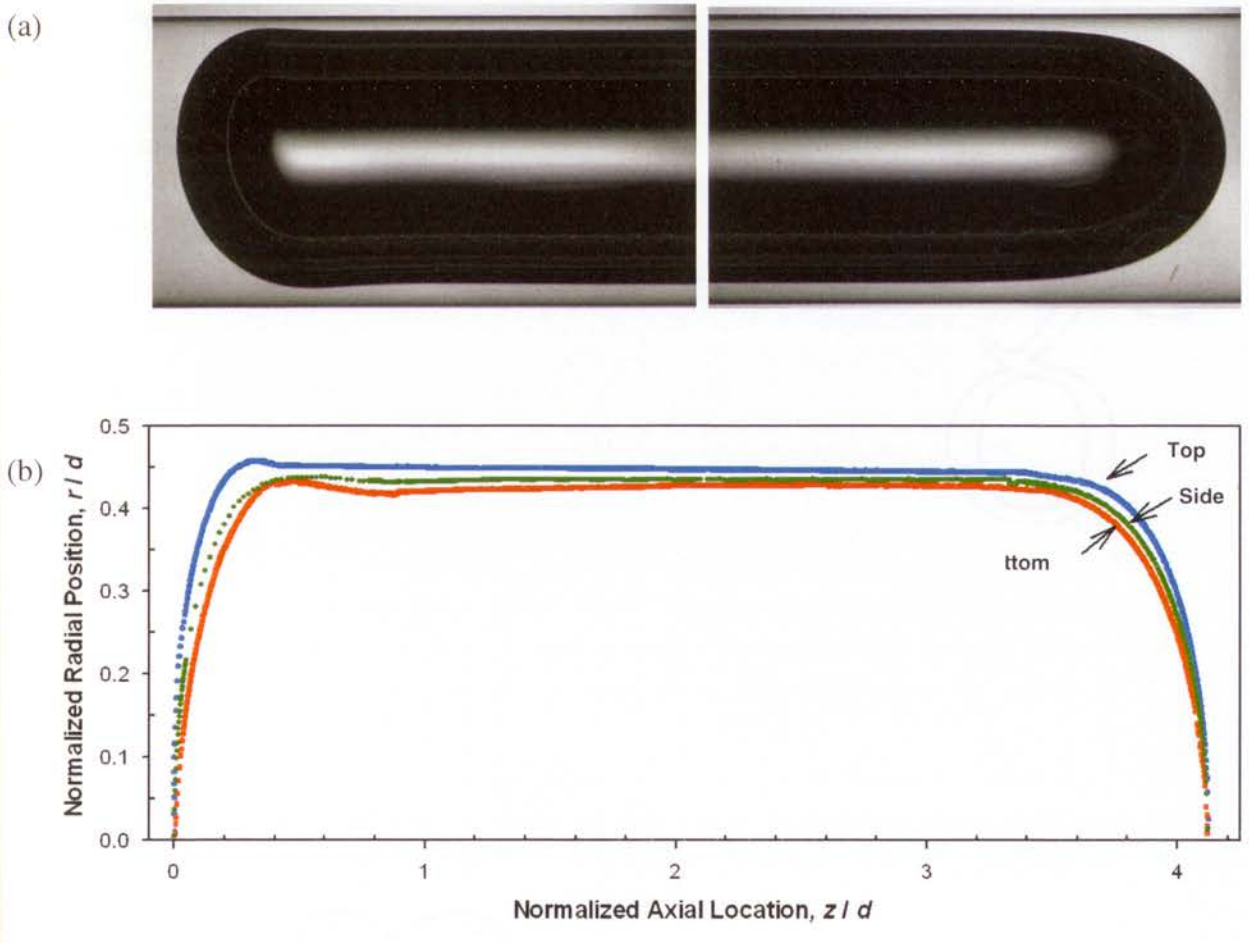

Figure 7.1: (a) Bubble shape observed in a 2.12 mm horizontal channel and (b) the digitized bubble interface on the vertical plane (Bo = 1.028, Re_{TP} = 10, Ca = 0.038, β = 0.47).

7.2.1 Effects of Bond number

Figure 7.2 shows the variations of the normalized top and bottom film thicknesses along the normalized bubble length about the vertical plane for flows with similar Ca (~0.073) and Re_{TP} (~15) for three different channel diameters to yield different Bond numbers (d = 1.12, 1.69 and 2.12 mm giving Bo = 0.287, 0.653 and 1.028). Due to the effect of gravity, liquid drains circumferentially from the top to the bottom in the liquid film. The drainage effect accumulates along the bubble to cause the thickness of the top film to decrease and that of the bottom film to increase linearly along the bubble for regions away from the bubble ends. Therefore, the difference in thickness between the top and bottom films at the bubble tail then becomes more pronounced as the bubble becomes longer.

According to de Ryck (2002), the normalized film thickness is a function of Capillary number only for negligible gravitational and inertial effects. Since the Capillary numbers were kept relatively constant and the ratios of the Reynolds to Capillary numbers, Re_{TP}/Ca, were small enough ($200 < Re_{TP}/Ca < 400$) to ignore the inertial effect, the initial film thicknesses and hence the shapes of the bubble nose should be similar if the gravitational effect is insignificant in all channel sizes studied. As seen in the enlarged nose region in Figure 7.2, the bubble noses obtained from the 1.12 and 1.69 mm channels are almost symmetric, whereas that obtained from the 2.12 mm channel loses its symmetry. Similar experimental observations were reported by Jensen *et al.* (1987). They highlighted that the Taylor bubble nose in a horizontal channel became asymmetric at high Bond numbers ($Bo >$ 1) and small Capillary numbers ($Ca < 0.1$), for which the film became thicker and the length of the transition region became longer at the bottom interface.

Since the bubble lengths obtained for the three Bond numbers are different, direct comparison of the degree of bubble asymmetry at the tail region does not provide a good indication of the effect of Bo on the drainage flow. Alternatively, the Bo effect is examined by comparing the gradients of the film thicknesses ($\Delta\delta_F/\Delta z$) in the linear region. The gradients of the bottom films in the 2.12 mm (Bo = 1.028) and the 1.69 mm (Bo = 0.653) channels are found to be 4.7 and 2.8 times higher than that observed for the 1.12 mm channel (Bo = 0.287), respectively, indicating a stronger gravitational effect in larger channels.

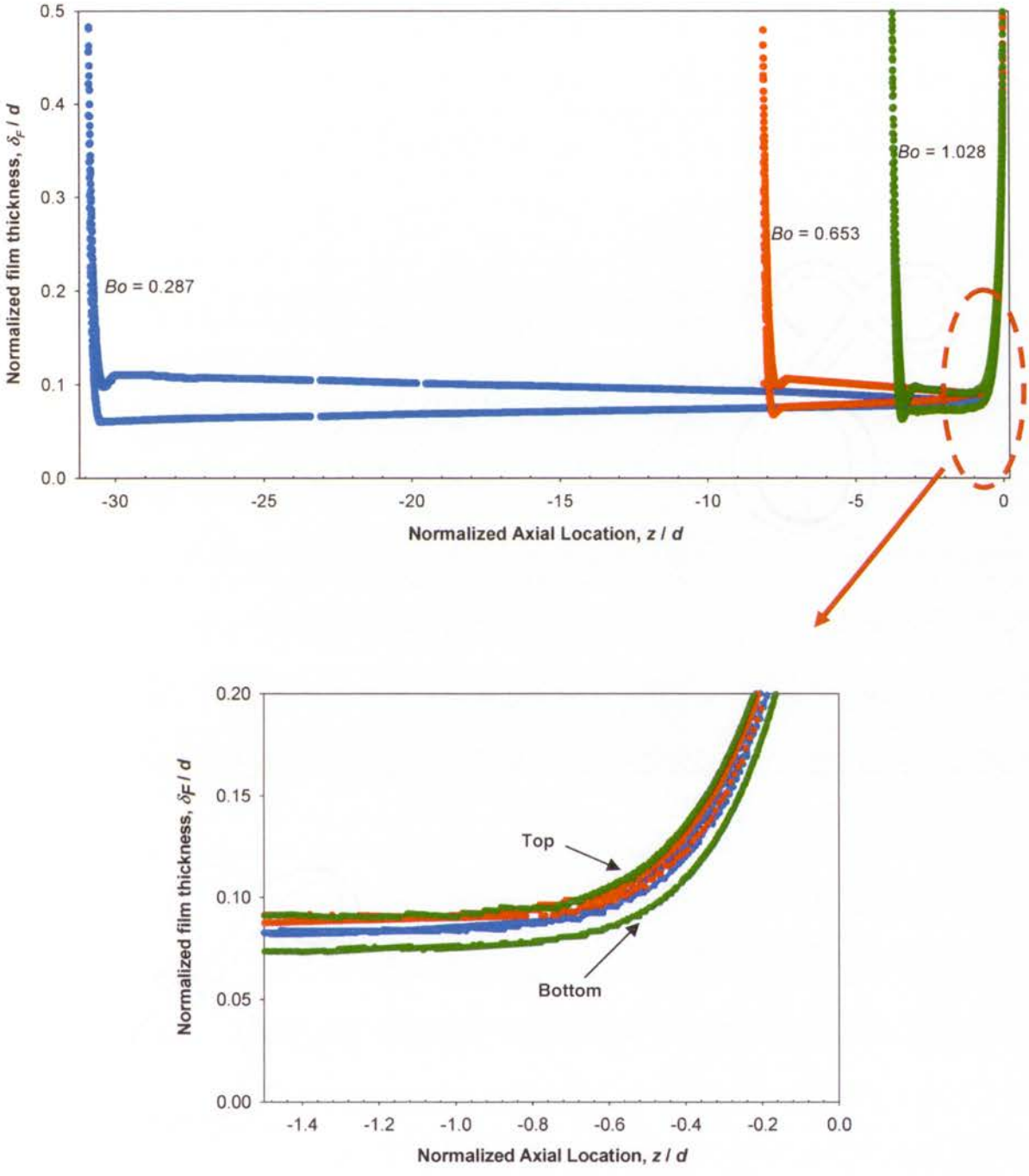

Figure 7.2: Effect of Bond number on the variation of the top and bottom film thickness for flow with similar Capillary (~0.073) and Reynolds (~15) numbers. The bubbles are aligned at the bubble nose.

7.2.2 Effect of bubble length

Since the bubble length has been identified as affecting the degree of bubble asymmetry (difference between the thicknesses of top and bottom films), bubbles of different lengths ($1.9 < L_B/d < 20.7$) were generated by varying the homogeneous void fraction ($0.09 < \beta < 0.9$)

at fixed Bo, Re_{TP} and Ca. As seen in Figure 7.3, the asymmetric shape of the bubble noses caused by gravity is independent of the bubble length. Also, the gradients of the film thicknesses away from the bubble ends are similar for bubbles of different lengths. This suggests that the drainage flow caused by gravity is independent of the bubble length. However, the amount of liquid drained from the top to the bottom increases with the bubble length to give larger differences between the top and bottom film thickness at the bubble tail for longer bubbles.

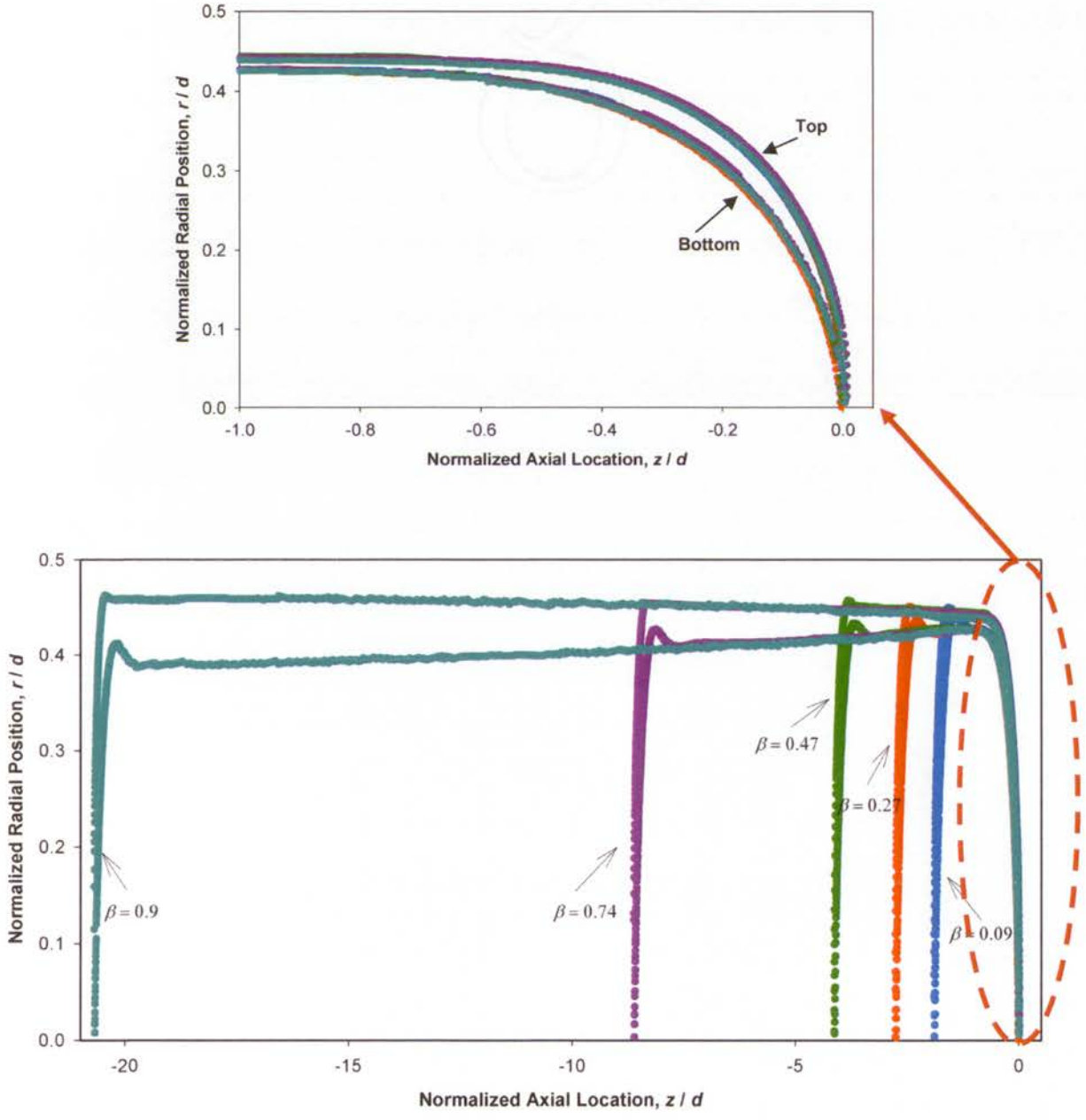

Figure 7.3: Comparisons of bubble shape for superimposed bubble noses on the vertical centre plane for different values of β at Bo = 1.028, Ca = 0.038 and Re_{TP} = 10.

7.2.3 Effect of Capillary number and Reynolds number

As shown in Figure 7.4, the bubbles obtained from the 2.12 mm channel (Bo = 1.028) for four different mixture velocities are all asymmetric on the vertical plane under the effect of gravity. As the mixture velocity increases (increasing Ca and Re_{TP}), the bubble head becomes sharper, while the bubble tail becomes flatter to attain a bullet-shape. As U_{TP} increases from 0.09 to 0.45 m s^{-1}, the bubble length decreases from 8.74 to 4.23 mm. The decreasing bubble length is due to the combination of the slightly decreasing value of β and the increasing value of Ca. The bubble size was reported to be inversely proportional to the Capillary number for bubbles generating in the shearing regime, $Ca > 0.02$ (Thorsen *et al.*, 2001, Xu *et al.*, 2008).

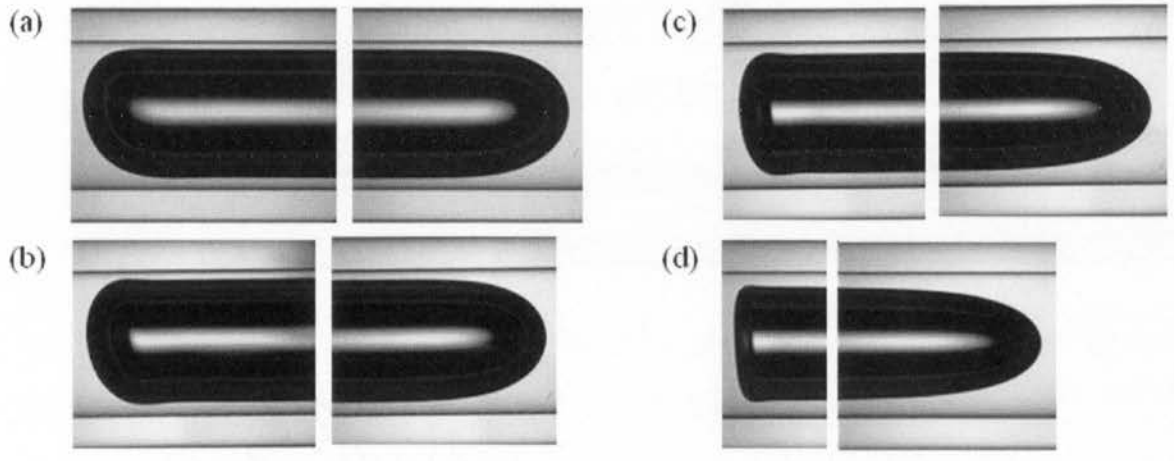

Figure 7.4: Bubble shapes obtained using a 2.12 mm channel (Bo = 1.028) for different mixture velocities (a) 0.09 m s^{-1} (β = 0.47, Re_{TP} = 10, Ca = 0.038), (b) 0.17 m s^{-1} (β = 0.45, Re_{TP} = 20, Ca = 0.073), (c) 0.32 m s^{-1} (β = 0.41, Re_{TP} = 37, Ca = 0.136), (d) 0.45 m s^{-1} (β = 0.37, Re_{TP} = 52, Ca = 0.193).

The effects of gravity on the bubble shape for different mixture velocities are shown more explicitly in Figure 7.5. For constant Bo, the difference between the top and bottom films decreases with increasing Ca, which is consistent with the results reported by Jensen *et al.* (1987). The linear variations of the top and bottom film thicknesses along the bubble due to gravity are more apparent for long bubbles obtained at low mixture velocities (case 7.4 (a-c)). For short bubbles obtained at high mixture velocity (case 7.4 (d)), the thicknesses of both the top and bottom films diminish smoothly from the nose to the tail as the length of the transition region becomes comparable with the bubble length at high value of Ca (de Ryck,

2002, Taha and Cui, 2004, Feng, 2009). Also, the variation of the difference between the top and bottom interfaces along the bubble is less apparent. This is because the liquid film thickness decreases rapidly in the transition region which masks the effect of the accumulation of liquid drainage from the channel top to bottom as observed in the long bubbles.

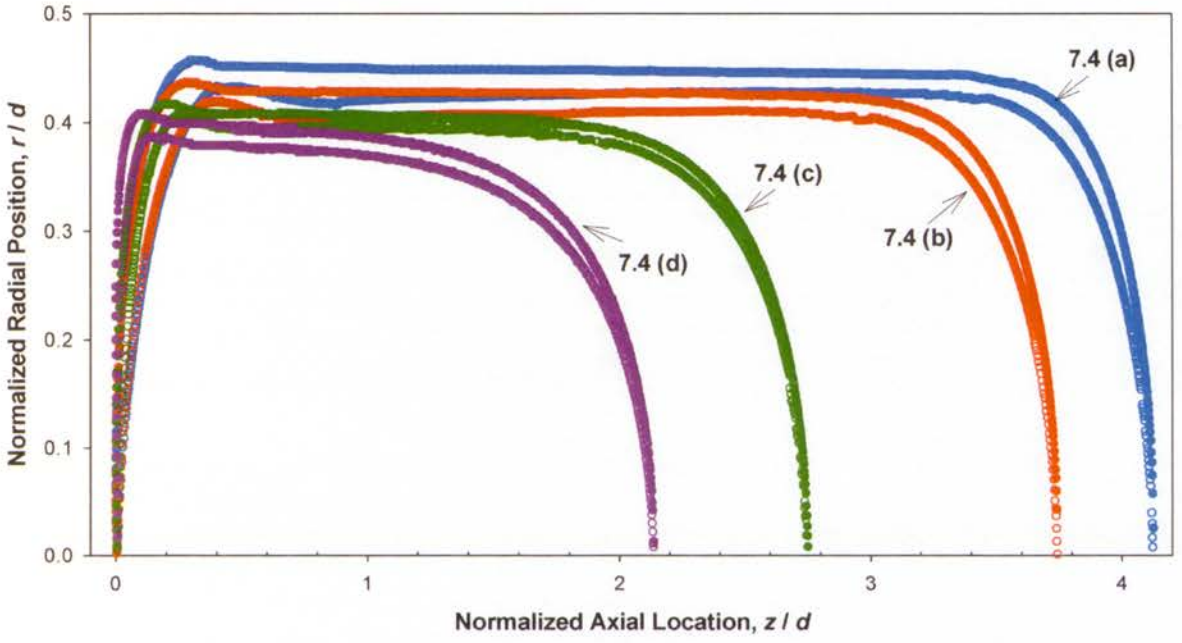

Figure 7.5: Comparisons of bubble shapes on the vertical plane obtained using a 2.12 mm horizontal channel (Bo = 1.028) for different mixture velocities.

7.2.4 Variation of film thickness in the circumferential direction

The variation of the film thickness in the circumferential direction was investigated by recording backlit images at different circumferential positions as indicated in Figure 3.14. Since the drainage flow is symmetric about the vertical plane passing through the tube centre, the information obtained from circumferential positions in the 180°–270° region is reflected to the 90°–180° regions. For bubbles with a relatively constant film thickness region, the normalized film thickness obtained at 1d from the bubble nose is depicted in Figure 7.6. For short bubbles without such a region (case 7.4 (d)), the reported film thickness was obtained near the bubble tail. As liquid drains from the top to the bottom in the circumferential direction, the normalized film thickness increases continually from the top to the bottom for this set of study conditions.

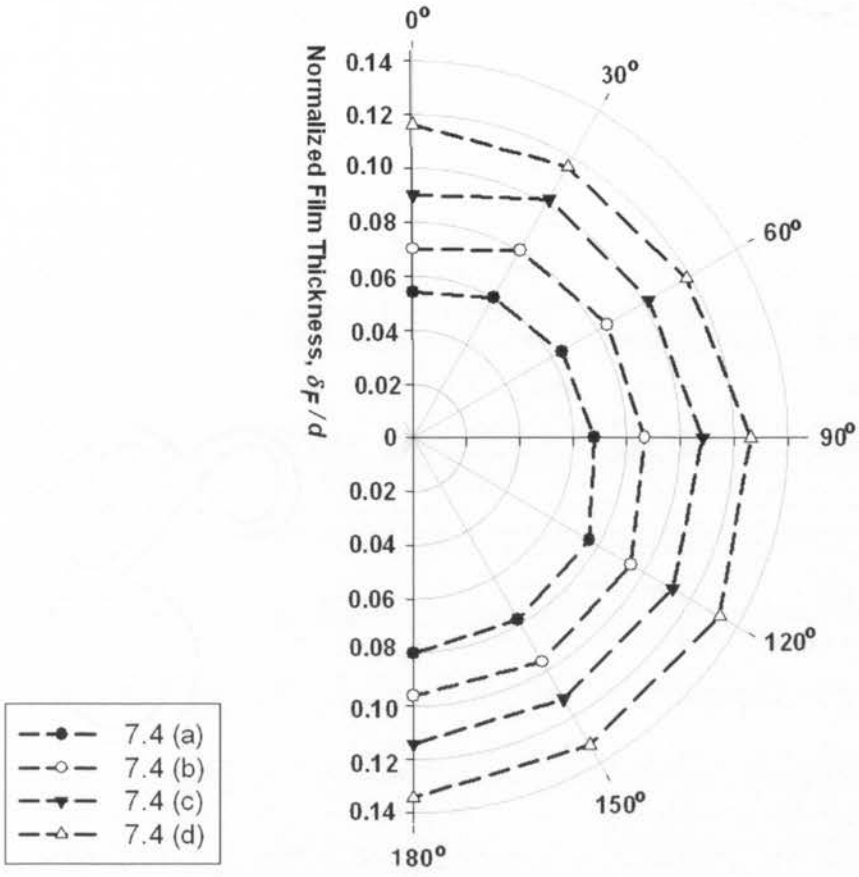

Figure 7.6: Variation of normalized film thickness in the circumferential direction from the top to the bottom with the film thickness obtained 1*d* from the bubble nose for cases 7.4 (a) to (c) and near the bubble tail for case 7.4 (d).

The normalized film thickness is also compared with the correlations suggested by Aussillous and Quéré (2000) (Eq. 4.6) and Irandoust and Andersson (1989a) (Eq. 4.7) in Figure 7.7. The film thickness is found to increase with increasing *Ca* for all circumferential positions. For the same *Ca*, the normalized film thicknesses at different circumferential positions vary between the prediction of Eq. (4.6) and Eq. (4.7) which give better representations for the thicknesses of top and bottom films, respectively. It is believed that this observation is just a coincidence without any mechanistic reason as Eq. (4.6) was derived semi-analytically for cases with negligible inertia and gravity and Eq. (4.7) is an empirical correlation derived over a wide range of operating conditions, with neither of them taking the effect of gravity into account in their derivations.

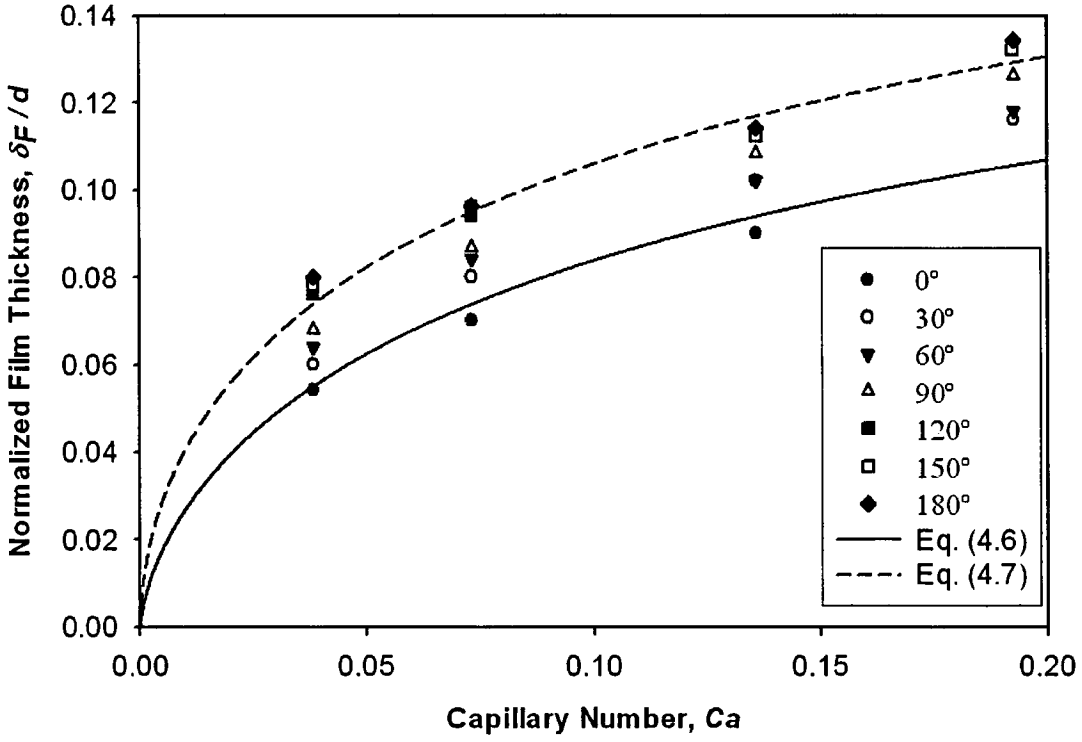

Figure 7.7: Comparisons of the normalized film thickness obtained at various circumferential positions with Eq (4.6) and Eq (4.7). The experimental film thicknesses were obtained from the bubble nose for cases 7.4 (a) to (c) and near the bubble tail for case 7.4 (d).

7.3 μPIV measurements

As seen in the brightfield microscopy results, significant distortions of the bubble symmetry for some conditions were noted. The flow field in the liquid film region leading to such asymmetric bubble shape was visualized using the μPIV technique as described in Chapter 3. In addition to the flow field in the film region, the effect of gravity on the flow pattern inside the liquid slug was of interest, as any gravity-induced flow interactions between the upper and bottom halves of the liquid slug may lead to significant changes in the resulting heat and mass transfer rates. Therefore, μPIV measurements were also performed in the slug region to characterize the flow pattern there.

7.3.1 Drainage flow in the liquid film

Figure 7.8 shows the temporal variation of the magnitude of the vertical (drainage velocity) and horizontal (axial velocity) components of velocity at $\theta = 90°$ (i.e. horizontal plane) at

different distances from the wall for horizontal flow using a 2.12 mm channel (Bo = 1.028) for U_{TP} = 0.09 ms^{-1} (Re_{TP} = 10, Ca = 0.038) and β = 0.47. In order to capture the velocity data in the film around the bubble region, the PIV settings were optimized for the low film velocities during the passage of a bubble. Therefore, during the passage of a liquid slug, the velocity data are discarded. Periodic variation, where the drainage velocities are higher at the bubble nose and decrease steadily towards the tail, is observed. It is also noted that the drainage velocities are higher for positions further away from the wall and closer to the gas-liquid interface. These are consistent with the computational results reported by Gupta *et al.* (2010c), who showed that the tangential velocity near the bubble nose was higher than that at the bubble tail and increased from the wall towards the interface.

The axial film velocities during the passage of a bubble for a region far from the bubble ends are much smaller than the drainage velocities in the laboratory frame of reference, as seen in Figure 7.8. Alternatively, in the frame of reference moving with the bubble, the liquid film is moving quickly from front-to-back of the bubble with a velocity $U_F - U_B \sim -U_B$, providing the source of the fluid that drains along the bubble. Rather than the bubble rising with time, it is tilted with the head pointing towards the centre as the balance of forces varies along the bubble. Therefore, the drainage flow in the liquid film is continuous and steady.

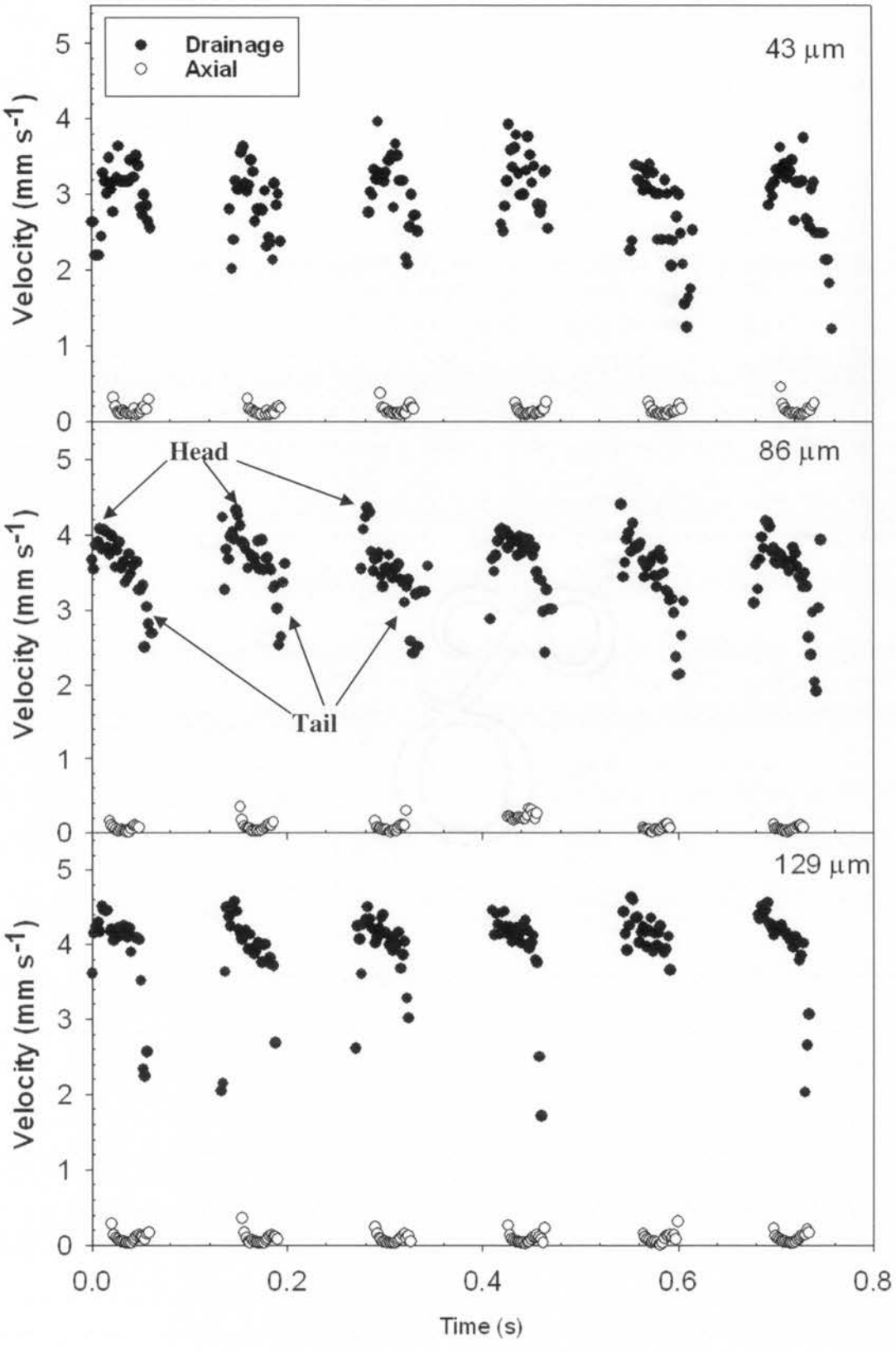

Figure 7.8: Transient recording of liquid film drainage and axial velocities in a 2.12 mm horizontal channel (Bo = 1.028) for U_{TP} = 0.09 ms^{-1}, (Re_{TP} = 10, Ca = 0.038) and β = 0.47 at a distance of (a) 43 μm, (b) 86 μm and (c) 129 μm from the wall.

7.3.2 Flow field inside the liquid slug

For Taylor flow with $U_B < 2U_{TP}$ and negligible gravitational effect, two symmetric counter-rotating vortices about the channel axis inside the liquid slug are present in a reference frame moving with the bubble (Taylor, 1961, Thulasidas *et al.*, 1997). As discussed in Chapter 6, the size of the recirculation zone inside the liquid slug (recirculation centre, r_0, and the dividing streamline, r_1) can be expressed solely as a function of the Capillary number, in the absence of gravitational and inertial effects. However, this may not be the case when the gravitational force is not negligible. Recently, Zheng *et al.* (2007) showed computationally the dependence of the size and number of vortices present in the liquid slug on the Bond number and the flow parameters, including the Capillary number, slug length and flow orientation. They also reported that gravity causes flow of the liquid from the upper liquid film near the nose to the liquid film at the tail of the preceding bubble through the liquid slug core, as shown in Figure 2.9.

(a)

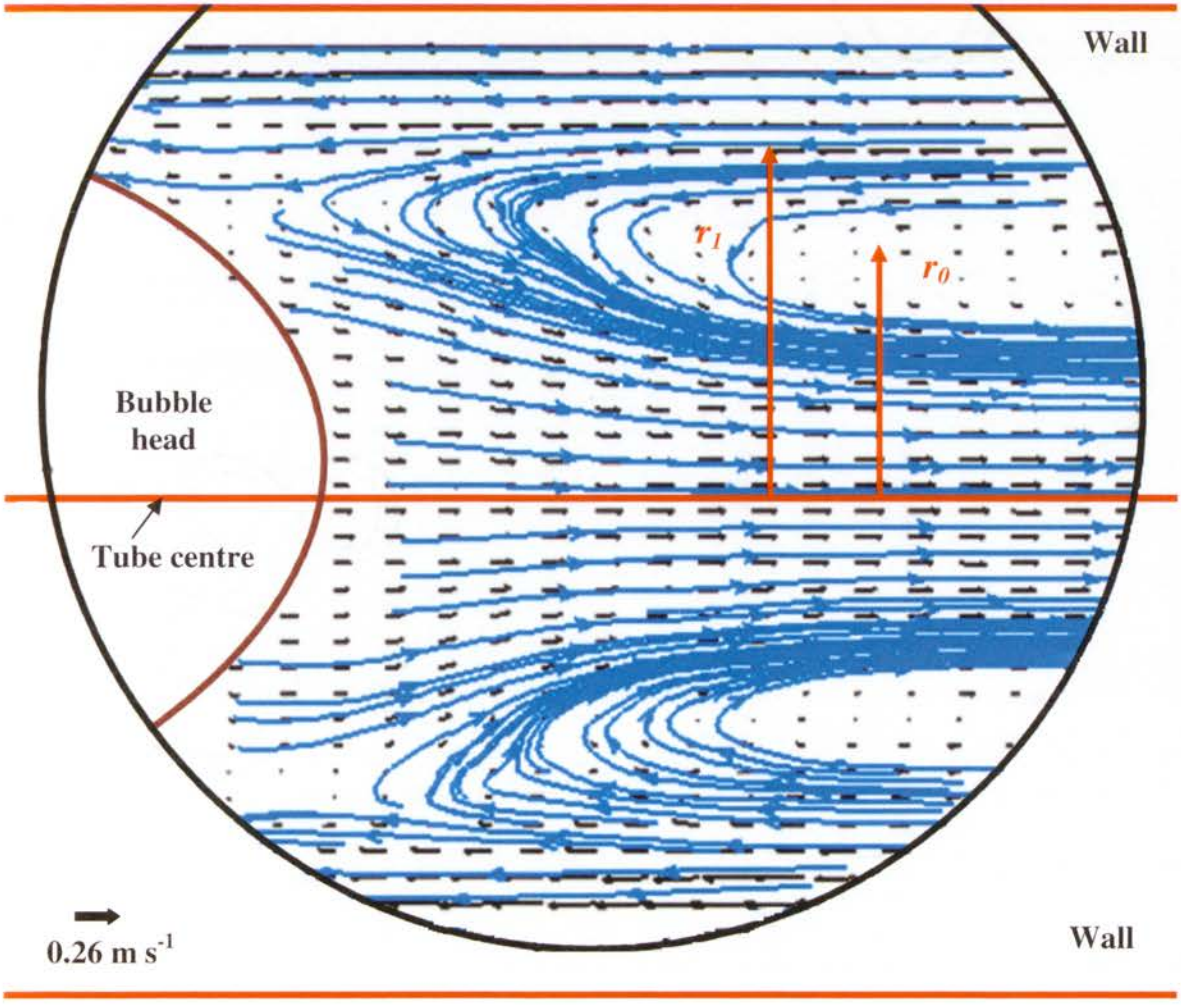

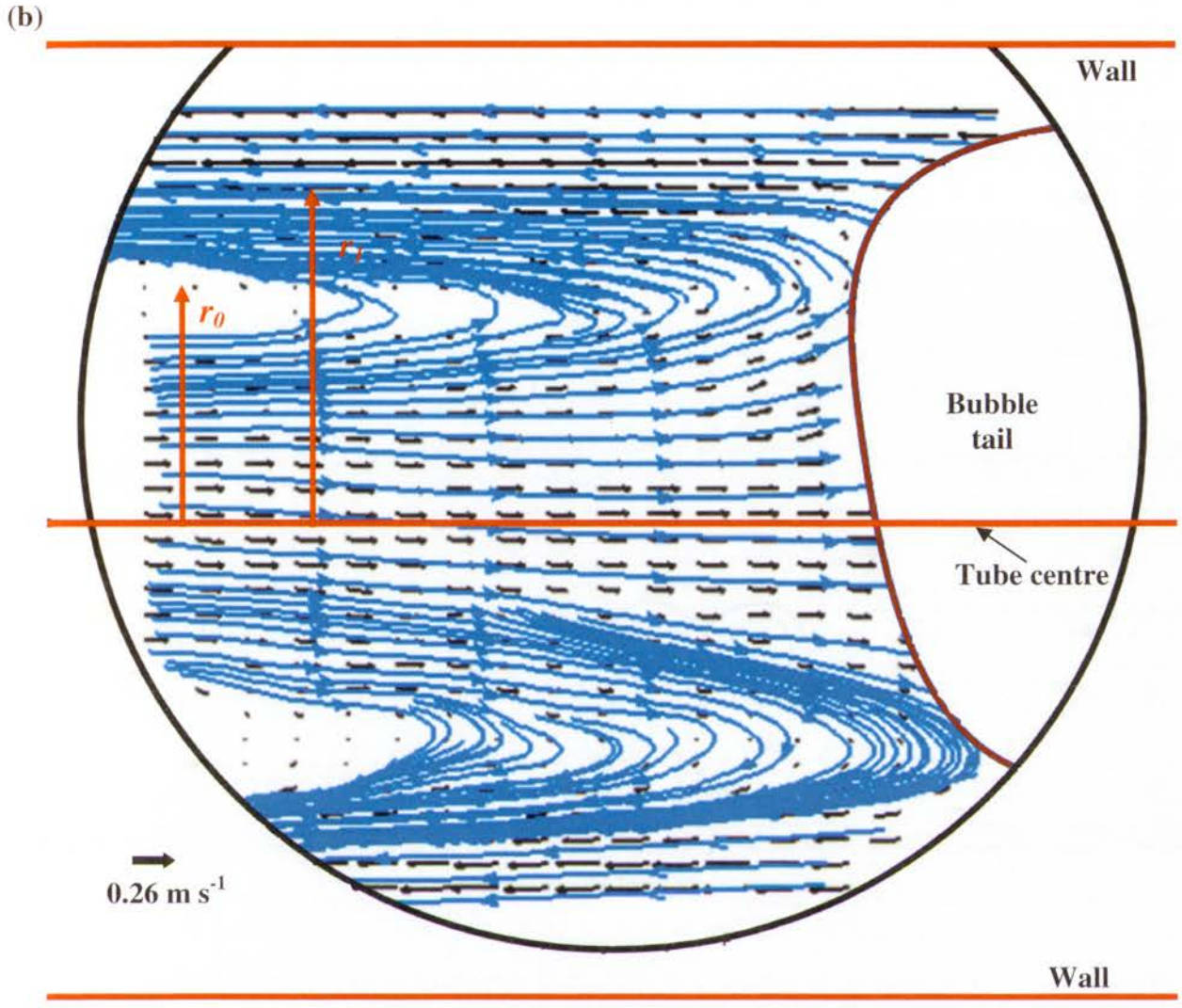

Figure 7.9: Typical plots of relative velocity vectors in a frame of reference moving with the bubble for regions (a) near the bubble head and (b) bubble tail obtained at the vertical centre plane using the 1.69 mm channel (Bo = 0.653, Re_{TP} = 17, Ca = 0.076). The black and brown curves indicate the field of visualization and gas-liquid interface, respectively. The black arrows and blue lines are the relative velocities and streamlines, respectively. The red arrows show the radial positions of the recirculation centre (r_0) and streamline dividing the recirculation zone from the wall film layer (r_1).

The recirculation motions (in a frame of reference moving with the bubble) inside the liquid slug near the tail of the preceding bubble and the nose of the trailing bubble obtained for flow at Bo = 0.653, Re_{TP} = 17, Ca = 0.076, L_S/d = 8.35 are depicted in Figure 7.9. No flow interaction is observed between the lower and upper halves of the liquid slug as was reported in Zheng *et al.* (2007). Also, there is no observed interaction between the wall film layer and

the recirculation fluid in the slug region. The liquid film flows into the head of the slug through the annular bubble film of thickness δ_F, expanding to thickness $R - r_1$ before contracting again to leave at the back of the slug.

The normalized radial positions of the recirculation centre (r_0/R) and streamline dividing the recirculation zone from the wall film layer (r_1/R) for the above case are estimated from Figure 7.9 to be 0.52 and 0.74 which are consistent with the values calculated using Eqs. (6.5) and (6.7). The two counter-rotating vortices inside the liquid slug are rather symmetric at the bubble head region about the horizontal centre plane for the case studied here and slightly asymmetric near the bubble tail region due to the distorted bubble tail. Overall, the effect of gravity on the flow pattern inside the slug region is weak in these long slugs.

7.4 Fluid dynamics model for the drainage flow

The effect of gravity on the bubble shape and the flow field in the liquid film for horizontal Taylor flow in millimetre-size channels is clearly observed in the experimental results for the conditions studied here. Gravity gives rise to a circumferential flow of the liquid from the top film to the bottom film. This flow is symmetric about the vertical plane passing through the tube centre, where the thickness of the liquid film surrounding the bubble increases continuously from the top to the bottom in the circumferential direction.

The axial velocity in the draining liquid film is found experimentally to be negligible when compared with the drainage velocity for a region sufficiently far away from $\theta = 0°$ and 180°, and the bubble ends. Therefore, the drainage flow in such a region may be reduced to a two-dimensional problem. Due to the similarity, a simple analysis analogous to Nusselt's solution for laminar film condensation on a horizontal tube (Nusselt, 1916) can be performed to estimate the drainage velocity in the liquid film at a cross-section far enough from the bubble ends. The main assumptions of the analysis are:

1. The flow is incompressible and the properties of the fluids are constant.
2. The film Reynolds number is low for which the liquid inertia is negligible.
3. Pressure is hydrostatic inside the bubble.
4. Axial and radial velocities can be neglected as being small compared with the circumferential velocity.

5. The film thickness is small when compared with the tube radius, $\delta_F << R$.
6. The cross-section of the bubble become non-circular under the effect of gravity, but the distortion is minor and a cylindrical bubble shape is assumed.

Figure 7.10 shows (a) a schematic of a bubble in a horizontal tube, and (b) an arbitrary cross-section (AA) in the bubble region far away from the bubble ends. Since the film thickness is much smaller than the tube radius ($\delta_F << R$), Cartesian coordinates ($x = R\theta$, $y = R - r$) are used for the circumferential flow. The radii of the tube and the bubble are R and R_B, respectively. The film thickness, δ_F, varies circumferentially as a result of the liquid drainage. The velocity components in the x- and y-directions are denoted by u and v, respectively.

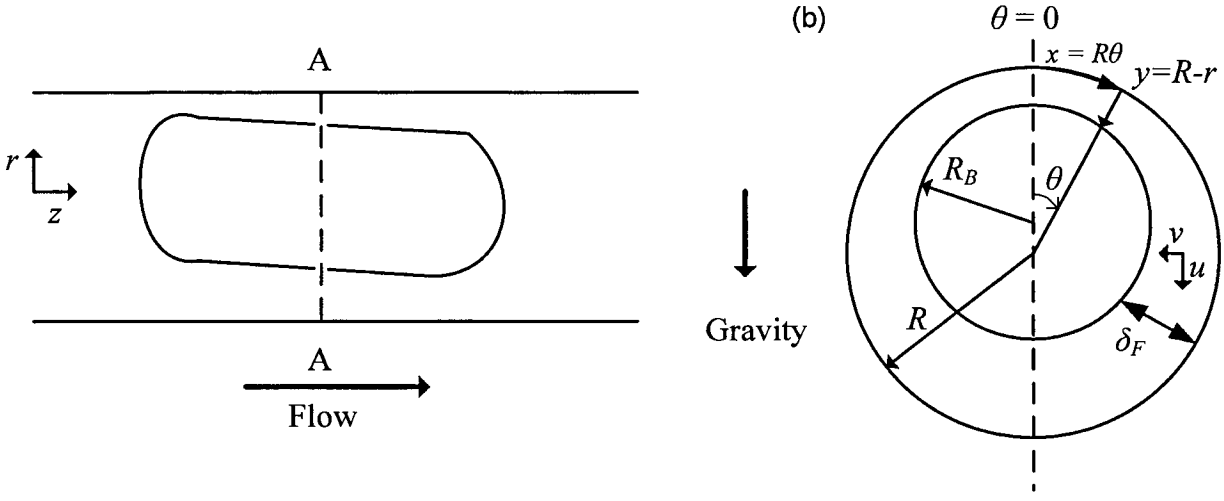

Figure 7.10: (a) Schematic of a bubble, (b) cross-section in the bubble region away from the bubble ends.

The momentum conservation equations in the x- and y-direction for the liquid film can be expressed as

$$-\frac{\partial P_L}{\partial x} + \rho_L g \sin\theta + \mu_L \left(\frac{\partial^2 u}{\partial y^2}\right) = 0 \tag{7.1}$$

$$-\frac{\partial P_L}{\partial y} + \rho_L g \cos\theta = 0 \tag{7.2}$$

where P_L is the liquid pressure and g is the acceleration due to the gravity. The liquid has constant viscosity (μ_L) and density (ρ_L). The gravitational components in the circumferential and radial direction at an angle θ from the top are expressed as $g\sin\theta$ and $g\cos\theta$, respectively, in the Cartesian coordinates.

With the assumption of a hydrostatic pressure profile in the gas phase, the gas pressure, P_G, can be expressed as

$$P_G = P_{\text{ref}} - \rho_G g R\cos\theta \tag{7.3}$$

where P_{ref} is the reference pressure at the centre of the tube and ρ_G is the density of the gas phase.

At the interface, y = δ_F, we have

$$P_G = P_L + \frac{\sigma}{R_B} \Rightarrow \frac{\partial P_G}{\partial \text{y}} = \frac{\partial P_L}{\partial \text{y}} \tag{7.4}$$

For simplicity, the small change in curvature of the interface around the bubble is neglected in the surface tension force and the bubble radius is replaced by that of the tube.

Integrating Eq. (7.2) and using Eqs. (7.3) and (7.4) to obtain

$$P_L = \rho_L g(y - \delta_F)\cos\theta + P_{ref} - \rho_G g R\cos\theta - \frac{\sigma}{R} \tag{7.5}$$

Thus $\partial P_L / \partial x$ can be expressed as

$$\frac{\partial P_L}{\partial x} = \frac{1}{R}\frac{\partial P_L}{\partial \theta} = -\frac{\rho_L g(y - \delta_F)}{R}\sin\theta + \rho_G g\sin\theta \tag{7.6}$$

Substituting this into Eq. (7.1), we get

$$\mu_L\left(\frac{\partial^2 u}{\partial y^2}\right) = -\frac{\rho_L g(y - \delta_F)}{R}\sin\theta - (\rho_L - \rho_G)g\sin\theta \tag{7.7}$$

Integrating Eq. (7.7) twice and applying the boundary conditions that $u = 0$ at $y = 0$ and $\partial u/\partial y = 0$ at $y = \delta_F$, the drainage velocity profile in the liquid film is obtained as

$$u(y) = -\frac{\rho_L g \sin\theta}{6\mu_L R}[(y-\delta_F)^3 + (\delta_F)^3] - \frac{(\rho_L - \rho_G) g \sin\theta}{2\mu_L}[(y-\delta_F)^2 - (\delta_F)^2] \tag{7.8}$$

The average drainage velocity can then be determined as

$$U_d = \frac{\int_0^{\delta_F} u(y)dy}{\delta_F} = -\frac{\rho_L g \sin\theta {\delta_F}^3}{8R\mu_L} + \frac{\Delta\rho g \sin\theta {\delta_F}^2}{3\mu_L} = \frac{\Delta\rho g {\delta_F}^2}{3\mu_L}\left(1 - \frac{3}{8}\frac{\delta_F}{R}\right) \sin\theta \tag{7.9}$$

For flow with $\delta_F << R$, Eq. (7.9) can be simplified by neglecting the cubic term and it is rewritten using the conventional dimensionless terms given by Eq. (7.10). To make the trends explicit, the small variation of the thickness of the liquid film surrounding the gas bubble is neglected, with δ_F estimated using Eq. (4.5)

$$\frac{U_d}{U_{TP}} \approx \frac{0.45 \cdot Bo \cdot Ca^{1/3}}{(1 + 3.35Ca^{2/3})^2} \sin\theta \tag{7.10}$$

From the above analysis, the normalized drainage velocity (U_d/U_{TP}) is found to be a function of the Bond number and Capillary number, as well as the circumferential position, θ. It is worth reiterating that Eq. (7.10) is only valid for a region far away from the bubble ends and for a film region away from the top and bottom films because of the assumptions made in its development.

According to Eq. (7.10), U_d/U_{TP} increases linearly with the Bond number for fixed values of Ca and θ. The variation of U_d/U_{TP} with Ca for the Bond numbers used in the present study (Bo = 0.287, 0.653 and 1.028) at $\theta = 90°$ is shown explicitly in Figure 7.11. The normalized drainage velocity first increases sharply from zero at $Ca = 0$ to a maximum value reached at $Ca = 0.031$, beyond which it decreases exponentially to a value of zero as $Ca \to \infty$. Therefore, the drainage velocity is negligible compared with the mixture velocity for flow with very small Bond numbers and/or $Ca \to 0$ or $Ca \to \infty$.

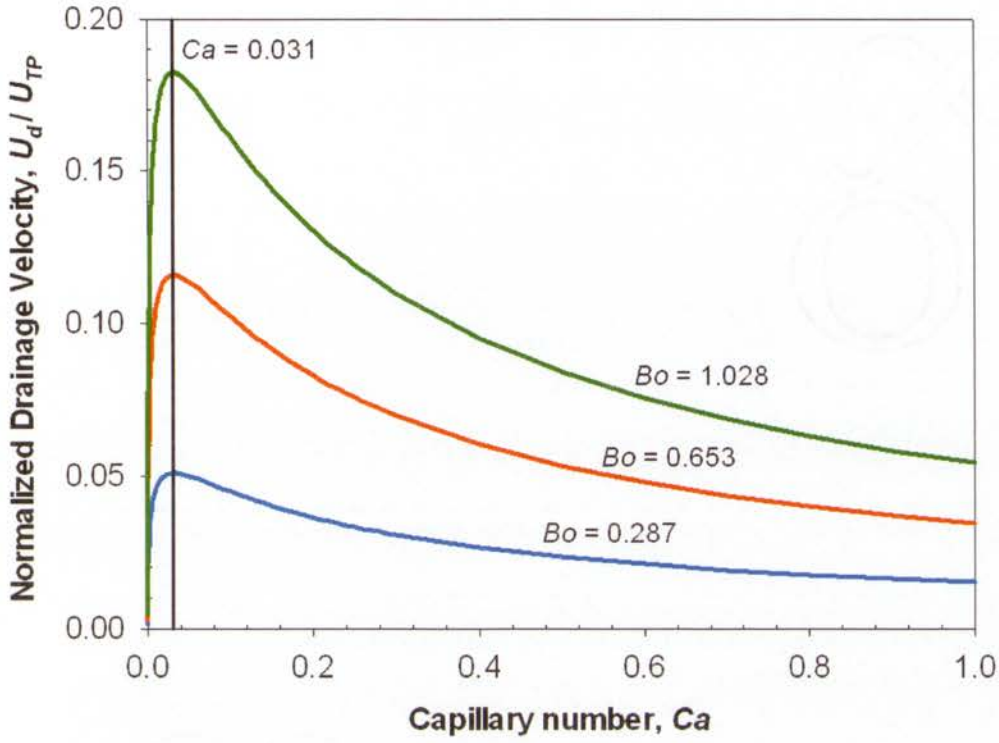

Figure 7.11: Variations of U_d/U_{TP} with Ca for fixed values of Bo at $\theta = 90°$.

7.4.1 Comparison of experimental results with the analytical solution

The experimental drainage velocity profiles at the horizontal centre-plane ($\theta = 90°$) obtained for flows with different film thicknesses are compared with Eq. (7.8) in Figure 7.12. As shown in Figure 7.8, the drainage velocity in the liquid film decreases steadily from the bubble nose to tail. Therefore, the experimental velocity data presented here were obtained by taking the average drainage velocities across the bubble, with the error bars indicating the range of values measured along the bubble. The experimental results show parabolic profiles and agree reasonably well with the analytical solutions (Eq. 7.8) calculated based on the average film thickness, suggesting that the physics governing the drainage flow in the liquid film are captured correctly by the simple fluid dynamics model. Better agreement is achieved between the analytical solutions and the experimental data for flow with smaller drainage velocity (and thinner film).

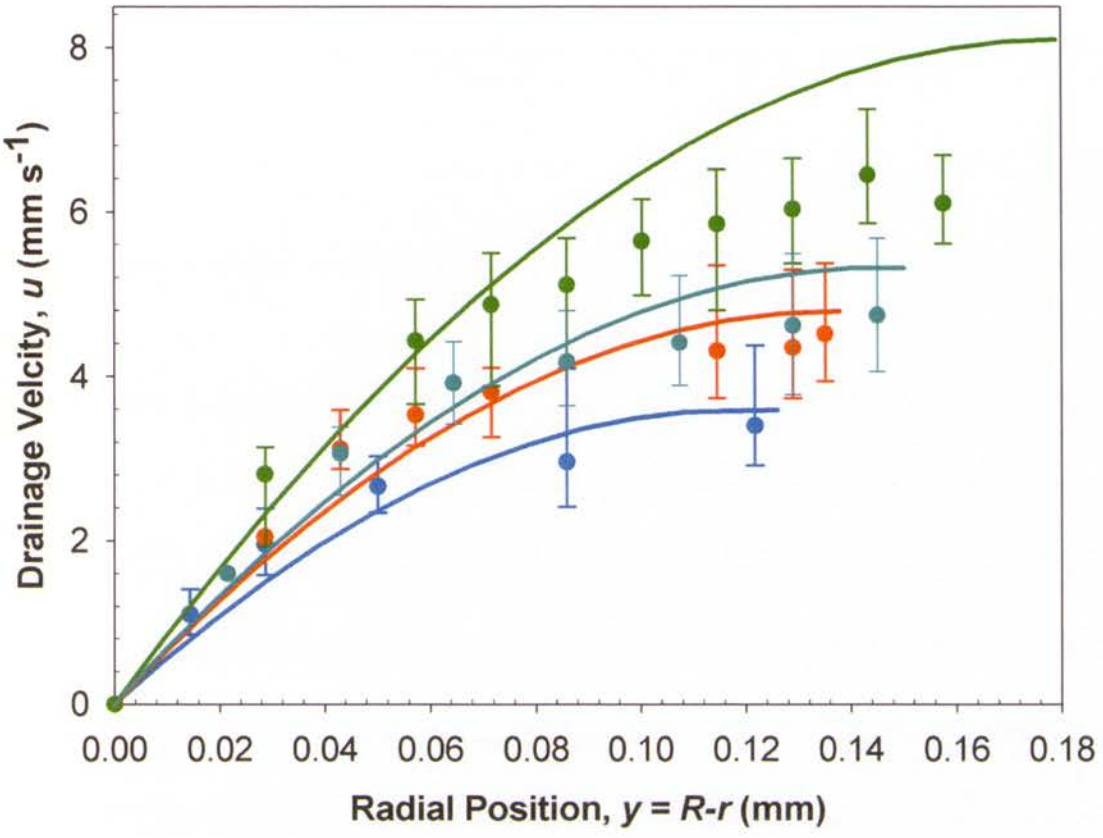

Figure 7.12: Comparisons of the experimental drainage velocity profile with the analytical solution for different flow conditions: (●) $Bo = 0.653$, $Re_{TP} = 10$, $Ca = 0.046$, (●) $Bo = 0.653$, $Re_{TP} = 17$, $Ca = 0.076$, (●) $Bo = 1.028$, $Re_{TP} = 10$, $Ca = 0.038$, and (●) $Bo = 1.028$, $Re_{TP} = 20$, $Ca = 0.073$. The lines with the corresponding colours show the prediction values using Eq. (7.8).

As mentioned previously in Section 7.2, the thickness of the top film decreases while that of the bottom film increases linearly along the bubble due to the accumulation of the drainage effect. To relate the angle of inclination of the bubble to the drainage velocity, a volumetric balance between the drainage volume and the bubble displacement was performed. At $\theta = 90°$, the drainage flow represents the total flow from above the bubble centre-line to below it. The volumetric flow rate of this flow through the films on either side of the axis for a length Δz is

$$\Delta Q_d = 2\delta_F U_d(\theta = 90°)\,\Delta z = \frac{2\Delta\rho g {\delta_F}^3}{3\mu_L}\left(1 - \frac{3}{8}\frac{\delta_F}{R}\right)\Delta z \qquad (7.11)$$

Neglecting any change in bubble shape or size along its length (in the z direction), the bubble must be shifted upward in the channel after Δz by a distance Δh in order to balance the drainage volume, ΔQ_d. In the stationary frame, the volume displaced after the bubble rises a differential height Δh is

$$\Delta V = \Delta h . \Delta A_{\text{projected}} \tag{7.12}$$

where the projected area of the bubble is the centreline area normal to the rise direction, $\Delta A_{\text{projected}} = 2\,(R - \delta_F) \cdot \Delta z$. Since $\Delta Q_d = \Delta \text{V}/\Delta \text{t}$, writing $\Delta z = U_B \Delta t$ gives

$$\Delta Q_d = 2\,(R - \delta_F)\,\Delta h\, U_B \tag{7.13}$$

Equating Eqs. (7.11) and (7.13), we get

$$\frac{\Delta h}{\Delta z} = \frac{\Delta \rho g {\delta_F}^3}{3\mu_L R\, U_B} \cdot \frac{\left(1 - \frac{3}{8}\frac{\delta_F}{R}\right)}{\left(1 - \frac{\delta_F}{R}\right)} \sim \frac{\Delta \rho g {\delta_F}^3}{3\mu_L R\, U_B} = \frac{2}{3} \cdot \frac{Bo}{Ca} \cdot \left(\frac{\delta_F}{\text{d}}\right)^3 \cdot \frac{U_{TP}}{U_B} \tag{7.14}$$

Rearranging the above equation, the normalized film thickness, δ_F/d, can be expressed as

$$\frac{\delta_F}{d} \approx \left(\frac{3}{2} \cdot \frac{Ca}{Bo} \cdot \frac{U_B}{U_{TP}} \cdot \frac{\Delta h}{\Delta z}\right)^{1/3} \tag{7.15}$$

where $\Delta h = |\Delta \delta_F|$ for the top and bottom films.

It is recognised that δ_F in Eq. (7.15) is the film thickness at $\theta = 90°$. As shown in Figure 7.2, gradients of the film thicknesses ($\Delta \delta_F/\Delta z$) of the top and bottom films in a region far away from the bubble ends are relatively constant, suggesting a constant film thickness at $\theta = 90°$, which has been confirmed by the white light visualization measurements as shown in Figure 7.1. In fact, this seems to be reasonable as the bubble interface and wall are parallel to the direction of bubble rise at that position.

Figure 7.13 compares the experimental film thickness and the calculated values at $\theta = 90°$ using Eq. (7.15) based on the average gradient of the top and bottom films. Good agreement is achieved between the experimental normalized film thicknesses and the calculated values, with the experimental data scattering within 15% of the predicted values. The results suggest

that the simple model does describe the relationship between the angle of inclination of the bubble and the drainage flow around the bubble properly.

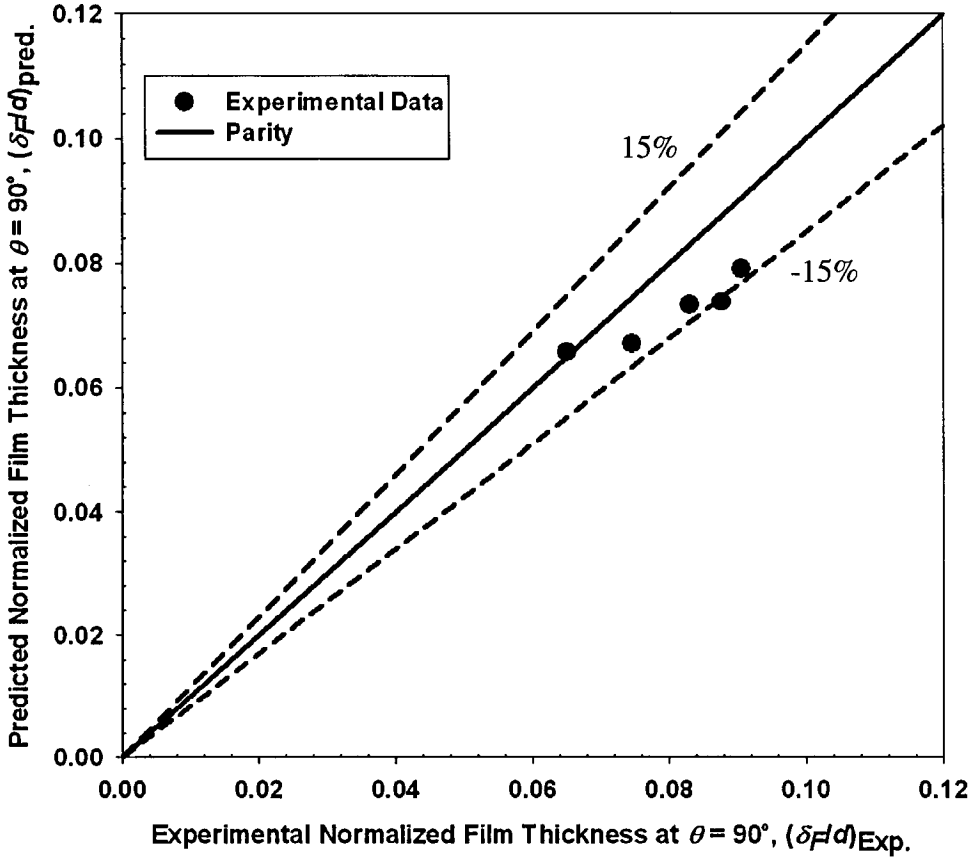

Figure 7.13: Comparison between the experimental film thicknesses and the calculated values using Eq. (7.15) at $\theta = 90°$, with the broken lines represent the $\pm$ **15%** bounds of the predicted values.

7.5 Heat transfer

As observed in the visualization experiments, the liquid film is not uniform around the bubble at the wall due to the drainage of liquid from the top to the bottom of the channel under the effect of gravity. To investigate the effect of gravity on the heat transfer rate, heat transfer experiments for horizontal Taylor flow were performed in a 2.00 mm channel (Bo = 0.915) for selected flow conditions (β ~ 0.5, 10 < Re_{TP} < 65 and 0.036 < Ca < 0.172) using the multi-block heating system. Figure 7.14 shows a comparison of the normalized Nusselt number ($Nu^* = Nu_{TP}/Nu_{LO}$) between the horizontal and vertical flow systems. Similar heat

transfer rates are noted for the two flow orientations with the differences falling within the uncertainty in the measurements. The small difference in the heat transfer rate between the two systems suggests there is only a minor effect of gravity on Taylor flow heat transfer. This can be explained by the absence of flow interaction between the top and bottom halves of the liquid slug region (two almost symmetric counter-rotating vortices observed in a frame of reference moving with the bubble). The results further confirm the heat transfer mechanisms proposed in Chapter 6 – the liquid film only acts as an energy storage region, with that energy being taken up by mixing with the overtaking slug and most of the heat being carried by the liquid slug. Therefore, the effect of flow orientation on the heat transfer rate would only be observed when the flow pattern inside the liquid slug is affected by the gravity.

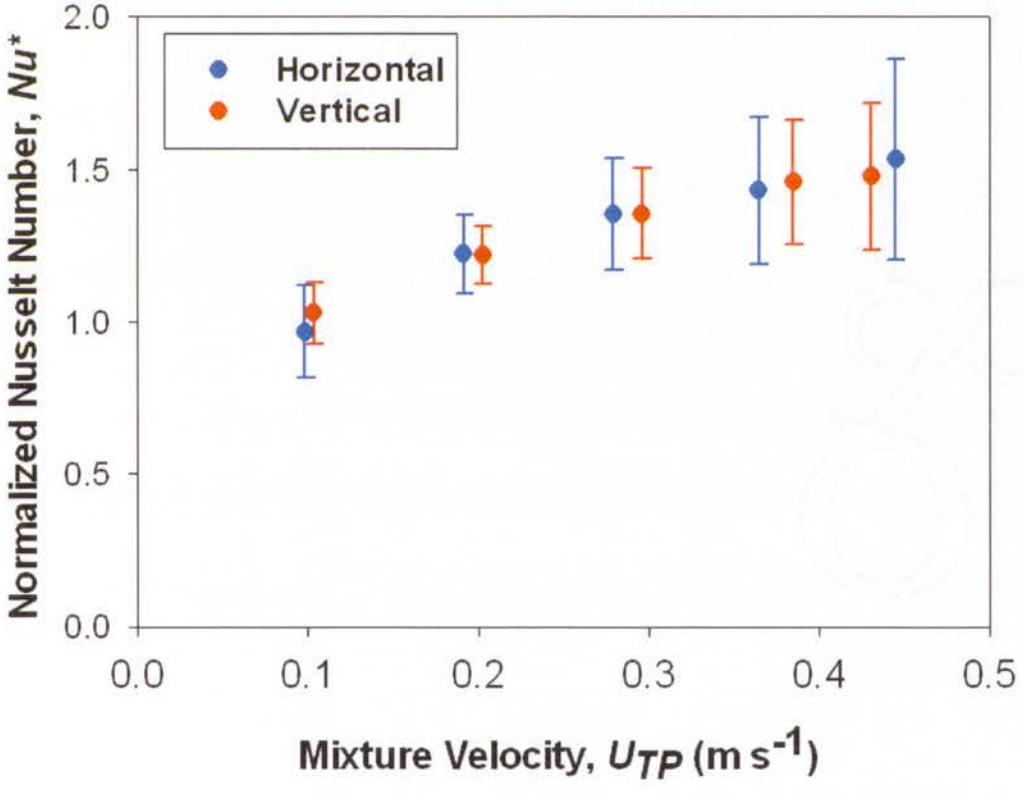

Figure 7.14: Comparisons of the normalized Nusselt number in the fully-developed region between the horizontal and vertical systems for $\beta \sim 0.5$. The error bar indicates one standard deviation for the normalized Nusselt number (Nu^*).

7.6 Summary

The effect of the gravity on the bubble behaviour of gas-liquid Taylor flow was studied experimentally in three different millimetre-size channels (d = 1.12, 1.69, 2.12 mm giving Bo = 0.287, 0.653 and 1.028). Nitrogen and ethylene glycol were used as the gas and liquid phases, respectively. By careful matching of the refractive indices of the tube material and the liquid phase, a well-defined gas-liquid interface was visible to allow direct measurement of the liquid film thickness and digitization of the bubble shape for comparison of the top and bottom halves of the bubble interface.

The visualization results showed that bubbles become asymmetric under the influence of gravity for the conditions studied here. Due to the accumulation of drained liquid, the film thickness around the bubble varied both circumferentially and axially. The film thickness surrounding the bubble increases from the top to the bottom of the tube and the difference between the top and bottom film thicknesses increases from the bubble nose to the tail. From the parametric study, the Bond (Bo) and Capillary (Ca) numbers are identified as important parameters controlling the drainage flow.

The μPIV measurements showed clearly a drainage flow in the film region under the effect of gravity. The drainage velocity increases from the region near the wall to the gas-liquid interface and adopts a parabolic profile. Compared with the drainage velocity, negligible axial film velocities were noted during the passage of a bubble for a region far from the bubble ends. Performing μPIV measurements in the liquid slug region, two counter-rotating vortices in a reference frame moving with the bubble were identified. For the cases studied, no flow interaction were observed between the top and bottom halves in the slug region, with the liquid film moving along the wall layer without mixing with recirculation fluid inside the slug core.

A simplified model based on Nusselt's solution for laminar film condensation on a horizontal tube is derived to describe the drainage velocity profile in the liquid film at a cross-section away from the bubble ends. The analytical results agree qualitatively with the experimental data. A non-dimensional analysis of the model showed that the ratio of the average drainage to bubble velocities is a function of the Bond and Capillary numbers. The effect of gravity vanishes as the function of these groups tends to zero, which can be achieved using a very small Bond number and/or $Ca \rightarrow 0$ and as $Ca \rightarrow \infty$.

From the simple model (Eq. (7.14)) relating the angle of inclination of the bubble to the drainage velocity, it is recognized that the film thickness, δ_F, at $\theta = 90°$ can be estimated based on the gradients of the film thicknesses ($\Delta\delta_F/\Delta z$). Good agreement was achieved between the experimental data and the calculated values, with the experimental film thicknesses falling within 15% of the prediction.

Although an asymmetric bubble shape was observed for horizontal Taylor flow for all channel sizes studied here, the heat transfer rate of Taylor flow in a 2.00 mm horizontal channel was not significantly different from that obtained for a vertical system, indicating a minor effect of gravity on horizontal Taylor flow heat transfer.

Chapter 8
Preliminary Study of Annular Flow in Microchannels

Apart from Taylor flow, annular two-phase flow is another frequently encountered flow regime in micro-scale two-phase flow systems. This flow pattern occurs when the gas superficial velocity increases at low liquid superficial velocity, leading to breaching of the liquid slugs present in Taylor flow and the formation of a continuous gas core. Gas-liquid annular flows are of relevance for typical chemical engineering applications, such as falling film reactors, handling of cryogenic fluids, electronics cooling, space-based nuclear power generation, etc., because of the capability of giving higher throughputs. In addition, this flow regime arises naturally in phase-change applications even at a vapour quality as low as 0.2. Therefore, a good understanding of heat transfer without phase change in the annular flow regime would provide more fundamental knowledge of the complex phenomena of flow boiling in microchannels (Bertsch *et al.*, 2008, Liu, 2011) and condensation (Baird *et al.*, 2003, Chen *et al.*, 2008).

In view of its practical importance, two-phase annular flow in large diameter channels has been studied extensively and several empirical or semi-empirical correlations have been proposed to predict the liquid film thickness, liquid entrainment in the gas core, void fraction and pressure gradient (Hewitt and Hall-Taylor, 1970). Several studies have attempted to extrapolate the correlations for conventional channels to predict the hydrodynamic parameters of annular flow in microchannels (Bao *et al.*, 2000, Chen *et al.*, 2002b, Cioncolini *et al.*, 2010). However, such direct extrapolation may not be suitable because the surface forces (e.g. surface tension) which are usually neglected in large channels become more important when compared with other forces (e.g. gravity or fluid inertia) as the channel size reduced. Differences in flow behaviour were noted between annular flows in micro- and macro-channels. For example, the flows in both the liquid film and gas core are turbulent for macro-scale annular flow, while the flow in the liquid film usually falls in the laminar regime with the gas core falling in the transition or turbulent regimes for micro-scale annular flow.

Also, the liquid droplets dispersed in the gas core generally seen in large diameter channels are rarely observed in microchannels.

Whilst gas-liquid Taylor flow in microchannels has been well-characterised and the corresponding heat and mass transfer enhancements have received increasing attention, studies of the annular flow regime have been generally neglected. This can be mainly attributed to the greater complexity associated with this flow regime. The unstable and transient nature of annular flow provides significant challenges to study this flow pattern experimentally.

Significant heat transfer enhancement brought about by gas-liquid annular flow in microchannels was reported experimentally (Bar Cohen *et al.*, 1995, Bao *et al.*, 2000, Liu *et al.*, 2006). However, the heat transfer characteristics of the annular flow regime are much more complicated than those for Taylor flow due to coupled convective and evaporative heat transfer mechanisms. Also, the presence of transient waves at the gas-liquid interface gives rise to additional complexity in understanding the heat transfer mechanisms.

This chapter explores the suitability of extending the experimental techniques which were developed for Taylor flow to the study of the flow and heat transfer characteristics of non-boiling, gas-liquid annular flow in microchannels. Also, experimental challenges for a comprehensive annular flow study are identified through performing preliminary experiments in a circular channel having an internal diameter of 2.00 mm.

8.1 Modifications of the experimental set-up

8.1.1 Flow loop design

The flow loop design for studying the hydrodynamics and heat transfer rates of gas-liquid annular flow in a vertical tube of internal diameter, d = 2.00 mm (Figure 8.1) was modified from that used for the ethylene glycol Taylor flow experiments. Since a much higher gas flow rate was used to generate annular flow, the gas flow was regulated by a different calibrated mass flow controller (Sierra Smart-Trak, C100L) which allows a flow rate of up to 10 slpm. To minimize the effect of evaporation in the heating section, nitrogen was saturated by bubbling the dry nitrogen through a flask partially filled with water prior to it entering the mixing zone. A K-type thermocouple was added to measure the gas inlet temperature. The

amount of vapour present in the gas inlet was then determined based on an adiabatic saturation calculation using the steam table.

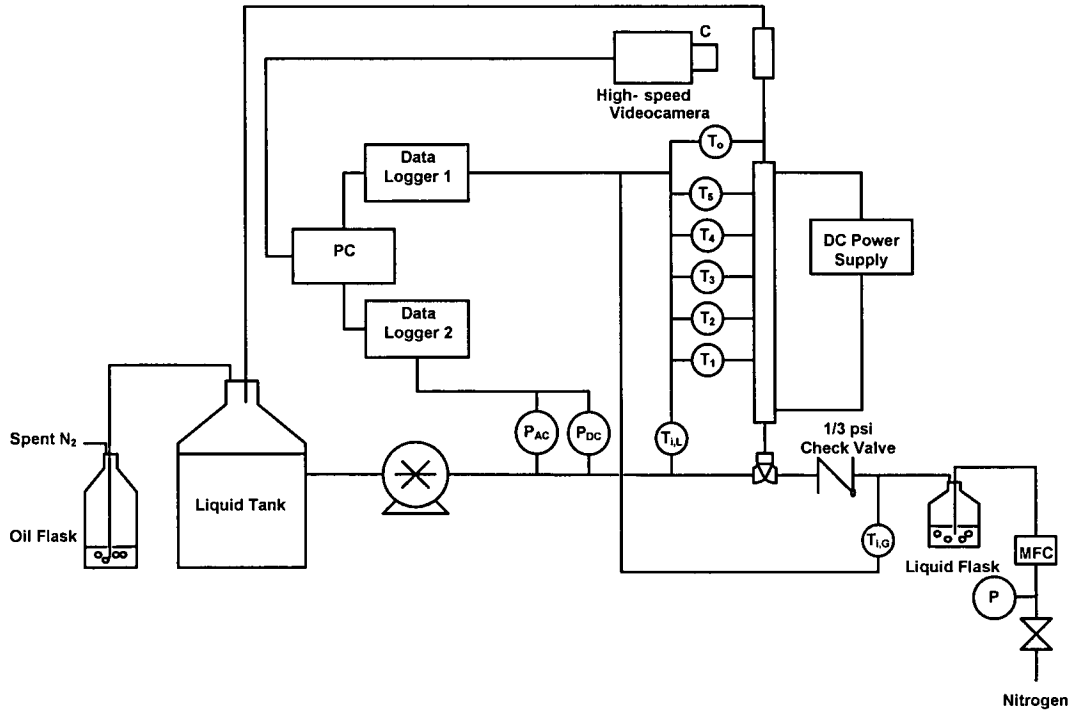

Figure 8.1: Schematic of the experimental facility for annular flow experiments.

8.1.2 Visualization tests

All visualization experiments were conducted in a 300 mm long silica tube of internal diameter $d = 2.00$ mm under isothermal condition (21 °C). The visualization techniques employed in the Taylor flow study demonstrated clearly the capabilities of obtaining high-quality brightfield pictures and time-resolved velocity data, as presented in the previous Chapters. The suitability of extending these to study the flow characteristics of the intermittent slug-annular/annular flow regime have also been demonstrated in our research group (Fouilland, 2008, Fouilland *et al.*, 2010). Fouilland studied nitrogen-water two-phase flow spanning Taylor to slug-annular/annular flow in a 1.73 mm diameter tube. The transient waves along the gas-liquid interface and the transient flow field in the liquid film for annular flow were captured successfully. Therefore, it is likely that we can use the same apparatus to perform a systematic experimental study on the hydrodynamics of gas-liquid annular flow in microchannels.

8.1.3 Heating test section

As discussed in Chapter 3, the thermal time constant of the multi-block heating system is ~200 s. Such a long thermal time constant means that a long start up time (typically a few hours) is required for the system to reach a steady state and the wall temperature is unlikely to be sensitive to the waves present in annular flow. Liu (2011) in our research group studied the effect of thermal capacity of the test section on boiling flow and heat transfer characteristics by comparing results obtained for a multi-block heating system (the same apparatus as used in the present study) with those obtained for bare tube heating systems of significantly shorter thermal time constants (~5 ms). He found that the thermal time constant of the test section and the channel materials had little influence on the boiling flow and heat transfer behaviour. With the much shorter time constant of the bare tube heating systems, the time required for steady state operation was reduced from hours to minutes.

Based on the observations reported by Liu (2011), a bare tube heating section was constructed to study the heat transfer characteristics of non-boiling, gas-liquid annular flow. It uses a 300 mm long hard-drawn stainless steel circular channel of 2.00 mm internal diameter with a wall thickness of 0.5 mm. Five small surface resistance thermometers (RdF Corporation, R-MINI 29223) were mounted on the wall surface along the heating test section using high temperature resistant tape. The axial locations of the surface thermometers from the entrance of the heating section are given in Table 8.1. The heating section was wrapped in closed cell foam insulation to minimize ambient heat losses and the effect of environmental changes. A constant wall heat flux boundary condition in the heating section was achieved by Joule heated using a high current DC power supply (Xantrex, XFR 7.5-300), with a total heating length of 260 mm. Since the heating section starts right after the mixing zone, simultaneously hydrodynamic and thermal developing flow was encountered at the entrance region.

Table 8.1: Axial locations of surface thermometers.

Thermometer #	T1	T2	T3	T4	T5
Axial location (mm)	72.0	104.5	134.5	163.5	205.5

8.1.3.1 System calibration

A series of experiments without fluid flow were first performed for system calibration. The overall heat loss constant, C_{loss}, to the ambient was determined as

$$Q_{in} = Q_{loss} = C_{loss}(\overline{T_w} - T_a) \tag{8.1}$$

where Q_{in} and Q_{loss} are the total heat input and the heat loss to the environment, respectively; $\overline{T_w}$ and T_a are the mean wall temperature for the entire heating zone and the ambient temperature, respectively. The overall heat loss constants were found to be almost constant (~0.058 W K^{-1}) for the average wall temperature ranged 25 – 65 °C, as seen in Figure 8.2.

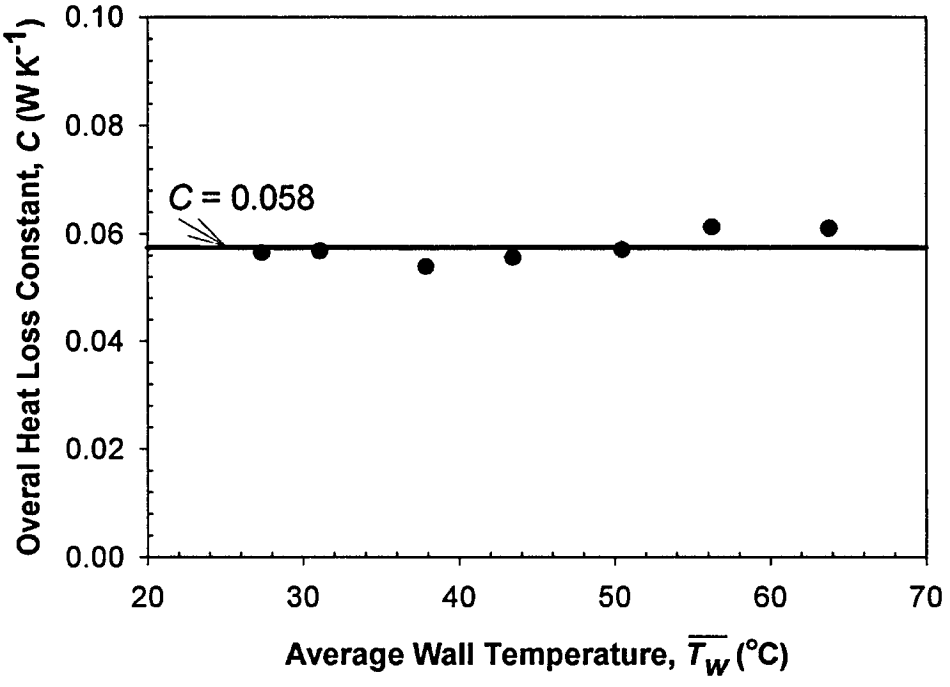

Figure 8.2: Variation of heat loss constant with average wall temperature.

8.1.3.2 Single-phase verification

The system was also tested for a series of single-phase flow heat transfer measurements. The bulk mean temperature and the heat transfer rate were determined in a similar way to that used in the multi-block system.

$$\dot{m}\hat{C}_p(T_{bz} - T_{in}) = \dot{m}(\hat{H}_z - \hat{H}_{in}) = \left(Q_{in} - C(\overline{T_w} - T_a)\right)\frac{z}{L_{heating}} \tag{8.2}$$

$$Nu_z = \frac{h_z d}{k_L} = \frac{q_{av}}{\Delta T}\cdot\frac{d}{k_L} = \frac{Q_{in} - C(\overline{T_w} - T_a)}{\pi d L_{heating}(T_{wz} - T_{bz})}\cdot\frac{d}{k_L} \tag{8.3}$$

where z is the axial location of the resistance thermometer and $L_{heating}$ is the total heating length, h_z is the local heat transfer coefficient; q_{av} is the average wall heat flux; T_{wz} and T_{bz} are the wall and bulk temperatures temperature at the axial location z, respectively; ΔT is the temperature difference between the wall and bulk temperatures. Experimental data are compared with the theoretical solution for simultaneously developing laminar flow for constant wall heat flux boundary conditions (Shah and London, 1978) in Figure 8.3. Excellent agreement was achieved, with most of of the experimental Nusselt numbers falling within 5% (some are in the range 5-10%) of the theoretical values.

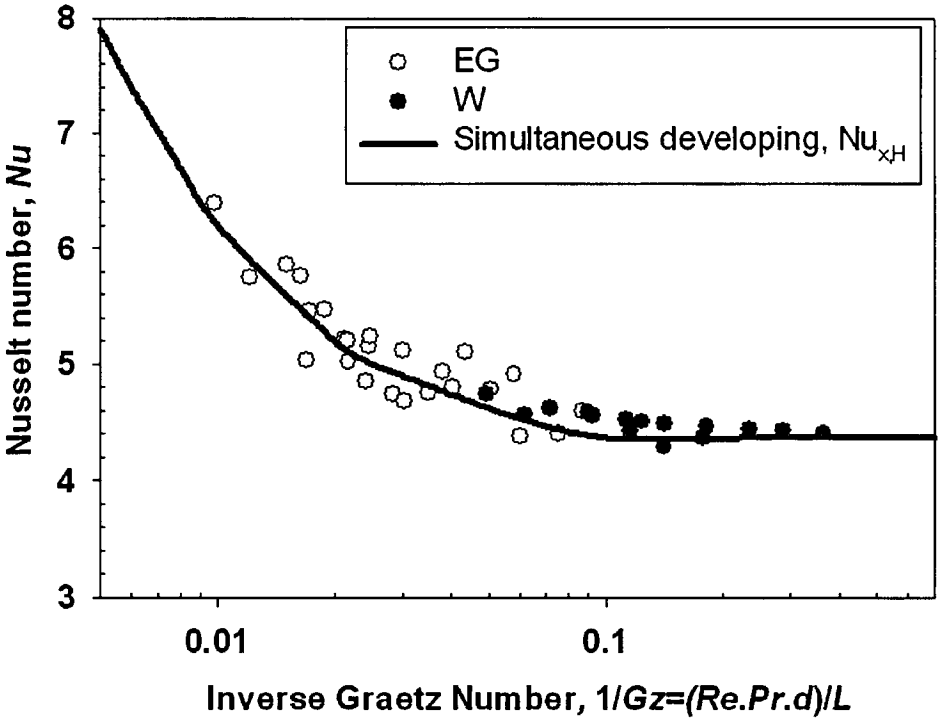

Figure 8.3: Comparisons of the heat transfer rate for single-phase laminar flows with the theoretical value for simultaneously developing flow for constant wall heat flux boundary conditions.

8.1.3.3 *Taylor flow heat transfer*

Taylor flow heat transfer experiments were also performed using the bare tube heating section for selected flow conditions to investigate the impact of the wall thickness on the heat transfer rates. The two-phase heat transfer rates were determined in a manner similar to that used in the multi-block Taylor flow experiments, with the homogeneous specific heat capacity, $\hat{C}_{p,TP}$ and specific enthalpy, $\hat{H}_{TP}$, calculated using Eqs. (3.15) and (3.16) and the evaporation energy determined from Eqs. (3.17) and (3.18). The block-wise Nusselt numbers obtained from the multi-block heating test section are compared with the bare tube results in Figure 8.4 and 8.5 using water and ethylene glycol as the liquid phase, respectively.

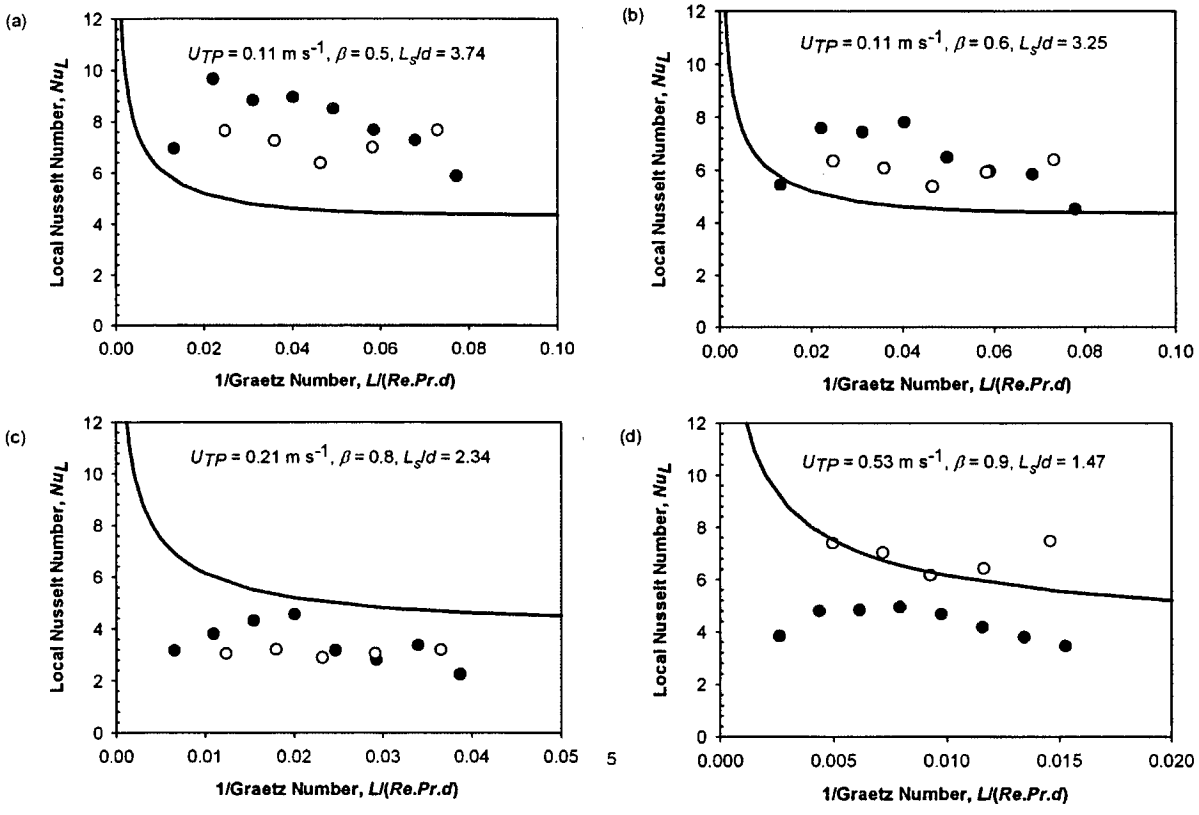

Figure 8.4: Comparisons of the Nusselt number between the multi-block (●) and bare tube (o) heat transfer experiments using water as the liquid phase. The solid line represents the theoretical results for thermally developing laminar tube flow under a constant wall heat flux boundary condition suggested by Shah and London (1978).

For the water experiments using the bare tube test section, the Nusselt numbers are almost constant throughout the monitoring length, indicating thermally fully-developed flow is achieved. For flows at low mixture velocities (Figure 8.4 (a)-(c)), results obtained from both heating systems are very close to each other. As U_{TP} increases, the local Nusselt numbers obtained from the bare tube system is significantly higher than that obtained from the multi-block system, as seen in Figure 8.4 (d). The reasons for such discrepancy are not clear yet.

As discussed in Chapter 4, a greater length was required for the flow to become thermally fully-developed when ethylene glycol was used as the liquid phase in the multi-block heat transfer experiments. A similar observation is noted for the bare tube experiments as seen in Figure 8.5. Relative constant Nusselt numbers are generally attained from the position where the third thermocouple is located (134.5 mm from the inlet). A good match between the two heating systems is observed at low mixture velocities (Figure 8.5 (a) – (c)). Similar to the experiments using water as the liquid phase, the Nusselt numbers obtained from the bare tube system become greater than those obtained from the multi-block system as the mixture velocity increases (Figure 8.5 (d) – (e)).

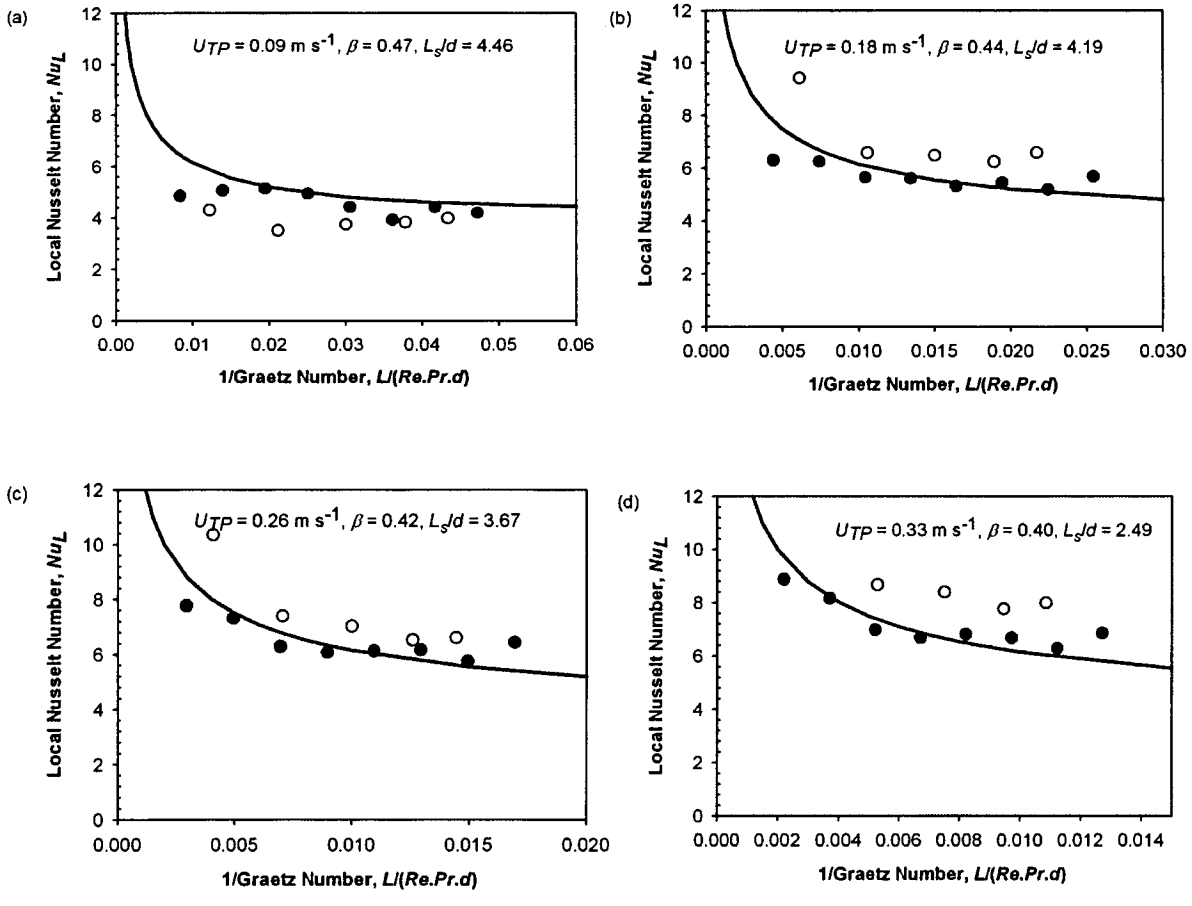

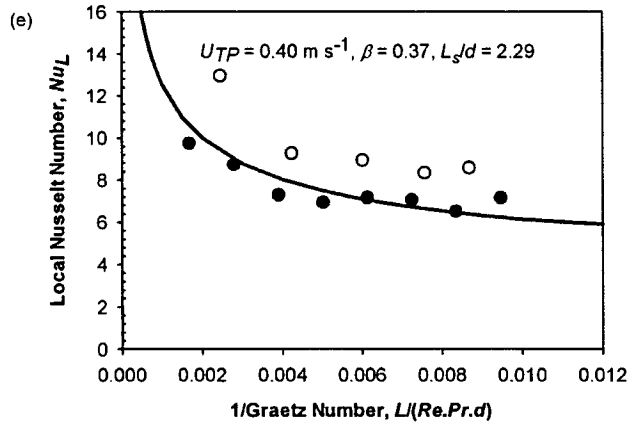

Figure 8.5: Comparisons of the Nusselt number between the multi-block (●) and bare tube (o) heat transfer experiments using ethylene glycol as the liquid phase. The solid line represents the theoretical results for thermally developing laminar tube flow under a constant wall heat flux boundary condition given by Shah and London (1978).

To obtain the fully-developed heat transfer rate for the bare tube heating test section, the two-phase Nusselt numbers (Nu_{TP}) for water experiments are determined by averaging the Nusselt numbers for locations T1 to T5, while those for the ethylene glycol experiments are determined by averaging the Nusselt numbers for locations T3 to T5. Figure 8.6 shows a comparison of the normalized Nusselt number ($Nu^* = Nu_{TP}/Nu_{LO}$) between the two heating systems. Apart from case 8.4 (d) for which unsteadiness was observed near the bubble tail region due to the relative higher Reynolds number employed (Re_{TP} = 1100), the discrepancies between the two heating systems are within the uncertainty in the measurements. The agreement in the heat transfer rate between the two heating systems suggests there is only a minor effect of the thermal capacity of the test sections on Taylor flow heat transfer. Also, it confirms the suitability of using the bare tube heating systems to study the heat transfer characteristics of gas-liquid two-phase flows.

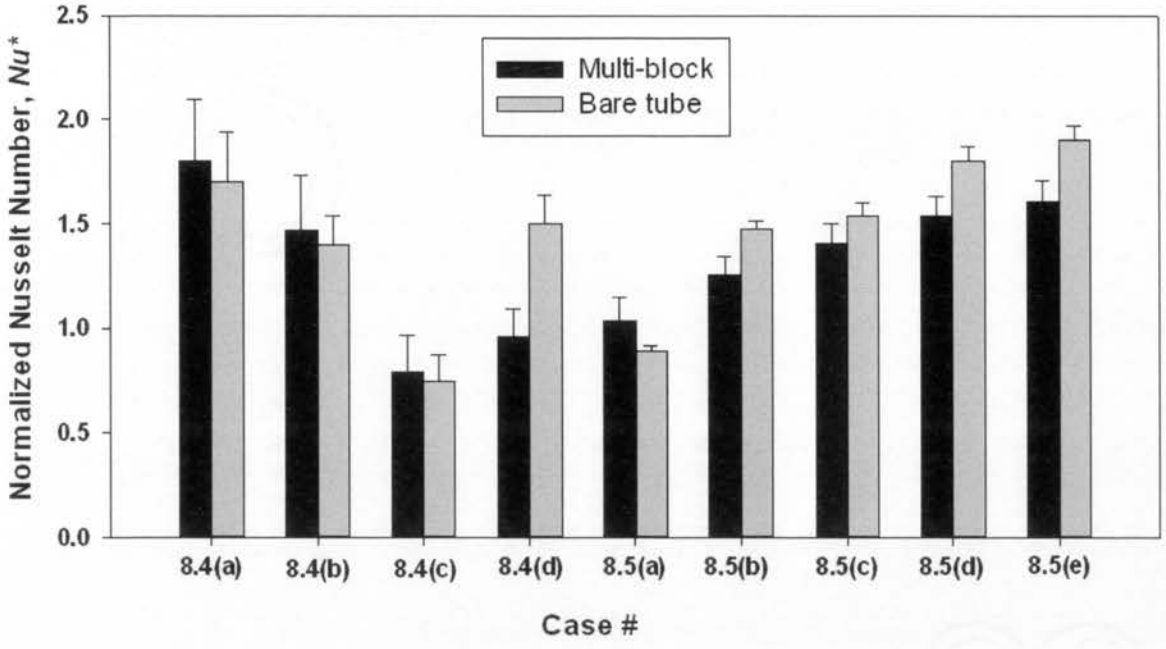

Figure 8.6: Comparisons of the normalized Nusselt number in the fully-developed region between the two heating systems. The error bar indicates one standard deviation for the fully-developed heat transfer data used to obtain the normalized Nusselt number (Nu^*).

8.2 Flow conditions

After finishing the system modification and verification experiments, preliminary tests on non-boiling, gas-liquid annular flow were carried out to identify the potential challenges for a further study of the flow and heat transfer characteristics of this flow regime. The effect of liquid phase properties on the annular flow pattern was first examined by using water and ethylene glycol as the liquid phase for a condition of U_L = 0.02 m s^{-1} and U_G = 9.5 m s^{-1}. Then, a series of nitrogen-water flows with a constant liquid superficial velocity (0.02 m s^{-1}, Re_L = 43 and gas superficial velocity varying from 4.8 to 26.0 m s^{-1} ($530 < Re_G < 2890$) were studied. The effect of liquid flow rate ($0.02 < U_L < 0.11$, $43 < Re_L < 217$) at constant nitrogen flow rate (9.5 m s^{-1}, Re_G = 1930) was also studied. Table 8.2 summarises the tested conditions, covering the slug-annular and annular flow regimes.

Table 8.2: Summary of the flow conditions studied.

Parameters	Water (W)	Ethylene glycol (EG)
Gas superficial velocity, U_G (m s^{-1})	4.8- 26.0	9.5
Liquid superficial velocity, U_L (m s^{-1})	0.02-0.11	0.02
Homogeneous void fraction, β	0.978-0.999	0.998
Gas Reynolds number, Re_G	530-2890	1060
Liquid Reynolds number, Re_L	43-217	2
Capillary number, Ca	0.064-0.336	7.422
Weber, We	625-18000	14100

8.3 Flow Visualization

Gas-liquid annular flow in microchannels is characterised by a central gas core surrounded by a thin wavy liquid film on the channel wall. Figure 8.7 shows typical flow images obtained for the case with U_L = 0.02 m s^{-1} and U_G ~ 9.5 m s^{-1} using nitrogen as the gas phase, and (a) water and (b) ethylene glycol as the liquid phase. For this flow condition large-amplitude waves were observed in both systems, with the wave pattern being transient and propagating along the flow direction. While ripples (small-amplitude waves) were observed near the large-amplitude waves for water, the gas-liquid interface for ethylene glycol was relatively smooth for region away from the large-amplitude wave. Due to the mismatch of the refractive index between the silica tube (R.I. = 1.46) and water (R.I. = 1.33), optical distortion arose from the inner curved surface of the tube and made it very difficult to identify the gas-liquid interface from the images directly, as described in Chapter 4. The visibility at the near wall region was increased when a longer aperture opening time or slower shutter speed (Δt = 1/100000 s) than that used in the Taylor flow experiments (Δt = 1/500000 s) was employed (Figure 8.7 (a)). However, this is compromised by the sharpness of the image, as the displacement of the moving interface (δ_z) within one frame period which can be estimated using Eq. (8.4) is directly proportional to the shutter speed.

$$\delta_z = U_{TP}\Delta t \tag{8.4}$$

For flow with a superficial gas velocity of 9.5 m s^{-1}, the displacement of the interface in one frame period can be up to ~100 μm, which is about ~100 times of a typical Taylor flow recording reported in Chapter 4. Therefore, the new setting is not really desirable for capturing the highly transient annular flow pattern but represents the best compromise with the available apparatus. To improve the visibility at the near wall region without sacrificing the sharpness of images, a stronger illumination source such as a flash is suggested in the future.

As seen in Figure 8.7 (b), a lot of small gas bubbles were dispersed in the liquid film surrounding the gas core when ethylene glycol was used. These dispersed bubbles are not desired and may increase the complexity in understanding the heat transfer behaviour a great deal. Therefore, all future experiments were done using water as the liquid phase, where dispersed bubbles were not seen in the liquid film.

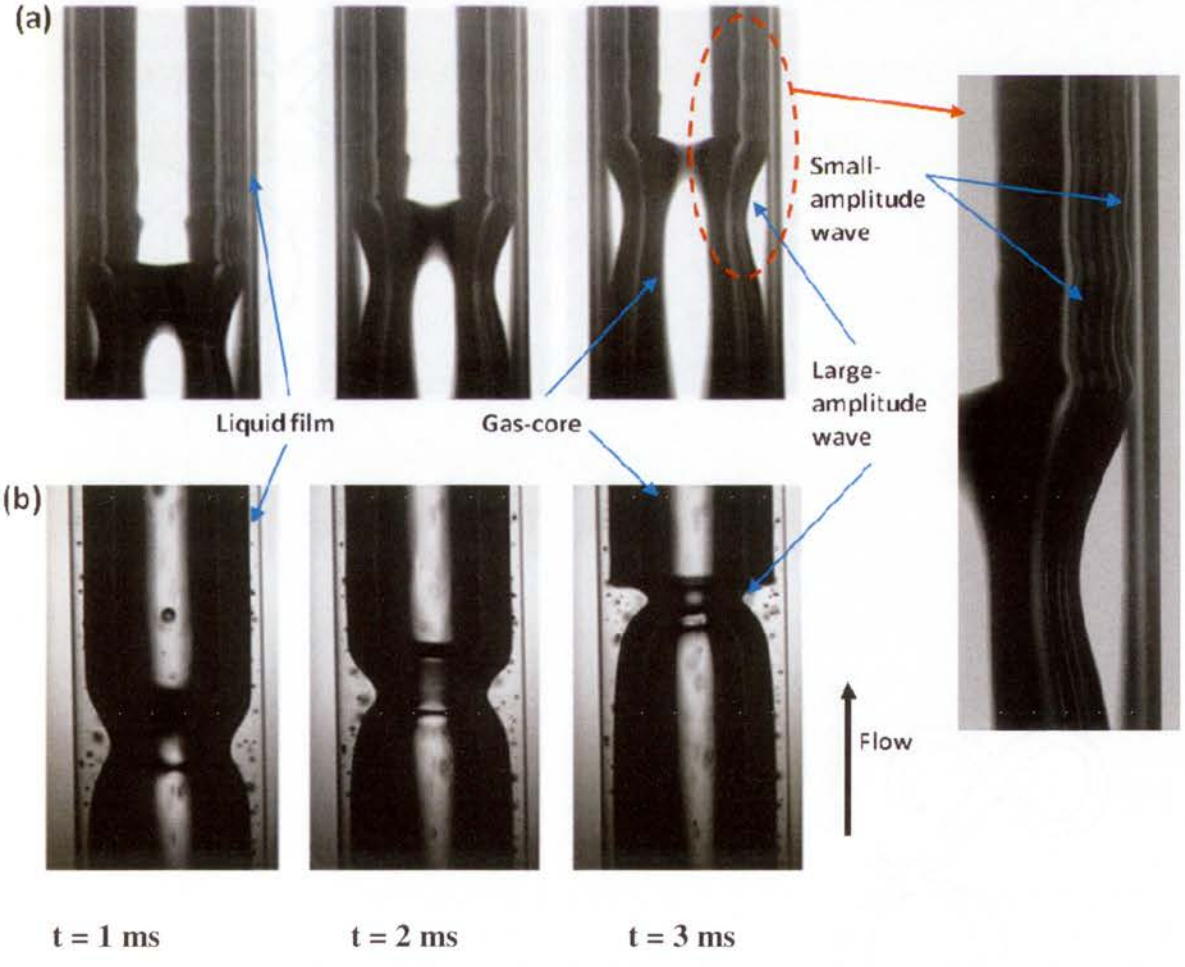

Figure 8.7: Typical images for flow with U_L = 0.02 m s^{-1} and U_G ~ 9.5 m s^{-1} using (a) water and (b) ethylene glycol as the liquid phase.

8.3.1 Effect of gas and liquid flow rates

The effects of the gas and liquid flow rates on the flow structures are shown in Figure 8.8 and Figure 8.9, respectively. Bubble breakage was observed for flow with relatively lower gas superficial velocity (Figure 8.8 (a)), and such pattern is named slug-annular flow. For annular flow at higher gas flow rates (Figure 8.8 (b)-(d)), the wave patterns are asymmetric, and transient in nature. As the gas superficial velocity increases at constant liquid flow rate, the amplitudes of the waves decrease, while the wave frequency increases. For a constant gas flow rate, the wave amplitude and frequency were found to increase with increasing liquid velocity. Moreover, the flow was found to become less stable at higher liquid flow rates (Figure 8.9 (b)).

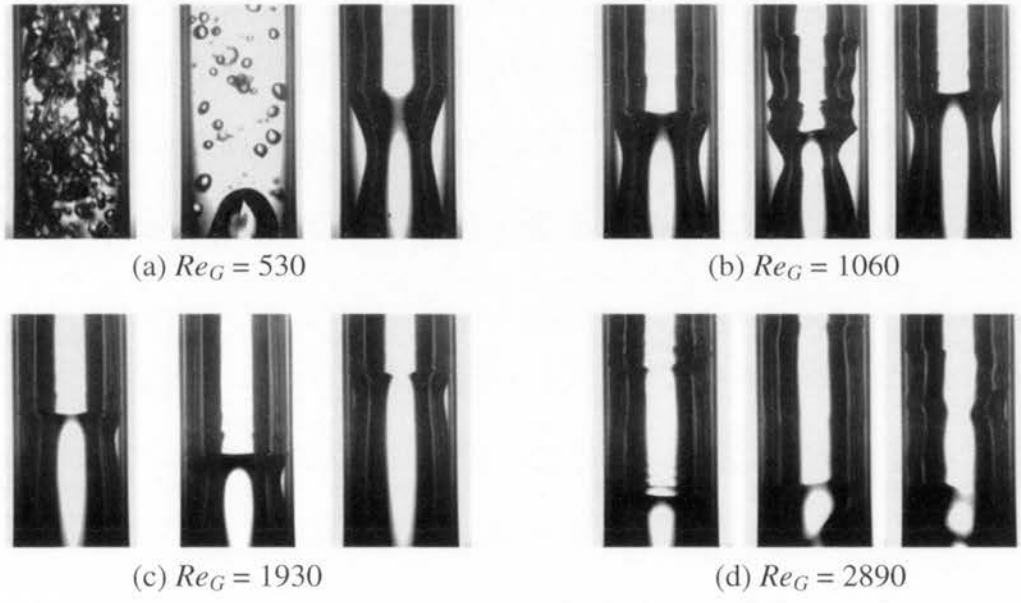

Figure 8.8: Typical flow structures at discrete time moment for flow with different gas velocities, (a) U_G = 4.8 m s^{-1}, Re_G = 530 (b) U_G = 9.5 m s^{-1}, Re_G = 1060 (c) U_G = 17.3 m s^{-1}, Re_G = 1930 and (d) U_G = 26.0 m s^{-1}, Re_G = 2890 at constant liquid velocity (U_L = 0.02 m s^{-1}, Re_L = 43).

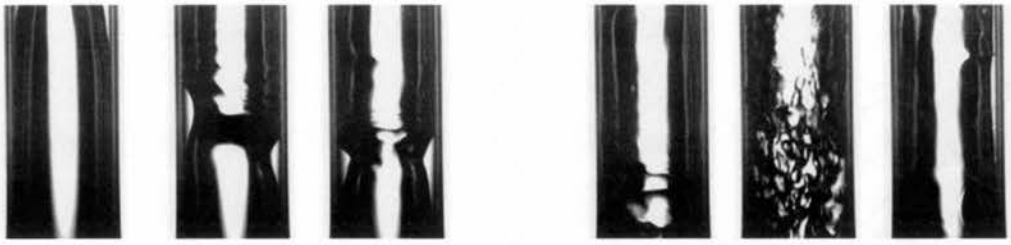

(a) $Re_L = 113$ (b) $Re_L = 217$

Figure 8.9: Typical flow structures at discrete time moment for flow with different liquid velocities, (a) $U_L = 0.05$ m s^{-1}, $Re_L = 108$, and (b) $U_L = 0.11$ m s^{-1}, $Re_L = 217$ at constant gas velocity ($U_G = 17.3$ m s^{-1}, $Re_G = 1930$).

8.4 Pressure drop

Figure 8.10 shows the variation of the inlet pressure measured at the liquid stream near the T-mixer with the gas Reynolds number for flow with constant liquid flow rates. The inlet pressure increases with increasing gas and liquid Reynolds number. For all liquid flow rates studied ($U_L = 0.02$–0.11 m s^{-1}, $Re_L = 43$–217), the inlet pressure first increases slowly as U_G increases from 4.9 to 9.5 m s^{-1}, then it increases more steeply as the gas flow rate is increased further. Similar observations were reported by Bao *et al.* (2000) who studied the pressure drop and heat transfer characteristics of two-phase flow encompassing Taylor, slug-annular and annular flow regimes in a circular channel of 1.95 mm diameter. For the variation of pressure gradient with gas superficial velocity, they showed an inflection point at around $U_G \approx 6$–8 m s^{-1}, where they proposed transition from slug to annular flows occurred. Beyond the infection point, the pressure gradient increased sharply with increasing U_G.

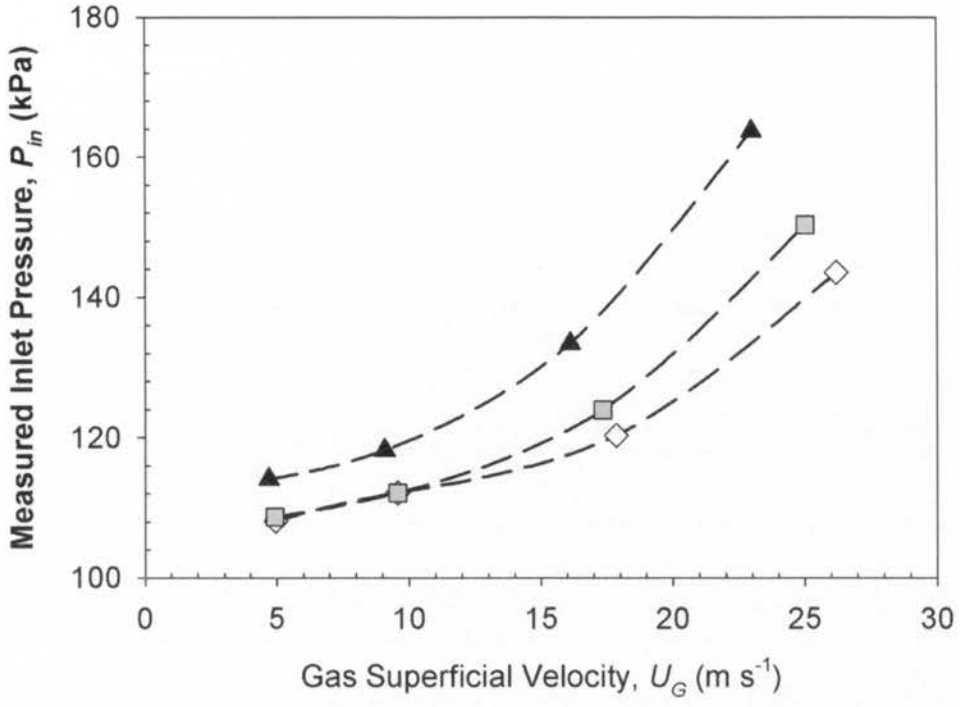

Figure 8.10: Inlet pressure measured at the liquid stream near the T-junction mixer for (◇) $Re_L = 43$, (▫) $Re_L = 108$, and (▲) $Re_L = 217$ as a function of the gas superficial velocity.

For nitrogen-water annular flow heat transfer experiments, evaporation of liquid into the gas phase is inevitable due to the variation of temperature and pressure along the test section. Therefore, an accurate prediction of the pressure drop along the system is critical in evaluating the evaporation rate (Eq. 3.17) and hence the amount of energy that goes into evaporation (Eq. 3.18). Satisfactory predictions of the pressure drop using the separated flow model of Lockhart-Martinelli correlation (1949) were reported previously (Bao *et al.*, 2000, Zhao and Bi, 2001, Kawahara *et al.*, 2002). Figure 8.11 compares the measured inlet pressure with the values calculated using the Lockhart-Martinelli correlation. Good agreement is achieved between the experimental data and the predicted values. Though the Lockhart-Martinelli correlation gives a good representation of the data collected here, it is worth mentioning that the correlation was not developed specifically for the annular flow regime but for various flow patterns for conventional channels. Furthermore, it has been reported that the frictional pressure drop of two-phase flow in microchannels is flow regime dependent (Triplett *et al.*, 1999b, Bao *et al.*, 2000). Therefore, more experimental data are required to validate the use of the Lockhart-Martinelli correlation in predicting pressure drop of gas-liquid annular flow in microchannels or to gain more physical insights for the development of a new pressure drop correlation.

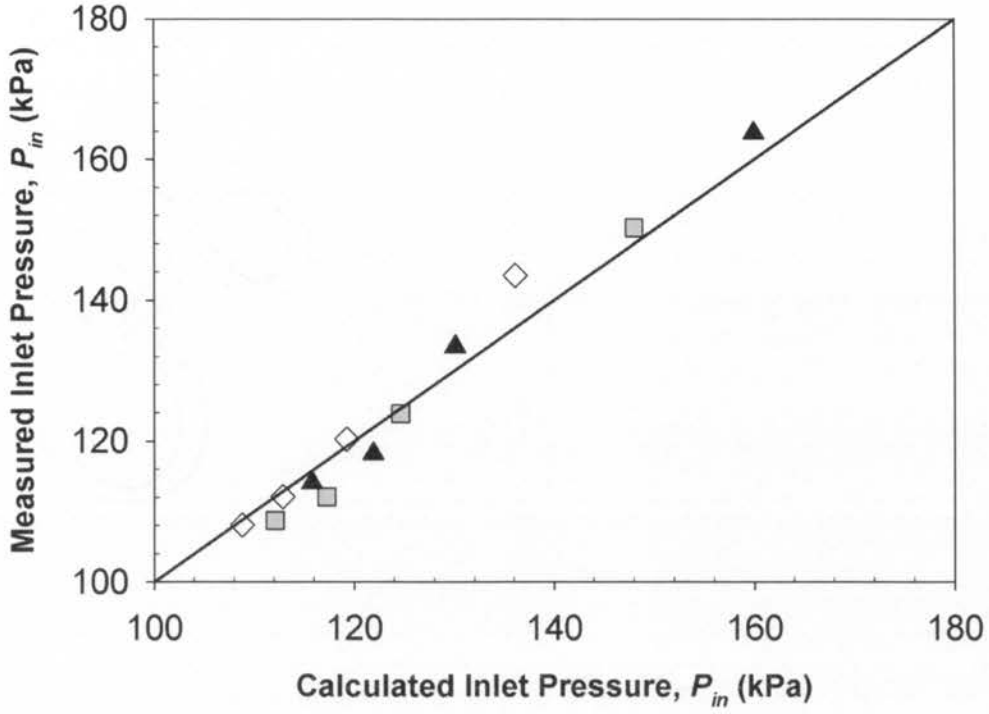

Figure 8.11: Comparisons of the measured inlet pressure with the calculated values using the Lockhart-Martinelli correlation (1949) for (◇) $Re_L = 43$, (▫) $Re_L = 108$, and (▲) $Re_L = 217$.

8.5 Heat transfer

The heat transfer characteristics of non-boiling, nitrogen-water annular flow in a 2 mm circular channel were studied. Figure 8.12 shows the temperature profiles along the wall, together with the inlet and outlet temperatures for flows with a fixed liquid flow rate ($Re_L = 43$) and various gas flow rates ($530 < Re_G < 2890$) for the same heat input $Q_{in} = 4.7$ W. For comparison, the data collected for single-phase liquid flow ($Re_L = 43$) are also shown in Figure 8.12. The wall and outlet temperatures for gas-liquid annular flow are significantly lower than those of the single-phase liquid flow, indicating a more effective cooling with the introduction of the fast moving gas. It is also note that the cooling efficiency increases with increasing gas flow rate. Similar experimental observations were reported experimentally by Bar Cohen *et al.* (1995) and Liu *et al.* (2006). Both studies suggested that the high cooling ability of gas-liquid annular flow is attributed to the coupled evaporative cooling and convective heat transfer.

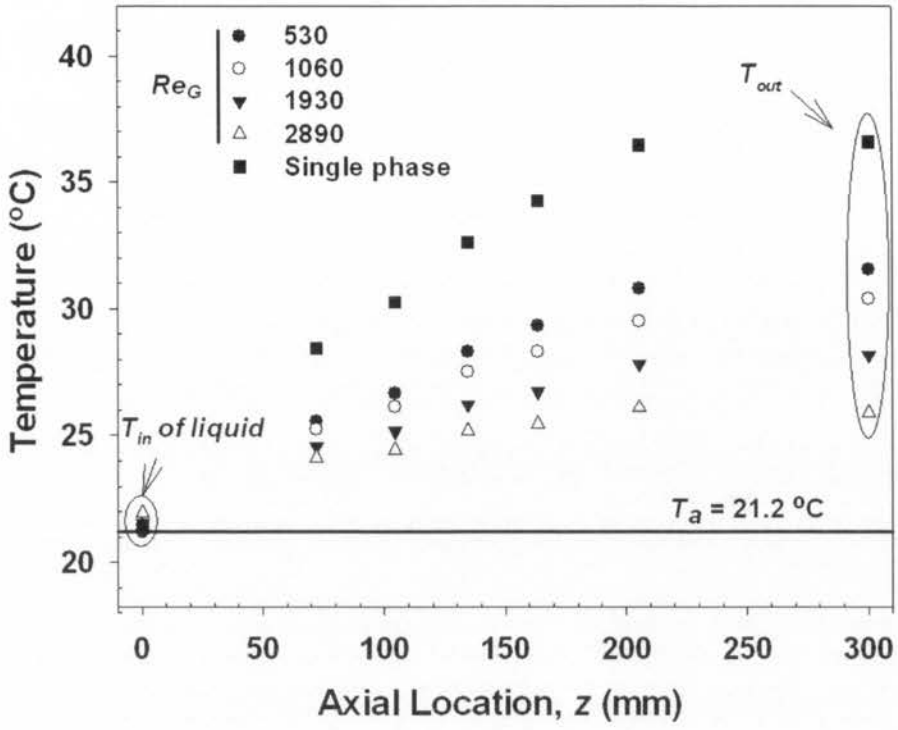

Figure 8.12: Temperature profiles along the wall, inlet and outlet temperatures for flows with a fixed liquid flow rate ($Re_L = 43$) and various gas flow rates ($530 < Re_G < 2890$) for the same heat input, $Q_{in} = 4.7$ W.

The heat transfer rates for gas-liquid annular flow were determined in the same manner as that used for Taylor flow heat transfer. Figure 8.13 shows the variation of the normalized Nusselt number and the proportion of the total heat input go to evaporation with the gas Reynolds number for corresponding conditions used in Figure 8.12. The value of Nu* first decreases with increasing Re_G then remains relatively constant for $1060 < Re_G < 2890$. The trend is different from that reported by Bao (1995) and Bao *et al.* (2000) who showed the heat transfer coefficient increased monotonically with the gas Reynolds number at constant liquid flow rate for $Re_G > 1000$ for conditions where evaporation was negligible. For the present study conditions, it is noted that significant fraction of heat input ends up in evaporation and the amount of energy increases with increasing gas flow rate. As evaporation occurs, the composition of the gas and liquid phases varies along the tube. Estimating the bulk temperature using the homogeneous properties at the inlet (Eq. 3.15 and 3.16) is of concern. Nonetheless, the results confirm that the evaporative cooling contributes appreciably in the heat transfer enhancement brought about by the gas-liquid annular flow observed here.

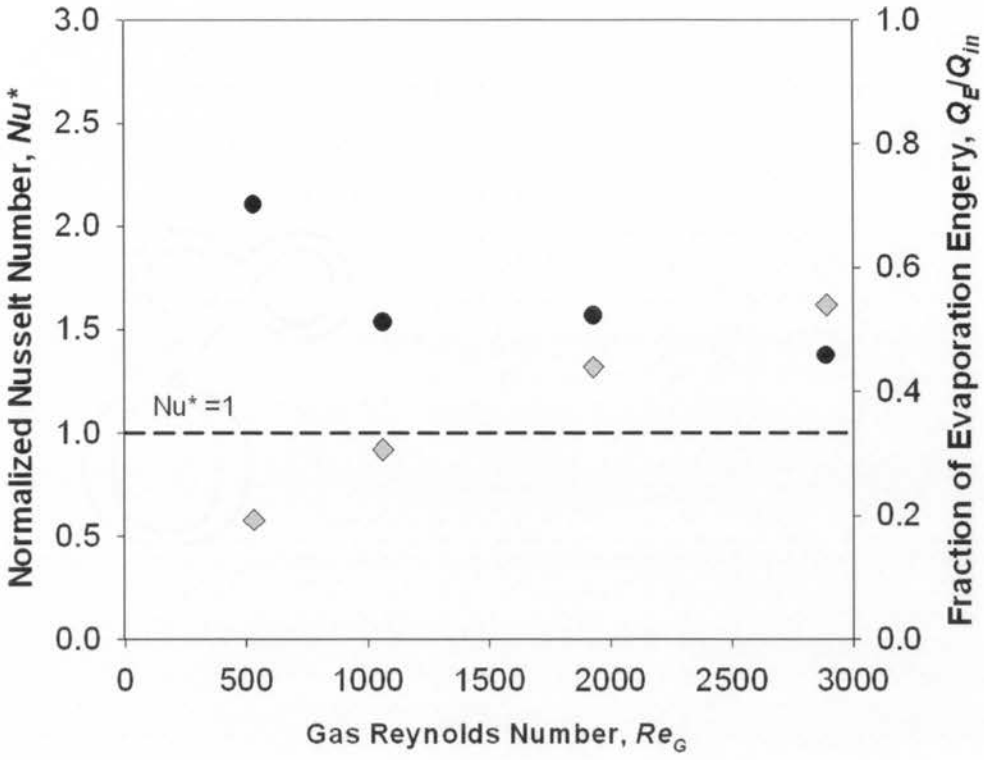

Figure 8.13: Variations of the normalized Nusselt number (●) and the fraction of evaporation energy (◈) with the gas Reynolds number for corresponding conditions used in Figure 8.12.

8.5.1 Effect of evaporation

To have better understanding of the effect of evaporation for nitrogen-water annular flow in a microchannel, a series of experiments without heating for the above flow conditions (Re_L = 44 and 530 < Re_G < 2890) were conducted and the results are shown in Figure 8.14. While the wall temperature profile shows only a minor effect of evaporation for flow with relatively lower gas flow rates (Re_G = 530 and 1060), evaporation becomes more significant for flow with higher Re_G (1930 and 2890) for which the wall temperatures drop below the ambient temperature (T_a) and decrease along the test section. Also, the outlet temperature drops below the inlet liquid temperature. As the system pressure drops along the test section, evaporation take place at the gas-liquid interface. Since no heating was supplied to the system which was well insulated, the evaporation energy can only be drawn from the internal energy of the water or nitrogen, resulting in a decrease of the liquid and gas temperature and subsequently the wall temperature. Such evaporative cooling is more apparent for flows with higher gas flow rates due to the more significant pressure drop along the test section.

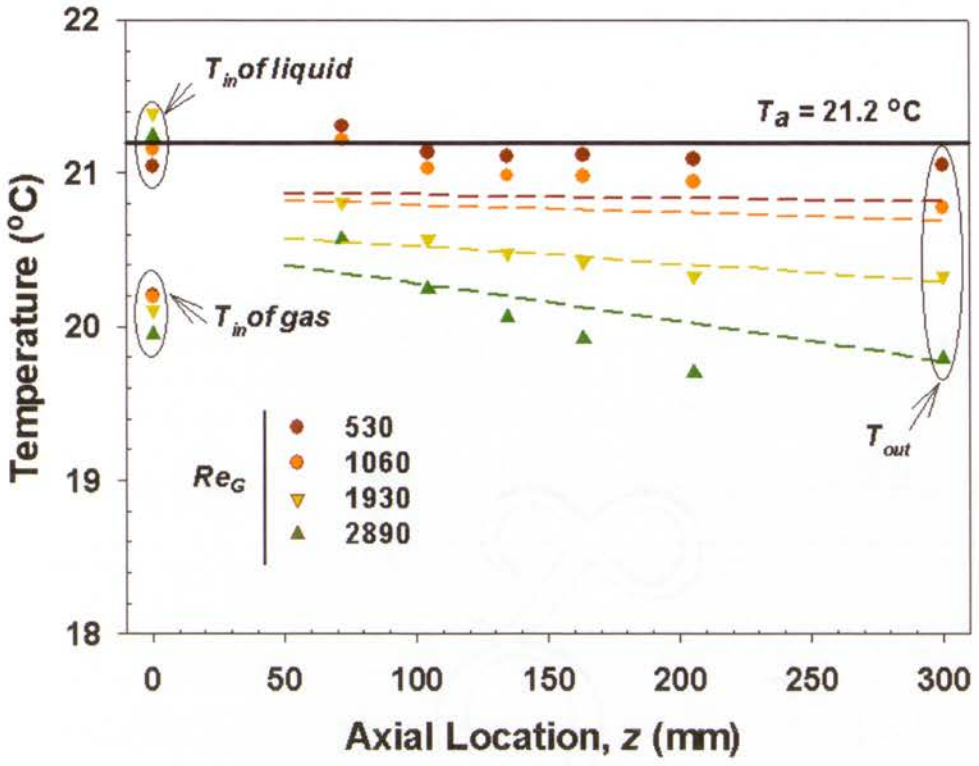

Figure 8.14: Temperature profiles along the wall, inlet and outlet temperatures for annular flows with a fixed liquid flow rate (Re_L = 43) and various gas flow rates (530 < Re_G < 2890) without heating. The lines of corresponding colours are adiabatic saturation temperature estimated using Aspen HYSYS software.

The adiabatic saturation temperature along the tube was estimated using Aspen HYSYS software with the pressure drop determined using the Lockhart-Martinelli correlation. Figure 8.15 shows a schematic of the process flowchart used in Aspen HYSYS to determine the equilibrium temperature.

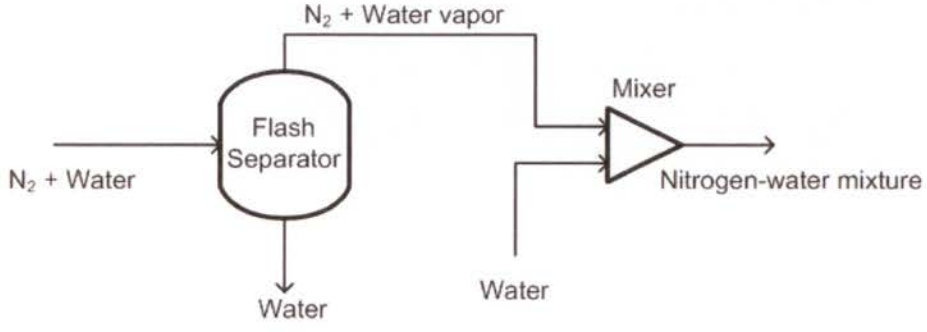

Figure 8.15: Schematic of Aspen HYSYS process flowchart.

The calculated values are compared with the experimental data in Figure 8.14 and reasonably good agreement was achieved. The small discrepancy can be attributed to the combined effects of the inaccuracy of the thermocouples used and the estimation of the pressure drop along the test section, as well as the uncertainty of the degree of saturation of the gas inlet. Nonetheless, the results suggest that it might be possible in future work to determine the local pressure from measurements of the wall temperature profile when the inlet conditions, including the gas and liquid inlet temperatures, degree of saturation of the gas inlet, are known.

The effect of evaporation for nitrogen-water annular flow heat transfer at different wall heat fluxes for constant liquid and gas flow rates (Re_L = 43 and Re_G= 1930) is shown in Figure 8.16. The outlet temperature would follow the line for Q_E/Q_{in} = 0, if there were no evaporation taking place in the system. However, for the annular flow conditions studied here, evaporation is always important and cannot be decoupled from the convective heat transfer. As the heat input increases from 4.7 W to 68.3 W, a larger portion of the heat input (from 50% to ~75%) goes to evaporation. This coupling effect enhances the complexity of understanding the heat transfer characteristics of annular flow considerably. As the liquid film evaporates, its thickness decreases gradually along the test section. Also, estimation of the bulk temperature in the same manner as was done for Taylor flow using the homogeneous properties at the inlet may no longer be correct.

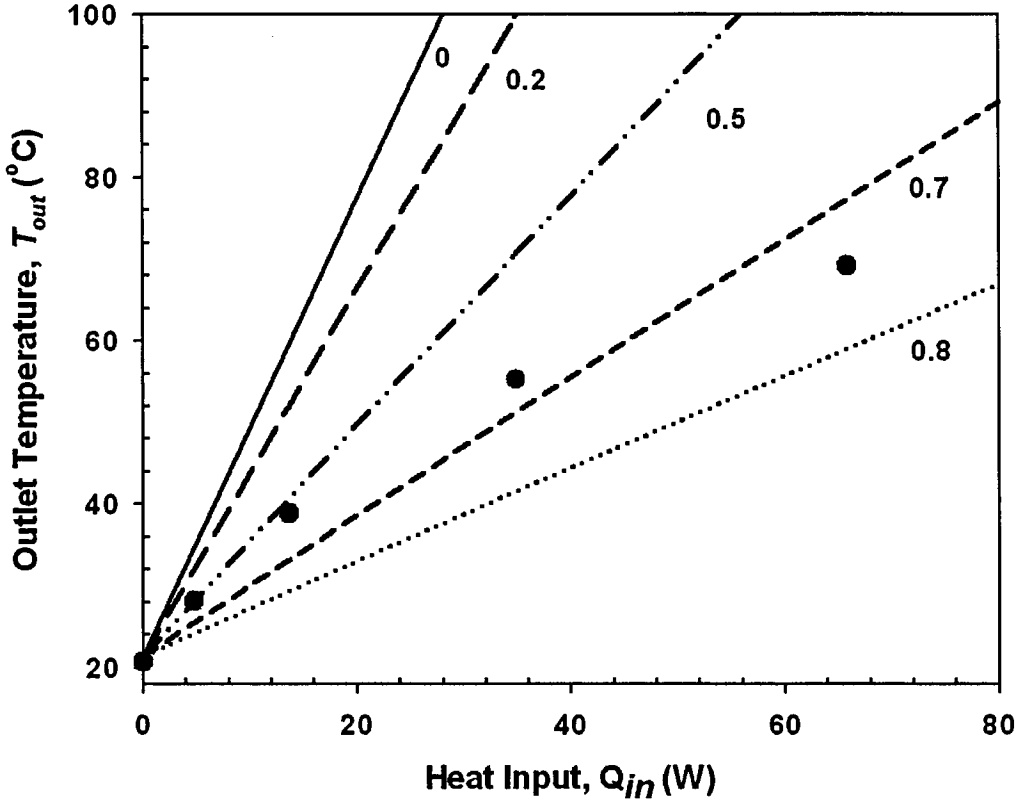

Figure 8.16: The variation of the outlet temperature with the wall heat flux for fixed liquid and gas flow rates (Re_L = 43 and Re_G = 1930). The lines are the calculated outlet temperature for which a fixed portion of the heat input (Q_E/Q_{in} = 0, 0.2, 0.5, 0.7 and 0.8) goes to evaporation.

8.6 Summary

A bare tube heating test section with a much smaller time constant (~5 ms) than that of the multi-block heating test section (~200 s) was constructed to investigate the heat transfer characteristics of gas-liquid annular flow in microchannels. The effect of wall characteristics of the test section on Taylor flow heat transfer was first examined. Similar heat transfer rates were obtained for the two different heating systems, suggesting a minor effect of the thermal capacity of the test section on Taylor flow heat transfer. Taking advantage of the small time constant of the bare tube heating test section, the operation time for gas-liquid two-phase heat transfer experiments was reduced from hours to minutes.

Preliminary visualization and heat transfer tests of gas-liquid annular flow in a vertical upward tube of d = 2.00 mm were performed for different flow conditions ($2 < Re_L < 217$,

$530 < Re_G < 2890$). Various experimental challenges in studying the flow and heat transfer characteristics of this flow regime have been identified and recommendations for further study are summarized:

1. When ethylene glycol was used as the liquid phase, many small gas bubbles were found to disperse in the liquid film, giving rise to higher complexity in understanding the flow and heat transfer characteristics for this flow pattern. Since ethylene glycol has a similar refractive index as that of the silica tube, the gas-liquid interface can be directly visualized to allow direct measurement of the average film thickness and characterization of the transient waviness. Therefore, the generation of an annular flow without small bubbles distributed in the liquid film would be beneficial to investigate the relationship between the flow characteristics (average film thickness, wave amplitude, wave frequency, etc.) and heat transfer rates. This may be achieved by using other inlet geometries, for example flow focusing mixing devices, co-flowing configurations, etc., which allow the liquid phase to form a film at the wall without significant mixing with the gas phase at the mixing zone.

2. The transient waviness at the gas-liquid interface for nitrogen-water annular flow was captured successfully and found to be asymmetric with waves being observed to propagate along the flow direction. The frequency of the waves was found to increase with increasing gas and liquid flow rates. While the wave amplitude increased with increasing liquid flow rate, it decreased with increasing gas flow rate. Though the visibility at the near wall region were enhanced by employing a longer aperture opening time, the effect of refraction at the inner curved surface of the tube due to the mismatch of refractive indices between the liquid phase and tube material still existed. In addition, the sharpness of the images, which is very important to capture the highly transient structure, was compromised. Replacing the silica tube (R.I = 1.46) by fluorinated ethylene propylene (FEP) Teflon tube which has similar refractive index (R.I. = 1.35) as that of water (R.I. = 1.33) for nitrogen-water annular flow may improve the image quality significantly. Since the surface of natural FEP tube is hydrophobic, surface treatment may be required to create a hydrophilic inner surface to allow the formation of a continuous liquid film at the wall.

3. Preliminary heat transfer experiments showed that the wall temperatures for non-boiling nitrogen-water annular flow were significantly lower than those for single-phase flow of the same liquid flow rate ($Re_L = 43$). The wall temperature was found to be the lowest for flow with the largest gas flow rate ($Re_L = 43$, $Re_G = 2890$). The heat transfer enhancement brought about by the nitrogen-water annular flow was attributed to a combination of evaporation of the liquid film and convective heat transfer. It is found that the effect of evaporation cannot be decoupled from the convective heat transfer when water was used as the liquid phase. Complexity in understanding the annular flow heat transfer characteristics then arises from the coupling of these two heat transfer mechanisms. Further experiments need to be conducted using a liquid with negligible vapour pressure to decouple the two heat transfer mechanisms.

4. Reasonably good agreement was achieved between the wall temperature profiles for gas-liquid annular flow without heating and those obtained based on adiabatic saturation calculation. This finding opens up a possibility for local pressure measurements by simply measuring the wall temperature along the tube. The validation of this method have to be confirmed by more accurate measurements of the inlet conditions, including the gas and liquid inlet temperatures and degree of saturation at the gas inlet.

Chapter 9
Conclusions and Recommendations

This thesis presented a comprehensive experimental study of the hydrodynamics and heat transfer characteristics of non-boiling, gas-liquid Taylor flow in microchannels for vertical upward flow. Analysis of data collected across a wide range of conditions was performed to understand the underlying physical mechanisms governing the hydrodynamics and heat transfer of Taylor flow. The gravitational effect on horizontal Taylor flow which has generally been neglected in the past was examined and quantified. Preliminary non-boiling, gas-liquid annular flow visualization and heat transfer experiments were performed to identify the potential experimental challenges for study of this flow regime in microchannels. This Chapter summarizes the conclusions drawn from this work and provides recommendations for future research in the field.

9.1 Conclusions

9.1.1 Experimental design

The thickness of the fully-developed film surrounding the gas bubbles and size and intensity of the recirculation zone inside the liquid slug region are expected to have significant effects on the heat transfer enhancement brought about by Taylor flow in microchannels. The dependence of these flow characteristics on the fluid properties as expressed in terms of the Capillary number is well documented (Bretherton, 1961, Taylor, 1961, Thulasidas *et al.*, 1997). Therefore, experiments were performed in a 2.00 mm diameter vertical upward circular channel using water (W), 50 wt% ethylene glycol/water mixture (EG/W) and pure ethylene glycol (EG) as the liquid phases to cover a wide range of Capillary numbers ($0.001 < Ca < 0.180$) for the investigation of its influence on the heat transfer rate of Taylor flow.

The slug length, as another important parameter controlling the heat transfer rate of Taylor flow, was either not well-controlled and/or its effect was coupled with other flow parameters for experimental studies in the past (Oliver and Wright, 1964, Oliver and Young Hoon, 1968). A reliable and repeatable technique to produce Taylor bubbles using a T-junction mixer was

established. Moreover, three T-junction mixers of different internal diameters were used to generate bubbles and slugs of different lengths for the same mixture velocity and homogeneous void fraction. Therefore, a direct examination of the effect of slug length on Taylor flow heat transfer without the interference of the effects of the mixture velocity and homogenous void fraction was achieved.

9.1.2 Flow and heat transfer characteristics of vertical upward Taylor flow

Taylor flow with regular bubble and slug lengths was first characterized by performing visualization tests under isothermal condition (21 °C). The range of slug lengths studied in this thesis varied from 1 to 220 tube diameters for the range of mixture velocity of $0.10 < U_{TP} < 0.53$ m s^{-1} and homogeneous void fractions in the range $0.03 < \beta < 0.90$. High quality pictures showing a clear gas/liquid interface at the near wall region were achieved by matching the refractive indices of the silica tube and ethylene glycol used as the liquid phase. The trends of the experimental film thickness and the ratio of the void fraction to the homogenous void fraction (ε_G/β) with the Capillary number were found to agree well with the established literature (Irandoust and Andersson, 1989a, Aussillous and Quéré, 2000, Liu *et al.*, 2005). Scatter of these values was observed at a given Capillary number due to the use of different homogeneous void fractions (β). A modified scaling law based on the work of Garstecki *et al.* (2006) was proposed to predict the bubble lengths and is given by

$$\frac{L_B}{d} = \left(\frac{d_M}{d}\right)^3 \left(\alpha_1 + \alpha_2 \frac{Q_G}{Q_L}\right) \tag{9.1}$$

where $\alpha_1 = 1.10$ and $\alpha_2 = 1.25$. Generally, good agreement was found between the generated bubble length and the predicted values, with most of the experimental data falling within $\pm 30\%$ of the predictions. For flows where the curvature of the bubble caps and tails can be neglected, the corresponding slug length can be approximated as $L_S \approx L_B(1-\beta)/\beta$.

Systematic heat transfer experiments for well-characterized Taylor flow were performed for constant wall heat flux boundary conditions using a multi-block heating section. The maximum heat transfer enhancement achieved in the present study was 3.2 times that of single-phase fully-developed laminar flow. The dependencies of the heat transfer rate on the slug length, mixture velocity, homogenous void fraction and fluid properties were identified. The two-phase Nusselt number was found to increase with increasing mixture velocity with

its influence being more pronounced for flow with shorter slugs. For the same mixture velocity and homogeneous void fraction, flow with shorter slugs gave a higher heat transfer rate because the number of complete cycles of liquid recirculation in the same heating length increases with decreasing slug length, leading to more intensive transport of hot fluid from the region near the wall to the tube centre. Due to the combined effects of the presence of internal recirculation zones inside the liquid slug and the reduction of the thermal mass with the introduction of the gas, an optimal homogenous void fraction was found for Taylor flow heat transfer. The value of β at which the maximum heat transfer rate occurred varied between $0.1 < \beta < 0.3$, depending on the mixture velocity, unit cell length, as well as the fluid used. For a similar mixture velocity, homogeneous void fraction and slug length, the order of heat transfer augmentation was always found to be W > EG/W > EG.

9.1.3 Taylor flow heat transfer modelling

Heat transferred from the wall in Taylor flow goes alternately to the bubble and slug regions as a succession of bubble and slug passes through the system. Analysis of Taylor flow heat transfer was, therefore, performed on a unit cell basis which consists of a gas bubble surrounded by a thin liquid film and a liquid slug. Three physical mechanisms governing the heat transfer of Taylor flow were suggested: (1) heat transfer from the wall to the bubble film, where it accumulates until the passage of the next slug; (2) heat transfer from the bubble film to the liquid slug, and (3) heat transfer from the wall to the recirculating slug. Depending upon the wall boundary conditions imposed on the system, the bubble film plays different thermal roles for the thermally fully-developed regions. While it is largely irrelevant for a constant wall temperature boundary condition, it provides a significant energy storage region for a constant wall heat flux boundary, with that energy being taken up by mixing with the overtaking slug. Regardless of the boundary conditions imposed, most of the heat is carried by the liquid slug for gas-liquid Taylor flow. Therefore, the overall heat transfer coefficient (h_{TP}) is just that arising in the slug where the contact surface with the wall/liquid film has an area proportional to L_S/L_{UC}.

Since the flow and heat transfer behaviour in the slug remains hydrodynamically and thermally developing laminar flow, a good correlation was found between the slug heat transfer coefficient ($Nu_L^* = Nu_{TP} \cdot L_{UC}/L_S$) and the dimensionless slug length equivalent to an inverse Graetz number based on the slug length ($L_S^* = L_S/(Re_{TP} \cdot Pr \cdot d)$). A Hausen-type

correlation was developed specifically for nitrogen-water Taylor flow heat transfer, due to its potential for industrial use and is given by

$$Nu_L^* = Nu_{LO} + \frac{c_1}{L_S^* + c_2 L_S^{*1/3}} \tag{9.2}$$

where c_1 = 0.29 and c_2 = 0.15. The correlation described the experimental data using water as the liquid phase with an accuracy of $\pm$20% of the measured values, but it did not provide an accurate description for other fluids. It was found that the result for individual fluids followed the general form for heat transfer in developing laminar flow, with $Nu_L^* = f(L_S^*)$ specific to each fluid.

The difference in the heat transfer performance observed for different fluid systems is attributed to the different flow structures, including the thickness of the film surrounding the bubble and the strength of the recirculation inside the liquid slug, which depends strongly on the fluid properties expressed in terms of the Capillary number. The slug recirculation impacts on the heat transfer process in the slug through interactions between the bubble film and the recirculating flow in the slug, which was also found to be a strong function of the Capillary number.

An empirical model correlating all the identified dimensionless groups, including the apparent slug Nusselt number, the dimensionless slug length and the Capillary number, was proposed for the heat transfer of Taylor flow, taking the form

$$Nu_L^* = Nu_{LO} + c_3 (L_S^*)^p (Ca)^q \tag{9.3}$$

where c_3 = 0.13, $p = -0.46$ and $q = -0.30$. Good agreement between the experimental data obtained for all fluid systems and the correlation was achieved, indicated by a small relative standard deviation (14%).

9.1.4 Gravitational effect on horizontal Taylor flow

Neglecting the effect of gravity for horizontal gas-liquid Taylor flow in millimetre-size channels may not always be appropriated. Significant bubble asymmetry was observed for nitrogen-ethylene glycol Taylor flow in three circular channels of different internal diameters (d = 1.12, 1.69, 2.12 mm giving Bond numbers (Bo) of 0.287, 0.653 and 1.028). High quality

white light images were digitized to allow direct comparison of the top and bottom halves of the bubble on the vertical plane passing through the channel axis. The results showed that the thickness of the top film decreased gradually while that of the bottom film increased along the bubble. In addition to the axial variation, the film thickness surrounding the bubble was found to increase from the top to the bottom of the tube. From the parametric study, the Bond (Bo) and Capillary (Ca) numbers were identified as important parameters controlling the drainage flow.

μPIV measurements indicated a significant gravity-induced drainage flow from the top to the bottom of the channel in the film region across the bubble. For a region far from the bubble ends, the axial velocity was negligible when compared with the drainage velocity. The drainage velocity was found to increase from the wall to the gas/liquid interface and to adopt a parabolic profile. A simplified model derived based on Nusselt's solution for laminar film condensation on a horizontal tube described reasonably well the drainage velocity profile in the liquid film at a cross-section away from the bubble ends. A non-dimensional analysis of the model showed that the ratio of the average drainage to bubble velocities is a function of the Bond and Capillary numbers as follows

$$\frac{U_d}{U_{TP}} \approx \frac{0.45 \cdot Bo \cdot Ca^{1/3}}{(1 + 3.35Ca^{2/3})^2} \sin\theta \tag{9.4}$$

The gravitational effect on the bubble behaviour vanishes for small value of Bo and/or Ca. The drainage model was also able to explain the measured tilt of the bubble.

No significant influence of gravity on the heat transfer rates of Taylor flow in a 2.00 mm microchannel was observed between the horizontal and vertical heating systems, regardless of the non-uniform film thickness surrounding the gas bubble noted in the horizontal flow direction. This is consistent with the physical picture of Taylor flow heat transfer developed in this thesis.

9.1.5 Annular flow

A bare tube heating test section with a short thermal time constant (~5 ms) was constructed to investigate the heat transfer characteristics of gas-liquid annular flow in microchannels. Various experimental challenges in studying the flow and heat transfer characteristics of non-

boiling, gas-liquid annular flow were identified through performing preliminary visualization and heat transfer tests in a vertical upward flow in a 2.00 mm diameter tube for different flow conditions ($2 < Re_L < 217$, $530 < Re_G < 2890$).

Many small gas bubbles were found to disperse in the liquid film when ethylene glycol was used as the liquid phase. The waviness at the gas/liquid interface for nitrogen-water annular flow was found to be highly transient and asymmetric. The wave frequency was found to increase with both the gas and liquid flow rates. While the wave amplitude increased with increasing liquid flow rate, it decreased with increasing gas flow rate.

Preliminary heat transfer experiments showed significant heat transfer enhancement brought about by the nitrogen-water annular flow. This augmentation was attributed to the combination of evaporation of the liquid film and convective heat transfer. Using water as the liquid phase, it was found that the effect of evaporation cannot be decoupled from the convective heat transfer.

9.2 Recommendations for future work

9.2.1 Taylor flow

The insights provided in this thesis have improved the understanding of the hydrodynamics and their relation to heat transfer of non-boiling, gas-liquid Taylor flow in circular microchannels significantly. Nonetheless, there are areas which require further investigation.

- The long thermal development length observed for systems using ethylene glycol/water mixture and ethylene glycol as the liquid phase was not found in the nitrogen-water system, regardless of the similar ranges of Péclet number for all systems. Explanation to account for the difference is lacking, but knowledge of this could be useful for reactor designs employing Taylor flow.

- Channels with a non-circular cross-sectional area are encountered in many microchannel heat exchangers and micro-fluidic devices. However, the understanding of the heat transfer characteristics of gas-liquid Taylor flow in non-circular microchannels is far less well developed than that for circular channels. The liquid film surrounding the bubble in these channels is no longer of constant thickness around the perimeter of the channel and

the recirculation zone may not be symmetric about the channel axis. Therefore, the heat transfer behaviour may be very different from that observed in circular microchannels. Further study on Taylor flow heat transfer in non-circular channels is worthwhile due to its practical relevance.

9.2.2 Annular flow

Given that the study of the flow and heat transfer characteristics of non-boiling, gas-liquid annular flow is still in its infancy, suggestions for further research are given.

- Good mixer designs to generate annular flow without tiny bubbles dispersing in the liquid film region are crucial for further study.

- Flow characteristics, including the average film thickness, wave amplitudes and frequency and the flow field inside the liquid film, could be important for the prediction of pressure drop, heat and mass transfer of annular flow in microchannels. Development of experimental techniques to collect such information is essential for a comprehensive study.

- Complexity in understanding the non-boiling, gas-liquid annular flow heat transfer characteristics arises from the coupling of evaporative and convective heat transfer mechanisms. Experiments conducted using a liquid with a very low vapor pressure to decouple the two heat transfer mechanisms would provide an important step for better understanding of the effect of the flow characteristics on the convective heat transfer behaviour of annular flow.

- The development of an evaporation model would be valuable to estimate the evaporative contribution to the overall heat transfer behavior for systems where evaporation is not negligible.

Reference

Akbar, M.K., Plummer, D.A. and Ghiaasiaan, S.M. 2003. On gas-liquid two-phase flow regimes in microchannels. *International Journal of Multiphase Flow,* 29, 855-865.

Akbar, M. K. and Ghiaasiaan, S. M. 2006. Simulation of Taylor flow in capillaries based on the volume-of-fluid technique. *Industrial & Engineering Chemistry Research,* 45, 5396-5403.

Angeli, P. and Gavriilidis, A. 2008. Hydrodynamics of Taylor flow in small channels: a review. *Proceedings of the Institution of Mechanical Engineers Part C-Journal of Mechanical Engineering Science,* 222, 737-751.

Anna, S. L., Bontoux, N. and Stone, H. A. 2003. Formation of dispersions using "flow focusing" in microchannels. *Applied Physics Letters,* 82, 364-366.

Armand, A. A. and Treschev, G. G. 1964. The resistance during the movement of a two-phase systems in horizontal pipe. *Izvestya Vsesoyuznogo Teplotekhnicheskogo Institua,* 1, 16-23.

Aussillous, P. and Quéré, D. 2000. Quick deposition of a fluid on the wall of a tube. *Physics of Fluids,* 12, 2367-2371.

Baird, J. R. 2001. *Phase-change heat transfer in narrow passages.* PhD Thesis, The University of Sydney.

Baird, J. R., Fletcher, D. F. and Haynes, B. S. 2003. Local condensation heat transfer rates in fine passages. *International Journal of Heat and Mass Transfer,* 46, 4453-4466.

Bao, Z. Y., Bosnich, M. G. and Haynes, B. S. 1994. Estimation of void fraction and pressure-drop for 2-phase flow in fine passages. *Chemical Engineering Research & Design,* 72, 625-632.

Bao, Z. Y. 1995. *Gas-liquid two-phase flow and heat transfer in fine passages.* PhD Thesis, The University of Sydney.

Bao, Z. Y., Fletcher, D. F. and Haynes, B. S. 2000. An experimental study of gas-liquid flow in a narrow conduit. *International Journal of Heat and Mass Transfer,* 43, 2313-2324.

Bar Cohen, A., Sherwood, G., Hodes, M. and Solbreken, G. 1995. Gas-assisted evaporative cooling of high-density electronic modules. *IEEE Transactions on Components Packaging and Manufacturing Technology Part A,* 18, 502-509.

Barnea, D., Luninski, Y. and Taitel, Y. 1983. Flow pattern in horizontal and vertical 2 phase flow in small diameter pipes. *Canadian Journal of Chemical Engineering,* 61, 617-620.

Barajas, A.M., Panton, R.L. 1993. The effects of contact angle on two-phase flow in capillary tubes. *International Journal of Multiphase Flow,* 19, 337-346.

Bercić, G. and Pintar, A. 1997. The role of gas bubbles and liquid slug lengths on mass transport in the Taylor flow through capillaries. *Chemical Engineering Science,* 52, 3709-3719.

Bertsch, S. S., Groll, E. A. and Garimella, S. V. 2008. Review and comparative analysis of studies on saturated flow boiling in small channels. *Nanoscale and Microscale Thermophysical Engineering,* 12, 187-227.

Betz, A. R. and Attinger, D. 2010. Can segmented flow enhance heat transfer in microchannel heat sinks? *International Journal of Heat and Mass Transfer,* 53, 3683-3691.

Brauner, N. and Maron, D. M. 1992. Identification of the range of small diameters conduits, regarding 2-phase flow pattern transitions. *International Communications in Heat and Mass Transfer,* 19, 29-39.

Bretherton, F. P. 1961. The motion of long bubbles in tubes. *Journal of Fluid Mechanics,* 10, 166-188.

Burns, M. A., Johnson, B. N., Brahmasandra, S. N., Handique, K., Webster, J. R., Krishnan, M., Sammarco, T. S., Man, P. M., Jones, D., Heldsinger, D., Mastrangelo, C. H. and Burke, D. T. 1998. An integrated nanoliter DNA analysis device. *Science,* 282, 484-487.

Chambers, R. D. and Spink, R. C. H. 1999. Microreactors for elemental fluorine. *Chemical Communications,* 883-884.

Chen, W. L., Twu, M. C. and Pan, C. 2002a. Gas-liquid two-phase flow in micro-channels. *International Journal of Multiphase Flow,* 28, 1235-1247.

Chen, I. Y., Yang, K. S. and Wang, C. C. 2002b. An empirical correlation for two-phase frictional performance in small diameter tubes. *International Journal of Heat and Mass Transfer,* 45, 3667-3671.

Chen, L., Tian, Y. S. and Karayiannis, T. G. 2006. The effect of tube diameter on vertical two-phase flow regimes in small tubes. *International Journal of Heat and Mass Transfer,* 49, 4220-4230.

Chen, Y., Shi, M., Cheng, P. and Peterson, G. P. 2008. Condensation in microchannels. *Nanoscale and Microscale Thermophysical Engineering,* 12, 117 - 143.

Chen, Y., Kulenovic, R. and Mertz, R. 2009. Numerical study on the formation of Taylor bubbles in capillary tubes. *International Journal of Thermal Sciences,* 48, 234-242.

Chisholm, D. 1967. A theoretical basis for the Lockhart–Martinelli correlation for two-phase flow. *International Journal of Heat and Mass Transfer,* 10, 1767-1778.

Christopher, G. F., Noharuddin, N. N., Taylor, J. A. and Anna, S. L. 2008. Experimental observations of the squeezing-to-dripping transition in T-shaped microfluidic junctions. *Physical Review E, 78,* 036317.

Chung, P. M. Y. and Kawaji, M. 2004. The effect of channel diameter on adiabatic two-phase flow characteristics in microchannels. *International Journal of Multiphase Flow,* 30, 735-761.

Cioncolini, A., Thome, J. R., Consolini, L. and Ong, C. L. 2010. Microscale adiabatic gas-liquid annular two-phase flow: analytical model description, void fraction, and pressure gradient predictions. *Heat Transfer Engineering,* 31, 310-320.

Cox, B. G. 1964. An experimental investigation of the streamlines in viscous fluid expelled from a tube. *Journal of Fluid Mechanics,* 20, 193-200.

Cubaud, T. and Ho, C.M. 2004. Transport of bubbles in square microchannels. *Physics of Fluid,s* 16, 4575-4585.

Cubaud, T., Ulmanella, U., Ho, C.M. 2006. Two-phase flow in microchannels with surface modifications. *Fluid Dynamics Research,* 38, 772-786.

Dai, L., Cai, W. F. and Xin, F. 2009. Numerical study on bubble formation of a gas-liquid flow in a T-Junction microchannel. *Chemical Engineering & Technology,* 32, 1984-1991.

de Menech, M., Garstecki, P., Jousse, F. and Stone, H. A. 2008. Transition from squeezing to dripping in a microfluidic T-shaped junction. *Journal of Fluid Mechanics,* 595, 141-161.

de Ryck, A. 2002. The effect of weak inertia on the emptying of a tube. *Physics of Fluids,* 14, 2102-2108.

Edvinsson, R. K. and Irandoust, S. 1996. Finite-element analysis of Taylor flow. *AICHE Journal,* 42, 1815-1823.

El-Ali, J., Gaudet, S., Gunther, A., Sorger, P. K. and Jensen, K. F. 2005. Cell stimulus and lysis in a microfluidic device with segmented gas-liquid flow. *Analytical Chemistry,* 77, 3629-3636.

Fairbrother, F. and Stubbs, A. E. 1935. Studies in electro-endosmosis Part VI The "bubble-tube" method of measurement. *Journal of the Chemical Society,* 1, 527-529.

Feng, J. Q. 2009. A long gas bubble moving in a tube with flowing liquid. *International Journal of Multiphase Flow,* 35, 738-746.

Foong, A. J. L., Ramesh, N. and Chandratilleke, T. T. 2009. Laminar convective heat transfer in a microchannel with internal longitudinal fins. *International Journal of Thermal Sciences,* 48, 1908-1913.

Fouilland, T. S. 2008. *Micro PIV measurements and Modelling of Gas-Liquid Flow in Microchannels.* PhD Thesis, The University of Sydney.

Fouilland, T. S., Fletcher, D. F. and Haynes, B. S. 2010. Film and slug behaviour in intermittent slug-annular microchannel flows. *Chemical Engineering Science,* 65, 5344-5355.

Fu, T. T., Ma, Y. G., Funfschilling, D., Zhu, C. Y. and Li, H. Z. 2010a. Squeezing-to-dripping transition for bubble formation in a microfluidic T-junction. *Chemical Engineering Science,* 65, 3739-3748.

Fu, T. T., Funfschilling, D., Ma, Y. and Li, H. Z. 2010b. Scaling the formation of slug bubbles in microfluidic flow-focusing devices. *Microfluidics and Nanofluidics,* 8, 467-475.

Fukagata, K., Kasagi, N., Ua-Arayaporn, P. and Himeno, T. 2007. Numerical simulation of gas-liquid two-phase flow and convective heat transfer in a micro tube. *International Journal of Heat and Fluid Flow,* 28, 72-82.

Garstecki, P., Fuerstman, M. J., Stone, H. A. and Whitesides, G. M. 2006. Formation of droplets and bubbles in a microfluidic T-junction - scaling and mechanism of break-up. *Lab on a Chip,* 6, 437-446.

Geyer, P. E., Rosaguti, N. R., Fletcher, D. F. and Haynes, B. S. 2006. Laminar flow and heat transfer in periodic serpentine mini-channels. *Journal of Enhanced Heat Transfer,* 13, 309-320.

Ghiaasiaan, S. M. and Abdel-Khalik, S. I. 2001. Two-phase flow in microchannels. *In:* Hari, G. G. & Charles, A. H. (eds.) *Advances in Heat Transfer,* 34, 145-254.

Giavedoni, M. D. and Saita, F. A. 1997. The axisymmetric and plane cases of a gas phase steadily displacing a Newtonian liquid - A simultaneous solution of the governing equations. *Physics of Fluids,* 9, 2420-2428.

Goldsmith, H. L. and Mason, S. G. 1963. Flow of suspensions through tubes. II. single large bubbles. *Journal of Colloid Science,* 18, 237.

Günther, A. and Jensen, K. F. 2006. Multiphase microfluidics: from flow characteristics to chemical and materials synthesis. *Lab on a Chip,* 6, 1487-1503.

Guo, F. and Chen, B. 2009. Numerical study on Taylor bubble formation in a micro-channel T-junction using VOF method. *Microgravity Science and Technology,* 21, 51-58.

Gupta, R., Fletcher, D. F. and Haynes, B. S. 2010a. Taylor flow in microchannels: A review of experimental and computational work. *The Journal of Computational Multiphase Flows,* 2, 1-32.

Gupta, R., Fletcher, D. F. and Haynes, B. S. 2010b. CFD modelling of flow and heat transfer in the Taylor flow regime. *Chemical Engineering Science,* 65, 2094-2107

Gupta, R., Hägnefelt, H., Fletcher, D. F. and Haynes, B. S. 2010c. On the importance of buoyancy in Taylor flow in horizontal microchannels. *7th International Conference on Multiphase Flow, ICMF 2010.* Tampa, Florida, USA.

Gupta, R. 2010. *CFD simulations of gas-liquid flow in microchannels.* PhD Thesis, The University of Sydney.

Hägnefelt, H. 2009. *Adiabatic two-phase flow in vertical microchannels: Investigation of gravitational effects in the Taylor flow regime.* Master of Science, Lund University, Sweden.

Han, Y. and Shikazono, N. 2009. Measurement of the liquid film thickness in micro tube slug flow. *International Journal of Heat and Fluid Flow,* 30, 842-853.

He, Q., Hasegawa, Y. and Kasagi, N. 2010. Heat transfer modelling of gas-liquid slug flow without phase change in a micro tube. *International Journal of Heat and Fluid Flow,* 31, 126–136.

Heil, M. 2001. Finite Reynolds number effects in the Bretherton problem. *Physics of Fluids,* 13, 2517-2521.

Hetsroni, G., Mosyak, A., Pogrebnyak, E. and Yarin, L. P. 2005. Fluid flow in micro-channels. *International Journal of Heat and Mass Transfer,* 48, 1982-1998.

Hetsroni, G., Mosyak, A., Pogrebnyak, E. and Segal, Z. 2009. Heat transfer of gas-liquid mixture in micro-channel heat sink. *International Journal of Heat and Mass Transfer,* 52, 3963-3971.

Hewitt, G. F. and Hall-Taylor, N. S. 1970. *Annular two-phase flow,* Oxford, Pergamon Press Ltd.

Hong, Y. P. and Wang, F. J. 2007. Flow rate effect on droplet control in a co-flowing microfluidic device. *Microfluidics and Nanofluidics,* 3, 341-346.

Hong, F. J. and Cheng, P. 2009. Three dimensional numerical analyses and optimization of offset strip-fin microchannel heat sinks. *International Communications in Heat and Mass Transfer,* 36, 651-656.

Horvath, C., Solomon, B. A. and Engasser, J. M. 1973. Measurement of radial transport in slug flow using enzyme tubes. *Industrial & Engineering Chemistry Fundamentals,* 12, 431-439.

Hughmark, G. A. 1965. Holdup and heat transfer in horizontal slug gas-liquid flow. *Chemical Engineering Science,* 20, 1007-1010.

Husny, J. and Cooper-White, J. J. 2006. The effect of elasticity on drop creation in T-shaped microchannels. *Journal of Non-Newtonian Fluid Mechanics,* 137, 121-136.

Ide, H., Kariyasaki, A. and Fukano, T. 2007. Fundamental data on the gas-liquid two-phase flow in minichannels. *International Journal of Thermal Sciences,* 46, 519-530.

Irandoust, S. and Andersson, B. 1989a. Liquid-film in Taylor flow through a capillary. *Industrial & Engineering Chemistry Research,* 28, 1684-1688.

Irandoust, S. and Andersson, B. 1989b. Simulation of flow and mass-transfer in Taylor flow through a capillary. *Computers & Chemical Engineering,* 13, 519-526.

Jensen, M. H., Libchaber, A., Pelce, P. and Zocchi, G. 1987. Effect of gravity on the Saffman-Taylor meniscus - theory and experiment. *Physical Review A,* 35, 2221-2227.

Kandlikar, S. G. 2004. Heat transfer mechanisms during flow boiling in microchannels. *Journal of Heat Transfer-Transactions of the Asme,* 126, 8-16.

Kapteijn, F., Nijhuis, T. A., Heiszwolf, J. J. and Moulijn, J. A. 2001. New non-traditional multiphase catalytic reactors based on monolithic structures. *Catalysis Today,* 66, 133-144.

Kawahara, A., Chung, P. M. Y. and Kawaji, M. 2002. Investigation of two-phase flow pattern, void fraction and pressure drop in a microchannel. *International Journal of Multiphase Flow,* 28, 1411-1435.

Kawahara, A., Sadatomi, M., Nei, K. and Matsuo, H. 2009. Experimental study on bubble velocity, void fraction and pressure drop for gas-liquid two-phase flow in a circular microchannel. *International Journal of Heat and Fluid Flow,* 30, 831-841.

Khan, S. A., Gunther, A., Schmidt, M. A. and Jensen, K. F. 2004. Microfluidic synthesis of colloidal silica. *Langmuir,* 20, 8604-8611.

Kobayashi, J., Mori, Y., Okamoto, K., Akiyama, R., Ueno, M., Kitamori, T. and Kobayashi, S. 2004. A microfluidic device for conducting gas-liquid-solid hydrogenation reactions. *Science,* 304, 1305-1308.

Kreutzer, M. T., Du, P., Heiszwolf, J. J., Kapteijn, F. and Moulijn, J. A. 2001. Mass transfer characteristics of three-phase monolith reactors. *Chemical Engineering Science,* 56, 6015-6023.

Kreutzer, M. T., Van Der Eijnden, M. G., Kapteijn, F., Moulijn, J. A. and Heiszwolf, J. J. 2005a. The pressure drop experiment to determine slug lengths in multiphase monoliths. *Catalysis Today,* 105, 667-672.

Kreutzer, M. T., Kapteijn, F., Moulijn, J. A., Kleijn, C. R. and Heiszwolf, J. J. 2005b. Inertial and interfacial effects on pressure drop of Taylor flow in capillaries. *AIChE Journal,* 51, 2428-2440.

Kreutzer, M. T., Kapteijn, F., Moulijn, J. A. and Heiszwolf, J. J. 2005c. Multiphase monolith reactors: Chemical reaction engineering of segmented flow in microchannels. *Chemical Engineering Science,* 60, 5895-5916.

Laborie, S., Cabassud, C., Durand-Bourlier, L. and Laine, J. M. 1999. Characterisation of gas-liquid two-phase flow inside capillaries. *Chemical Engineering Science,* 54, 5723-5735.

Lakehal, D., Larrignon, G. and Narayanan, C. 2008. Computational heat transfer and two-phase flow topology in miniature tubes. *Microfluidics and Nanofluidics,* 4, 261-271.

Leclerc, A., Philippe, R., Houzelot, V., Schweich, D. and De Bellefon, C. 2010. Gas-liquid Taylor flow in square micro-channels: New inlet geometries and interfacial area tuning. *Chemical Engineering Journal,* 165, 290-300.

Lee, C.Y. and Lee, S.Y. 2008. Influence of surface wettability on transition of two-phase flow pattern in round mini-channels. *International Journal of Multiphase Flow,* 34, 706-711.

Liu, H., Vandu, C. O. and Krishna, R. 2005. Hydrodynamics of Taylor flow in vertical capillaries: Flow regimes, bubble rise velocity, liquid slug length, and pressure drop. *Industrial & Engineering Chemistry Research,* 44, 4884-4897.

Liu, Z. H., Yi, J. and Ma, Z. F. 2006. Experimental investigation of highly effective cooling with an evaporating annular flow in a small vertical tube. *Chemical Engineering Communications,* 193, 1469-1481.

Liu, Y. 2011. *Boiling flow in microchannels.* PhD Thesis, The University of Sydney.

Lockhart, R. W. and Martinelli, R. C. 1949. Proposed correlations of data for isothermal two-phase two-component flow in pipes. *Chemical Engineering Progress,* 45, 39-48.

Muzychka, Y. S., Walsh, E. and Walsh, P. 2011. Heat transfer enhancement using laminar gas-liquid segmented plug flows. *Journal of Heat Transfer,* 133, 041902.

Narayanan, C. and Lakehal, D. 2008. Two-phase convective heat transfer in miniature pipes under normal and microgravity conditions. *Journal of Heat Transfer-Transactions of the ASME,* 130, 074502.

Nijhuis, T. A., Kreutzer, M. T., Romijn, A. C. J., Kapteijn, F. and Moulijn, J. A. 2001. Monolithic catalysts as efficient three-phase reactors. *Chemical Engineering Science,* 56, 823-829.

Nusselt, W. 1916. Des Oberflachenkondensation des Wasserdamfes. *Z. Vereines Deutsch. Ing.,* 60 (541–564), 569–575.

Oliver, D. R. and Wright, S. J. 1964. Pressure drop and heat transfer in gas-liquid slug flow in horizontal tubes. *British Chemical Engineering* 9, 590-596.

Oliver, D. R. and Young Hoon, A. 1968. Two-phase non-Newtonian flow II. Heat transfer. *Tran. Instn. Chem. Engrs* 46, 116-122.

Park, H. S. and Punch, J. 2008. Friction factor and heat transfer in multiple microchannels with uniform flow distribution. *International Journal of Heat and Mass Transfer,* 51, 4535-4543.

Pehlivan, K., Hassan, I. and Vaillancourt, M. 2006. Experimental study on two-phase flow and pressure drop in millimeter-size channels. *Applied Thermal Engineering,* 26, 1506-1514.

Qian, D. Y. and Lawal, A. 2006. Numerical study on gas and liquid slugs for Taylor flow in a T-junction microchannel. *Chemical Engineering Science,* 61, 7609-7625.

Rosaguti, N. R., Fletcher, D. F. and Haynes, B. S. 2007. Low-Reynolds number heat transfer enhancement in sinusoidal channels. *Chemical Engineering Science,* 62, 694-702.

Saisorn, S. and Wongwises, S. 2008. Flow pattern, void fraction and pressure drop of two-phase air-water flow in a horizontal circular micro-channel. *Experimental Thermal and Fluid Science,* 32, 748-760.

Santos, R. M. and Kawaji, M. 2010. Numerical modeling and experimental investigation of gas-liquid slug formation in a microchannel T-junction. *International Journal of Multiphase Flow,* 36, 314-323.

Serizawa, A., Feng, Z. P. and Kawara, Z. 2002. Two-phase flow in microchannels. *Experimental Thermal and Fluid Science,* 26, 703-714.

Shah, R. K. and London, A. L. 1978. *Laminar flow forced convection in ducts,* New York.

Shao, N., Salman, W., Gavriilidis, A. and Angeli, P. 2008. CFD simulations of the effect of inlet conditions on Taylor flow formation. *International Journal of Heat and Fluid Flow,* 29, 1603-1611.

Shao, N., Gavriilidis, A. and Angeli, P. 2009. Flow regimes for adiabatic gas-liquid flow in microchannels. *Chemical Engineering Science,* 64, 2749-2761.

Song, H., Tice, J. D. and Ismagilov, R. F. 2003. A microfluidic system for controlling reaction networks in time. *Angewandte Chemie-International Edition,* 42, 768-772.

Sun, T. F. and Teja, A. S. 2003. Density, viscosity and thermal conductivity of aqueous ethylene glycol, diethylene glycol, and triethylene glycol between 290 K and 450 K. *Journal of Chemical and Engineering Data,* 48, 198-202.

Suo, M. and Griffith, P. 1964. Two-phase flow in capillary tubes. *Journal of Basic Engineering,* 86, 576-582.

Suresh, V. and Grotberg, J. B. 2005. The effect of gravity on liquid plug propagation in a two-dimensional channel. *Physics of Fluids,* 17.

Taha, T. and Cui, Z. F. 2004. Hydrodynamics of slug flow inside capillaries. *Chemical Engineering Science,* 59, 1181-1190.

Taylor, G. I. 1961. Deposition of a viscous fluid on the wall of a tube. *Journal of Fluid Mechanics,* 10, 161-165.

Thiers, R. E., Reed, A. H. and Delander, K. 1971. Origin of lag phase of contnuous-flow analysis curves. *Clinical Chemistry,* 17, 42-48.

Thome, J. R. 2004. Boiling in microchannels: a review of experiment and theory. *International Journal of Heat and Fluid Flow,* 25, 128-139.

Thorsen, T., Roberts, R. W., Arnold, F. H. and Quake, S. R. 2001. Dynamic pattern formation in a vesicle-generating microfluidic device. *Physical Review Letters,* 86, 4163-4166.

Thulasidas, T. C., Abraham, M. A. and Cerro, R. L. 1995. Bubble -train flow in capillaries of circular and square cross-section. *Chemical Engineering Science,* 50, 183-199.

Thulasidas, T. C., Abraham, M. A. and Cerro, R. L. 1997. Flow patterns in liquid slugs during bubble-train flow inside capillaries. *Chemical Engineering Science,* 52, 2947-2962.

Triplett, K. A., Ghiaasiaan, S. M., Abdel-Khalik, S. I. and Sadowski, D. L. 1999a. Gas-liquid two-phase flow in microchannels - Part I: two-phase flow patterns. *International Journal of Multiphase Flow,* 25, 377-394.

Triplett, K. A., Ghiaasiaan, S. M., Abdel-Khalik, S. I., Lemouel, A. and Mccord, B. N. 1999b. Gas-liquid two-phase flow in microchannels - Part II: void fraction and pressure drop. *International Journal of Multiphase Flow,* 25, 395-410.

Van Steijn, V., Kreutzer, M. T. and Kleijn, C. R. 2007. μ-PIV study of the formation of segmented flow in microfluidic T-junctions. *Chemical Engineering Science,* 62, 7505-7514.

Van Steijn, V., Kleijn, C. R. and Kreutzer, M. T. 2010. Predictive model for the size of bubbles and droplets created in microfluidic T-junctions. *Lab on a Chip,* 10, 2513-2518.

Vrentas, J. S., Duda, J. L. and Lehmkuhl, G. D. 1978. Characteristics of radial transport in solid-liquid slug flow. *Industrial & Engineering Chemistry Fundamentals,* 17, 39-45.

Waelchli, S. and Von Rohr, P. R. 2006. Two-phase flow characteristics in gas-liquid microreactors. *International Journal of Multiphase Flow,* 32, 791-806.

Walsh, E., Muzychka, Y., Walsh, P., Egan, V. and Punch, J. 2009. Pressure drop in two phase slug/bubble flows in mini scale capillaries. *International Journal of Multiphase Flow,* 35, 879-884.

Walsh, P. A., Walsh, E. J. and Muzychka, Y. S. 2010. Heat transfer model for gas-liquid slug flows under constant flux. *International Journal of Heat and Mass Transfer,* 53, 3193-3201.

Warnier, M. J. F., Rebrov, E., De Croon, M., Hessel, V. and Schouten, J. C. 2008. Gas hold-up and liquid film thickness in Taylor flow in rectangular microchannels. *Chemical Engineering Journal,* 135, S153-S158.

Warnier, M. J. F., De Croon, M., Rebrov, E. V. and Schouten, J. C. 2010. Pressure drop of gas-liquid Taylor flow in round micro-capillaries for low to intermediate Reynolds numbers. *Microfluidics and Nanofluidics,* 8, 33-45.

Xiong, R. Q., Bai, M. and Chung, J. N. 2007. Formation of bubbles in a simple co-flowing micro-channel. *Journal of Micromechanics and Microengineering,* 17, 1002-1011.

Xu, J. H., Li, S. W., Tan, J., Wang, Y. J. and Luo, G. S. 2006a. Controllable preparation of monodisperse O/W and W/O emulsions in the same microfluidic device. *Langmuir,* 22, 7943-7946.

Xu, J. H., Li, S. W., Tan, J., Wang, Y. J. and Luo, G. S. 2006b. Preparation of highly monodisperse droplet in a T-junction microfluidic device. *AIChE Journal,* 52, 3005-3010.

Xu, J. H., Luo, G. S., Li, S. W. and Chen, G. G. 2006c. Shear force induced monodisperse droplet formation in a microfluidic device by controlling wetting properties. *Lab on a Chip,* 6, 131-136.

Xu, J. H., Li, S. W., Tan, J. and Luo, G. S. 2008. Correlations of droplet formation in T-junction microfluidic devices: from squeezing to dripping. *Microfluidics and Nanofluidics,* 5, 711-717.

Yang, C. Y. and Shieh, C. C. 2001. Flow pattern of air-water and two-phase R-134a in small circular tubes. *International Journal of Multiphase Flow,* 27, 1163-1177.

Yue, J., Luo, L. G., Gonthier, Y., Chen, G. W. and Yuan, Q. 2008. An experimental investigation of gas-liquid two-phase flow in single microchannel contactors. *Chemical Engineering Science,* 63, 4189-4202.

Zhao, T. S. and Bi, Q. C. 2001. Co-current air-water two-phase flow patterns in vertical triangular microchannels. *International Journal of Multiphase Flow,* 27, 765-782.

Zheng, Y., Fujioka, H. and Grotberg, J. B. 2007. Effects of gravity, inertia, and surfactant on steady plug propagation in a two-dimensional channel. *Physics of Fluids,* 19, 082107.

Appendix A: Micro-Particle Image Velocimetry (μPIV) System

Setup

A picture of the actual μPIV system from ILA is given in Figure A1, and consists of a dual cavity diode pumped Nd:YLF laser (New Wave Research, Inc., Pegasus), an inverted epi-fluorescent microscope (Olympus IX71), a high-speed PIV camera (Photron Fastcam 1024 PCI) and a control system (ILA synchroniser) synchronising the cameras with the laser pulses for high speed measurements. Another setup with side-positioned microscope is used in this thesis to study both vertical and horizontal flows, as seen in Figure A2.

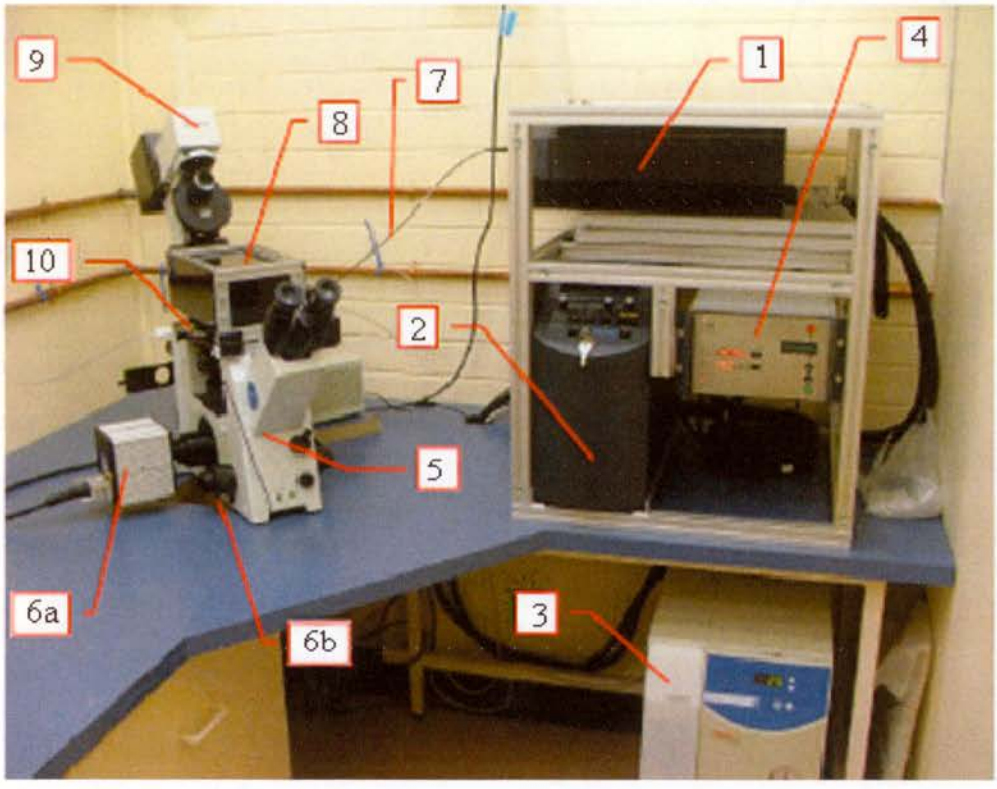

Figure A1: A detailed description of the μPIV system in the laboratory. (1) Dual cavity, (2) Power supply and control unit, (3) Chiller, (4) ILA synchroniser, (5) Epi-fluorescent microscope, (6a & b) High-speed PIV cameras, (7) Optic fibre, (8) Beam trap, (9) Illumination pillar and (10) Test section. Taken from Fouilland (2008).

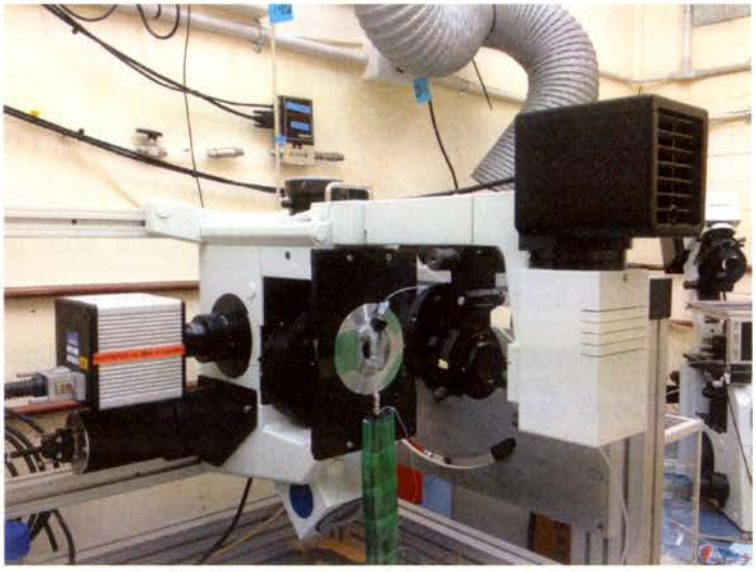

Figure A2: The vertical microscope setup used in this work.

Data analysis

Images were recorded using this μPIV system with a 10× objective giving an area of view of 1.74×1.74 mm^2 at full 1024×1024 pixels resolution. Raw images were pre-processed using the ImageJ software to improve the image contrast by removing low-intensity images of out-of-focus particles, before they were analysed using the Vidpiv software package from ILA to yield velocity fields. As shown in Figure A3, the Vidpiv software has a tree-type interface where each node represents a particular function.

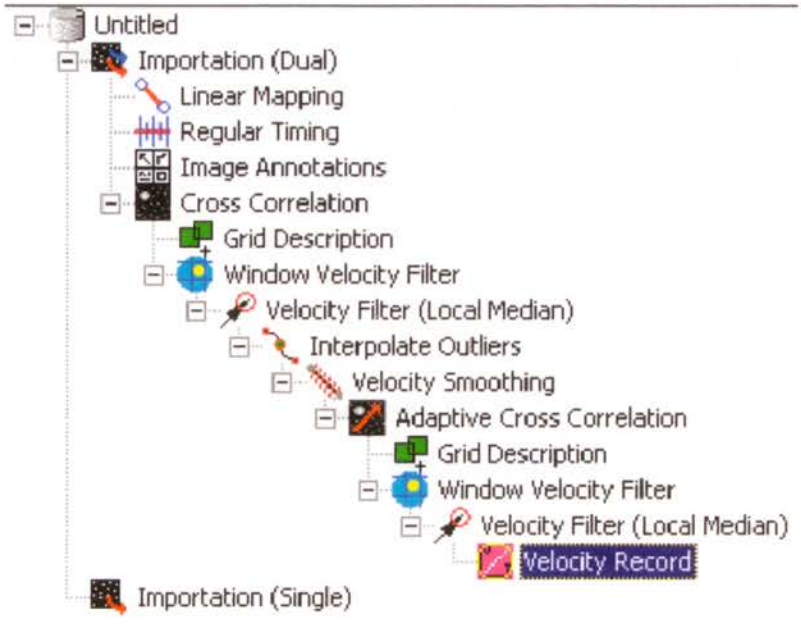

Figure A3: Typical post-processing tree of Vidpiv from ILA.

After importing image pairs via the Importation (Dual) node, the Linear Mapping node is used for scaling the pixel unit to real units based on a calibration image (i.e. image of a micro-ruler) imported via the Importation (Single) node. The timing information of the acquired images, such as the measurement frequency and the pulse interval, is edited through the Regular Timing node. Image Annotations node is employed to mask regions without valid data or corresponding to flow boundaries. The image is then divided into small interrogation regions which generally overlapped by 50%, and a cross-correlation algorithm (based on a Fast Fourier transform) is used to estimate statistically the average displacement of the particles in each interrogation window. The size of the interrogation window depends on the particle concentration and on the magnitude of the particle displacement (64 pixels × 64 pixels with spatial resolution 110 μm × 110 μm were used for most cases). The Cross Correlation node is followed by a global and a local filter functions to remove the scattered values in the vector map. The Window Velocity Filter node (global) discriminates the individual vectors by comparing whether they are consistent or not with the whole vector map. The Velocity Filter (Local Median) node filters the remaining erroneous velocity vectors by comparing whether they are consistent with their nearest neighbours.

To improve the accuracy of the PIV measurements, an adaptive cross-correlation method, which uses a complex interrogation window deformation technique, is used. First a complete vector map is generated by replacing filtered vectors using an interpolation and a velocity smoothing functions (Interpolate Outliers node and Velocity Smoothing node) to achieve a higher data density. Then the adaptive cross-correlation with smaller interrogation areas (32 pixels × 32 pixels with spatial resolution 55 μm × 55 μm) is performed to generated vector map with higher spatial resolution. Finally, the Velocity Recording node enables the export of velocity data as a function of time to Excel to enable the determination of average mean velocity field.

Measurement depth

Based on the assumption that only particles observed with intensities above 10% of the maximum contribute to the measurement, Meinhart *et al.* (2000) provided a formula (Eq. A1) to estimate the measurement depth z_{corr}.

$$z_{corr} = \frac{3(RI)\lambda_0}{(NA)^2} + \frac{2.16 d_{particle}}{\tan\theta} + d_{particle} \qquad (A1)$$

where RI is the refractive index of the imaging medium, λ_0 is the wavelength of the imaged light in vacuum, NA is the numerical aperture of the microscope objective, θ is the light collecting angle of the microscope objective ($NA = n \sin\theta$) and $d_{particle}$ is the fluorescent particle diameter.

According Eq. A1, the measurement depth achieved with a 10×, 0.3 N.A. objective with 3 μm particles suspended in ethylene glycol (RI = 1.432) is of the order of 40 μm. However, the images were pre-processed (ImageJ) to eliminated low-intensity out-of-focus particles. Therefore, the effective depth of measurement is < 20 μm.

The focusing knob of the microscope was motorised using a step motor to enable probing of velocity data at different chosen depths (z). Each step of the motor corresponded to 1 μm displacement. The actual distance between two probing locations, Δz, is determined as

$$\Delta z = 1.432 N_S \qquad (A2)$$

where 1.432 is the refractive index of ethylene glycol and N_S is the number of steps which the objective is moved with the step motor.

Taylor flow PIV measurement

Due to limitations in the micro-PIV technique, it is not possible to measure velocities of the near wall liquid in the bubble and slug regions at the same time. To obtain velocity profiles in the liquid film, the PIV conditions (pulse separation) and analysis procedure (image pre-processing) were optimized to resolve film velocities during the passage of gas bubbles. For each flow condition, the measurements were carried out at different depths in the liquid film from the wall to the gas-liquid interface. At each depth about 500 pairs of images, covering the passage of at least four gas bubbles, were recorded and analysed. Only a small region of the flow close to the horizontal centreline of the channel was used for the PIV analysis to yield an instantaneous average velocity, $v(z,t)$. A drainage velocity profile in the liquid film was then established by taking the average drainage velocity across the bubbles at each depth.

To study the effect of gravitation on the flow field inside the liquid slug region, the PIV conditions and analysis procedure were optimized to measure the slug velocity at the vertical channel centre.